



**I  
N  
A  
O  
E**

**Environmental Effects on the  
Physical Properties of Galaxies:  
Clues to the Formation of S0  
Galaxies**

by

**Christopher Añorve-Solano**

**A thesis submitted to the Instituto Nacional  
de Astrofísica, Óptica y Electrónica  
for the degree of Doctor of Philosophy  
in the department of Astrophysics.**

**Supervisors:  
Dr. Omar López-Cruz  
Dr. James Wadsley**

**Sta. Ma. Tonantzintla, Pue.  
July, 2012**

**©INAOE 2012  
El autor otorga al INAOE el permiso  
de reproducir y distribuir copias en su  
totalidad o en partes de esta tesis**





ENVIRONMENTAL EFFECTS ON THE PHYSICAL  
PROPERTIES OF GALAXIES:  
CLUES TO THE FORMATION OF S0 GALAXIES

Christopher Añorve-Solano



# *Abstract*

In this thesis, we have investigated the origin of S0 galaxies and the density morphology relation (DMR Dressler 1980b). The DMR states that elliptical and S0 galaxies inhabit regions of high galaxy density, such as clusters of galaxies. Many scenarios try to explain this relation, and range from environmental effects to clusters' intrinsic properties. Among the identified environmental effects are tidal effects, galaxy harassment, ram pressure, starvation, galaxy encounters, or thermal evaporation. To address this problem, we have analyzed the structure of galaxies of low-redshift ( $z$ ) X-ray selected Abell Clusters, using  $R$ -band wide field CCD images obtained with the Kitt Peak National Observatory (KPNO) 0.9 m telescope. We have developed the Driver for GALFIT on Cluster Galaxies (DGCG), a script program in PERL to drive GALFIT code (Peng et al. 2002) almost automatically on crowded fields. DGCG has build-in routines to select objects, and depending on their proximity it can either mask or model neighboring objects. We have tested DGCG with synthetic models of galaxies, and have shown that the simultaneous fitting approach is better than the masking method for galaxies that are close together in the line of sight. The final sample contains 1453 galaxies out of 2419 from 21 galaxy clusters from the Low-Redshift Optical Cluster Survey (LOCOS López-Cruz et al. 2004). DGCG fitted 2419 galaxies using two approaches: a single Sérsic model and two-component model (Sérsic + Exponential). As a result, 2227 (92%) galaxies have reached suitable models. As an important part of this thesis, we have proposed a new classification scheme by combining bulge to total luminosity ratio, axis ratio, bumpiness and Sérsic index, which has allowed us to segregate three classes: spiral, S0 and elliptical (S-S0-E) galaxies. We used Dressler (1980a) classifications to calibrate this proposed classification method. We have recovered the DMR, the Kormendy relation (KR), the luminosity-size relation (LSR), the Faber-Jackson relation (FJR), and the fundamental plane (FP). We have identified bulges and pseudobulges using the KR; this has allowed us to discover that the FJR can also be used to segregate pseudobulges from bulges. The FP for bulges and pseudobulges have different slopes. Using the distribution of the Sérsic index and the surface brightness profiles by morphological type, we have provided evidence that gravitational dynamical processes formed S0 galaxies. These processes include tidal truncation, galaxy harassment, and the mean effect of the global cluster gravitational field; ram pressure is unnecessary, but we briefly explored it with SPH simulations. We have proposed that spirals evolve into S0 galaxies by dynamical processes in which the bulge modifies their structure.



# *Resumen*

En esta tesis, se investigó el origen de las galaxias S0 y la relación densidad morfología (DMR Dressler 1980b). La DMR establece que galaxias elípticas y S0 habitan en las regiones de alta densidad galáctica, como lo son los cúmulos de galaxias. Muchos son los escenarios que tratan de explicar esta relación, que van desde los efectos ambientales hasta las propiedades intrínsecas de los cúmulos. De los efectos ambientales identificados están los efectos de marea, interacciones entre galaxias, presión de barrido, inanición galáctica, fusiones entre galaxias, o evaporación térmica. Para hacer frente a este problema, se analizó la estructura de galaxias de cúmulos de Abell de bajo corrimiento al rojo ( $z$ ), usando la banda  $R$  de imágenes CCD obtenidas con el telescopio de 0.9 metros del observatorio nacional de Kitt Peak (KPNO). Para lograr este objetivo, se elaboró el programa "Manejador de GALFIT en cúmulos de galaxias" (DGCG), este es un programa script escrito en PERL para controlar GALFIT (Peng et al. 2002) casi automáticamente en campos densos. DGCG tiene rutinas hechas para seleccionar objetos y dependiendo de la proximidad entre estos puede enmascarar o modelar las galaxias vecinas. Se probó el código DGCG con modelos de galaxias sintéticas, y se comprobó que el ajuste simultáneo es mejor aproximación que el método de enmascaramiento para galaxias que están demasiado cercas en la línea de visión. La muestra final contiene 1453 galaxias de un total de 2419 de 21 cúmulos de galaxias tomadas de la base de datos Low-Redshift Optical Cluster Survey (LOCOS López-Cruz et al. 2004). DGCG ajustó 2419 galaxias usando dos aproximaciones: un modelo único de Sérsic y un modelo de dos componentes (Sérsic + exponencial). Como resultado, 2227 (92%) galaxias lograron modelos adecuados. Como una parte importante de esta tesis, se propuso un nuevo esquema de clasificación al comparar la razón entre la luminosidad del bulbo y la total, razón de los ejes, protuberancias de la galaxia, y el índice de Sérsic. Esto nos permitió segregar tres clases: galaxia espiral, S0 y elíptica (S-S0-E). Se usaron las clasificaciones de Dressler (1980a) para calibrar este método. Se recuperaron la DMR, la relación de Kormendy (KR), la relación luminosidad tamaño (LSR), la relación Faber-Jackson (FJR), y el plano fundamental (FP). Se identificaron bulbos y pseudobulbos usando la KR; esto nos ha permitido descubrir que la FJR puede ser usada para separar pseudobulbos de bulbos. El FP para bulbos y pseudobulbos tienen diferentes pendientes. Usando la distribución del índice de Sérsic y los perfiles de brillo superficial por tipo morfológico, hemos proveido evidencia de que los procesos dinámicos gravitacionales formaron a las galaxias S0. Estos procesos incluyen la truncación por marea, interacciones entre galaxias, y el efecto global del potencial gravitacional del cúmulo; la presión de barrido no es necesaria, pero se exploró brevemente con simulaciones de SPH. Se propone que las galaxias espirales evolucionan en galaxias

S0 mediante procesos dinámicos en los cuales el bulbo modifica su estructura.

*The more I examine the universe and the details of its architecture, the more evidence I find that the universe in some sense must have known we were coming.*

- Freeman Dyson

*A l'alta fantasia qui manc possa;  
ma gi volgeva il mio disio e 'l velle,  
s come rota ch'igualmente mossa,  
l'amor che move il sole e l'altre stelle.*

- Dante Alighieri. *La Divina Commedia*.

*Don't tell me it's impossible, tell me you can't do it. Tell me it's never been done ... the only things we really know are Maxwell's equations, the three laws of Newton, the two postulates of relativity, and the periodic table. That's all we know that's true. All the rest are man's laws.*

- Dean Kamen.



## *Agradecimientos*

En primer lugar quiero agradecer a mi familia, ya que sin la formación y el apoyo que recibí de ellos no estaría haciendo lo que mas me gusta. Todos fueron parte importante para mí especialmente mi Mamá, mi hermana Marcia, mi sobrinos Paola y Edgar, y aquellas dos personas que ya no estan conmigo y que me motivaron a estar en este camino: mi hermano Edgar Gilberto y mi Papá, que en paz descansen.

También quiero agradecer al Conacyt ya que sin la beca otorgada, esta tesis no hubiera sido posible.

La estancia en este instituto fue muy agradable y me ofreció un buen lugar para formar de la mejor manera mi carrera como investigador. Cada uno del personal del instituto me ofreció su ayuda cuando lo necesitaba. A todo el INAOE muchas gracias.

Muchas gracias a mis amigos cercanos y no tan cercanos que me apoyaron a lo largo de este proceso. Especialmente quiero mencionar a Johnathan León, Alfredo Montaña, Joel Molina, Gloria Delgado, Giannina Dalle Mese, Mario Lopez, José Luis Barajas, Alejandro de Jesus, Joaquín Alvira, Teresa Zamora, Guillermo Herrera, Hector Alonso, Gerardo Moreno, José Gutierrez, Lissy Garcia, Tessa Eckholm, Vahram Chavushyan, Mirna Medrano, Hector Becerra, Martha Bello, Izbeth Hernandez, Miguel Chavez, Juan Carlos Gomez, Joannes Bosco Hernandez, Ana Torres, Francisco Ucán, Sofia Paredes, Jorge Lopez Coronado, Susana Torres, Pedro Aaron, David Romero, Dayana Peñalver, Virgilio, Joel Herrera, Rachael Sills, Liliana Perea, Ezequiel Molinar, Moises Moreno, Edgar Colín, Ricardo Chavez, Roberto Romano Felipe Perez, Javier Osorio, Rogelio Cuevas, Luis Villalvazo, Edgar Jimenez, Emmanuel Acuña, Sergei Garcia, Toño Leal, Violeta Flores, Dunia Cruz, Máximo Rivera, Bernardo Rivera, Miguel Bello, Rosa López, Salvador Cortes, Edgar Huante, Naina Rao, Marco Gurrola, Oscar Aguilar, Karla Puga, Oscar Hernández, Juan de Dios Alvarez, Milagros Zeballos, David Sanchez, Emmaly, Salvador Ventura, Enrique Aguayo, Victor Carrillo, Cesar Gomez, Lenia Rosas, Hashem Ali, Mehdi Sanjari, Elena Armenteros, Malek Han-

nouf, Pablo Gallego, Alicia Morales, Ivan Candelas, Karla Nieves, Hector Ibarra, Juan Pablo Torres Papaqui, Rosario Porras, Toño Novoa, Juan Carlos Marquez, Olga Barrios, Olga Vega, Daniel Rosa, Miguel Angel Aragón, Julio Zamora, Julio Guzmán, Ibrahím Gutiérrez, Salvador Revelo, Fernando Maciel, Patrick Rogers, Daid Kahl, Yari Juarez, Nathan Leigh, Luis Morales, Greg Stinson, Sijing Shen, Nicolas Petitclerc, Kristin Woodley, Ricardo Retes, Mayra Santiago y Víctor de la Luz. Al último, sin restar importancia y mucho mas que una amiga, agradezco a Karla Gonzalez porque de alguna manera siempre me apoyo desde antes de comenzar.

Un agradecimiento especial a mi asesor de tesis, Omar López-Cruz por haberme guiado en el camino de la astronomía. Agradezco también a mi asesor externo James Wadsley por darme la oportunidad de usar el código Gasoline y permitirme realizar una estancia en Canadá en la cual aprendí mucho tanto en ciencia y como experiencia personal. También un agradecimiento especial para Chien Peng por haber creado el fabuloso programa GALFIT del cual esta tesis no haya sido posible y por haber respondido a todos mis correos electrónicos cuando solicitaba ayuda.

A mis sinodales Carlos del Burgo, Niv Drory, Felipe Barrientos, Raul Mújica y Elsa Recillas muchas gracias por sus comentarios y correcciones.

Definitivamente este trabajo no se habría podido realizar sin la colaboración de muchas personas que me brindaron su ayuda; siempre resulta difícil agradecer a todos aquellos que de una u otra manera me han acompañado en el desarrollo de esta investigación, porque nunca alcanza el tiempo, el papel o la memoria para mencionar o dar con justicia todos los créditos y méritos a quienes se lo merecen. Por lo tanto, quiero agradecer a esa persona que se me olvidó mencionar pero que de alguna manera me ayudo en esta tesis, ya sea en alguna discusión de los resultados, me apoyo cuando estaba decaído, me puso de buen humor para poder seguir trabajando, o simplemente se interesó sobre mi investigación. Así que gracias a todos aquellos que ayudaron para que este trabajo saliera adelante de la mejor manera posible.

**A mi familia**  
**Con dedicación especial para Edgar y Gilberto**



# Contents

<b>1</b>	<b><i>Introduction</i></b>	<b>1</b>
1.1	Galaxy Formation in a Cosmological Context . . . . .	2
1.2	Classification of Galaxies . . . . .	3
1.2.1	Galaxy Classification Systems . . . . .	5
1.2.2	Automatic Classification of Galaxies . . . . .	8
1.2.3	Eyeball Classification of Galaxies . . . . .	10
1.3	Properties of Galaxies . . . . .	11
1.3.1	Properties of E Galaxies . . . . .	11
1.3.2	Properties of S Galaxies . . . . .	12
1.3.3	Properties of S0 Galaxies . . . . .	12
1.3.4	Properties of Bulges . . . . .	13
1.4	Clusters of Galaxies . . . . .	14
1.4.1	Galaxy Cluster Classification . . . . .	15
1.5	Physical Processes in Clusters . . . . .	17
1.5.1	Ram Pressure Stripping . . . . .	17
1.5.2	Galaxy-Galaxy interaction . . . . .	18
1.5.3	Tidal Truncation by the Mean Gravitational Potential of the Cluster	19
1.5.4	Merging of sub-clusters . . . . .	19
1.5.5	Starvation . . . . .	19
1.5.6	Thermal evaporation . . . . .	20
1.6	This Thesis . . . . .	20
1.6.1	Motivation . . . . .	20
1.6.2	Problems Addressed in this Thesis . . . . .	20
1.6.3	Problems not covered in this Thesis . . . . .	21
1.6.4	General Outline . . . . .	21
<b>2</b>	<b><i>Observations and Data Reductions</i></b>	<b>23</b>
2.1	Sample Selection Criteria . . . . .	23

2.2	Observations . . . . .	24
2.3	Data Reductions . . . . .	25
2.4	Photometric Reductions . . . . .	26
2.4.1	Object Finding and Photometry . . . . .	26
2.4.2	Object Finding . . . . .	26
2.4.3	Photometry . . . . .	27
2.4.4	Color Determination . . . . .	28
2.4.5	Star/Galaxy Classification . . . . .	29
2.4.6	Transformation to the Kron-Cousins Standard System . . . . .	30
2.4.7	$\kappa$ -correction and correction for galactic absorption . . . . .	30
2.4.8	Absolute Magnitude . . . . .	31
2.5	Cluster and Galaxy Velocities . . . . .	32
2.6	Selected Clusters for this Thesis . . . . .	32
2.7	Summary . . . . .	32
<b>3</b>	<b><i>Methodology: The Driver for GALFIT on Cluster Galaxies (DGCG)</i></b>	<b>35</b>
3.1	Surface Brightness Models . . . . .	35
3.2	Surface Brightness Fitting . . . . .	37
3.2.1	GALFIT . . . . .	38
3.3	A New Approach to Fit Surface Brightness Models to Cluster Galaxies: DGCG . . . . .	40
3.3.1	Preparation of Inputs for DGCG . . . . .	40
3.3.2	DGCG: The Algorithm . . . . .	44
3.3.3	Other wrapping scripts: GALAPAGOS, SIGMA and PYMORPH . . . . .	53
3.4	DGCG Performance: Surface Brightness Photometry on Artificial Galaxies . . . . .	56
3.4.1	Fits on GEMS artificial galaxies (Bulge only) . . . . .	56
3.4.2	Fits on artificial galaxies (Bulge + Disk models) . . . . .	59
3.5	Summary . . . . .	61
<b>4</b>	<b><i>Results: Magnitudes, Catalog, and a New Quantitative Classification Scheme</i></b>	<b>63</b>
4.1	Model Fitting Results . . . . .	64
4.1.1	DGCG Performance . . . . .	64
4.1.2	Selection of the Best Fits . . . . .	64
4.1.3	Signal to Noise Ratio of our Sample . . . . .	66
4.1.4	Magnitude Comparison: GALFIT vs. PPP . . . . .	66
4.2	Morphological Classification of Galaxies . . . . .	68

4.2.1	A New Classification Method: B/T, BPN, Sérsic index and Axis Ratio . . . . .	69
4.3	Disks in Elliptical Galaxies and the Modified Bayesian Information Criterion	72
4.3.1	Ellipticals with one component (Single Bulges) . . . . .	74
4.3.2	Es with two components (Embedded disks) . . . . .	81
4.4	Final Catalog . . . . .	98
4.5	Summary . . . . .	101
<b>5</b>	<b><i>Analysis: Scaling Relations, Structural Properties of Cluster Galaxies and the Formation of S0 Galaxies</i></b>	<b>103</b>
5.1	Galaxy Scaling Laws . . . . .	103
5.1.1	Density-Morphology Relation . . . . .	104
5.1.2	The Kormendy Relation . . . . .	106
5.1.3	Luminosity-Size Relation . . . . .	108
5.1.4	Color-Magnitude Relation . . . . .	111
5.1.5	The Faber-Jackson Relation . . . . .	113
5.1.6	Fundamental Plane and its Dispersion . . . . .	114
5.1.7	Correlations Suggested in Modern Works . . . . .	118
5.2	Structural Properties of Cluster Galaxies: Clues to the formation of S0 Galaxies . . . . .	118
5.2.1	Distribution of Sérsic Index . . . . .	119
5.2.2	$B - R$ Color and Structural Properties . . . . .	120
5.2.3	Luminosity vs Sérsic Index . . . . .	122
5.2.4	Are S0 Galaxies originated by Ram Pressure? . . . . .	123
5.3	Discussion . . . . .	134
5.3.1	Structural Properties of Galaxies in Clusters at Low Redshift . . . . .	134
5.3.2	Important Physical Processes acting on Cluster Galaxies . . . . .	136
5.3.3	How are S0 galaxies formed? . . . . .	137
<b>6</b>	<b><i>Conclusions and Suggestions for Future Work</i></b>	<b>139</b>
6.1	Conclusions . . . . .	139
6.2	Future Work . . . . .	143
<b>A</b>	<b><i>The Levenberg Marquardt algorithm</i></b>	<b>147</b>
<b>B</b>	<b><i>The Sérsic Profile: A Mathematical Reference</i></b>	<b>149</b>
<b>C</b>	<b><i>Maximum distance allowed for Galaxies to remain in the Sample</i></b>	<b>157</b>

<i>D</i> <i>How to Use DGCG</i>	159
<i>E</i> <i>Hydrodynamical Simulations of Ram Pressure Stripping</i>	167
E.1 Introduction . . . . .	167
E.2 Description of the Code . . . . .	168
E.3 Simulations . . . . .	168
E.4 Results . . . . .	170
E.5 Future work . . . . .	172
E.6 Conclusions . . . . .	173
<i>F</i> <i>DGCG Main Code</i>	175

# 1 *Introduction*

Galaxies are pleasant to the eye; we enjoy their symmetry and their capricious shapes. As we trace them to the largest distances, some of them seem to be completely formed. After a second examination, however, one can begin to wonder about the processes which could have shaped them up. Questions that could come to mind are: Is it gravity the main driver that determines their morphology? Is the morphology of a given galaxy relevant to understand their formation? In recent years, we have gathered some evidence, which seems to indicate that we are progressing towards unlocking the secret of galaxy formation.

Clusters of galaxies have been considered laboratories for the study of galaxy evolution (Dressler 1984; Borgani 2004). They are the unique places where galaxies are exposed to different physical processes induced by the environment. The outcome of such processes has been observed: cluster galaxies exhibit properties that set them apart from field galaxies.

Since the pioneering work of Wolf (1906), it is known that early-type galaxies tend to populate the denser regions of the galaxy clusters. Dressler (1980b) quantified this property by establishing that the number of early-type galaxies and  $S_0$  increases with local density. This is now called the density-morphology relation (DMR) or the Dressler relation. Baum (1959) observed that early-type galaxies were not scaled-up versions of globular clusters. Hand rather, the stellar make-up of early-type galaxies was different from globular clusters. Baum also noticed that as he observed brighter early-type galaxies, their respective colors were redder than the fainter ones. This is the so called color-magnitude relation (CMR). Measurements for larger samples of galaxies and applications of the CMR were developed by Sandage & Visvanathan (Visvanathan & Sandage 1977; Sandage & Visvanathan 1978a,b) using photoelectric aperture photometry. The universality of the CMR was suggested by Sandage & Visvanathan (1978b) and Bower et al. (1992) and generalized by López-Cruz et al. (2004). Dressler et al. (1997) showed that that DMR was set in place at  $z > 3$ . This epoch is similar for the formation of the CMR (e.g., Bower et al. 1992; Gladders et al. 1998). However, the proportion of  $S_0$  has dramatically increased at low  $z$ . The morphological mixture varies among clusters. Irregular clusters have a higher population of spiral galaxies (S) than the regular ones. Regular clusters seem to be more evolved than the irregular ones, close to dynamical equilibrium. An evolutionary sequence from irregular-to-regular galaxy distribution in clusters was suggested from morphological studies (Sarazin 1988) and by incipient N-body simulations (e.g., White 1976).

It has been suggested that S galaxies turn into  $S_0$  galaxies through mechanisms that are

particular to galaxy clusters. It is important to test this hypothesis in order to identify the main driver mechanism that induces this morphological transformation. Ram pressure stripping (Gunn & Gott 1972) has been invoked as the main mechanism of formation of S0 galaxies. In this mechanism, the ram pressure<sup>1</sup> causes a strong drag force on S galaxy, which is stripped from its hot gas by its interaction with the intracluster medium (ICM)<sup>2</sup> as it moves inside the cluster. Although widely popular and accepted, the ram pressure model suffers from a nagging drawback: S0 galaxies are also found in groups or in the field where there is little hot gas to interact with them.

In this thesis, we have found evidence that suggests that ram pressure stripping is not the main driver for S0 galaxy formation. Instead, we suggest that tidal stripping, orbital heating and other dynamical mechanisms such as mergers, harassment are more important during the early phases of cluster assembling. These findings are in agreement and support the earlier ideas of Dressler (1980b).

## 1.1 Galaxy Formation in a Cosmological Context

About  $13.75 \pm 0.11$  Gyr ago, the Universe was hot and dense (Jarosik et al. 2011). As it began to expand, the density and the temperature dropped. During the early phases, the Universe was highly homogeneous but included very tiny perturbations. Those small perturbations in the density field collapsed and coalesced to form the first halos. These halos are believed to be dominated by dark matter (DM) (Trimble 1987).

Baryons followed the collapse of dark matter halos, via different processes such as cooling, star formation and feedback. We believe that those processes regulate galaxy formation (e.g., White & Rees 1978). In order to conserve angular momentum, gas settles down in rotating disks. Star formation is regulated by supernovae feedback, although the assembling of the first galaxies was affected by the feedback of the first stars known which form the putative population III (Heger & Woosley 2002; Bromm & Yoshida 2011). This process is shown in Figure 1.1. All this activity essentially resulted in the large variety of galaxies observed today, including our own Milky Way (MW).

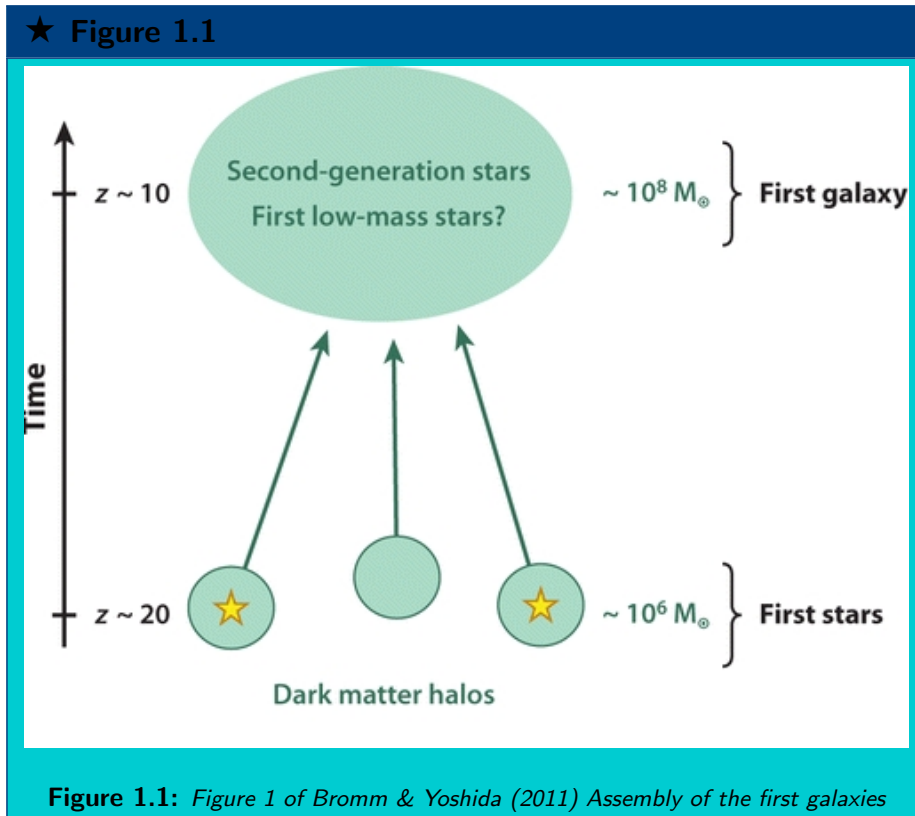
The accepted view is that the first galaxies were much closer to each other. This led to a series of continuous mergers of smaller systems, which lead to larger structures. Those mergers had a fundamental role in the formation and evolution of galaxies. This theory is known as the hierarchical (bottom-up) galaxy formation in a cold dark matter (CDM) framework (White & Rees 1978).

CDM is believed to be made of weakly interacting massive particles that had low velocities (non-relativistic) when they decoupled from the expansion of the Universe. The original CDM scenario has been modified to include dark energy and is now called the  $\Lambda$ CDM model. Among the triumphs of  $\Lambda$ CDM we encounter its remarkable agreement with the measurements of the cosmic microwave background (Spergel et al. 2007), and the

---

<sup>1</sup> $P \sim \rho v^2$ , where  $\rho$  is density and  $v$  is the systematic galaxy velocity.

<sup>2</sup>Most of the baryons are found in the ICM in the form of a tenuous hot plasma. ( $T \sim 3 \times 10^7 K$ ,  $\rho \sim 10^{-3} cm^{-3}$ )



reproduction of the observed distribution of galaxies on large scales (Springel et al. 2005). It has been recently found that black holes also play a role in galaxy formation (Merritt 2006). In galaxy mergers, gas settle down at the center feeding the black hole. The result of this process is likely to be an early-type galaxy, where black hole activity has quenched star formation. However, this process also occurs in S galaxies. When the gas component cools and settles in the halo, it ignites star formation. However, if this is accreted by the black hole, the feedback halts star formation. This could explain why S galaxies are not bigger than  $\sim 2 \times 10^{11} M_{\odot}$  (Cattaneo et al. 2009).

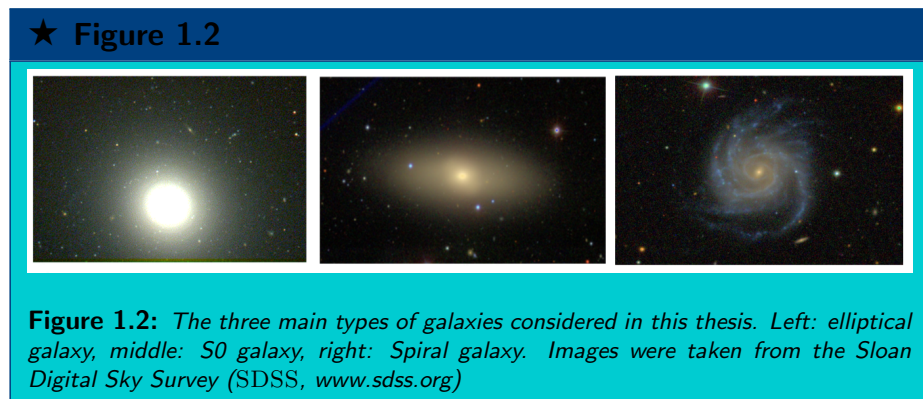
## 1.2 Classification of Galaxies

The scientific process, as interpreted by Francis Bacon, considers classification as the first step to understand the nature. However, the selection of a pattern or quality is somewhat arbitrary. This is not particular to the natural sciences; in Set Theory the arbitrary selection of sets or subsets is allowed by the Axiom of Choice. Nevertheless, it was in the Theory of Essences of Aristotle, where a meaningful way to create a classification system was

provided. Aristotle assumed that anything in the universe could be reduced to some very basic properties or qualities that were fundamental and immutable. Aristotle called those fundamental qualities "essences". A premier example of Aristotle thought is reflected in the modern Atomic Theory of Matter. A hydrogen atom carries all the information to characterize the physical properties of all the hydrogen in the universe. However, to arrive at the atom, chemists created ways to classify the elements by their reacting properties, densities, textures, etc. When, they finally reached the Periodic Table they had isolated the essences of matter. We hope that a detailed morphological analysis could help to understand the working of evolutionary effects and arrive to some definitive clues about the formation of galaxies.

Unfortunately, since the discovery of galaxies (Hubble 1926) up to now, we still lack a compelling classification scheme for galaxies. In the past, some schemes were based on properties such as bars, rings or shape of spirals arms. Now, we know that these properties are transient, which gives poor understanding of fundamental properties. A classification scheme that could associate morphology with fundamental parameters of galaxies such as mass, density, or angular momentum is still missing.

Some examples of these galaxy types are depicted in Figure 1.2.



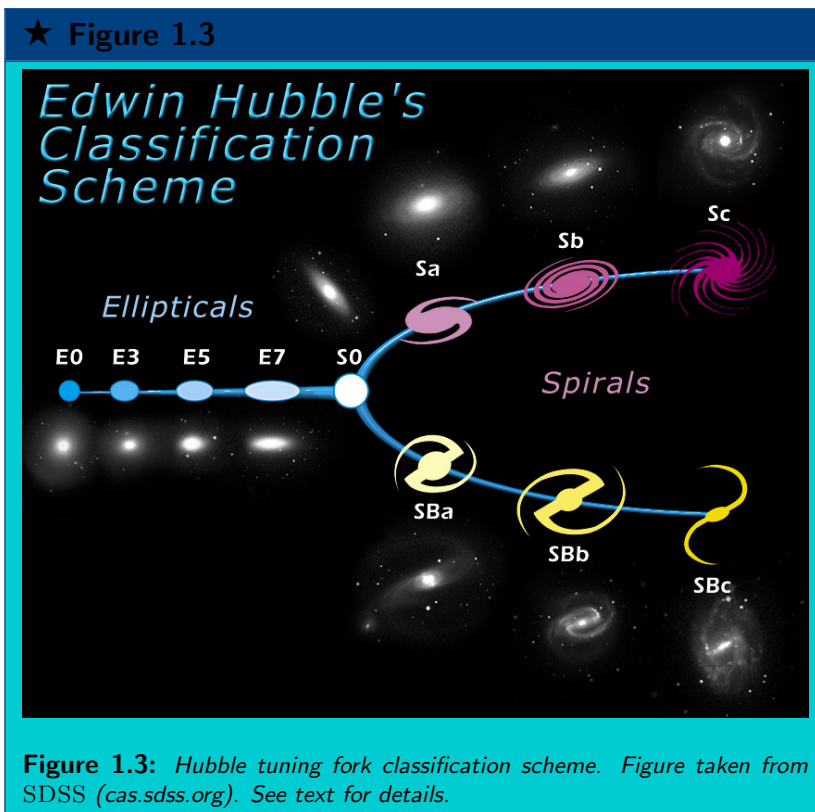
An important limitation for any galaxy classification system is that the "visible" part of galaxies is only a small fraction of the matter content of the whole galaxy (90% of the total mass is DM).

Below, we briefly review some galaxy classification schemes that have been implemented. We also comment on the recent developments on automatic classification of galaxies. The reader is referred to Sandage et al. (1975); Sandage & Bedke (1994); van den Bergh (1998); Sandage (2005) for excellent reviews on the philosophy and practice of galaxy classification.

## 1.2.1 Galaxy Classification Systems

### The Hubble Diagram

This is the most popular classification system. The types are arranged in a diagram known as the Tuning Fork; it is depicted in Figure 1.3. It shows 3 different kinds of galaxies: elliptical (E), lenticulars (S0) and spirals (S). Early types galaxies include E and S0, and late type S.



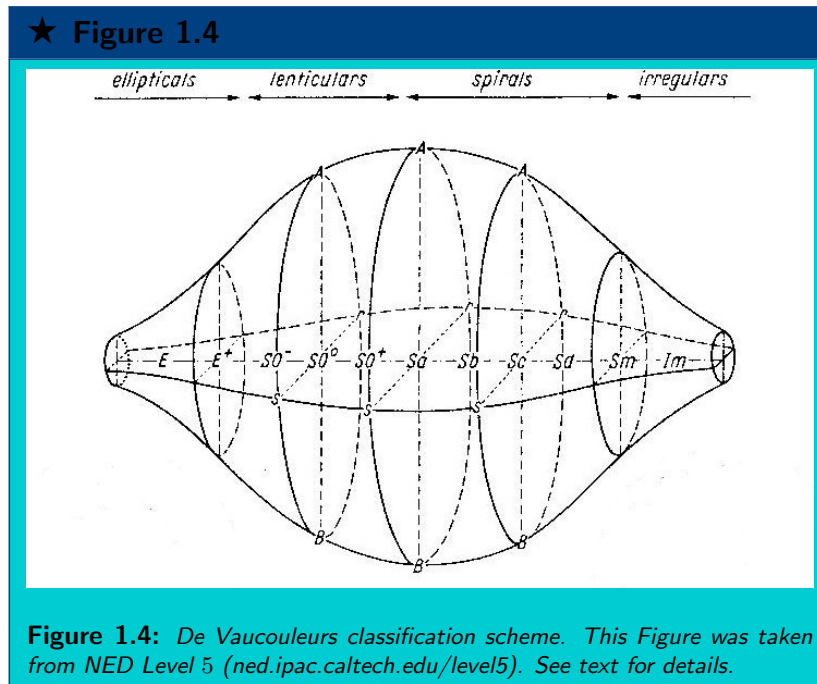
On the left hand side of the diagram of Fig. 1.3, E galaxies are separated by their projected ellipticity, which increases from left to right. On the right hand side of the Hubble diagram, there are 2 branches where S galaxies can be distinguished. S galaxies are at the top branch, and barred S galaxies are at the bottom branch. The bulge to disk ratio (B/D) decreases toward later types. S0 galaxies complete this diagram becoming the transition point between S and E.

Some physical properties have been found in support of the morphological sequence suggested by the tuning fork. Just to name a few, going from left to right, in the Hubble diagram: gas fraction, star formation, and dust content increase, and random to rotational components decreases (van den Bergh 1998).

On the other hand, ellipticity is not related with any galaxy property, such as color, size or mass. Moreover, total mass or luminosity or both are not directly related in the Tuning Fork. In addition, this scheme does not include low surface brightness galaxies nor dwarf galaxies. Therefore, the Tuning Fork remains an incomplete scheme.

### The de Vaucouleurs Diagram

In 1959, Gerard de Vaucouleurs proposed his own diagram, and it is depicted in Figure 1.4 (see Buta et al. 2007, for an updated overview).



De Vaucouleurs system is characterized by 3 parameters: the main parameter  $T$  distinguishes the sequence from  $E$  to Irregulars with some fine tunings  $+$ ,  $0$ ,  $-$  for  $S0$  galaxies and  $+$  for  $E$  galaxies.  $(+)$  and  $(-)$  stand for patchy and smooth, respectively. The second parameter gives the position in the sequence  $SA$ - $SAB$ - $SB$  which denotes no bar, weak bar and strong bar, respectively. Finally, the third parameter emphasizes differences among ring ( $r$ ) and spiral ( $s$ ) and mixed ( $rs$ ).

This classification scheme has some disadvantages. For instance, the subclassifications  $-$ ,  $0$  and  $+$  can be hard to distinguish for distant galaxies. Differences in the ring and spiral are due to the density wave; hence these are not related to their main parameters. In the sequence  $Sc$ - $Sd$ - $Sm$  the galaxies become fainter and bluer simultaneously with the same parameter  $T$ . Finally, some galaxies, such as dwarf galaxies, are not included in this Diagram.

In Table 1.1, the correspondence of the T type with the Hubble types is shown.

Class	E0	E+	S0-	S0	S0+	S0/a	Sa	Sab	Sb	Sbc	Sc	Scd	Sd	Sdm	Sm	Im
T	-5	-5	-3	-2	-2	0	1	2	3	4	5	6	7	8	9	10

**Table 1.1:** Correspondence of the T type with Hubble type. Data table has been taken from Nair & Abraham (2010)

## Other Classification Systems

Apart from the Hubble and the de Vaucouleurs classification systems, there have been other attempts to classify galaxies. In this section, we briefly review the ones that have most widely used.

The Morgan's classification (Morgan 1958, 1959) organizes galaxies in a single parameter. The categories are *a-f-g-k* with intermediate class *af,fg,gk*. Galaxies with "a" classification tend to have early type A stellar spectra, and "k" tend to have K stellar spectra. This one-dimensional parameter of classification is based on light concentration index. Unfortunately, this scheme hardly distinguishes between S0 and E galaxies.

Van den Bergh (1960) made a classification of galaxies according to luminosity. He found both surface brightness and spiral arm structures were a function of luminosity. Five classes can be found: I super giants, II bright giants, III giants, IV sub-giants and V dwarfs. Grand design spiral arms can be found in classes I-II and flocculent in the others. This is because grand design and flocculent types are a function of luminosity.

Finally, based on spiral arm shape, Elmegreen et al. (1982); Elmegreen & Elmegreen (1987) made a classification of S galaxies. They introduced 12 types of spirals arms. This range from 1 "flocculent" to 12 "grand design". Type 1 has patchy arms with not defined structure. In contrast, Type 12 are galaxies with strong and well defined spiral arms. This spiral arm classification scheme is related to the density wave but unrelated with Hubble stage classification system. Recent conferences have been devoted to galaxy classifications, most notably the ones organized by Block & collaborators (e.g. Block et al. 2000).

## Summary

The choice of the classification scheme depends on the attribute one wishes to tackle. Studies of spiral arms could be aided by Van den Bergh's or Elmegreen's systems. If galaxy spectra are available, then Morgan's system is useful for automatic classification of galaxies.

Strictly speaking, a classification system must be able to separate different classes of galaxies in such a way that objects with different physical properties must be distinguished. The other use of a classification system is to segregate the peculiar objects from the normal ones.

Apparently, E classification in the Hubble's scheme based on axial ratio has no physical meaning because it is due to projection effects. In addition, probably S0 galaxies are not

the galaxy transition between E and S galaxies as has been argued by van den Bergh (1998). This had been debated from the first time when Hubble introduced this class. Finally, galaxies at high redshift become peculiar and difficult to fit in the Hubble's Tuning Fork scheme.

Nowadays, Hubble's system is still popular. It describes a basic classification that separate physical properties (with the exceptions described above). De Vaucouleurs system includes too many morphological tracers that probably are not related to the fundamental properties. Hubble's classification probably need a re-formulation including isophote shape as suggested by Kormendy & Bender (1996). This may allow a smooth transition from E to S0 galaxies. Finally, this new scheme must be extended to dwarf and irregular galaxies.

## 1.2.2 Automatic Classification of Galaxies

Astrophysics has entered a data rich era. It is possible to get information for millions of galaxies (for instance Sloan Digital Sky Survey<sup>3</sup>). Without the proper tools, lots of information could not be analyzed. Efforts have been made to develop efficient data mining techniques. Normally, speed sacrifices quality and vice versa. Below, a brief overview is presented on the automated classification of galaxies.

### Artificial Neural Networks

An artificial neural network (ANN) is a computational model that emulates the biological neural system. Each neuron of the ANNs takes many input signals and produces an output signal that is sent as an input to another neuron. ANNs have been used in many real life applications such as regression analysis, classification, data processing, and robotics.

ANNs analysis had been applied to galaxy classification by Lahav et al. (1996) for the first time. Lahav et al. (1996) found that artificial neural networks replicate the classification within 2 T type units (See Table 1.1), which is similar to the scatter between two human experts.

If the ANNs analysis could be a good promise for large data bases, problems would arise when there are galaxy peculiarities such as two blended galaxies, edge-on galaxies, etc.

In the same way, differences between E and S0 would be hard to separate.

ANNs have been trained to distinguish between E and S galaxies for the Galaxy Zoo project (see §1.2.3). It was trained on 75,000 objects, and it classified almost 1 million objects. This machine learning program has a 90% agreement with the classifications done by humans (Banerji et al. 2010). ANNs seem to work properly if it is well trained.

### The CAS system

Conselice (2003) made an extension of Morgan's light concentration system and created

---

<sup>3</sup><http://www.sdss.org/>

the CAS system. This system measures light concentration ( $C$ ), Asymmetry ( $A$ ) and clumpiness ( $C_s$ ) for every galaxy.

$C$  is related to the bulge-to-total flux ratio ( $B/T$ ). It correlates with Hubble type. The concentration light is defined by the following formula:

$$C = 5 \times \log(r_{80\%}/r_{20\%}), \quad (1.1)$$

where  $r_{80\%}$  and  $r_{20\%}$  are the 80% and 20% curve of growth radii, respectively, within 1.5 times the Petrosian inverted radius at  $r(\eta = 0.2)$  (Petrosian 1976). A curve of growth is a plot of the variation of the measured magnitude with increasing aperture size applied to a luminous object. As the aperture gets larger, more galaxy's flux is included, until it levels off to an asymptotic value, which encompasses the total flux of the galaxy.

According to Conselice, the parameter  $A$  is indicative of mergers and interactions among galaxies.  $A$  is measured on the subtracted image of the original and a 180-degree rotated image of itself. The flux of the residual image is normalized by the flux of the original image; hence  $A$  is defined as follows:

$$A = \frac{\text{abs}(\mathcal{I} - \mathcal{R})}{\mathcal{I}}, \quad (1.2)$$

where  $\mathcal{I}$  is the original image, and  $\mathcal{R}$  is the 180 degrees rotated image.

The clumpiness indicates the patchiness of the light distribution on a galaxy.  $C_s$  is measured on the subtracted image of the original and a smoothed image of itself. Therefore,  $C_s$  is defined by the ratio of the fluxes, defined below:

$$C_s = \frac{\text{abs}(\mathcal{I} - \mathcal{B})}{\mathcal{I}}, \quad (1.3)$$

where  $\mathcal{B}$  is the smoothed image using a filter with a determined width.  $C_s$  value range between  $-0.1$  and  $1$ . Therefore, star forming galaxies will have large  $C_s$  values while an E galaxies will have a smaller  $C_s$ .

The CAS system provides information on the star formation activity in galaxies and indicates merging or interacting systems, which is very useful additional information; however, it fails to distinguish between E and S0 galaxies.

### Sérsic index vs. Bumpiness

Blakeslee et al. (2006) separate galaxy morphology using Sérsic index ( $n$ , check §3.1) vs. *Bumpiness* (BPN). BPN is a finer indicator of the patchiness of the light distribution of a given galaxy. It was defined as follows:

$$BPN = 10 \frac{\sqrt{\langle [I - S(Re, n)]^2 \rangle - \langle \sigma_s^2 \rangle}}{\langle S(Re, n) \rangle}, \quad (1.4)$$

where  $I$  is the galaxy intensity,  $S(Re, n)$  is the Sérsic fitted model,  $Re$  is the effective radius,  $n$  is the Sérsic index, and  $\sigma_s$  is the flux uncertainty of the galaxy intensity.

Since spirals are bumpier than E galaxies, the BPN parameter has been used to determine galaxy morphologies. We have extended the application of sc BPN to segregated S0 galaxies from Es.

### 1.2.3 Eyeball Classification of Galaxies

So far, computer algorithms have been unable to classify galaxies automatically. Maybe this is not so surprising, computers still can not recognize a human face as precisely and rapidly as a human child (Nair 2009). The brain-eye system in animals is equivalent to pattern recognition machines that have been perfected by some millions of years of evolution. Ironically, the advances in information technology have been enabled the interface human-machine, allowing thousands of humans to classify galaxies interactively.

#### Galaxy Zoo

The Galaxy Zoo project (Lintott et al. 2008) was developed to allow people, without any previous knowledge of astronomy, to classify galaxies.

Galaxy classification was done on line. After some training and validation, volunteers were asked to judge if galaxies were E or S. If S, the next question was whether the galaxy rotates in the clockwise or anticlockwise direction. This project has been a gigantic success, just after its first year, 150 000 volunteers classified over 50 million galaxies.

Galaxy Zoo re-introduced red S galaxies, which were discovered by van den Bergh (1976). van den Bergh called them *anemic* S galaxies. Red S galaxies are S galaxies with poor star formation, hence their arms are loosely defined.

The re-discovery of red S galaxies indicates there is a difference in time scale between color change and morphology. If S galaxies become S0 galaxies, then S galaxies turn red before they change their morphology (Skibba et al. 2009).

The first phase of the project was completed. Now, the second phase, called Galaxy Zoo 2 has been launched. It will look for substructures in S galaxies like a fraction of S with spiral arms and bars. In addition, Galaxy Zoo 2 is also trying to identify S0 galaxies and hints for the past of E galaxies.

Galaxy Zoo project is already an excellent galaxy morphology source to train classification algorithms.

#### Galaxy Classification by Professional Astronomers

Recently, Preethi Nair, in her thesis (Nair 2009), classified  $\sim 14,000$  galaxies including fine structure such as bars, rings, lenses, tails, warps, dust lanes, arms flocculence and multiplicity.

Nair's most important results are summarized below:

- 1) The distribution of mass of barred galaxies is bimodal. The mass that separate the bimodality is the same as the color bimodality.
- 2) Bars are more frequently found in red and massive galaxies.
- 3) Dispersion in the luminosity-size relation is produced by color and central concentration.
- 4) Slope, zero point, and scatter in the luminosity-size relation are independent of galaxy environment.
- 5) The distribution of galaxies along the luminosity-size relation is dependent of galaxy environment. Large and luminous galaxies are found in dense environments.
- 6) Rings are frequent in Active Galactic Nuclei (AGN).

## 1.3 Properties of Galaxies

Galaxies are mainly composed of gas, stars and dark matter (DM). Galaxies range from  $0.1 \text{ kpc}$  to  $1 \text{ Mpc}$  in size, and masses from  $10^7$  to  $10^{14} M_{\odot}$ . As explained before, galaxies are mainly classified as in 3 flavors: E, S and an intermediate class S0. As far as we know, it seems that galaxies have a black hole in their centers (Cattaneo et al. 2009; Heckman & Kauffmann 2011). The classes of galaxies have different compositions in gas and stars, and different distributions in mass, and DM. In addition, they have different star-formation rates, amounts of hot and cold gas, etc. Hence, it is expected that different morphologies are evolving in different ways.

### 1.3.1 Properties of E Galaxies

There are various subtypes of E galaxies: normal E, dwarf E, cD galaxies, blue compact dwarf galaxies, and dwarf spheroidal galaxies.

Dwarf spheroidal galaxies (dSphs) have very low luminosity and surface brightness. For this reason, dSphs have been only found in the Local Group. dSphs have a maximum absolute magnitude of  $M_B \sim -8$  (Schneider 2006).

Blue compact dwarf E galaxies have a stronger star formation and gas than the other E galaxies. Their color index (B-V) is between 0.0 and 0.3 while for Normal E (B-V) is  $\sim 0.95$ .

cD galaxies are the most luminous and massive of all galaxies. Their magnitude could be up to  $M_B \sim -25$  and size up to  $R \lesssim 1 \text{ Mpc}$ . cD galaxies are only found in clusters of galaxies and contain an extended diffused halo (Oemler 1976).

Dwarf E galaxies are compact E galaxies with low surface brightness and metallicity. The Sérsic index is close to  $\sim 1$ .

Normal E galaxies cover a range in absolute magnitude between  $M_B \sim -23$  to  $M_B \sim -15$ . S0 galaxies share physical properties with this type. Both types are usually referred as early-types galaxies. Their mass range between  $10^8 M_{\odot}$  to  $10^{13} M_{\odot}$  (Schneider 2006).

Except for blue compact dwarfs, E galaxies are red, and consequently metal rich. Hot gas temperature is around  $10^7 K$ , and it has been detected by its X-rays emission. Metallicity increases towards the center of the galaxy. They are dominated by dispersion velocity, but disks have been found in some E galaxies (Capaccioli 1987; Peletier et al. 1990; Emsellem et al. 2004; Krajnović et al. 2008).

### 1.3.2 Properties of S Galaxies

S galaxies are composed of a disk of gas and stars, a dark matter halo and a stellar/gas bulge. Disk contains a large population of young blue stars. Bulges have velocity dispersion traced by old stars. In contrast, some bulges, normally called pseudobulges (see §1.3.4), can have a rotational component with a Sérsic index less than 2 (Kormendy & Kennicutt 2004; Fisher et al. 2010).

S galaxies can be classified in Sa, Sb, Sc and Sd/Sm with intermediate class (see §1.2.1). In the sequential order Sa-Sd/Sm, the bulges become less luminous while the fraction of cold gas in the disk increases (van den Bergh 1998).

The disk rotates with a constant velocity at large radius. This supports the idea that S galaxies are embedded in massive dark matter halos.

Bars are common in S galaxies. Bars are able to modify the gravitational potential of the galaxy. As a result, the gas, stars, and dark matter are redistributed. In addition, gas can be driven through the bar reaching the bulge of the galaxy [and references therein](Kormendy & Kennicutt 2004).

The absolute magnitudes of S galaxies range from  $-16 \gtrsim M_B \gtrsim -23$  and masses range from  $10^9 \lesssim M \lesssim 10^{12} M_\odot$  (Sandage 2005, and references therein).

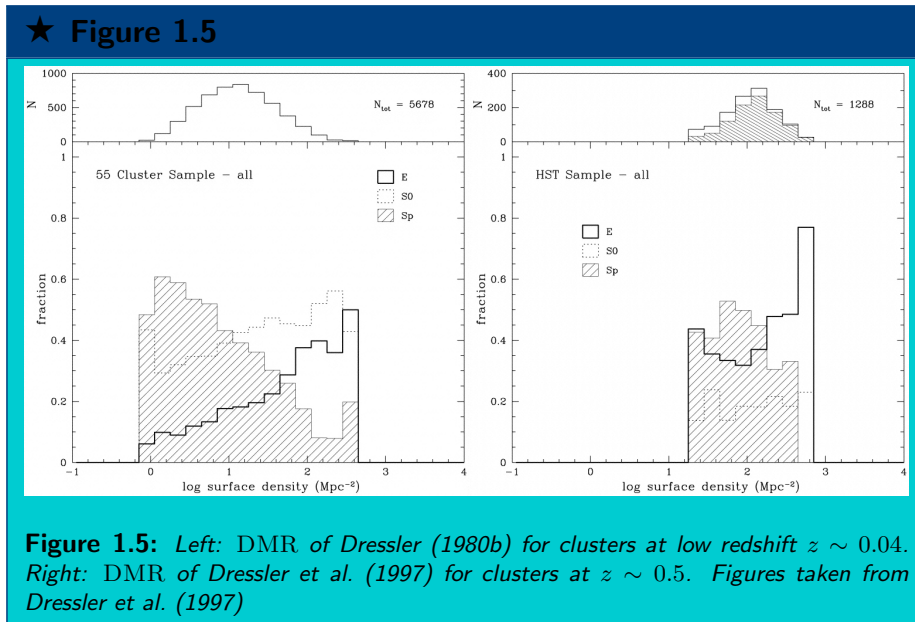
### 1.3.3 Properties of S0 Galaxies

S0 galaxies are the transition between E and S galaxies in the Hubble sequence. S0 galaxies share physical properties with E and S galaxies. S0 galaxies have a bulge and disk with old stellar population. Like E galaxies, the metallicity increases towards the center. In the same way as S, some S0 galaxies have bars, but S0 galaxies do not have spiral arms (Sandage & Tammann 1981; Sandage 2005; van den Bergh 2012).

The magnitudes of S0 galaxies range from  $-17 \gtrsim M_B \gtrsim -22$  and masses range from  $10^{10} \lesssim M \lesssim 10^{12} M_\odot$  respectively.

According to Dressler (Dressler 1980b; Dressler et al. 1997), at high redshift ( $z \gtrsim 0.7$ ) the percentage of S galaxies is higher than S0 galaxies. On the other hand, for low redshift clusters ( $z = 0$ ) the percentage of S0 galaxies is higher than S galaxies. In Figure 1.5 can be seen that there is a decrement in the population of S galaxies in the center of the clusters, and there is a difference in population of S0 and S galaxies for clusters at different redshift. Thus, young clusters have a larger population of S galaxies than old clusters and vice versa for S0 galaxies. This may indicate that there is a change in morphology from S to S0 galaxies when S galaxies fall into the cluster.

The Butcher-Oemler effect (Butcher & Oemler 1978) shows that clusters galaxies at high-



redshift are bluer than clusters galaxies at low-redshift. Couch et al. (1994, 1998) have found that Butcher-Oemler galaxies are S galaxies. Therefore, the Butcher-Oemler effect seems to indicate that the population of S galaxies is larger at high redshift as can be seen in Figure 1.5.

### 1.3.4 Properties of Bulges

There are two types of bulges: classic bulges (or normal bulges) and pseudobulges. The first ones are small scale versions of E within disks, and consequently they follow the same physical relations as E galaxies. They are dominated by dispersion velocities and are populated by old stars. They also have Sérsic indexes above 2 (Nipoti et al. 2006, see also §3.1). Classic bulges are the result of mergers according to the CDM framework (White & Rees 1978; Springel et al. 2005).

On the other hand, pseudobulges do not follow the same physical relations as classic bulges and E galaxies. Their apparent flattening is similar to the one of disks. They have Sérsic indexes between 1 and 2 (§3.1). They are dominated by rotation velocities and are populated by young stars. They are built by secular processes (Kormendy & Kennicutt 2004).

## 1.4 Clusters of Galaxies

Galaxy clusters are the largest gravitational bound structures in the Universe. Their sizes range from  $2 Mpc$  to  $10 Mpc$  and their masses from  $10^{14}$  to  $10^{15} M_{\odot}$ . Clusters are composed of galaxies, hot gas, and dark matter; their proportions are 5%, 10% and 85%, respectively. Thermal *bremstrahlung* is the main mechanism that originates the X-Ray emission in clusters (Sarazin 1988).

Strictly speaking, there is no clear distinction between clusters and groups of galaxies. A group could be considered a poor cluster of galaxies. Nevertheless, there are some differences among them, which allow us to make an operational distinction. Cluster membership is around 50 – 1000 galaxies while groups have 30 – 50 galaxies. X-ray emission for clusters is higher than for groups. The X-ray luminosities lie in the range  $10^{36}$  to  $10^{38} W$ , and, on the other hand, groups present  $10^{33}$  to  $10^{36} W$  (Sarazin 1988; Mulchaey et al. 2003). While the brightest galaxy in a given group could have morphologies ranging from S to E, Brightest Cluster Members (BCM) are usually E or cD galaxies.

BCM are massive, with a mass ranging  $10^{13} - 10^{14} M_{\odot}$  (Kormendy & Djorgovski 1989, and references therein). They are close to the center of potential energy and coincidentally close to the peak of X-ray emission. Giant elliptical (gE), D and cD<sup>4</sup> are subclassifications of BCM. cD galaxies have a big diffuse halo whose surface brightness is shallower at large radius than given by a de Vaucouleurs profile.

As can be seen in Figure 1.6, early-type galaxies are preferentially found in galaxy clusters. The DMR (Dressler 1980b) establishes that E and S0 galaxies are found in regions of high galaxy density. On the contrary, S are found in regions of low galaxy density.

Many physical processes act simultaneously transforming galaxies within clusters. Some of this process include ram pressure stripping, tidal truncation, galaxy-galaxy interaction, harassment, etc. (see §1.5.1). Nevertheless, the main issue is to identify the physical process that has the most significant impact. In this way, clusters can be seen as “galaxy laboratories” (Dressler 1984).

Clusters concentrate a large number of galaxies, which represent a significant contrast over the field. Although clusters concentrate many galaxies, the abundance of clusters in the Universe is low: less than 10% of the galaxy population is found in clusters with masses  $> 10^{14}$  solar masses (Bower & Balogh 2004). This proportion is similar for star clusters and field stars. It is more likely to find a field star rather than a star cluster in the night sky.

Galaxy clusters have other properties. For instance, they interact with the cosmic microwave background (CMB) via Sunyaev-Z’eldovich effect (Birkinshaw & Lancaster 2008). Their large mass concentrations allow them to act as gravitational lenses. They also host large scale magnetic fields. Those properties are not reviewed here, but the reader is referred to some excellent reviews: Dressler (1984); Bahcall (1999); Rosati et al. (2002); Plionis et al. (2008).

---

<sup>4</sup>D means diffuse while cD means that it is a super giant elliptical

★ Figure 1.6

**Figure 1.6:** *Perseus Cluster. Credit & Copyright R. Jay Gabany*

### 1.4.1 Galaxy Cluster Classification

Galaxy clusters have been usually classified morphologically using either the Bautz-Morgan (Bautz & Morgan 1970) or Rood-Sastry (Rood & Sastry 1971) classification schemes. Leir & van den Bergh (1977) classified 1889 clusters, later a compilation of Bautz-Morgan types was published by Abell et al. (1989). While, the most comprehensive study provided so far is based on the Rood-Sastry systems for 2712 Abell clusters (Struble & Rood 1987). The Bautz-Morgan system and the Rood-Sastry classification schemes are summarized in Tables 1.2 and 1.3 respectively.

Type	Description	Standard
I	Clusters containing a centrally located cD galaxy	A2199, A2029
I-II	Intermediate	
II	Clusters where the brightest galaxy or galaxies are intermediate in appearance between class cD and the Virgo-type gEs0	A194, A1656, A2197
II-III	Intermediate	
III	Clusters containing no dominant galaxies. This type can be subdivided into III-E and III-S, according to the absence or presence (or both) of considerable numbers of bright S galaxies	A426, A400 Virgo A2065

**Table 1.2:** *The Bautz-Morgan classification and its standards. Table taken from López-Cruz (2003)*

Type	Description	Standard
cD	A cluster that contains a cD galaxy	A401, A2199
B (binary)	The cluster contains a pair of bright galaxies in the center. They are separated by $\leq 10$ times the diameter of the brightest galaxy and have a combined size of $\geq 3$ times larger than other members	A1656, A154
L (line)	Three or more line up with comparable separations	A426
C (core-halo)	The four or more brightest galaxies located near the center with comparable separations and surrounded by fainter members	A2065
F (flat)	The galaxy distribution is in an oblate configuration	A397
I (irregular)	The galaxies are distributed irregularly, or without a well defined center.	A400

**Table 1.3:** *The Rood-Sastry classification and its standards. Table taken from López-Cruz (2003)*

## 1.5 Physical Processes in Clusters

Below we describe some of the known different environmental effects in galaxy clusters.

### 1.5.1 Ram Pressure Stripping

When galaxies fall in the cluster, the disk gas in the S galaxy feels a pressure produced by the intra-cluster medium (ICM) and the galaxy velocity. If this pressure, known as ram pressure (Gunn & Gott 1972), is greater than the gravitational attraction between the stellar and gas disks, then the gas disk will be removed from the galaxy. This is allegedly the most popular environmental effect that can explain the DMR and S0 galaxy formation. Ram pressure is a good candidate to explain at least the differences between cluster and field S galaxies. In addition, it also can explain why cluster S galaxies have less active star formation.

To ram pressure to occur, the following analytic condition must be satisfied (Gunn & Gott 1972):

$$\rho_{ICM}\nu_{gal} > 2\pi G\Sigma_s\Sigma_g, \quad (1.5)$$

where  $\rho_{ICM}$  is the density of ICM  $\rho_{ICM} \sim 10^{-3} \text{cm}^{-3}$ ,  $\nu_{gal}$  is the velocity of the galaxy through the cluster,  $\Sigma_s$  is the density of stellar gas, and  $\Sigma_g$  is the density of disk gas. The radius where the pressure of the ICM is equal to the gravitational pressure of the galaxy is called the stripping radius.

From equation 1.5, it can be concluded that ram pressure becomes most effective when galaxies plunge into the clusters centers where  $\nu_{gal}$  and  $\rho_{ICM}$  are maximum.

Sarazin (1988) reordered the terms in equation , giving the following formula:

$$\left(\frac{n_g}{10^{-3} \text{cm}^{-3}}\right) \left(\frac{\sigma_r}{10^3 \text{km/s}}\right)^2 \gtrsim 3 \left(\frac{M_D}{10^{11} M_\odot}\right)^2 \left(\frac{r_D}{10 \text{kpc}}\right)^{-4} \left(\frac{M_{ISM}}{0.1 M_D}\right), \quad (1.6)$$

where  $n_g$  is the number density of atoms in the intracluster medium,  $\sigma_r$  is the velocity dispersion.  $M_D$  and  $r_D$  are the disk mass and the disk radius respectively. Finally,  $M_{ISM}$  is the mass of the interstellar medium (gas, dust) in the disk.

Ram pressure stripping is a multi-stage process. In the first stage, ram pressure pushes the disk gas out of the galaxy for radii larger than the stripping radius. This displacement takes about 10 Myr. Second, the gravitational potential of the galaxy tries to rebound the stripped gas. Unbinding the stripped gas from the disk takes a few 100 Myr.

At the last stage, when gas outside from the stripping radius has been removed, the Kelvin-Helmholtz instability (KH) starts to develop. The KH instability acts on the remaining disk gas. Gas is lost due to this continuous turbulent-viscous stripping and the disk starts to loss mass at a low rate ( $\lesssim 1 \text{Myr}$ ) (Nulsen 1982). In addition to this problem, magnetic fields could prevent the formation of KH instabilities<sup>5</sup>.

<sup>5</sup>This depends on the direction of magnetic fields and the position of disk gas with the magnetic fields.

Hydrodynamic simulations of ram pressure produce realistic scenarios of the passage of S galaxies in clusters. Variations of orbits, galaxy velocity and ICM density have been possible. Different Hydrodynamic simulations methods have their advantages and disadvantages (Agertz et al. 2007).

Hydrodynamics simulations can not model the multiphase stage of the interstellar medium yet despite the improvements during the last years. Up to now, hydrodynamic simulations have modeled only the diffused HI. This is due to the need to resolve a huge range of scales; i.e. resolve from sub-parsecs for molecular clouds to at least 100 *kpc*.

In addition to this problem, the ICM is poorly constrained (McNamara & Nulsen 2007); hence hydrodynamic simulations of ram pressure stripping must deal with different viscosities for the ICM.

Despite of the lacking of resolution for molecular clouds, simulations agree with observations indicating that outside of stripped disk radius, star formation ceases (Roediger 2009). In some way, the internal dynamics of the ISM connect the cloudy and diffuse phase (HI) and thus star formation to the diffuse phase.

For the remaining inner disk, it is expected that the ICM pressure compresses gas and enhance star formation. In simulations, there is star formation associated to the stripped gas. For some galaxies, observations indicate that, in the remaining disk, star formation is enhanced except for the stripped gas (Koopmann & Kenney 2004). Nevertheless, other observations do not find any enhancement in the star formation (Abramson & Kenney 2009).

Observations of ram pressure stripping have been identified as an ongoing process in some galaxies of the Virgo cluster. For instance, NGC4402, NGC4430, NGC4569 and NGC4522 show signs of ram pressure stripping in their HI disks (Roediger 2009, and references therein).

In this thesis, we have investigated some limited cases of ram pressure using the Smooth Particle Hydrodynamics (SPH) code *GASOLINE* (Wadsley et al. 2004) see Appendix E. Our results are in agreement with the formula given by Gunn & Gott (1972).

## 1.5.2 Galaxy-Galaxy interaction

Galaxy-galaxy interaction can modify the morphology of galaxies. Depending on cluster mass and richness, these interactions can be divided into fast and slow. Fast encounters can be found in clusters such as Coma cluster ( $\sigma \sim 1000 \text{ km/s}$ ). Slow clusters and groups present with low velocity dispersion ( $< 500 \text{ km/s}$ ). The cluster itself can have both types of encounters during its evolution.

For fast multiple encounters of galaxies, this process is called "Galaxy Harassment" (Moore et al. 1996). In their simulations harassment change the morphology of galaxies. Low luminosity S galaxies become like dwarf spheroidals. Also, they found similarities between their simulated disturbed S galaxies and the S galaxies in a cluster at  $z \sim 0.4$ . The response of S galaxies to fast encounters depends on the structural properties of the galaxy (Aguilar & White 1985; Mihos 2004).

Slow encounters are able to drive a strong response in S galaxies. During slow encounters,

simulations show that galaxies develop intense bars and spiral arms (Mihos 2004). This can produce strong inflow and central activity. Slow collisions heat and strip galaxies more efficiently than high speed encounters.

Mergers of S galaxies can produce E galaxies (e.g. Toomre & Toomre 1972; White 1979; Naab & Burkert 2003) or even an S0 for unequal mass mergers (Bekki 1998). Nevertheless, the high speed velocities of galaxies inside clusters make galaxy mergers uncommon.

### 1.5.3 Tidal Truncation by the Mean Gravitational Potential of the Cluster

Tidal interaction by cluster potential can also have an important effect on galaxy morphology (Byrd & Valtonen 1990). Star clusters present significant tidal effects, and these are just  $10^4$  times smaller than those in galaxies. Galaxies are just 30-100 times smaller than clusters; hence galaxies have suffered strong tidal effects. This mechanism was pointed out by Noonan (1970) for the first time.

Gnedin (2003) performed N-body simulations of galaxies orbiting galaxy clusters with different sizes and cosmological parameters in order to study the effect of tidal interaction on galaxy morphology. Gnedin found that S galaxies have thickened their disk by a factor of 2-3, but stellar surface density remains constant. In addition, dark matter halos were truncated at  $30 \text{ kpc}$ . Dwarf spheroidal and low surface brightness galaxies were completely disrupted, and their stars became part of the intra-cluster light. It was also found that tidal interaction can transform S into S0 galaxies, but it is insufficient to transform an S into an E.

### 1.5.4 Merging of sub-clusters

Merging groups with clusters can be an alternative to explain the Butcher-Oemler effect. Bekki (1999) made merger simulations between groups and cluster of galaxies with a relative velocity of  $602 \text{ km/s}$ . The time-dependent tidal of group-cluster merging triggered star-burst without changing morphology.

### 1.5.5 Starvation

Starvation, strangulation or suffocation are mechanisms to produce the removal of the gas-rich envelope of S galaxies (Larson et al. 1980). The removal of these neighboring gas envelope is caused by interactions with neighboring galaxies, specially when neighboring galaxies are more massive. For instance, in the Local Group, the Milky Way and Andromeda galaxies take all the gas supply because they are the most massive galaxies. Conversely, dwarf spheroidal galaxies starve.

As opposite to ram pressure, starvation takes several Gyrs in order to stop galactic star formation.

### 1.5.6 Thermal evaporation

The difference in temperature between hot ICM ( $\sim 10^7 K$ ) and the ISM medium ( $10^5 K$ ) produce a temperature gradient, which leads to thermal evaporation. Cowie & Songaila (1977) derived solutions of mass losses for oblate and prolate systems. Unlike ram pressure, thermal evaporation can remove gas in the inner region of galaxies.

## 1.6 This Thesis

### 1.6.1 Motivation

After 30 years of the DMR, revising the methods to measure the surface brightness of cluster galaxies, has become timely. This is possible, thanks to advances in technology with access to large memory space and computing capacities, and the advent of large databases and new algorithms.

Attempts have been made to study the properties of galaxies in clusters (e.g., Tran et al. 2003; Trujillo & Aguerri 2004; Coenda et al. 2005). However, the works previously mentioned have studied single clusters, or either they lack appropriate tools and detail, for instance the use of one dimensional surface brightness models (e.g., Jedrzejewski 1987) instead of two dimensional ones §3.2. Also, studies such as Gadotti (2009); Simard et al. (2011) are not specific to clusters.

Moreover, an appropriate software to study the surface brightness of galaxies in dense environments is nonexistent. GALaxy FITting (GALFIT), a program developed by Peng et al. (2002), has shown to be robust enough to handle the modeling of the surface brightness of galaxies in two dimensions (Häussler et al. 2007). Nevertheless, it requires human intervention in every fit.

In addition, an appropriate classification scheme to separate E from S0 is absent. This is hard to do because S0 show significant similarities with E galaxies, and sometimes S0 disks are not prominent enough. However, we want to build and improve over some new parametric classification techniques, such as the CAS system (Conselice 2003). Recently, it has been proposed that some E galaxies with axis ratio around 0.5 must be S0 galaxies (van den Bergh 2009). This introduces a new problem and proposes a reorganization of the Hubble classification scheme.

### 1.6.2 Problems Addressed in this Thesis

In this thesis, we developed an algorithm to study the surface brightness of cluster galaxies. This algorithm addresses the problem of model fitting in regions of high galactic density. Criteria were introduced to decide on the minimum number of components necessary to model cluster galaxies.

A new galaxy classification scheme is presented that distinguishes three classes: S, S0, E galaxies.

Given the parameters of surface brightness models, the galactic structure of each mor-

phological type is analyzed. We discuss how the physical processes within clusters (see §1.5) could affect their structural parameters.

### 1.6.3 Problems not covered in this Thesis

Despite of the description of different physical processes in clusters, it is not covered how hydrodynamic processes could affect morphology. Nevertheless, we partially dealt with this problem in the appendix E.

In addition, this study has not considered finer details in the morphological appearance of galaxies such as disk or boxy isophotes, spiral arms, and bars. Nevertheless, they will be implemented it in the future.

### 1.6.4 General Outline

In this thesis, we have quantified the morphology of cluster galaxies and have recovered the most important galaxy relations. Our aim was to find clues about how galaxies form and evolve. We have analyzed in detail the surface brightness distribution for 1453 galaxies in 21 nearby Abell clusters. For this aim, a code was developed for the automatic modeling of the surface brightness distribution using every pixel on the galaxies' image. Our code is a driver programmed in PERL<sup>6</sup> for GALFIT. We have named it a Driver for GALFIT on Cluster Galaxies (DGCG). In this thesis, we present the implementation and the first time application of DGCG.

We have also introduced a new classification system to segregate galaxies into three classes: E, S0, and S (§4.2). Furthermore, the classical relations among galaxies such as, the DMR, the Kormendy relation, the Fundamental Plane, the CMR and the scale-size relation have been revisited (§5.1). The properties of bulges and pseudobulges are analyzed in §5.1. Finally, The physical differences among E, S0, and S have been reviewed (§5.2.4).

This thesis contains six chapters and five appendices. Chapter 1 is a general introduction. The observations, data reductions, photometry, and catalogs are presented in Chapter 2. In Chapter 3, the philosophy and implementation of DGCG is fully described. In Chapter 4, the results and classifications are presented. In Chapter 5, the most important galaxy scaling laws are revisited, and the physical differences among E, S0 and S galaxies in terms of the surface brightness models are described. Finally, the conclusions of the present work are presented in Chapter 6, along with some perspectives for future work.

The description of the Levenbergh-Marquart method which is the heart of GALFIT (and DGCG as well) is given in appendix A. In Appendix B, presents useful formula for the Sérsic function. In Appendix C, we show that the apparent magnitude cut limit of our observations does not introduce bias to our computed parameters. Appendix D is a short manual for DGCG. In Appendix E, it is shown some hydrodynamic simulations of ram pressure using smooth particle hydrodynamics. Finally in Appendix F, a small part of the DGCG's code is introduced.

---

<sup>6</sup><http://www.perl.org/>

In this work, unless indicated otherwise, we have adopted the following cosmological parameters:  $H_0 = 73.00 \text{ km/sec/Mpc}$ ,  $\Omega_M = 0.27$ ,  $\Omega_\Lambda = 0.73$  (Spergel et al. 2007)

# Observations and Data Reductions

In this thesis, data from the Low-Redshift Cluster Optical Survey (LOCOS López-Cruz 1997; Lopez-Cruz 2001) have been used. Full detail about observations and data reductions are given in López-Cruz (1997); López-Cruz et al. (2004). Here, we provide a general overview.

## 2.1 Sample Selection Criteria

At low redshifts, clusters of galaxies can be identified without much sophistication as large galaxy over-densities  $\langle N_{cl} \rangle \gtrsim 200 \langle N_{field} \rangle$  (galaxies per  $Mpc^{-3}$  within  $1.5h^{-1}$  Mpc radius), where  $\langle N_{cl} \rangle$  is the average density of bright ( $\gtrsim L^*$ ) cluster galaxies, and  $\langle N_{field} \rangle$  is the average density of bright field galaxies. This property guided cluster selection in the past (e.g., Plionis et al. 2008). Abell (1958) devised selection criteria and applied to a the Palomar Observatory Sky Survey, which covered about one third of the sky using photographic plates, selecting 2712 clusters of galaxies by eyeball inspection. It is remarkable, giving the limitations, that Abell did not miss any of the nearby rich clusters. However, Abell's sample suffers from contamination and severe completeness effects; hence, some fake clusters were included. Spurious clusters can result from chance galaxy projections. Indeed, they came across A1725 that is reported as Abell richness class ARC=1, and Bautz-Morgan Class I-II, and an estimated  $z \sim 0.179$  in NED<sup>1</sup>; however, a closer inspection shows that A1725 is a fake cluster. They suppose that Abell was misled by the two bright galaxies closely spaced in the field of view. To avoid the inclusion of spurious clusters in LOCOS, they combined optical and X-ray data. The list of targets was generated by cross matching Abell (1958) catalog with a compilation of X-ray cluster made by Jones & Forman (1999). This selection strategy leaves out clusters whose intracluster medium (ICM) is not hot or dense enough to be very luminous in the X-rays. Nevertheless, the LOCOS is representative, since it contains clusters covering the widest possible range in richness, mass (as traced by the cluster velocity dispersion or the X-ray luminosity), cluster morphology, and galaxy mixture. The sample selection was guided by the following selection criteria:

- 1) The clusters should be at high galactic latitude,  $|b| \geq 30^\circ$ ;

---

<sup>1</sup><http://ned.ipac.caltech.edu/>

- 2) their redshifts ( $z$ ) should lie within the range  $0.04 \leq z \leq 0.20$ ;
- 3) the Abell richness ( $R$ ) should be greater than **0**;
- 4) the declination  $\delta \geq -20^\circ$ .

Criterion (i) was introduced to prevent large galactic extinction corrections, and to avoid the high stellar-density regions close to the plane of the Galaxy; however, due to observational constraints, the low galactic latitude cluster A407 ( $b = -19.9465$ ) was included. With the aid of criterion (ii), they ensure the sampling the brightest X-ray emitting regions for low- $z$  clusters. Although, at high- $z$  their sampling could cover the entire Abell radii, they are limited by the depth of the Abell Catalog and the depth of LOCOS observing set-up. Criterion (iii) was introduced aiming at reaching high galaxy counts inside the surveyed area, for this reason some cluster  $ARC = 1$  were selected despite having low X-ray luminosities (e.g. A1213). They should remark that about one quarter of the LOCOS clusters are  $ARC = 0$ : those clusters were included because their optical morphology (e.g., B-M I) or their X-rays morphology (e.g., regular, single-peaked emission, cooling cores) were indicative of advanced dynamical evolution. This strategy turned out to be very apt: Yee & López-Cruz (1999) quantified Abell's richness scale, and showed that the poorest clusters considered in this thesis are systematically richer than the average of the richness distribution of  $ARC = 0$  clusters. Finally, criterion iv) is a constraint imposed by the geographical location of the optical observatory. This restriction ensures that they do not have to apply second or higher order corrections for atmospheric extinction; however, the cluster A2384 (at  $\delta \approx -29^\circ$ ) was observed due to, again, observational constraints. Coma (A1656), the most studied nearby rich cluster of galaxies (see Biviano 1998, for a historical overview), should have been excluded from the LOCOS due its low redshift ( $z = 0.02$ ). Despite of that, they have included Coma to allow comparisons with previous studies. Its observations were used to anchor photometric and X-ray observations (e.g., López-Cruz et al. 2004).

## 2.2 Observations

The observations were conducted during five observing runs (the fourth run was completely unsuccessful due to poor weather conditions), throughout 1992 and 1993, at Kitt Peak National Observatory (KPNO)<sup>2</sup> with the 0.9 m telescope in the direct imaging mode (see Table 2.1). The T2KA CCD<sup>3</sup> ( $2048 \times 2048$  pixels) was used as the detector. The field covered by this array is  $23.2' \times 23.2'$  with a scale of  $0.68''/\text{pixel}$ , i.e.,  $\sim 1.5$  Mpc at  $z = 0.04$  and  $\sim 6$  Mpc at  $z = 0.20$ . The average seeing<sup>4</sup> registered during the observations was  $1.7''$  FWHM.

<sup>2</sup>Kitt Peak National Observatory, National Optical Astronomy Observatories, which is operated by the Association of Universities for Research in Astronomy, Inc. (AURA) under cooperative agreement with the National Science Foundation.

<sup>3</sup> Information on the 0.9 telescope and the T2KA CCD, and imaging capabilities at KPNO can be found in Massey & Silva (1994b), and Massey & Silva (1994a)

<sup>4</sup>Degradation of an object's image due to atmospheric turbulence.

RUN	DATE	$\frac{\# \text{ Of Useful Nights}}{\# \text{ Of Nights}}$	# OF CLUSTERS
1	Jan. 27-30, 1992	4/4	16
2	Jun. 26-29, 1992	4/4	10
3	Sep. 26-30, 1992	3.5/4	16
4	Mar. 25-29, 1993	0/4	0
5	Dec. 15-18, 1993	1.5/4	3

**Table 2.1:** Log of observations

The sensitivity of the T2KA is almost flat from 4000 Å to 8000 Å (peaking at 6000 Å with a DQE<sup>5</sup> of 70.1%). This permits us to efficiently sample a reasonable spectral range away from the sensitivity peak of the CCD. They have selected the *R*, *I*, and *B* filters from the “Harris Set”. These filters belong to the Johnson-Kron-Cousins photometric system (Landolt 1983), which is also referred in the literature as the Kitt Peak system. This system is very well-defined, stable, and has ready access to a large number of standard stars (Landolt 1992). This gives it an important advantage over other photometric systems with a less well-defined set of standards.

In summary, an extensive three-color imaging survey of the central region of X-ray selected clusters of galaxies have been carried out. The applied calibrations and reduction procedures ensure a high degree of homogeneity in all the measured quantities. The final sample contains 45 clusters listed in Table 2.2 of López-Cruz (1997).

## 2.3 Data Reductions

A raw CCD image is not ready for analysis, the CCD itself introduces some effects that alter the incoming signal. Therefore, a series of corrections must be applied to retrieve the original signal.

Two generic types of spatial errors should be considered: additive spatial errors and multiplicative spatial errors. Cosmetic errors are the simplest of all the additive errors. These errors are due to imperfections on the CCD's individual pixels (bad pixels) or series of pixels (bad columns). Another additive error is the electronic pedestal (bias) level which physically indicates zero photons being counted. The most important multiplicative errors are the DQE and optical transmission variations ( $\sigma_{tv}$ ) across the chip. Interference fringes are an additive spatial error. Images contaminated with fringes are produced when monochromatic light interferes constructively and destructively on the window of the CCD. They can distinguish two cases that produce favorable conditions for the generation of fringes. Firstly, the use of narrow-band filters could generate the conditions for monochromaticity that can produce fringes. Secondly, narrow bright atmospheric emission lines transmitted through a broad-band filter can also produce fringes. Fringes manifest themselves only in the *I*-band images.

---

<sup>5</sup>Detective quantum efficiency.

In general, the resulting detected signal can be expressed as:

$$C(x, y, \lambda) = B(x, y) + S(x, y, \lambda) [F(x, y, \lambda) + D(x, y, \lambda) + I(x, y, \lambda)], \quad (2.1)$$

where  $C(x, y, \lambda)$  represents the counts<sup>6</sup> as a function of the position (x,y) on the CCD and the wavelength ( $\lambda$ );  $B(x, y)$  is the bias level;  $S(x, y, \lambda)$  is the sensitivity of the CCD:

$$S(x, y, \lambda) = \text{DQE}(x, y, \lambda) \text{otv}(x, y, \lambda), \quad (2.2)$$

where both the DQE and  $\text{otv}$  vary across the CCD's surface and depend strongly on the wavelength of the incoming radiation.  $F(x, y, \lambda)$  is the fringe pattern;  $D(x, y, \lambda)$  denotes the cosmetic defects, which normally are  $\lambda$ -independent; and  $I(x, y, \lambda)$  is the incoming signal as it reaches the telescope. Provided that the proper calibrations are performed, then Equation 2.1 can be inverted to retrieve  $I(x, y, \lambda)$ .

The reductions were done using IRAF (Image Reduction and Analysis Facility)<sup>7</sup>. The recipe for the CCDRED package, given in Massey & Jacoby (1992), was followed. A brief description of the steps and calibrations involved is provided below. See López-Cruz (1997) for details, or López-Cruz et al. (2004). A general overview on CCD preprocessing is given in Howell (2000).

## 2.4 Photometric Reductions

The photometric reductions were carried out with PPP (Picture Processing Package Yee 1991). This package has been optimized to do galaxy photometry in moderately crowded fields. PPP includes algorithms to perform automatic object finding, star/galaxy classification, and total magnitude determination. Object classification and total magnitude determination are performed simultaneously by applying growth curve analysis. This study has exploited a series of improvements to the 1991 version of PPP, which are described in Yee et al. (1996).

### 2.4.1 Object Finding and Photometry

### 2.4.2 Object Finding

The selection of objects is achieved by identifying local maxima (peaks) and choosing those with an intensity above a preset threshold level. PPP has subroutines which deal with the detection of low surface brightness objects and the discrimination between real objects and cosmic rays (Yee et al. 1996).

<sup>6</sup> Number of electrons ( $e^-$ ) generated by an event. Counts are usually expressed in 16 bit integers called ADUs (analog-to-digital units) the conversion factor is called the *gain* ( $g$ ) which has units of  $\frac{\# e^-}{\text{ADU}}$ .

<sup>7</sup> IRAF is written and supported by the IRAF programming group at the National Optical Astronomy Observatories (NOAO) in Tucson, Arizona.

To avoid the detection of spurious objects, the bright star halos, bleeding columns produced by saturated stars, and bright streaks produced by asteroids and man-made crossing satellites were corrected. Bleeding columns were repaired by interpolating across them, using intensity and noise information of the pixels in the immediate vicinity. The bright halos of saturated stars were masked. Bright stars, within half a degree from the pointed observation, produced internal reflections that caused small fuzzy patches that were also masked. The detection process is fully described in Yee (1991).

With the appropriate selection of threshold levels and rejection parameters, PPP detects most of the objects in LOCOS frames. However, interactive intervention is needed as: saturated stars are not selected by the program; very low surface brightness objects that can be detected by eye could be missed by the automatic object finding routines; HII regions in bright spiral galaxies, in some cases, are selected as objects; and some low energy cosmic rays situated on the halos of bright galaxies or stars can fool the rejection criteria.

The final object lists for each cluster were compiled from the detections on the  $R$  frames. The  $R$  frames were chosen, because the peak of the CCD sensitivity is within the bandwidth of the  $R$  filter. Therefore, the  $R$  frames have the shortest integration times but are slightly deeper than the other filters. On average, about 3000 objects were detected in each cluster field.

### 2.4.3 Photometry

PPP applies curve of growth analysis to determine the *total magnitudes* of all the identified objects in every field. A sequence of 30 concentric circular apertures is used for this procedure. The minimum aperture size is  $2''$  (three pixels), which corresponds to approximately the diameter of the seeing disk. The apertures are increased in steps of  $0.68''$  (one pixel), extending to a maximum aperture of  $20''$ . In a normal object, the expected behavior is that, as the apertures increase in size, the flux increases monotonically. The opposite behavior is shown by the surface brightness profile until it is dominated by the sky and its monotonically decreasing trend is interrupted. The behavior of the surface brightness profile is characterized by the first derivative of the growth curve. The aperture which is chosen to define the amount of light of a given galaxy is called the optimal aperture. This aperture is selected as the smallest of the following apertures:

- (1) The maximum allowable aperture.
- (2) The aperture where the growth curve's first derivative indicates an inflection point.
- (3) The aperture where the growth curve turns downward more than expected from noise fluctuations.
- (4) The diameter where the decrease of the derivative is not seen for two consecutive apertures.

Condition (1) indicates the normal termination for isolated objects with relatively high S/N. Condition (2) occurs when contaminating objects lie within the aperture. Intruders, such as comic-ray events, improperly masked nearby objects, bleeding columns, or diffraction spikes manifest themselves by introducing an abrupt change in the derivative of the growth curve. Condition (2) limits the size of the optimal aperture for a large fraction of

faint objects; in particular for those in the vicinity of bright galaxies. Conditions (3) and (4) apply to relatively isolated faint objects, where random noise at large apertures dominates the total signal. The algorithm tries to compensate for the effect of a background which has been selected too high or too low.

Because most faint objects reach their optimal aperture at sizes smaller than  $20''$ , a correction is applied to correct their magnitudes to total magnitudes. This is done by extrapolating the flux to the maximum allowable aperture. The correction is based on the growth curve of a reference star. It should be mentioned that this extrapolation gives a correction which is not exactly correct for resolved galaxies. However, in the case of faint galaxies, where the extension of the light is dominated by the seeing and PSF smearing, such a correction represents a first-order approximation to using a uniform aperture for all objects. For bright galaxies, galaxies whose apparent  $R$  magnitude is brighter than 18.5, an aperture of  $20''$  is insufficient for the determination of the total magnitude. In a second iteration, the analysis is extended to larger apertures. The curve of growth is recomputed to a maximum aperture of  $81''$  for only those objects that have been classified as bright galaxies. The step increment and the selected large number of apertures allowed enough resolution and range to determine optimal apertures for both faint and bright objects.

Any photometric technique based on aperture photometry would underestimate the total magnitude of cD galaxies. The main reasons are the ellipticity and large size of the bright component and the even larger size ( $\geq 1$  Mpc) of the extended faint envelope which could be as luminous as the bright component (Schombert 1988). Therefore, to get total magnitudes for cD galaxies, the full modeling of their surface brightness distribution is necessary. Second, the problem of close neighbors is solved by masking them when photometry is performed. PPP automatically masks objects within  $40''$  away from a considered object. Very close neighbors do not produce a severe statistical effect in low redshift clusters, as only about 10 to 25 close pairs are detected per cluster. In some cases, there is some indication of mergers since their morphology looks distorted. Good photometric measurements for these objects cannot be claimed, even after masking. However, the most important problem is confusion arising from the cD galaxy. cDs rest in the cores of rich clusters, where the galaxy density peaks. In addition, due to their large size, cDs engulf nearby galaxies. To solve this problem, the isophotes of cD galaxies were modeled by ellipses and subtracted from the original frames by Brown (1997). PPP photometry was then carried out on the cD-removed frames. Thus, with the exception of cD galaxies, the adoption of the strategies discussed in this section allows us to estimate total magnitudes for all the galaxies in a cluster from dwarfs to giants.

#### 2.4.4 Color Determination

Total magnitudes are determined in the  $R$  images, and the colors are determined using fixed aperture on the images from the three filters. In López-Cruz (1997), an aperture of 11 kpc physical size is used to compute the colors of bright cluster galaxies at low redshift  $z < 0.06$  and an angular aperture of  $6''$  for clusters at higher redshift. The apertures size has been chosen in order to sample the identical region of galaxies in different colors. The approach increases the accuracy because only the central parts of the objects are used. The effects of color gradients in  $B - R$  are very small for early type galaxies; color

gradients  $\Delta(B - R)/\Delta \log r = -0.09 \pm 0.02$  mag per dex in radius (Peletier et al. 1990) are present in elliptical galaxies. However, larger color gradients are found in late type galaxies (de Jong 1995) where galaxies could be bluer by as much as  $B - R = 0.8$  mag towards the outer regions. However, those color-gradients do not seriously affect LOCOS color determinations because late type galaxies are not the dominant population in rich clusters of galaxies.

Because the large range of cluster galaxies sizes and the sampled redshifts range ( $0.04 \leq z \leq 0.18$ ), they adopt the following scheme. For bright galaxies ( $R \leq 17.5$ ) at  $z \leq 0.06$ , a maximum physical aperture of 11 kpc varies in angular size from  $10''$  for  $z = 0.04$ , to  $6''$  for  $z = 0.06$ . For bright objects at larger redshift the maximum allowable aperture has been fixed at  $6''$ , corresponding to 25 kpc at  $z = 0.18$ . This change in aperture for the objects at redshift larger than  $z = 0.06$  is introduced because the angular size of an 11 kpc aperture becomes too small at those redshifts<sup>8</sup>. Using too small an aperture introduces large errors due to seeing and variations of the PSF; hence, a minimal color aperture of  $3 \times FWHM$  should be used to avoid these effects. Overall the internal accuracy in the color determinations should be about 0.005 magnitudes in  $B - R$  for bright objects. For faint objects, the physical size is often smaller than 11 kpc; hence, the smallest optimal aperture is used, giving a photometric error for faint objects that can be as large as 0.5 magnitudes in  $B - R$ . The total magnitudes in the  $I$  and  $B$  images are determined using the color differences with respect to the  $R$  images.

### 2.4.5 Star/Galaxy Classification

Star/galaxy separation is a very important issue in wide-field galaxy photometry because the foreground stellar contribution is large at the bright end, and has overall large variations from field to field. Some fields, despite their high galactic latitude, have an over-abundance of stars by as much as a factor of three with respect to mean stellar counts. They have found that those fields are in the direction of the bulge of the Galaxy.

PPP uses a classifier that is based on the comparison of the growth curve of a given object and that of a reference star. The reference star is generated as the average of the growth curve of high  $S/N$ , non-saturated stars within the frame.

The classifier  $C_2$  is defined by the following expression (Yee 1991):

$$C_2 = \frac{1}{N_A - 2} \sum_{i=3}^{N_A} (m_i^* - m_i) - C_0, \quad (2.3)$$

where  $N_A$  is the adopted largest aperture number;  $m_i$  and  $m_i^*$  are the instrumental magnitudes from the  $i^{\text{th}}$  aperture of the object and the reference star, respectively.  $C_0$  is a normalization constant estimated by the difference between the magnitudes of the object and the reference star within either the first or second aperture depending on the pixel size.  $C_2$  measures the "compactness" of the object by effectively comparing the ratio of the fluxes of inner and outer parts of the object with respect to the reference star.

<sup>8</sup> In López-Cruz (1997), a value of  $50 \text{ km s}^{-1} \text{ Mpc}^{-1}$  for Hubble Constant was used. With the actual value ( $H_0 = 73$ ), The real aperture was  $7.54 \text{ kpc}$  at  $z = 0.06$

The reliability of the classifier depends strongly on the S/N, the seeing, and the stability of the PSF across the frame.

It has been found both by empirical calibrations and simulations that for well-sampled data with high S/N, five classes of objects can be defined:

CLASS	$C_2$ RANGE	OBJECT TYPE
0	$C_2 > 0.1$	false detection
1	$C_2 \leq -0.15$	galaxy
2	$-0.15 < C_2 \leq -0.075$	normally considered as galaxy
3	$-0.075 < C_2 \leq 0.1$	star
4		saturated star.

## 2.4.6 Transformation to the Kron-Cousins Standard System

Instrumental magnitudes were calibrated to the Kron-Cousins systems by observing standard stars from Landolt (1992) list. Landolt's compilation is a very large set of standard (526 stars) located in selected regions near the celestial equator. Their magnitude range ( $11.5 < V < 16.0$ ) permits us to use reasonable integration times before saturation is reached. The color properties of the standard stars covers a large color range that encompass those of elliptical galaxies and spirals. Up to 45 standard stars can be accommodated in a single frame.

The transformations were done by the solving the following set of equations (cf. Massey et al. 1989):

$$B = b + A_{10} + A_{11}(B - R) + A_{12}X \quad (2.4)$$

$$R = r + A_{20} + A_{21}(I - R) + A_{22}X \quad (2.5)$$

$$I = i + A_{30} + A_{31}(R - I) + A_{32}X \quad (2.6)$$

where  $B$ ,  $R$  and  $I$  are the standard magnitudes,  $b$ ,  $r$  and  $i$  are the measured instrumental magnitudes, and  $X$  is the airmass. The airmass terms are held fixed to the values  $A_{12} = -0.270$ ,  $A_{22} = -0.100$  and  $A_{32} = -0.040$  (in units of magnitudes per air mass). Nightly solutions for the remaining coefficients were obtained. However, changes in the color coefficients ( $A_{11}$ ,  $A_{21}$ ,  $A_{31}$ ) are not expected to occur during a four-night run.

The estimated coefficients are tabulated in Table 2.2. The r.m.s in the residuals of individual fittings is in the range 0.020 – 0.040. These were considered systematic calibration errors.

## 2.4.7 K-correction and correction for galactic absorption

K-corrections come about because the wavelength of light emitted by an object at redshift  $z$  will have increased by a factor  $(1 + z)$  by the time the light reaches the observer. This is due to cosmic expansion. K-corrections were generated by interpolating on the tables of Coleman et al. (1980). They do not include the effects of galaxy evolution. However, for the redshift range that we have considered the effects of evolution are negligible.

Jan 27–30, 1992					June 26–29, 1992			
$A_{11} = 0.015, A_{21} = -0.012, A_{31} = 0.057$					$A_{11} = 0.052, A_{21} = -0.072, A_{31} = 0.065$			
$A_{10}$	21.373	21.393	21.352	21.377	21.530	21.496	21.504	21.591
$A_{20}$	21.471	21.510	21.471	21.502	21.672	21.663	21.712	21.629
$A_{30}$	20.673	20.687	20.614	20.649	20.815	20.833	20.811	20.837
$N_{stars}$	3	26	18	17	16	20	15	17
Sep. 26–30, 1992					Dec. 15–18, 1993			
$A_{11} = 0.034, A_{21} = -0.010, A_{31} = 0.011$					$A_{11} = 0.054, A_{21} = 0.047, A_{31} = 0.016$			
$A_{10}$	21.418	21.451	21.410	21.470	21.436	21.436		
$A_{20}$	21.630	21.627	21.610	21.647	21.793	21.817		
$A_{30}$	20.781	20.788	20.790	20.822	20.978	20.995		
$N_{stars}$	66	47	40	33	47	49		

**Table 2.2:** Transformation Coefficients to the Kron-Cousins Standard System

$\kappa$ -correction is morphology dependent, but, for this work, the E's  $\kappa$ -correction is applied for all the galaxies. The reason is that E galaxies are the dominant population (in conjunction with S0 galaxies) in clusters at low redshift. In contrast, S galaxies are rarer in clusters at low redshift. Moreover, S galaxies in clusters are more affected by the cluster environment, then their spectral energy distributions are different from field S galaxies. Finally, we notice that correcting classified S galaxies with the standard S  $\kappa$ -correction produces an over correction: they turn redder than E galaxies.

Even when that the cluster sample is at high galactic latitude, correction for Milky Way extinction was done. They take values for galactic extinction from NED (NASA/IPAC Extragalactic Database), which uses values of Schlegel et al. (1998)

Table 2.3 contains the values for  $\kappa$ -corrections and extinction used through this work.

## 2.4.8 Absolute Magnitude

Absolute magnitudes for galaxies were computed using the following equation:

$$M = m - DM - K - A, \quad (2.7)$$

where  $m$  is the apparent magnitude,  $DM$  is the distance modulus,  $K$  is the  $\kappa$ -correction, and  $A$  is the extinction. Distance modulus is defined as:

$$DM \equiv 5 \log \left( \frac{D_L}{10 \text{ pc}} \right), \quad (2.8)$$

where  $D_L$  is the *luminosity distance*.

## 2.5 Cluster and Galaxy Velocities

Velocities of clusters and galaxies from Ibarra-Medel thesis (Ibarra-Medel 2010) have been used. Ibarra-Medel used data from SDSS.<sup>9</sup> Our sample have 440 galaxies in common.

Galaxy velocity dispersions were computed from spectra, using direct line-profile fitting (Rix & White 1992) and cross-correlation method (Tonry & Davis 1979).

Cluster membership was determined by Ibarra-Medel (2010) using the 3-Sigma velocity dispersion estimator (Yahil & Vidal 1977). This method only include galaxies as members of the cluster if their velocity dispersion is within 3-sigma from the mean.

## 2.6 Selected Clusters for this Thesis

From the three filter bands,  $R$  and  $I$  show the highest signal to noise ratio (SNR) and low integration time (hence less cosmic rays). Nevertheless the  $R$  frames do not exhibit fringing as the  $I$  frames. For that reason, in this  $R$  band was selected from Lopez-Cruz (LOCOS 2001) database.

The total LOCOS sample consists of 45 clusters. We found that clusters at  $z < 0.08$  have enough spatial resolution and SNR, which are suitable for a homogeneous study (see §4.1.3), allowing us to sample at least one magnitude below  $M^*$  ( $\sim -19.7$  mag). We will justify our selection in the next Chapter.

The final sample contains 21 clusters. These clusters have redshift between 0.0231 (Coma cluster) and 0.0849 (A1650). The Table 2.3 contains the main properties of the selected clusters.

## 2.7 Summary

The sample contains Abell clusters selected from the catalog of bright X-ray clusters made by Jones & Forman (1999). The clusters have high galactic latitude  $|b| \geq 30$ , and their redshifts lie within the range  $0.04 \leq z \leq 0.20$ . The Abell richness class is greater than 0. Data observations were obtained at Kitt Peak National Observatory. Using the 0.9 meter telescope and the T2KA CCD ( $2048 \times 2048$  pixels). The plate scale is  $0.68''/\text{pixel}$ . The average seeing registered during the observations was  $1.7''$  FWHM. The filters selected were  $R$ ,  $I$ , and  $B$  which belong to the Johnson-Kron-Cousins photometric system (Landolt 1992), but in this thesis we used the  $R$  filter. The  $B - R$  colors for the galaxies were obtained from López-Cruz (1997); López-Cruz et al. (2004). Star/galaxy classification is done by PPP through curves of growth analysis. Velocity dispersion is obtained from Ibarra-Medel (2010).

---

<sup>9</sup>Sloan Digital Sky Survey webpage: <http://www.sdss.org/>

Cluster (1)	z (2)	Ra (3) hh:mm:ss	Dec (4) deg:mm:ss	Rich. (5)	RS (6) Rood-Sastry	BM (7) Bautz-Morgan	Ar (8) mag	Ab (9) mag	K (10) mag	IT (11) sec
A85	0.053965	00:41:37.8	-09:20:33	1	cD	I	0.100	0.162	0.043	1400
A154	0.062538	01:10:58.1	+17:39:56	1	B	II	0.171	0.276	0.052	1200
A168	0.043944	01:15:09.8	+00:14:51	2	I	II-III	0.092	0.149	0.033	1000
A407	0.045576	03:01:43.7	+35:49:48	0	I	II	0.522	0.843	0.035	1200
A671	0.050925	08:28:29.3	+30:25:01	0	C	II-III	0.126	0.203	0.04	1200
A690	0.079573	08:39:14.2	+28:50:24	1	cD	I	0.149	0.240	0.07	1300
A957	0.044791	10:13:57.3	-00:54:54	1	L	I-II	0.112	0.181	0.034	1200
A1650	0.084940	12:58:46.2	-01:45:11	2	cD	I	0.046	0.074	0.075	1300
A1213	0.047898	11:16:29.1	+29:15:37	1	C	III	0.050	0.080	0.037	1000
A1656	0.023996	12:59:48.7	+27:58:50	2	B	II	0.021	0.035	0.021	400
A1795	0.063259	13:49:00.5	+26:35:07	2	cD	I	0.034	0.055	0.053	1100
A1913	0.053533	14:26:51.8	+16:40:34	1	I	II	0.066	0.106	0.043	1100
A1983	0.044228	14:52:44.0	+16:44:46	1	F	III	0.071	0.114	0.034	1000
A2255	0.080464	17:12:31.0	+64:05:33	2	C	II-III	0.073	0.118	0.07	1230
A2256	0.057961	17:03:43.5	+78:43:03	2	B	II-III	0.140	0.227	0.048	1000
A2399	0.056767	21:57:32.5	-07:47:40	1	I	III	0.104	0.168	0.046	900
A2593	0.040075	23:24:31.0	+14:38:29	0	F	II	0.116	0.188	0.03	900
A2657	0.038976	23:44:51.0	+09:08:40	1	F	III	0.338	0.546	0.029	900
A2670	0.075025	23:54:10.1	-10:24:18	3	cD	I-II	0.116	0.187	0.065	1200
A2415	0.056943	22:05:25.0	-05:35:23	0	C	III	0.177	0.286	0.047	900
A2626	0.054107	23:36:31.0	+21:09:36	0	cD	I-III	0.167	0.270	0.044	900

**Table 2.3:** Clusters used in this thesis. Column (1) name of cluster; (2) redshift; (3) Right Ascension; (4) Declination; (5) Richness; (6) Rood-Sastry Classification (Rood & Sastry 1971); (7) Bautz-Morgan Classification (Bautz & Morgan 1970); (8) extinction coefficient for R band; (9) extinction coefficient for B band; (10) K correction; (11) Integration Time.



# *Methodology: The Driver for GALFIT on Cluster Galaxies (DGCG)*

This Chapter describes a reliable procedure to fit surface brightness models for cluster galaxies. GALFIT was chosen over the rest of the public algorithms. It is explained how GALFIT was adapted to suit our aims. To this end, a wrapping PERL-script has been designed to fit cluster galaxies automatically using GALFIT. This script is called **Driver for GALFIT on Cluster Galaxies (DGCG)**. The efficiency, reliability, and limitations are shown. A user's manual can be found in the Appendix D. A fragment of the main part of the DGCG algorithm is shown in the Appendix F.

## **3.1 Surface Brightness Models**

E galaxies and bulges of S galaxies are well described by the Sérsic function (Sérsic 1968):

$$I(R) = I_e \exp \left( -k \left[ \left( \frac{R}{R_e} \right)^{1/n} - 1 \right] \right), \quad (3.1)$$

where  $I(R)$  is the surface brightness at the radius  $R$ ,  $I_e$  is the surface brightness at effective radius  $R_e$ , which is defined as the radius where the galaxy contains half of the light.  $n$  is the Sérsic index that defines the shape of the function.  $k$  is a parameter coupled to  $n$  in such way that  $I_e$  is the intensity at the effective radius. If  $n = 4$ , then  $k = 7.67$ , which corresponds to the well-known de Vaucouleurs profile (de Vaucouleurs 1948).

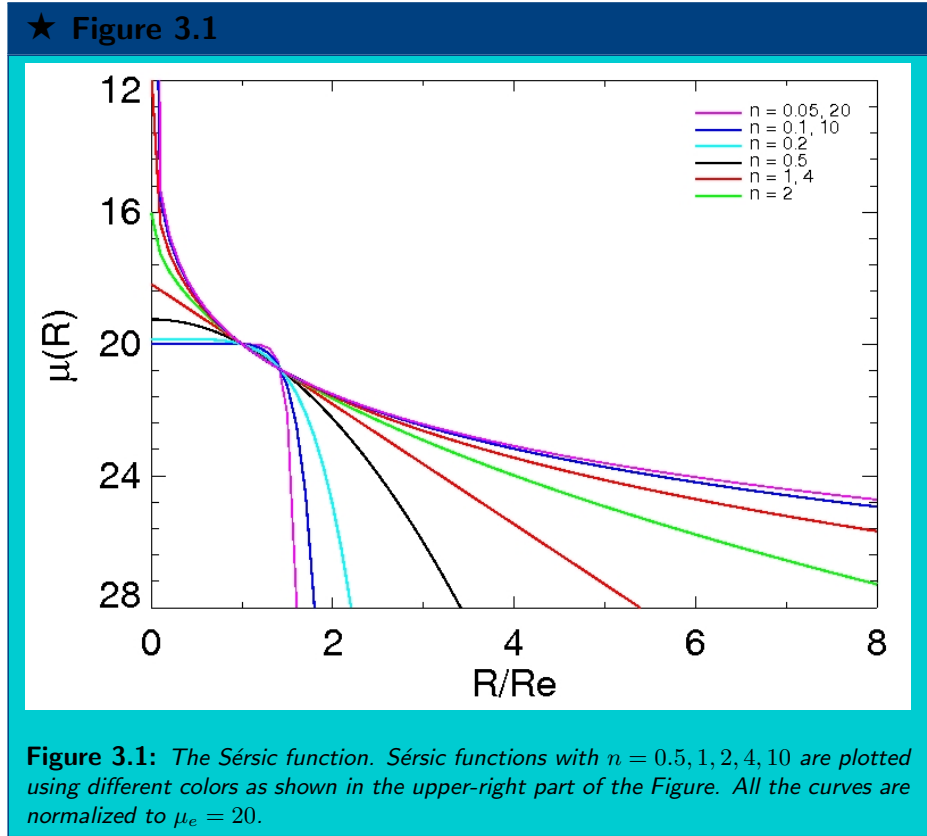
Disks of S and S0 galaxies are well fitted by the exponential function (Freeman 1970):

$$I(R) = I_0 \exp \left( -\frac{R}{R_s} \right), \quad (3.2)$$

where  $I_0$  is the central surface brightness, and  $R_s$  is the scale length of the disk. The relation between  $R_e$  and  $R_s$  is  $R_e = 1.678R_s$  (exponential function only). The exponential function is a special case of the Sérsic function when  $n = 1$ .

A mathematical reference for the Sérsic function is found in appendix B.

In Figure 3.1, it is shown the behaviour of the Sérsic profile as a function of radius and Sérsic index.



The bulge + disk combination gives the following formula for the surface brightness:

$$I_{b+d}(R) = I_b(R) + I_d(R) = I_e \exp\left(-k \left[\left(\frac{R}{R_e}\right)^{1/n} - 1\right]\right) + I_0 \exp\left(-\frac{R}{R_s}\right), \quad (3.3)$$

when integrating equation (3.3) by area from 0 to  $\infty$ , it gives that the total flux of the galaxy is:

$$F_{total,b+d} = F_b + F_d, \quad (3.4)$$

where the bulge ( $F_b$ ) and disk ( $F_d$ ) are:

$$F_b = 2\pi n q I_e R_e^2 \frac{e^k}{(k)^{2n}} \Gamma(2n), \quad (3.5a)$$

$$F_d = 2\pi q R_s^2 I_o, \quad (3.5b)$$

where  $q = \frac{a}{b}$  is the axis ratio,  $a$  is the semi-minor axis, and  $b$  is the semi-major axis. This axis ratio is independent for bulge and disk.  $\Gamma(2n)$  is the gamma function.

The ratio between the total flux of the bulge ( $F_{bulge}$ ) and the total flux of the bulge + disk ( $F_{disk}$ ) gives the bulge to total ratio ( $B/T$ ):

$$\frac{B}{T} = \frac{F_{bulge}}{F_{bulge} + F_{disk}}, \quad (3.6)$$

If the galaxy contains a bar, then a third component is added to the model. The bar model is a Gaussian (Sérsic index equal to 0.5). The  $B/T$  ratio including the bar is:

$$\frac{B}{T} = \frac{F_{bulge} + F_{bar}}{F_{bulge} + F_{bar} + F_{disk}}, \quad (3.7)$$

In this work, two approaches have been used to fit cluster galaxies, our first approach is to use a single Sérsic model; our second approach is to use a Sérsic + exponential model. Those surface brightness models are enough to study the structural differences among morphological types.

These two approaches allow us to extract as much galaxy's information as possible. Those surface brightness models are simply enough to study the structural parameters of the galaxies.

## 3.2 Surface Brightness Fitting

The first measurements of surface brightness profiles were the ones using 1-D fittings. 1-D profiles were extracted from elliptical isophotes from the galaxy's center to its outskirts. The surface brightness at a determined radius was obtained from the mean of the integrated flux over the area between isophotes. Then, a surface brightness profile was fitted to the data. ELLIPSE<sup>1</sup> (Jedrzejewski 1987) and GASPHOT (Pignatelli et al. 2006) codes are examples of that technique.

One dimensional profiles work well for some limited cases, but they dismiss relevant information from the 2-D image. Problems arise when galaxies have isophote twists, ellipticity variations as a function of radius, or bulge and disk long axis that are not in the same axis. Therefore, the radial profile can be poorly defined. In addition, galaxies have many

---

<sup>1</sup>IRAF package

complexities such as bars, nuclear cusps, S arms, or dust lanes which complicate the fitting.

For the problems mentioned above, 2–D modelling is preferred instead of 1–D for detailed galaxy decomposition. The performance of 2–D fittings over one-dimensional ones has been discussed extensively in the literature (e.g. Byun & Freeman 1995; Wadadekar et al. 1999).

Some popular 2 –  $D$  codes are: BUDDA (de Souza et al. 2004), BDBAR (Laurikainen et al. 2004), GIM2D (Simard et al. 2002), GASP2D (Méndez-Abreu et al. 2008), and GALFIT (Peng et al. 2002, 2010).

The GALFIT package was chosen because it can simultaneously fit an arbitrary number of components. This allows to fit galaxies that lie together (blended objects) in the line of sight. The use of masking to deal with blended objects cause poor accuracy fits (see §3.4.1); Häussler et al. (2007). In galaxy clusters, the high galaxy density, stars, and other artefacts makes object blending a quite frequent signature. Finally, GALFIT is fully documented, and is supported by Chien Peng who answers all questions regarding GALFIT. Also, Chien Peng maintains a blog in [FACEBOOK](#), where any user can exchange information.

### 3.2.1 GALFIT

The GALFIT package is a fitting algorithm that fits 2–D surface brightness functions to stars and galaxies on digital images. The functions, which GALFIT can fit, include<sup>2</sup>: Sérsic (Sérsic 1968), exponential (Freeman 1970), Gaussian, King profile (King 1961), Moffat (Moffat 1969), Nuker (Lauer et al. 1995), Edge-On disk, PSF profiles, and background sky.

As mentioned above, GALFIT can simultaneously fit an arbitrary number of components and combine different surface brightness functions. This allows to deblend galaxy components such as bar, disk bulge, AGN, and neighbor galaxies.

#### Overview of the GALFIT Algorithm

In order that GALFIT can fit surface brightness models, it uses the Levenberg-Marquardt algorithm (Press et al. 1992) (see Appendix A). The Levenberg-Marquardt algorithm minimizes the reduced  $\chi^2$  ( $\chi^2_\nu$ ), which is defined as:

$$\chi^2_\nu = \frac{1}{N_{dof}} \sum_{x=1}^{nx} \sum_{y=1}^{ny} \frac{(flux_{x,y} - model_{x,y})^2}{\sigma_{x,y}^2}, \quad (3.8)$$

where  $N_{dof}$  is the degrees of freedom during the fit (total data points - number of parameters in the model),  $nx$  and  $ny$  are the dimensions of the axis  $x$  and  $y$  respectively,

---

<sup>2</sup>For version 3.0.

$flux_{x,y}$  is the image flux at pixel  $(x, y)$ ,  $model_{x,y}$  is the sum of all the functions used in the fit at pixel  $(x, y)$ ,  $\sigma_{x,y}$  is the Poisson deviate<sup>3</sup> of the flux at pixel  $(x, y)$ .

The  $model_{x,y}$  is created from initial parameters. Firstly,  $model_{x,y}$  is previously convolved with a PSF using a fast Fourier transform (FFT) technique (Press et al. 1992).

Once the fit has finished, GALFIT estimates errors using ellipses in the parameter space. The program makes an ellipse centered at the point of global (or local) minimum covering an area that gives  $\Delta\chi = 1$ . Based on this ellipse the errors  $a_i$  for:

$$\sigma_{a_i} = \sqrt{\chi^2} \cdot \sum_{j=1}^n |v_j \cdot \hat{a}_i|, \quad (3.9)$$

where  $a_i$  is the parameter axis, and  $v_j$  is the semi-major axis vector of the ellipse.

More details about GALFIT are given in Peng et al. (2002, 2010).

### GALFIT setup

GALFIT uses an input FITS<sup>4</sup> image and a configuration parameter file, and optionally, a PSF image, sigma image, bad pixel mask, and parameter constraint files.

In the configuration parameter file photometric zero-point, scale plate and the initial parameters for the model must be provided.

If a sigma image ( $\sigma_{x,y}$ ) is not provided, GALFIT looks for the image header keywords *GAIN*, *RDNOISE* to create the sigma image. Also, it looks for *EXPTIME* and *NCOMBINE* header keywords to compute the flux.

The PSF image must be provided to remove the effects of seeing due to atmospheric turbulence and instrumental broadening. Galaxy surface brightness profile is significantly affected by the PSF at the galaxy's center. The PSF image can be obtained from high signal-to-noise image of a star or using a synthetic function. Thus, for Hubble images TINYTIM<sup>5</sup> can generate synthetic PSFs.

An image mask can be provided to avoid that external objects affect the fit.

If desired, some of the parameters can be varied within a range provided by the user. This can be done using a constraint file. For more details, see GALFIT manual<sup>6</sup>.

This setup must be done for every single galaxy in the image. In the case of galaxy clusters, the task can be very hard. A different approach must be followed.

<sup>3</sup>More exactly, it is Poisson noise plus read noise, and background sky noise added in quadrature.

<sup>4</sup>Flexible Image Transport System.

<sup>5</sup><http://www.stsci.edu/software/tinytim/tinytim.html>.

<sup>6</sup>[users.obs.carnegiescience.edu/peng/work/galfit/README.pdf](http://users.obs.carnegiescience.edu/peng/work/galfit/README.pdf).

### 3.3 A New Approach to Fit Surface Brightness Models to Cluster Galaxies: DGCG

As explained in the previous section (§3.2.1), there are many steps to prepare the fitting of one galaxy. Therefore, in one image, the fitting of each galaxy in one single image would become very difficult if it contains hundreds of galaxies as it is the case of galaxy clusters. Moreover, as we now live in the era of large databases, it is necessary to follow a different approach.

To that end, GALFIT needs a script which could format the necessary files in order to work without user's intervention. This allow us to separate the design of an algorithm to fit surface brightness models from the design of a script to fit models in regions of high object density. In this section, we focus on this last part because the first part of the problem is already solved by GALFIT.

To achieve this, we have developed DGCG (**D**river for **G**ALFIT on **C**luster **G**alaxies) to allow GALFIT to work automatically in crowded fields. Hence, DGCG is an information technology to perform 2-D surface brightness decomposition on cluster galaxies.

Similar to GALFIT, DGCG needs configuration files to work properly. Those files are explained in section §3.3.1. In section §3.3.2, the algorithm is explained, and in section §3.3.3, differences among DGCG and other scripts for GALFIT stand out.

#### 3.3.1 Preparation of Inputs for DGCG

Here, it is shown the used preparation for DGCG to fit galaxies for the LOCOS database. Below, it is described how to prepare the input files for DGCG. It is explained how the images were removed from cosmic rays. It is described the selection of PSFs, and how they were extracted from the image. The set up of the constraints file. How to stars and galaxies were classified. Finally, it is explained the SExtractor techniques to detect the largest number of objects.

##### Cosmic rays

In the first step, cosmic rays are removed from the image. The COSMICRAYS tool of IRAF to remove cosmic rays was used.

The *threshold* parameter was set to five times the standard deviation from sky level, and *fluxratio* was set to 5. After this, excluded cosmic rays were revised in the flux ratio vs. flux plot.

##### Selection and Extraction of PSFs

As explained before, GALFIT needs PSF images to remove the effects of atmospheric turbulence and/or optics telescope. For GALFIT, PSF images could be stars provided from the image with the sky pedestal removed.

For every cluster image, there were selected the brightest non-saturated stars ( $Mag \leq 16$ ) in the entire image area. To do this, `SEXTRACTOR` was used with `CHECKIMAGE_TYPE` set to `OBJECTS`. `SEXTRACTOR` returns the same input image with the sky pedestal removed. From this image, the stamp images were extracted for every star with the peak centered in the image.

Finally, every PSF was named *PSF-X-Y.fits*, where “X” and “Y” are the PSF positions in the cluster image. Hence, DGCG knows which PSF is the nearest to every galaxy.

### The constraints file

In order to avoid non-physical parameter values and save computing time, Some parameters were restricted to vary in a predetermined range.

For bulge and disk fittings, the  $x$ ,  $y$  positions of the bulge and disk models were constraint to have relative positions defined in the initial parameter file. In other words, the centers of the bulge and disk are always the same during the fitting.

The effective radius for the bulge and disk range between 0.1 and 500 pixels. Sérsic index can only have values between 0.02 to 12.

For the fittings with the Sérsic component, effective radius shift from 0.1 to 500 pixels, and Sérsic index from 0.02 to 12.

### SEXTRACTOR

`SEXTRACTOR` (Bertin & Arnouts 1996) is used to detect sources and make initial parameters for DGCG.

There are two main parameters that `SEXTRACTOR` uses to deblend and separate into different objects. These parameters are `DEBLEND_NTHRESH` and `DEBLEND_MINCONT`. These determine which pixels belong to every object above the threshold level. Specifically, `DEBLEND_NTHRESH` describe the number of deblending subthresholds, and `DEBLEND_MINCONT` determines the minimum contrast for deblending. Figure 3.2 shows how different objects are separated.

`SEXTRACTOR` is highly dependent of the set-up of the configuration input file, specially on `DEBLEND_NTHRESH` and `DEBLEND_MINCONT` parameters. It is hard to find a consistent set-up for `SEXTRACTOR` for the entire image. Häussler et al. (2007) also had this problem. For instance, for a determined parameter configuration, `SEXTRACTOR` detects and derives photometry for high density and high surface brightness objects. On the other hand, for a different configuration, it detects and estimates photometry for low density and faint objects.

In order to solve this problem, `SEXTRACTOR` was run 3 times on every image with different configurations. Every `SEXTRACTOR` configuration was divided among *hot*, *cold* and *warm* runs. Häussler et al. (2007) used a similar technique. Table 3.1 shows the `SEXTRACTOR` parameters for these 3 runs.

These 3 catalogs were merged into a single catalog containing photometric information of almost every object in the image. To create the final catalog, the objects of the

★ Figure 3.2

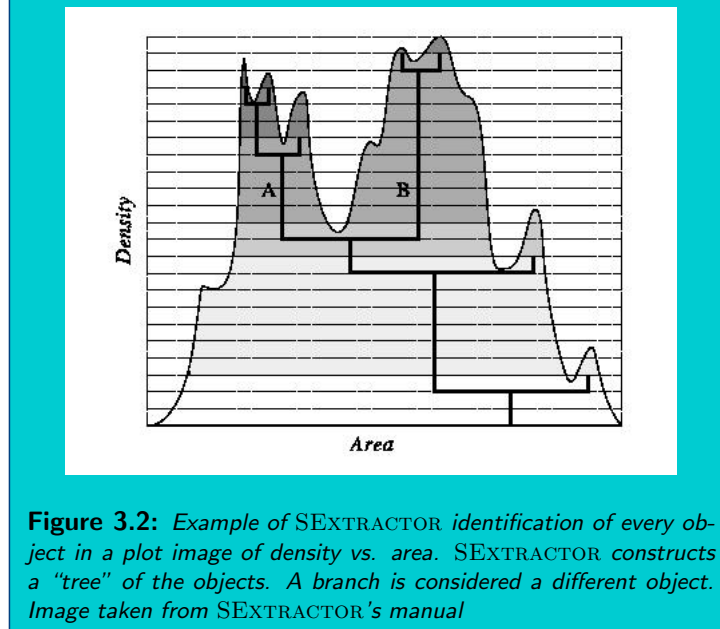


**Figure 3.2:** Example of SExtractor identification of every object in a plot image of density vs. area. SExtractor constructs a "tree" of the objects. A branch is considered a different object. Image taken from SExtractor's manual

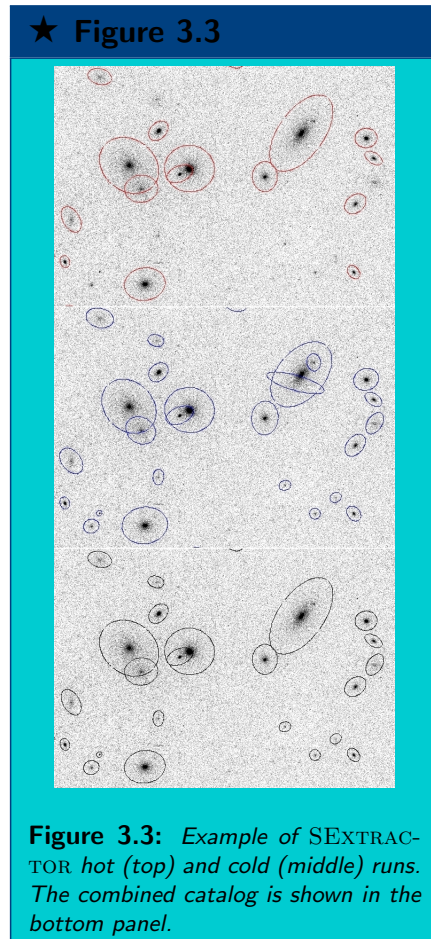
SExtractor parameters	hot	cold	warm
DEBLEND_NTHRESH	32	64	64
DEBLEND_MINCONT	0.0005	0.0001	0.0001
DETECT_THRESH	2.3	1.2	2
DETECT_MINAREA	50	15	30

**Table 3.1:** hot, cold and warm configurations for SExtractor

*cold* configuration were added to the HOT catalog if they are outside of 0.7 times the *KRON\_RADIUS* (Kron 1980) for the HOT objects. This output catalog was combined in the same manner with the *warm* catalog.

Figure 3.3 shows an example of the combination of the hot and cold runs. The final catalog (*warm*) is shown in the bottom panel of Figure 3.3. As can be seen, this catalog gives better results than the hot and cold catalogs (top and middle panels of Figure 3.3 respectively).

The combination of these two catalogs guarantees a better object recovering than single catalogs. It can be seen for the bright galaxy at the top right in the hot run that the same galaxy is divided into three fake galaxies for the cold run. For that reason, it is better run different configurations for SExtractor and combine them in one single catalog.



### PPP's Magnitudes and Star/Galaxy Classifications

In order to get a better estimation of initial parameters, the magnitude and star/galaxy classification of López-Cruz (1997) were used. López-Cruz et al. (2004) used PPP (Yee 1991) to measure total magnitudes using curve of growth analysis. The rows 6 and 14 columns of Table 3.2 (see §3.3.2) were changed with the values computed from PPP.

### DGCG Configuration file

The setup for DGCG for the galaxies in LOCOS is shown in Figure 3.4.

★ Figure 3.4

```

Img          = A85.fits      # Input image
SexCat       = a85.ppp      # SExtractor catalog
SigImg       = none        # sigma image
PsfDir       = psfs        # PSF location (directory)
MagZpt       = 21.630      # Photometric zpt (same as GALFIT)
PlateScale   = 0.68        # Plate scale
FitFunc      = BD          # Single sersic or B/D decomposition? (BD) or (sersic)
GalClas      = 0.0,0.6    # Range of good galaxies: 0.0 (galaxy) to 1.0 (star)
ConvBox      = 60         # Convolution box size (pixels)
FitBox       = 6          # Fitting region. Times the galaxy size
MagDiff      = 5          # Mag difference between main obj and neigh obj
KronScale    = 1.5        # Scale Factor by which Mask Kron Ellipses are enlarged
SkyScale     = 1.6        # Scale Factor by which Sky Kron Ellipses are enlarged
Offset       = 20         # Additional offset to scale factor for sky mask(pixel)
SkyAnnuli    = 40         # width of sky annuli around sky kron ellipse
NSer         = 1.5        # Sersic index initial parameter
MaxFit       = 10         # Max number of allowed objects for sim fitting
MagRange     = 0.0, 18    # Acceptable magnitude range (MagMin,MagMax)
FlagSex      = 4          # Objects with this SExtractor Flag will not be fitted
ConsFile     = const      # Parameter constraint file
Region       = 0          # (0) Whole image catalog or, (1) region of the image
Boundary     = 0, 0, 0, 0 # Boundary of the object region (xmin,ymin,xmax,ymax)
Split        = 5          # Split image into how many parts along one axis?
AutoSatRegion = 0        # Allow DGCG to determine size of saturated regions?
SatRegionScale = 2       # Scale Factor used to increase size of Sat regions
Ds9SatReg    = badbox.reg # DS9 input saturation box region file
FileOut      = a85bdfits   # Preposition name for output catalog files
SegFile      = seg.fits    # Preposition name for mask output segmentation file
SkyFile      = sky.fits    # Preposition name for sky output segmentation file
PixPrefix    = pixels     # Preposition name for obj pixel output files
Ds9OutName   = images     # Preposition name for output Ds9 data cube images
Ds9OutNum    = 40         # Maximum number of objects allowed for Ds9OutName
Ds9FitReg    = fit.reg     # Ds9 region output file for fitted objjs
BoxOut       = box.reg     # Ds9 region output file used for obj fitting
BoxSkyOut    = boxsky.reg # Ds9 region output file used for sky fitting
SexSort      = sexsort.cat # Output filename of sorted SExtractor catalog
Erase        = 0          # Erase all unnecessary files? 0 = no, 1 = yes
Nice         = 0          # Use the "nice" command when running GALFIT
Overwrite    = 0          # Overwrite mask and sky segmentation files
Execute      = 1          # 0: Sort catalog and create segmentation images
                    # 1: Execute everything
                    # 2: only computes sky and create input files
                    # 3: Execute everything except final output files

```

Figure 3.4: Example of the configuration file for DGCG.

### Manual Fitting

As the actual DGCG version can not fit bars automatically, the cluster images were checked to search those galaxies which shows the presence of a bar.

A bar component was added for those galaxies where it seems to be a problem for the fitting of bulge/disk components. A Gaussian component was used as a bar. Equation 3.1 was used with the Sérsic index fixed at 0.5. The results of the Sérsic + exponential fitting were used as initial parameters for the new fit.

### 3.3.2 DGCG: The Algorithm

DGCG is a wrapping script, written majority in PERL with some smaller parts in PYTHON, that extracts galaxy information from source extractor (SEXTRACTOR) (Bertin & Arnouts 1996) and provide it to GALFIT as initial parameters. Once DGCG created the necessary files, it runs GALFIT and computes output variables. DGCG works in

batch mode.

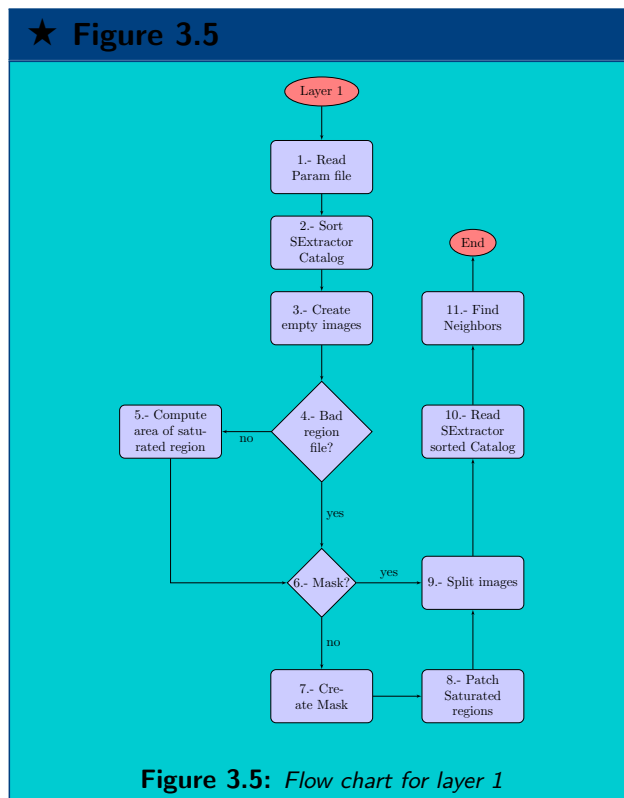
DGCG contains more than 8500 lines of code written by the author. In order to provide a detailed explanation, The algorithm is divided into four layers.

Hereafter, SExtractor parameter variables are shown in caps *ITALICS*, and DGCG parameter variables in SMALL CAPS font.

### First Layer

The first layer creates masks for each galaxy. It creates two mask images: 1) a mask to remove contamination for external objects during the fitting. 2) A mask to calculate the sky for each galaxy. The ellipse shape is used as a mask. After the masks are created on the image, DGCG patches the regions where pixels are saturated. Later, every mask image is divided into small mask images so that GALFIT can read them faster. Finally, it creates a list of the neighbor objects for every galaxy.

The first layer algorithm is shown as a flow Diagram in Figure 3.5. Below, it is explained the first layer. Numbers in **bold face** font represent number steps of the layer of Figure 3.5.



DGCG reads the parameter file (1). An example of such a file was shown in Figure 3.4. In the appendix D, it is shown the explanation of a basic set up for this file.

After reading the parameter file, DGCG reads the SExtractor catalog (see §3.3.1, 2). For the DGCG version used in this work, the SExtractor catalog must contain the parameters indicated in table 3.2.

Number	Parameter	Description	Units
1	NUMBER	Running object number	
2	ALPHA_J2000	Right ascension of barycenter (J2000)	[deg]
3	DELTA_J2000	Declination of barycenter (J2000)	[deg]
4	X_IMAGE	Object position along x	[pixel]
5	Y_IMAGE	Object position along y	[pixel]
6	MAG_BEST	Best of MAG_AUTO and MAG_ISOCOR	[mag]
7	KRON_RADIUS	Kron apertures in units of A or B	
8	FLUX_RADIUS	Fraction-of-lightradii	[pixel]
9	ISOAREA_IMAGE	Isophotal area above Analysis threshold	[pixel**2]
10	A_IMAGE	Profile RMS along major axis	[pixel]
11	ELLIPTICITY	1 - B_IMAGE/A_IMAGE	
12	THETA_IMAGE	Position angle (CCW/x)	[deg]
13	BACKGROUND	Background at centroid position	[count]
14	CLASS_STAR	S/G classifier output	
15	FLAGS	Extraction flags	

**Table 3.2:** SExtractor output parameters used for this version of DGCG

Once DGCG has read SExtractor file, DGCG creates two catalogs from SExtractor. First, it makes a catalog sorted by the magnitude (i.e. it starts from the brightest to the faintest object). Second, it makes a catalog sorted by ellipse area (i.e. it starts from the biggest to the lowest area).

The ellipse's area is given by:

$$Area = \pi * Scale * A_{im} * R_{Kron} * (1 - e) * R_{Kron}, \quad (3.10)$$

where *Scale* is given by KRONSCALE from the configuration file and  $A_{im}$ ,  $R_{Kron}$  and  $e$  are given by A\_IMAGE, KRON\_RADIUS and ELLIPTICITY from SExtractor catalog respectively. Each ellipse represents a mask for every object in the mask image.

The catalog sorted by ellipse's area is used only to draw masks. DGCG starts drawing the ellipse with the greatest area, and finishes with the smaller one. Thus, the ellipses with the smaller area are not erased by the ellipses of greater area. This is the only time this catalog is used. DGCG does not draw ellipses where one or more pixels are saturated.

Furthermore, DGCG creates a catalog sorted by magnitude because it starts fitting the brightest galaxy and finishes with the faintest one. During the fitting, the brightest galaxies are not relatively affected by the faintest ones, but the faintest ones are affected by the brightest ones (see equation 3.8). This way of fitting allows us a better parameter

computation in a short time because DGCG takes the parameters from the previous fit, and leaves them fixed for the next fitting.

Later, the program creates two empty images of the same size as the input FITS image (3). An empty image is used to mask neighbor objects, and the other one to estimate background sky level.

Once the empty images have been created, DGCG starts to draw ellipses from the largest to the lowest area (4). Ellipse masks are drawn using the following parametric equations:

$$x_{ell} = x_c + R * \cos\eta\cos\theta - B * \sin\eta * \sin\theta \quad (3.11a)$$

$$y_{ell} = y_c + R * \cos\eta\sin\theta + B * \sin\eta * \cos\theta, \quad (3.11b)$$

where  $(x_c, y_c)$  is the ellipse center,  $\theta$  is given by *THETA\_IMAGE*,  $B$  is  $(1 - e) * R$ . for neighbor mask  $R = KronScale * A\_IMAGE * KRON\_RADIUS$ , and for sky mask  $R = KronScale * A\_IMAGE * KRON\_RADIUS + Offset$ , while  $\eta$  is given by equation 3.12.

$$\eta = \arctan * \left( \frac{\sin\lambda}{B}, \frac{\cos\lambda}{R} \right), \quad (3.12)$$

$\lambda$  is the geometrical angle between the semi-major axis and the current point.

Example of a mask image is shown in Figure 3.6.

After ellipse mask is created for every object, DGCG patches the image regions indicated in the bad region file (8). In this file, it is indicated the regions where saturated stars or unwanted regions could affect the fitting. This file is created by the program DS9<sup>7</sup>. Users must save the bad regions as a “box” region file in DS9.

If *AUTOSATREGION* = 1, DGCG will try to determine the size of the bad region using the scale factor *SATREGIONSCALE* on those objects where its *SEXTRACTOR FLAG* indicates it is saturated (5).

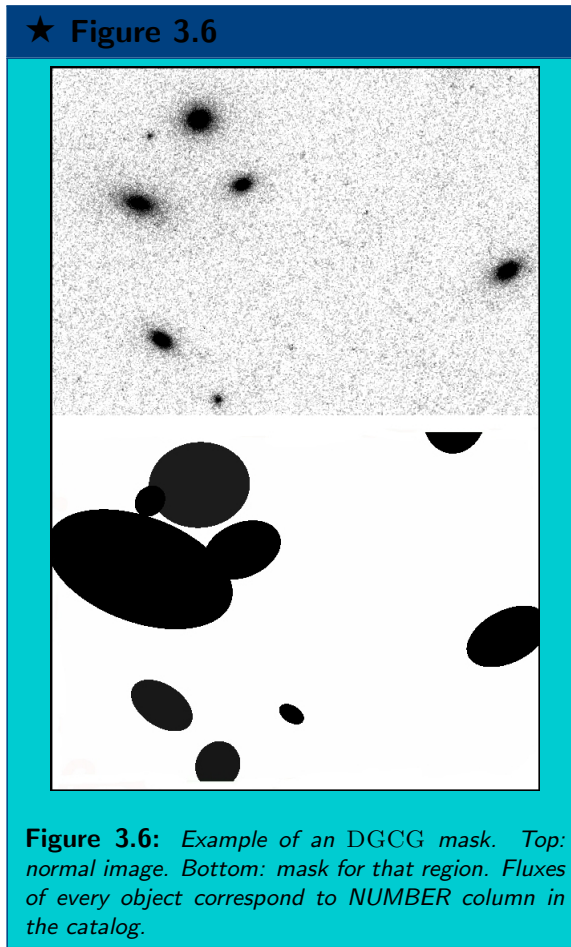
In order to save time when GALFIT reads an input image, DGCG splits the image along one axis (9). This is done according to the user’s input *SPLIT* from DGCG configuration file.

Finally, a list of neighbors for every object is created (11). We mean by neighbors those objects where ellipse masks overlap each other.

## Second Layer

The second layer computes the sky for every object. DGCG calculates the sky prior model fitting. Consequently the sky is leaved fixed during model fitting. This technique gives better results (Häussler et al. 2007).

<sup>7</sup><http://hea-www.harvard.edu/RD/ds9/site/Home.html>



To that end, DGCG uses the sky mask created in step **7** from layer 1. For every galaxy, DGCG computes the sky in an annuli on the outside of the ellipse mask. Subsequently, it uses the SKY function of GALFIT to fit those pixels.

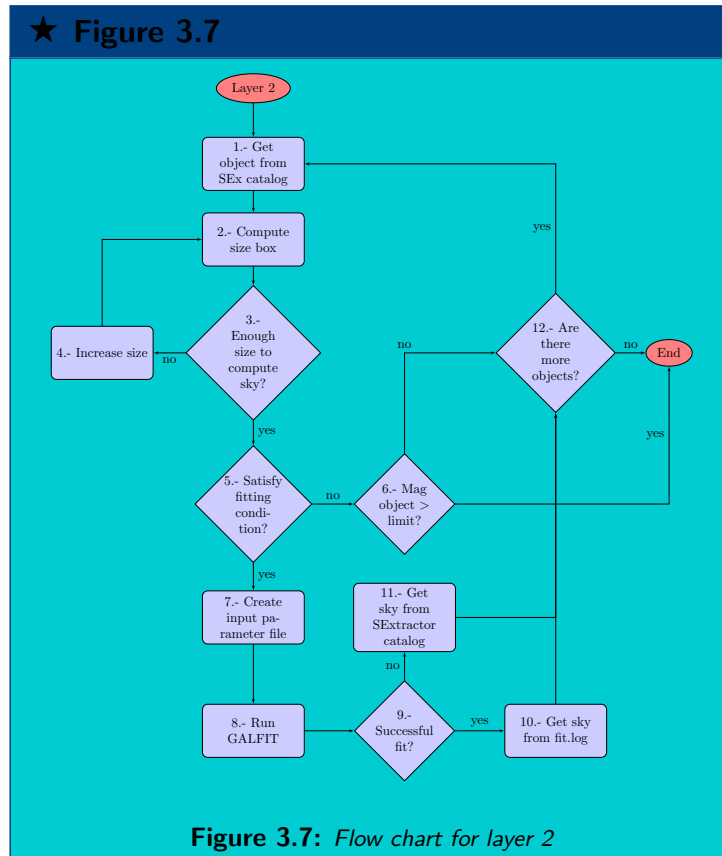
The second layer algorithm is shown as a flow Diagram in Figure 3.7. Below, it is explained the second layer. Numbers in **bold face** font represent number steps of the layer of Figure 3.7.

DGCG takes an object from the SExtractor catalog sorted by magnitude (**1**).

Later, DGCG computes the size of the fitting region to compute the sky (**2**). This size is computed in a rectangle with the size of the mask ellipse + SKYANNULI.

DGCG determines if the pixel area to compute sky is large enough **3**. If the number of pixels is not enough, DGCG increase the pixel area **4**.

Sky is only computed for objects which are going to be fitted for GALFIT (**5**). In this



way, it saves computing time. To satisfy this condition, they must be in the magnitude range given by `MAGRANGE`, galaxy classification given by `GALCLAS`, and within the pixel region given by `BOUNDARY` (if `REGION = 1`). Otherwise, another object from the catalog is taken.

If the object has reached the magnitude limit indicated by `MAGRANGE`, then this layer ends (6).

**DGCG** creates the input parameter file for the object and runs `GALFIT`.

If `GALFIT` converge into a solution, then the sky value is taken from *fit.log* (10). This file stores the parameters of the fittings. On the other hand, If the fit crashed, the sky is taken from `BACKGROUND` value of the `SExtractor` catalog (11).

If there is no remaining objects to compute sky, the layer 2 ends.



checks if it satisfies the fitting condition (3). This step is the same as step 5 in layer 2. Objects must be in the magnitude range given by MAGRANGE, galaxy classification given by GALCLAS, and within the pixel region given by BOUNDARY if REGION = 1. Otherwise, the next object from the SExtractor catalog is taken.

If the object has reached the magnitude limit indicated by MAGRANGE, this layer ends (4).

To remove the effect of atmosphere turbulence and telescope optics (see 3.3.1), DGCG selects the best PSF for every object (5). The best PSF for a determined object is the one that is closest to that object in the image.

Later, DGCG computes the initial parameters for every object from the catalog of SExtractor (6). The computed parameters by SExtractor are changed to initial parameters for single Sérsic and Sérsic + Exponential models accordingly to Table 3.3.

Component parameter	Single Sérsic	Bulge + Disk Description
Sérsic Mag	MAG_BEST	MAG_BEST +0.5
Sérsic Effective radius	FLUX_RADIUS	FLUX_RADIUS *0.7
Sérsic index	NSer	NSer
Sérsic axis ratio	1- ELLIPTICITY	0.8
Sérsic angular position	THETA_IMAGE -90	THETA_IMAGE -90
Exponential Mag		MAG_BEST +0.5
Exponential scale length		FLUX_RADIUS
Exponential axis ratio		1- ELLIPTICITY
Exponential angular position		THETA_IMAGE -90

**Table 3.3:** Initial parameters created for main object. Column 1 represents the model's parameter. The value for this parameter is assigned from SExtractor catalog if the model is either a single Sérsic (column 2) or Sérsic + Exponential (column 3). Whether DGCG fit either a single Sérsic or Sérsic + Exponential model depends of the value of FITFUNCTION

Once that, DGCG creates the initial parameter file for GALFIT (7), it creates a copy of the mask image (8) and removes the mask of the object that it is going to be fitted (9) from the mask image.

DGCG looks for neighbors objects from the list created in step 11 from layer 1. It checks if the object satisfy the criteria for simultaneous fitting (12). For this object can be fitted simultaneously, it should not be fainter in magnitude MAGDIFF times than the main object. Faint objects do not have a strong effect during the fitting of bright objects (see equation 3.8).

If the neighbor object were previously fitted (13), DGCG takes the fitted parameters and leave them fixed during the fitting of the main object (15). In this way, it saves computing time. If the neighbor object were not previously fitted, DGCG computes its initial parameters (16). Later, the neighbor object mask is removed from the mask image (17).

DGCG does this until there are no remaining objects in the list (10). Subsequently, it prints the sky value (computed in layer 2) in the initial parameter file as a fixed value

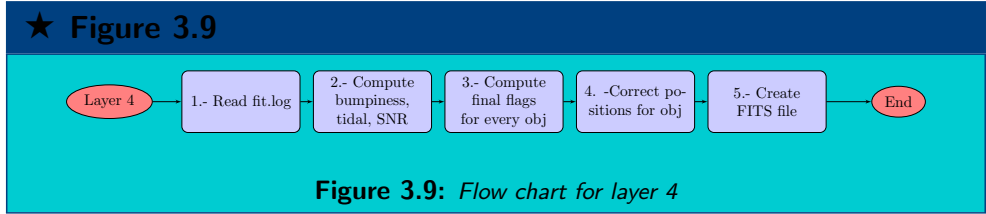
(18).

Thereafter, DGCG runs GALFIT (19). If the fit converges in a solution (20), DGCG takes the parameters of the fitted model and looks for neighbor objects. The searching radius is `TIMESRE` times the effective radius. If it finds new neighbor galaxies, DGCG updates the neighbor's list. If no more objects are found to fit, the layer 3 ends.

#### Fourth Layer

When GALFIT finishes of fitting the galaxies, the layer 4 computes the output variables. From the *fit.log* file, DGCG computes, inside an ellipse area of 1 Kron radius (see §3.3.1), Bumpiness (Blakeslee et al. 2006), Tidal (Tal et al. 2009) parameter, and signal to noise ratio. DGCG assigns a flag for every fit to estimate if this were acceptable. DGCG makes an extension of the `SEXTRACTOR` catalog and add the fitted parameters and output variables. At the end, DGCG returns a final catalog in table FITS file.

The fourth layer algorithm is shown as a flow Diagram in Figure 3.9. Below, it is explained the fourth layer. Numbers in **bold face** font represent number steps of the layer of Figure 3.9.



When layer 3 finished, DGCG reads the `FIT.LOG` file (1). It extracts all the values of the fitted parameters. Later, DGCG computes BPN (see §1.2.2), tidal parameter (Tal et al. 2009), local  $\chi^2_{\nu}$ , and signal to noise ratio (SNR) within Kron Radius<sup>8</sup> (2). GALFIT already gives an  $\chi^2_{\nu}$ , but this is for all the pixels included in the fitting. DGCG re-computes  $\chi^2_{\nu}$  within the radius previously defined. The tidal parameter is defined as:

$$T_{galaxy} = \left| \frac{I_{x,y}}{M_{x,y}} - 1 \right|, \quad (3.13)$$

where  $I_{x,y}$  are the pixel values of the object and  $M_{x,y}$  are the pixels of the model object. BPN is defined as (see §1.2.2):

$$BPN = 10 \frac{\sqrt{\langle [I - S]^2 \rangle - \langle \sigma_s^2 \rangle}}{\langle S \rangle}, \quad (3.14)$$

where,  $S$  is the galaxy model, and  $\langle \sigma_s^2 \rangle$  is the uncertainty of the observed object. We take  $\langle \sigma_s^2 \rangle$  from the sigma map computed by GALFIT.

<sup>8</sup>See §3.3.1

For BPN and tidal parameter, values are computed for pixels outside of an annulus of 2 pixels from the center of the galaxy. This avoids problems related to central deviations due to PSF.

In order to estimate whether GALFIT converge to a good solution, DGCG computes a flag value for every object. Table 3.4 shows the meaning of every flag (4). A flag value of 0 means that the model converged to an acceptable solution.

Flag	Description
0	converge to a solution
1	Ran into constraints
2	Parameters have caused numerical issues
4	Parameter model errors in fit.log are big

**Table 3.4:** DGCG Output flags

On the other hand, a flag value of 5 means that the fitted model has a large error and some parameter ran into constraints (4 + 1). Finally, DGCG creates a FITS file containing all the fitted parameters including the SExtractor catalog (6).

### 3.3.3 Other wrapping scripts: GALAPAGOS, SIGMA and PY-MORPH

During the course of this Thesis, 3 wrapping scripts for GALFIT were developed. GALAPAGOS<sup>9</sup> (Häussler et al. 2007; Barden et al. 2012) runs on IDL<sup>10</sup> and has been used in the STAGES<sup>11</sup> and GEMS<sup>12</sup> projects. A similar script is SIGMA<sup>13</sup> (Kelvin et al. 2012). It is written in R<sup>14</sup> language and has been used in the GAMA database (Driver et al. 2011). Finally, another script is PYMORPH (Vikram et al. 2010). It is written in PYTHON<sup>15</sup> language and uses the PYRAF<sup>16</sup>.

<sup>9</sup>Galaxy Analysis over Large Areas: Parameter Assesment by GALFITting Objects from SExtractor

<sup>10</sup><http://www.exelisvis.com/language/en-us/productsservices/idl.aspx>

<sup>11</sup><http://www.nottingham.ac.uk/astronomy/stages/>

<sup>12</sup><http://www.mpia.de/GEMS/gems.htm>

<sup>13</sup>Structural Investigation of galaxies via Model Analysis

<sup>14</sup><http://www.r-project.org>

<sup>15</sup><http://www.python.org/>

<sup>16</sup>[http://www.stsci.edu/institute/software\\_hardware/pyraf](http://www.stsci.edu/institute/software_hardware/pyraf)

GALAPAGOS	DGCG	SIGMA	PYMORPH
IDL	PERL	R	Python
Runs SExtractor twice	Read two SExtractor catalogs	Runs SExtractor once	Runs SExtractor once
Uses two image masks	Uses two image masks	Uses one image mask	Uses one image mask
Computes sky with intern routine previous to galaxy fitting	Computes sky with GALFIT previous to galaxy fitting	Computes and removes sky with SExtractor previous to galaxy fitting	Computes sky with GALFIT at the same time as galaxy fitting
Fitting starts from the brightest galaxy	Fitting starts from the brightest galaxy	Fitting starts from the first galaxy of the SExtractor catalog.	Fitting starts from the first galaxy of the SExtractor catalog.
runs in parallel	runs in serial	runs in parallel	runs in parallel
one PSF per image	several PSFs per image	several PSFs per image	uses PSFs from input image
one model: Sérsic	two models: Sérsic or Sérsic + Exponential	one model: Sérsic	two models: Sérsic or Sérsic + Exponential
Catalog of fitted parameters	Catalog of fitted parameters + BPN, Tidal, SNR, and object $\chi^2_b$	Catalog of fitted parameters	Catalog of fitted parameters + CAS

**Table 3.5:** Main differences among GALAPAGOS, SIGMA, PYMORPH and DGCG scripts.

Each script has its own advantages and disadvantages. The main differences among DGCG, GALAPAGOS, SIGMA, and PYMORPH are emphasized in Table 3.5. Each script is written in a different programming language. GALAPAGOS is available through its webpage<sup>17</sup>; however, it is not completely freeware because a software license must be bought for IDL. On the contrary, PERL, PYTHON, and R are open sources. Nevertheless, as far as we know, SIGMA source code is not available. DGCG and PYMORPH are available on request.

GALAPAGOS is the only one that runs SExtractor twice. It combines those catalogs to get the majority of objects in the image. In the DGCG preparation (§3.3.1), the user must do this manually (see §3.3.1). In this way, users can check whether output catalog parameters are fine (check DGCG manual in Appendix D). If the parameters are not appropriate, users can rerun SExtractor with different configurations until it gives suitable parameters for the galaxies. In the case of GALAPAGOS, the user must wait for GALAPAGOS to finish to check if SExtractor catalogs were appropriate. Hence, a checking of SExtractor catalog parameters before model fitting could save computing time as it is done in DGCG.

GALAPAGOS and DGCG use two mask images to compute sky and remove neighbor contamination. PYMORPH uses one mask image to remove neighbor contamination. To compute sky, it fits sky model at the same time with model fitting. SIGMA uses also one mask image, but it uses SExtractor parameters to compute the sky before the fitting. GALAPAGOS and DGCG also compute sky before model fitting.

In model fitting, SIGMA and PYMORPH follow the order of the SExtractor catalog and continues until the last object of the list. On the contrary, GALAPAGOS and DGCG starts from the brightest object of the SExtractor catalog, and continues until the faintest object of the list (see §3.3.2 for details).

All the codes, except for DGCG, can run GALFIT in parallel. In other words, the scripts can run GALFIT on different galaxies at the same time, but in order to do so the computer must have the appropriate hardware. Future versions of DGCG will include the option of parallel computing with the use of GPUs<sup>18</sup> and CUDA<sup>19</sup> language program.

All the codes, except for GALAPAGOS, use a list of PSFs per image. SIGMA uses PSFEX<sup>20</sup> which is a recently algorithm that extracts PSFs from the image with SExtractor. GALAPAGOS has the disadvantage of using only one PSF for the whole image. Hence, GALAPAGOS does not account for PSF variations across the image.

DGCG and PYMORPH can fit either a single Sérsic or Sérsic + exponential models while GALAPAGOS and SIGMA only fit a single Sérsic. The 4 scripts have the option of simultaneous fitting for neighbor galaxies (see §3.3.2).

In the final output catalog, besides the fitted parameters, PYMORPH and DGCG computes additional parameters for the models. PYMORPH computes CAS (see §1.2.2) while DGCG computes bulge to total luminosity ratio, tidal parameter, BPN, SNR and

<sup>17</sup><http://astro-staff.uibk.ac.at/~m.barden/galapagos/>

<sup>18</sup>Graphics Processing Unit [http://en.wikipedia.org/wiki/Graphics\\_processing\\_unit](http://en.wikipedia.org/wiki/Graphics_processing_unit)

<sup>19</sup>[http://www.nvidia.com/object/cuda\\_home\\_new.html](http://www.nvidia.com/object/cuda_home_new.html)

<sup>20</sup><http://www.astromatic.net/software/psfex>

object  $\chi^2_\nu$  (see §3.3.2).

Here, it has been highlighted the features of the 4 wrapping scripts for GALFIT. DGCG algorithm has been designed to satisfy thesis's needs, and it has been adapted to analyze cluster images specifically for LOCOS (López-Cruz 1997; Lopez-Cruz 2001) database. Moreover, DGCG is free software and, in the future, will have a webpage where anyone will be able to download it.

### 3.4 DGCG Performance: Surface Brightness Photometry on Artificial Galaxies

A way to check the performance of DGCG is using artificial images. To create these, galaxies with known values of model parameters are created and distributed along an image. Noise must be added to it to resemble a real image taken by the telescope. Later, DGCG can be used to fit those artificial galaxies. Once this is done, the output fitted parameters are compared with the true parameter values. In this way, one can know either the SNR or magnitude limit where fitted parameters are reliable.

To determine the SNR lower limit above which the parameters are properly recovered by DGCG, it was tested on the GEMS artificial galaxies (Häussler et al. 2007). Those artificial galaxies were created to test GALAPAGOS code, then DGCG can be compared with it. GEMS artificial galaxies are single de Vaucouleurs components which are good enough to test the reliability of the Single Sérsic components. To test the Sérsic + exponential components, Bulge + disk artificial galaxies have been created from the parameters distributions of the GEMS artificial catalogs.

#### 3.4.1 Fits on GEMS artificial galaxies (Bulge only)

Häussler et al. (2007) made fittings on images with artificial galaxies to compare GALFIT vs. GIM2D. They also used those galaxies to check the reliability of GALAPAGOS on GEMS data. Those artificial images resemble the noise of GEMS database and are available on the webpage of GEMS<sup>21</sup>. They contain de Vaucouleurs galaxies, exponential galaxies, and Sérsic galaxies.

---

<sup>21</sup><http://www.mpia.de/GEMS/gems.htm>

★ Figure 3.10

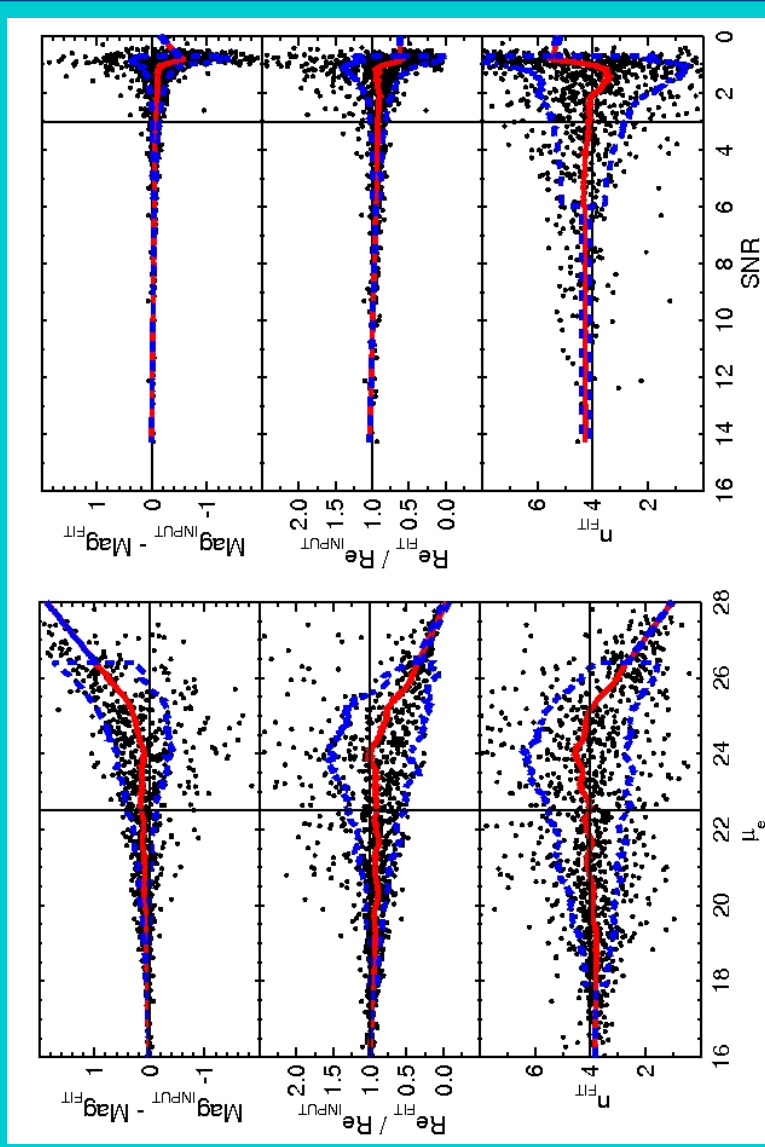


**Figure 3.10:** Left panel: Results of DGCG for GEMS simulated galaxies (Sérsic component). From top to bottom:  $\text{Mag}(\text{input}) - \text{Mag}(\text{fit})$ ,  $\text{Re}(\text{fit})/\text{Re}(\text{input})$ ,  $n(\text{fit})$ . Horizontal axis is the mean surface brightness at effective radius. The red solid line is the mean and the blue dashed one is 1 sigma. Vertical line represents the surface brightness of the sky. Right panel: same as left panel, but X-axis is the signal to noise ratio (SNR)

We have used those images to test DGCG code. Each image contains 800 galaxies. The two images that contain de Vaucouleurs galaxies has been used for this purpose. De Vaucouleurs artificial galaxies are Sérsic functions with  $n = 4$  (or de Vaucouleurs functions) and cover the following range of parameters:  $20 < mag < 26.5$ ,  $2 < R_e < 630$  (pixels),  $0.45 < q < 1$  (axis ratio) and  $0 < PA < 180$  (angular position). More details about how those images were created are found in Häussler et al. (2007).

To fit those artificial galaxies, it has been followed the procedure explained in §3.3.1. The input catalog for DGCG contained at least  $\gtrsim 750$  galaxies per image from a total of 800. Results of the performance of DGCG are shown in Figure 3.10.

Left panel of Figure 3.10 is very similar to the left panel of Figure 9 of Häussler et al. (2007). Therefore, the performance of DGCG is similar to GALAPAGOS.<sup>22</sup> One sigma (blue dashed line) becomes large for larger  $\mu_e$  (i.e. for fainter galaxies). The Sérsic index ( $n = 4$ ) is the hardest parameter to recover even though magnitude is well recovered for low SNR galaxies.

The sigma error results of Figure 3.10 were combined with GALFIT's error (see §3.2.1) for the galaxies fitted with Sérsic models. To assign the error values for each parameter, the SNR of each galaxy is compared with the SNR of the Figure 3.10.

### Deblending vs. Masking

In this section, it is shown that simultaneous fitting (§3.3.2) is a better approach than masking. To this end, the same artificial galaxies of the previous section (§3.4.1) were re-fitted by DGCG. The same SExtractor catalog and configuration file have been used. The only difference is that simultaneous fitting is not used. DGCG uses masking, for this run, as the only option to reduce neighbor contamination.

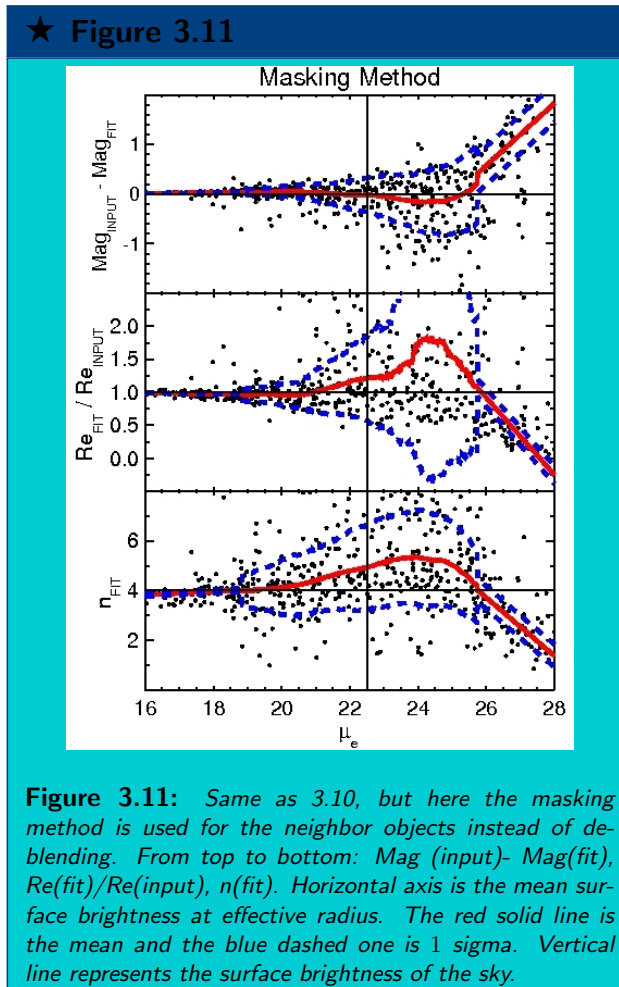
Results are shown in Figure 3.11. It can be seen that the method used in the left panel of Figure 3.10 gives better results than the one used for Figure 3.11. For a determined surface brightness, one sigma (blue dashed line) is greater in Figure 3.11 than in Figure 3.10. In addition, the mean (red solid line) is deviated from zero at brighter surface brightness in Figure 3.11 than in Figure 3.10.

The results shown in Figure 3.11 are similar to the right panel of Figure 9 of Häussler et al. (2007) where it shows the results for the fittings with the GIM2D code. This is due to GIM2D uses masking as its only option for neighbor galaxies.

It can be seen that deblending gives more accurate results than masking. The use of deblending is best for overlapping objects. Because galaxy crowding in an image is large for galaxy clusters, this effect must be taken into account for the fitting.

Masking neighbor objects is fine when they are relatively far enough from the interested object to fit. Nevertheless, if two objects are near each other, their luminosity profiles become blended in the line of sight. In this situation, masking is a bad option since it is difficult for the eye to keep track where one object ends and the other begins. This becomes problematic for galaxies with high Sérsic indexes because of their extended wings at larger radius (see Figure 3.1).

<sup>22</sup>DGCG is not parallelized yet. Hence GALAPAGOS is faster than DGCG



Finally, there is a hidden result in Figure 3.11: 2-D fittings perform better than 1-D fittings. 1-D techniques can not do simultaneous fitting because the profile is extracted from a 2-D image. To do this, the neighbor objects had to be masked. Then, as a consequence, 1-D fittings can not perform simultaneous fitting. Besides 1-D disadvantages explained in §3.2, regions of galaxy crowding, for example galaxy clusters, become problematic for 1-D techniques.

### 3.4.2 Fits on artificial galaxies (Bulge + Disk models)

In this section, we used artificial galaxies to test DGCG reliability for Bulge + disk models. To this end, images with Sérsic + exponential galaxies were created. Sérsic catalog in conjunction with the exponential one of GEMS were used to construct them.

★ Figure 3.12

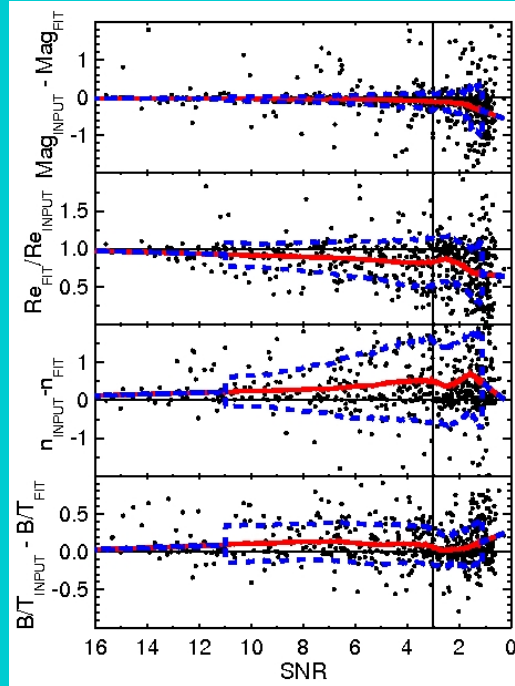


**Figure 3.12:** Results for the fitting of two components galaxies (Sérsic + Exponential) vs. their signal to noise ratio. From top to bottom:  $\text{Mag}(\text{input}) - \text{Mag}(\text{fit})$ ,  $\text{Re}(\text{fit})/\text{Re}(\text{input})$ ,  $n(\text{input}) - n(\text{fit})$ ,  $B/T(\text{input}) - B/T(\text{fit})$ . The red solid line is the mean and the blue dashed one is 1 sigma. Horizontal axis is the signal to noise ratio. The vertical solid line represents the value of the sky.

To create new images, Sérsic model catalog were randomly combined with the exponential model catalog. The range of values for the parameters for the Sérsic functions is the same for the de Vaucouleurs functions shown above (§3.4.1), but the Sérsic index range between  $0.2 < n < 8$ . In the case of exponential functions, the range of values for the parameters for the exponential functions is  $20 < \text{mag} < 26.5$  (magnitude),  $2 < \text{Re} < 316$  (effective radius),  $0.18 < q < 1$ , (axis ratio), and  $0 < PA < 180$  in angular position. The only condition to combine those functions was that the mean surface brightness at the effective radius of the bulge must be brighter than the disk by 0.5. This was done to distinguish the bulge from the disk.

The IDL program “simulate\_galaxy.pro”<sup>23</sup> (Häussler et al. 2007) was used to create the

<sup>23</sup>IRAF’s *smkobject* can not be used to create the artificial galaxies as explained in Häussler et al. (2007)

Sérsic + exponential galaxies. Each component was created and incorporate it to a blank empty image. Later, Poisson noise was added to it, and this image was convolved with a PSF image.

In order to fit those Sérsic + exponential galaxies, it has been followed the same procedure as §3.3.1 and §3.4.1. Results are shown in Figure 3.12. As can be seen, the sigma error (blue dashed line) for every parameter is larger for the Sérsic + exponential fits than the ones for the single Sérsic fits.

The sigma error results of Figure 3.12 were combined with GALFIT's error (see §3.2.1) for the galaxies fitted with Sérsic + exponential models. Error values were assigned following the same procedure as §3.4.1. Given the large errors found in the parameters in Fig. 3.12, galaxies with  $SNR$  greater than 5/10 were used to fit the known relations for galaxies (see §5.1) in order to diminish the estimated error for BD parameters.

### 3.5 Summary

It has been selected the Sérsic (Sérsic 1968) and exponential models to fit the cluster galaxies of the LOCOS database (§3.1). To extract as much galaxy's detail as possible, every galaxy has been fitted with a Sérsic and Sérsic + exponential models. We have selected GALFIT (Peng et al. 2002) to fit the galaxies over the other packages (§3.2).

As galaxy clusters contains hundreds and thousands of objects, the fitting of every single galaxy is very time consuming. For that reason, we have developed a program (DGCG) based on GALFIT (§3.3). It takes the SEXTRACTOR input and formats it for GALFIT. Also, DGCG computes initial parameters, makes masks, and selects the best nearest PSF for galaxy fitting.

If neighbor objects are very close to the galaxy of interest, DGCG simultaneously fits them as another component for the galaxy. The comparison of Figures 3.10 and 3.11 shows that this technique is better than the popular masking method.

The reliability of DGCG was tested with synthetic galaxies for Sérsic and Sérsic + exponential models. The results are shown in Figures 3.10 and 3.12. DGCG's users can estimate when a fit is not right with just checking the flags in Table 3.4.

The apparent magnitude cut limit for our sample was set at 18. The errors for every galaxy were computed from the fittings of synthetic galaxies and GALFIT's file FIT.LOG.



## *Results: Magnitudes, Catalog, and a New Quantitative Classification Scheme*

In this Chapter, it is shown the surface brightness results for the cluster galaxies of the LOCOS sample (López-Cruz 1997; Lopez-Cruz 2001). It is shown the computing resources to fit the whole sample. A criterion to separate “good” from “bad” fits was defined. Also, it is shown the SNR distribution of our sample, and the comparison between the magnitudes computed by DGCG and PPP.

The total number of galaxies with “good” surface brightness models is 1453. They are distributed in 21 low- $z$  ( $0.02 \leq z \leq 0.07$ ) Abell galaxy clusters fields. The photometric completeness limit was reached at  $R = 18 \text{ mag}$  (see appendix C). Single Sérsic (SS) and Sérsic + exponential (BD) models have been fitted to an original sample of 2419 galaxies. Solutions have been obtained for 2227 (92 %). Nevertheless, 1453 galaxies (60%) have both SS and BD acceptable fits. Moreover, there are 297 galaxies whose BD fits resulted in Sérsic index less than 0.2.

It has been devised an alternative scheme to estimate galaxy morphology quantitatively. With the aid of this alternative scheme, it has been able to segregate three main classes: E, S0, and S. Galaxies (265) in common with Dressler (1980a) classifications have been used as training set to calibrate our classification method. It has been generated diagnostic diagrams based on the bulge-to-total luminosity ratio (B/T), BPN,  $n$ , and mean axis ratio ( $q$ ) to generate this classification estimator. The 1453 galaxies included in this study has been classified; the final sample contains 330 E, 566 S0 and 557 S galaxies.

To determine whether a E contains a disk, it has been implemented a modified version of the Bayesian Information Criterion (Schwarz 1978) to determine whether a SS model or a BD model provide the best model for a E galaxy. In §4.3, it is explained this criterion, and it is shown some examples where E galaxies have disk components.

Finally, a sample of the final catalog with acceptable fits is shown in §4.4. The complete table can be downloaded from <http://tinyurl.com/7o2rm2q>.

## 4.1 Model Fitting Results

### 4.1.1 DGCG Performance

DGCG has been run on two computers: a Pentium 4 at 3.0 Ghz with 1 GB of RAM memory and another Pentium 4 at 3.2 Ghz with 6 GB of RAM memory. Table 4.1 shows the run time per galaxy cluster and number of fitted galaxies. It took 258.89 hrs ( $\sim 10.79$  days) in total for SS models, and 337.23 hrs  $\sim 15.72$  days for the BD models, respectively, to process the whole sample. DGCG is computing intensive because GALFIT employs all the pixels on the region of interest; the CPU time increases as more components are included. Future versions of DGCG will have to reduce the CPU time. A parallel version with GPUs or faster processors might be needed. We also would like to experiment with faster minimizations algorithms. Nevertheless, there is plenty of computing power available at INAOE such DGCG can run without affecting other projects.

Cluster name	CPU	Run Time (SS)	Run Time (BD)	Total Galaxies	Fitted Galaxies (SS)	Fitted Galaxies (BD)
	Ghz	hours	hours			
(1)	(2)	(3)	(4)	(5)	(6)	(7)
A2415	3.2	9.25	14.96	90	83	74
A2593	3.2	18.65	18.03	108	102	99
A2626	3.2	6.52	11.27	91	88	82
A2657	3.2	7.27	11.65	82	81	80
A2670	3.2	8.9	16.35	146	135	133
A407	3.2	26.6	43.97	103	92	86
A671	3.2	14.15	20.45	113	100	106
A690	3.2	8.7	14.47	81	79	75
A85	3.2	10.13	16.4	112	108	105
A957	3.2	4.66	7.80	78	74	75
A1213	3.0	7.32	11.14	163	161	159
A154	3.0	11.5	20.16	101	94	88
A1650	3.0	12.89	23.27	116	104	104
A1656	3.0	11.16	16.33	141	132	134
A168	3.0	3.02	5.73	83	83	82
A1795	3.0	11.55	19.1	120	115	110
A1913	3.0	6.3	12.04	122	121	118
A1983	3.0	9.28	14.03	101	101	98
A2255	3.0	27.86	32.93	181	168	165
A2256	3.0	32.47	33.86	185	166	179
A2399	3.0	10.71	13.29	102	98	96

**Table 4.1:** Run time spent per cluster using SS and BD models. Column (1): Abell number of the cluster; (2) CPU clock frequency; (3) Run time for SS model; (4) Run time for BD; (5) number used as input; (6) Fitted galaxies SS model; (7) Fitted galaxies BD model

### 4.1.2 Selection of the Best Fits

In Table 4.1, the raw numbers of column 3 mean that GALFIT converge to a solution, but it does not imply that GALFIT achieved a good fit. An *ideal* good fit must reflect the true surface brightness profile on every pixel of the galaxy. Also, the model parameters must range among physical values. To discern good fits from bad fits in our sample, we have used Table 3.4 from §3.3.2 to assign flags to the galaxies.

In addition to those DGCG flags, it has been compared SS and BD parameters to eliminate non-physical fits (normally from BD models). It has been eliminated models in the following cases: when 1) differences of total magnitudes between SS and BD models were greater than 1 mag, and 2) effective radius (BD) was greater than 2 times the disk effective radius (BD) when Sérsic index is less than 2.

The two above conditions allowed us to select realistic BD models. The scale length parameter of the exponential disk model is highly sensitive to fainter objects in the background. If SExtractor does not detect them, the scale length will be larger than the real value because it also will try to fit those faint objects. This last point can be prevented with criterion 1). Another problem is that, sometimes, the Sérsic model tries to fit the disk instead of the bulge, and the exponential model tries to fit the bulge instead of the disk. This can be prevented with criterion 2). Nevertheless, this last was a rare case.

Using table 3.4, we obtained a total of 1525 with flag = 0 for galaxies with SS and BD models. Using the two criteria explained above, it has been arrived to a final catalog of 1453 galaxies. Table 4.2 shows the total of galaxies fitted and the number of flagged galaxies.

Model	Input	Fitted	Flag 1	Flag 2	Flag 4	Flagged	no Flagged
(1)	(2)	(3)	(4)	(5)	(6)	(7)	(8)
S	2419	2300	141	114	121	131	2169
BD	2419	2227	170	472	261	609	1618

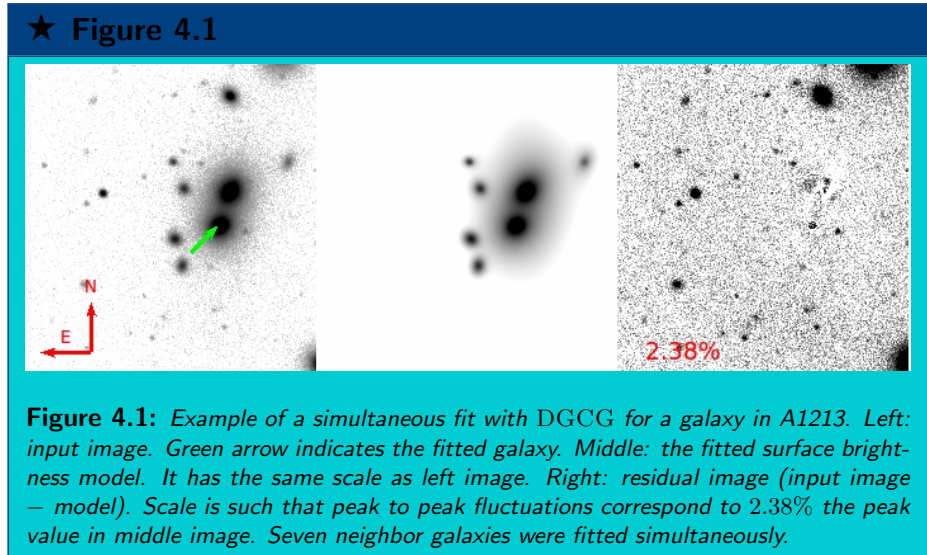
**Table 4.2:** Number of galaxies fitted with SS and BD models. Column (1): the model; (2) number of input galaxies in the SExtractor catalog; (3) Number of fitted galaxies; (4) number of galaxies with flag 1; (5) number of galaxies with flag 2; (6) number of galaxies with flag 4; (7) number of galaxies with flag > 0; (8) number of galaxies with no flag or flag 0.

Galaxies with flag values between 1 and 3<sup>1</sup> means that one or more parameters have reached some predetermined value that is considered unphysical. For example, when  $n \geq 12$  or  $n \leq 0.02$ .

About 297 galaxies, independently of their morphology, have  $n < 0.2$  (BD). In order to check that those galaxy models were not affected by systematics, the stellar PSF has been changed for Gaussian models. Then, the galaxy has been re-fitted with this new PSF. As a result, the same results has been obtained. Since those galaxies with  $n < 0.2$  have flat profiles (see Fig. 3.1), we believe that those galaxies could be best fitted with King profiles. This will be tested in a future work. For the moment, to avoid unphysical results, those galaxies have been excluded in the plots where the Sérsic index is involved.

Finally, as an example, Figure 4.1 depicts a successful fit for a galaxy in A1213. The model of this Figure is a BD model with flag = 0, B/T = 0.88,  $n = 4.56$ ,  $R_e = 8.13$  kpc and  $R_s = 1.45$  kpc. To achieve satisfactory fits, GALFIT had to fit seven galaxies simultaneously (see middle image of Fig. 4.1).

<sup>1</sup>A flag with value 3 means that the object has been flagged with 1 and 2



### 4.1.3 Signal to Noise Ratio of our Sample

Figure 4.2 shows the histogram of the SNR for the 1453 successfully fitted galaxies in our sample. As explained in §3.3.2, the SNR is computed within an ellipse defined by the Kron radius (Kron 1980).

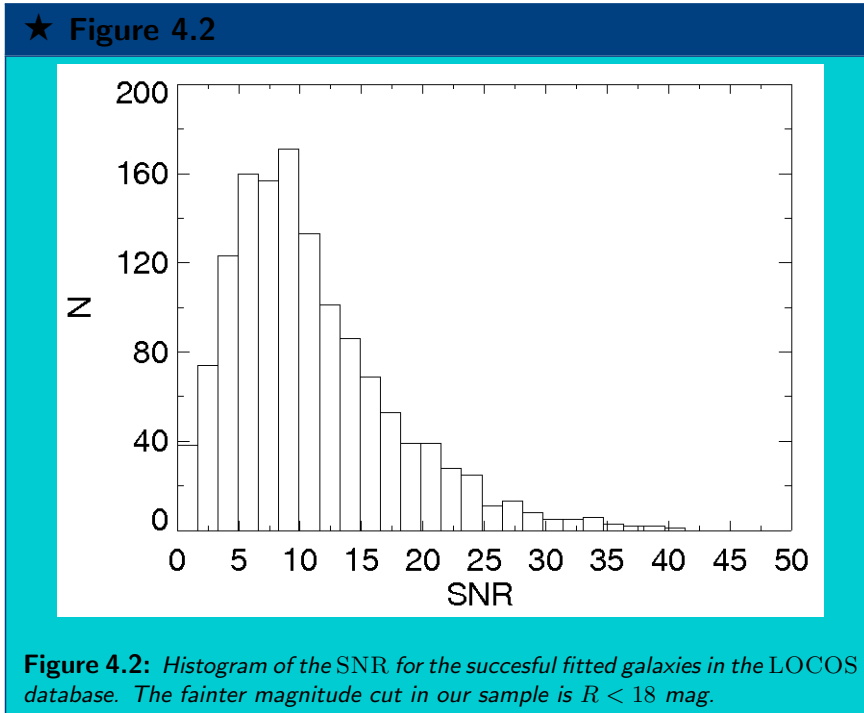
The galaxies included in the Figure 4.2 are those with apparent magnitudes brighter than 18. The SNR at this magnitude limit is between  $\sim 3.5$  and  $\sim 6.5$ .

As explained in §3.4, simulation errors for each parameter were computed from Figures 3.10 and 3.12 for SS and BD models respectively. The error was assigned accordingly to the galaxy's SNR.

### 4.1.4 Magnitude Comparison: GALFIT vs. PPP

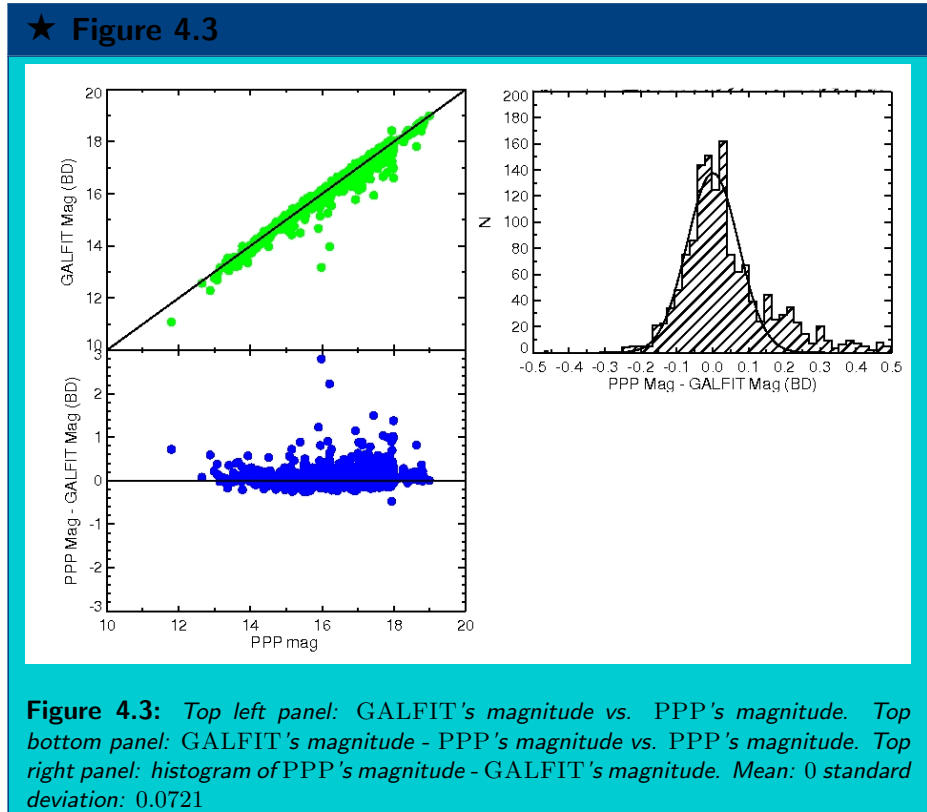
In Figure 4.3, it has been compared the GALFIT's magnitudes with the ones computed by PPP (Yee 1991; Yee et al. 1996; López-Cruz 1997; López-Cruz et al. 2004). PPP's magnitudes were computed using curve of growth analysis on circular apertures while GALFIT's magnitudes were obtained by integrating the fitted models from 0 to infinite radius (check Appendix B).

The histogram of Figure 4.3 shows a reasonable agreement between the PPP's magnitudes and GALFIT's magnitudes. Nevertheless, in the right side of the histogram, it can be seen that some galaxies have their magnitudes underestimated by PPP (i.e. they appear dimmer). This can be produced by improper masking of neighboring objects or variations on the background produced by flat-fielding. Although, PPP has gone to great pains in dealing with neighboring objects and variations of the background (Yee 1991), it is not free from the main drawbacks that affect any photometric technique based in



apertures; hence, it will invariably fail on very extended objects (i.e. cD galaxies). In contrast, model fitting has a best flat-fielding treatment because it controls the weight on every pixel with  $\chi^2_\nu$ . In addition, DGCG has an improved treatment of neighboring objects (see §3.4.1). Therefore, DGCC full surface brightness treatment overcomes the problems of aperture photometry made by either curves of growth or ellipse fitting.

Nevertheless, considering the limitations, it has been found considerable agreement between PPP asymptotic magnitudes and GALFIT integrated total magnitudes. Among the advantages of PPP over DGCG, it can be mentioned that PPP is faster and provides total magnitudes non-parametrically; hence, all the objects in a given CCD frame will have total magnitudes. At this point, it can be concluded that DGCG improves upon and complements PPP, and represents a significant progress on cluster galaxy photometry.

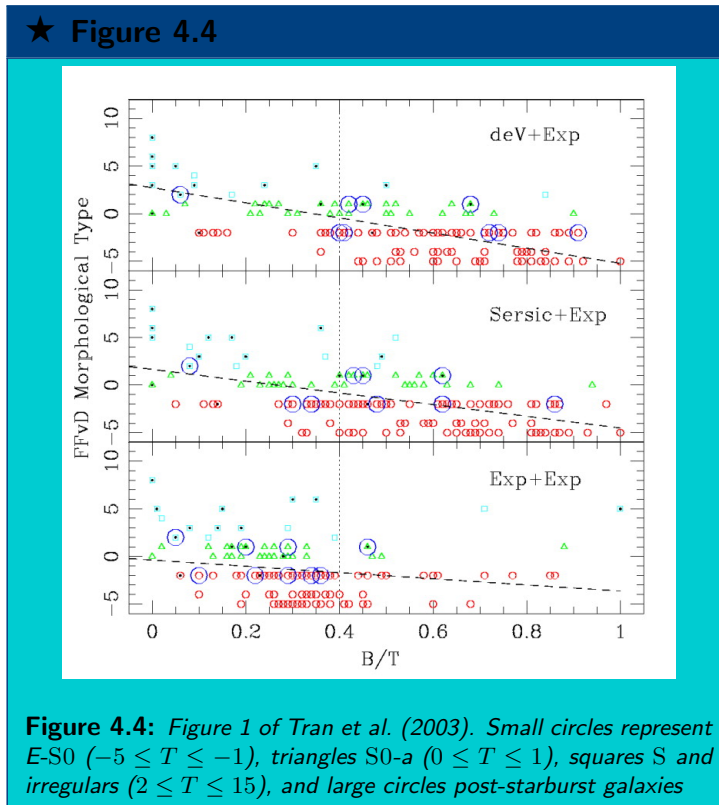


## 4.2 Morphological Classification of Galaxies

Galaxy classification is a fundamental task to unlock the mechanism of galaxy formation. For this work, it is important to distinguish at least the 3 main types of galaxies (S, S0, and E) to analyze the main physical properties of every morphological type. Here, it is suggested a novel approach to segregate S, S0, and E galaxies.

As it can be seen on the Hubble sequence (see Fig. 1.3), B/T correlates with morphology. For this reason, B/T had been used to classify galaxies (Tran et al. 2003; Trujillo & Aguerri 2004; Aguerri et al. 2004; Cibinel et al. 2012). Nevertheless, it has a high dispersion; hence, it is difficult to determine which value of B/T separates each morphological type. This dispersion is probably due to dust in galaxies with disk, and due to embedded disks within E galaxies (see §4.3). This dispersion can be observed in Figure 1 of Tran et al. (2003). It is shown in Figure 4.4.

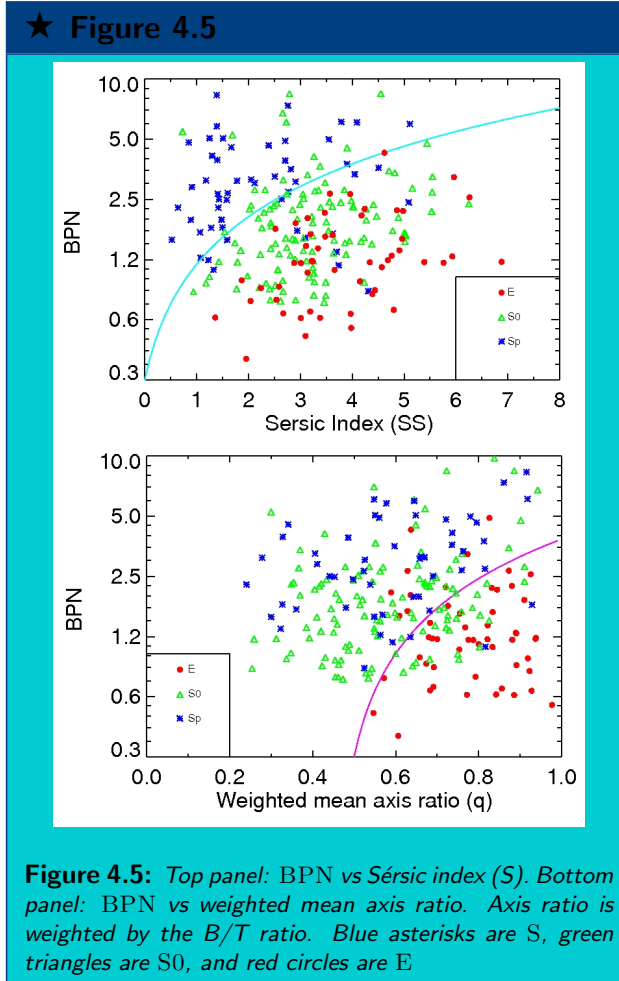
Those dispersions can be reduced if B/T and ellipticity are considered to separate E from S0 galaxies (Añorve et al. 2009). This seems to work because E are expected to be rounder than S0 galaxies (van den Bergh 2009).



#### 4.2.1 A New Classification Method: B/T, BPN, Sérsic index and Axis Ratio

B/T luminosity ratio is an inherent property for every morphology type along the Hubble sequence. B/T is useful to separate morphological types particularly at later types. Nevertheless, due to the high dispersion of B/T explained above, it is unclear which B/T values could separate E from S0 or S0 from S. In the literature, some B/T separation limits varies among authors (e.g., Trujillo & Aguerri 2004; Aguerri et al. 2004; Tran et al. 2003).

In order to reduce the dispersion shown in Figure 4.4, B/T has been combined with BPN (see §1.2.2), axis ratio ( $q$ ) and Sérsic index (SS). BPN vs. Sérsic index diagram has been used before to separate galaxy morphology (Blakeslee et al. 2006); here, it is used to separate S from E and S0. To determine the cut limits that separate different morphology types, Dressler (1980a) classifications have been used to calibrate our sample. It has 265 galaxies in common with Dressler (1980a).



The top panel of Figure 4.5 shows the BPN vs. Sérsic diagram. The equation of the blue line of the left panel of Figure 4.5 is

$$BPN = 0.855 \times n + 0.3, \quad (4.1)$$

as it was explained in §1.2.2, BPN quantifies the model's deviation from data. Since the presence of bulges and disks is obvious, SS models does not completely reproduce the full structures of S and S0. On the other hand, SS models are sufficient for E galaxies. Therefore, it is expected that BPN of S must be higher than the BPN of E. S0's BPN values should be something in the middle of E and S BPN values.

Following the BPN idea, BPN vs.  $q$  is used to separate E from S0 and S. As explained above, E galaxies are expected to be rounder than S0 galaxies (van den Bergh 2009). The BPN vs  $q$  diagram is shown in the bottom panel of Figure 4.5.

The red line equation of the right panel of Figure 4.5 is

$$BPN = 7 \times q - 3.2, \quad (4.2)$$

combining the plots of Figure 4.5 with B/T luminosity ratio, the following equations are obtained to classify E, S0 and S galaxies:

$$B/T \geq 0.7 \text{ or } (B/T \geq 0.5 \text{ and } BPN < 7q - 3.2) \Rightarrow E \quad (4.3a)$$

$$B/T \leq 0.3 \text{ or } (B/T < 0.6 \text{ and } BPN > 0.855n + 0.3) \Rightarrow S \quad (4.3b)$$

$$\text{rest} \Rightarrow S0, \quad (4.3c)$$

when this classification method was compared with Dressler's classifications (Dressler 1980b), it was able to recover 77% of the E galaxies, 64% of the S0, and 63% of the S galaxies. We believe that this is a very acceptable rate. It corresponds roughly to the intrinsic dispersions among classifiers (Lahav et al. 1995; van den Bergh 2012).

Fasano et al. (2012) argue that their morphological classification method, which is multi-parametric, gives satisfactory results when this is compared with the detailed morphological analysis of Fukugita et al. (2007); Nair & Abraham (2010) even though that they have a little shift towards early-type. In the next Chapter, it will be shown that their results are comparable with the classification method used here which it is simpler.

Finally, Table 4.3 shows the final classification that was assigned to the satisfactory fitted galaxies. In total, our sample has 330 E, 566 S0 and 557 S. Table 4.3 can help immediately to reproduce (Oemler 1974) cluster classification by galaxy population. It can be said that Coma (A1656) is a CD cluster with E:S0:S ratios of about 2:3:1, which is similar to the ratios 3:4:2 reported by Oemler. A2255 is a SPIRAL RICH cluster with E:S0:S ratios of about 1:2:3; while, A957 is a SPIRAL POOR cluster with E:S0:S ratios of about 1:2:1. Hence, this classification approach can reproduce galaxy and cluster classifications.

Cluster	E	S0	S
A1213	30	35	18
A1650	7	21	28
A168	25	25	18
A1983	15	38	21
A1913	29	43	18
A2256	27	56	36
A2593	6	26	30
A2670	18	39	31
A690	11	19	20
A957	17	33	11
A154	14	22	26
A1656	35	55	16
A1795	6	10	35
A2255	19	36	50
A2399	8	16	41
A2657	16	23	10
A671	16	21	30
A85	8	10	46
A407	8	16	21
A2626	7	13	31
A2415	8	9	20

**Table 4.3:** *Number of assigned morphologies for cluster galaxies. Only the good fits are shown. Column (1): Abell cluster; (2) number of E; (3) number of S0; (4) is number of S.*

### 4.3 Disks in Elliptical Galaxies and the Modified Bayesian Information Criterion

Every galaxy in our sample has been fitted by BD and SS models. The question is which model combination suits best for a galaxy? It is clear for S and S0 galaxies that they are best fitted with a BD models. The situation is not so clear for E galaxies and pure disks. Disks within E have been suggested before by Capaccioli (1987); Peletier et al. (1990). Later, the SAURON project (Emsellem et al. 2004) found rotating components embedded in E galaxies. More recently, Salim et al. (2012) found old stellar disks S0 type for their whole sample of E.

Here, in order to tell whether E galaxies have a disk, it is used a modified version of the Bayesian Information Criterion (BIC, Schwarz 1978). This criterion emerged from Akaike information criterion (Akaike 1974).

Given a different number of models, Akaike information criterion selects which model fits best for a determined data. This criterion selects preferably models that have low  $\chi^2$ , and, at the same time, avoids overfitting. The Akaike formula (AIC, Akaike 1974) is given

by:

$$AIC = \chi^2 + 2K, \quad (4.4)$$

where  $\chi$  is chi-square of the model, and  $K$  is the number of parameters used for the model. AIC is computed for every model; then, the best model is the one with the lowest AIC. The value of AIC does not matter; what it is relevant is the comparison of two, or more, AIC values.

The  $K$  in 4.4 penalizes every parameter added to the model. This is how it avoids overfitting.

Glattig et al. (2007) found that Akaike criterion is better than the F-test. Besides this, F-test does not have a parameter to avoid overfitting. In addition, different arbitrary values of F-test would work for different data.

Following Akaike's idea, Schwarz created the Bayesian Information Criterion (BIC) (Schwarz 1978). The BIC formula is given by:

$$BIC = \chi^2 + K * \ln(n), \quad (4.5)$$

where  $K$  is again the number of parameters, and  $n$  is the number of points. BIC penalizes more strictly the number of additional parameters than AIC. In this work, it is used a modified version of BIC (MBIC) to select which galaxies are best fitted by either a SS or BD models.

First, it is introduced the number of elements of resolution into BIC:

$$N_{res} = \frac{n_{pix}}{\pi * FWHM^2}, \quad (4.6)$$

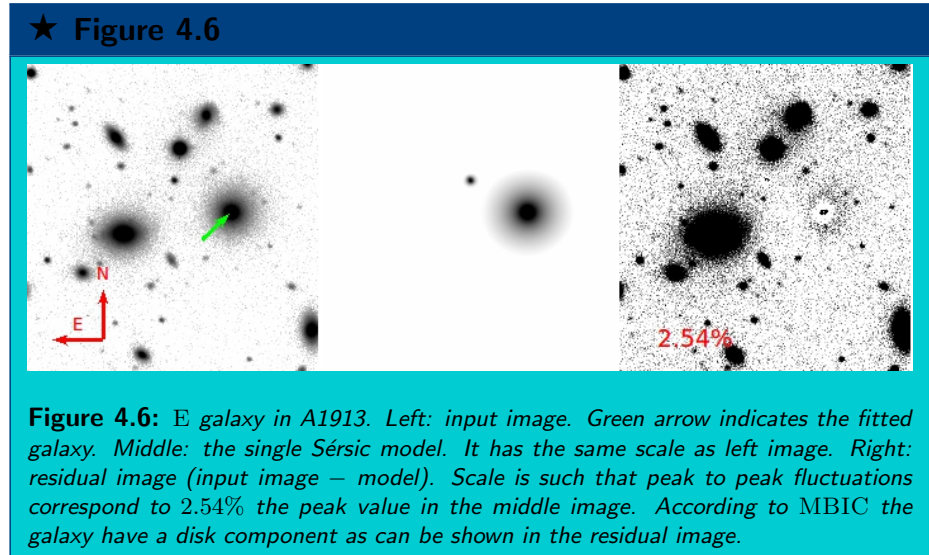
where  $n$  is the number of pixels, and  $FWHM$  is the full width at half maximum. Combining this equation with BIC, it gives the following equation:

$$MBIC = \chi^2 * (N_{res} - K) + K * \ln(N_{res}), \quad (4.7)$$

if the number of elements of resolution is large, MBIC becomes BIC<sup>2</sup>. The purposes of this new version of BIC are: 1) it could be used for any data; 2) it helps to decide whether another component is needed; 3) it penalizes any additional parameter when SNR is low. Comparing with the model's residuals, the MBIC gives better results than AIC.

MBIC formula was tested to select which galaxies are best fitted by SS. Two examples with and without disk are shown in Figure 4.6 and 4.7 respectively. Both galaxies were classified as E galaxies by Dressler (1980a).

<sup>2</sup>This is undesirable because of the Nyquist theorem



At low SNR, galaxies are hard to tell whether they are best fitted by either a SS or BD. To avoid this problem, it has been selected galaxies with SNR greater or equal than 10. For those galaxies, it has been found that 13% of the galaxies are best fitted with one component (SS), and 87% of the galaxies are best fitted with two components (BD).

Below, it is shown more examples of the MBIC applied to E galaxies classified by Dressler (1980a). Using this criterion, we found that 10 E galaxies are best fitted with one component ( $MBIC \text{ ratio} > 1$ ) i.e. pure bulges, and 30 E galaxies with two components ( $MBIC \text{ ratio} < 1$ ). Those E galaxies with two components are also recognized as having embedded disks.

In §4.3.1 and 4.3.2, it is depicted the fitting of SS models to E galaxies. The residual image (i.e. galaxy image – model image) shows whether it has an embedded disk.

### 4.3.1 Ellipticals with one component (Single Bulges)

Here, we shown E galaxies fitted with one component. Those Figures show Galaxy (left), Single Sérsic model(middle) and residual (right).

★ Figure 4.7

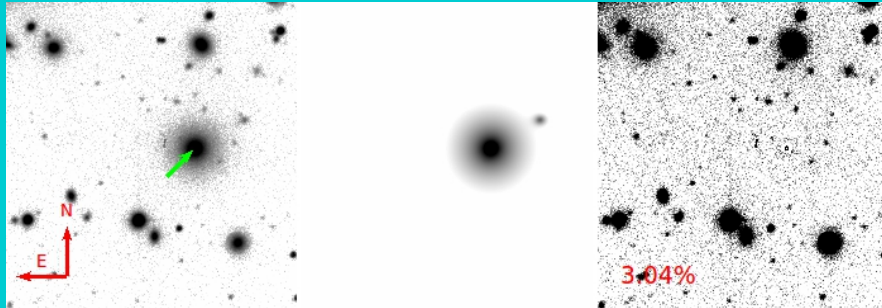


**Figure 4.7:** E galaxy in A2256. Left: input image. Green arrow indicates the fitted galaxy. Middle: the single Sérsic model. It has the same scale as left image. Right: residual image (input image – model). Scale is such that peak to peak fluctuations correspond to 3.04% the peak value in the middle image. According to MBIC the galaxy do not have a disk component as can be shown in the residual image.

★ Figure 4.8

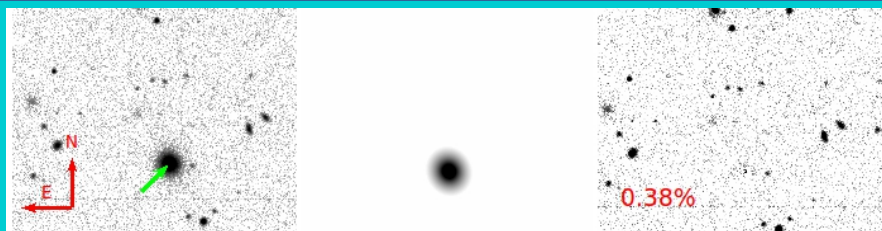


**Figure 4.8:** E with one component. Left: input image. Green arrow indicates the fitted galaxy. Middle: the fitted single Sérsic model. It has the same scale as left image. Right: residual image (input image – model). Scale is such that peak to peak fluctuations correspond to 0.38% the peak value in the middle image. MBIC ratio = 1.03

## ★ Figure 4.9

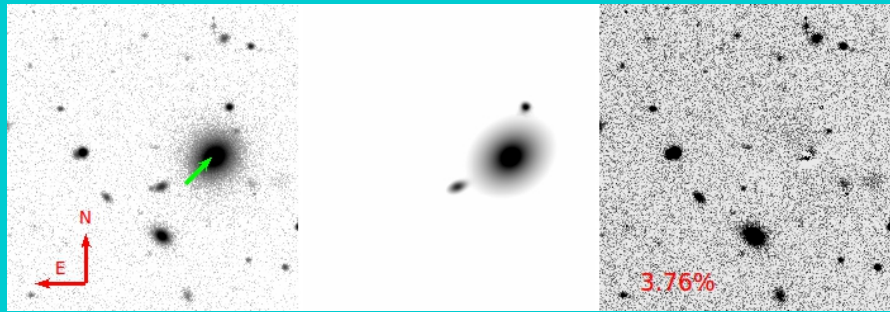


**Figure 4.9:** E with one component. Left: input image. Green arrow indicates the fitted galaxy. Middle: the fitted single Sérsic model. It has the same scale as left image. Right: residual image (input image – model). Scale is such that peak to peak fluctuations correspond to 3.76% the peak value in the middle image. MBIC ratio = 1.02

## ★ Figure 4.10

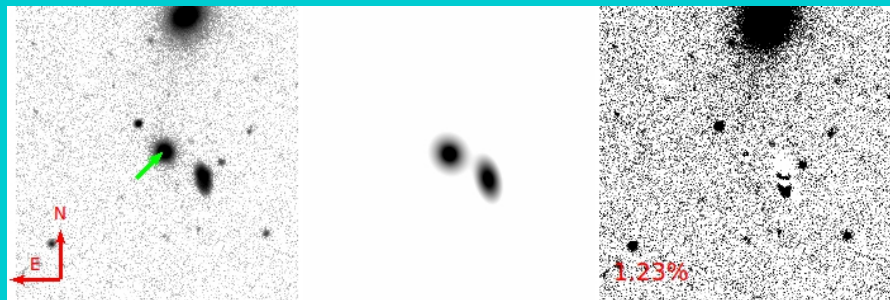


**Figure 4.10:** E with one component. Left: input image. Green arrow indicates the fitted galaxy. Middle: the fitted single Sérsic model. It has the same scale as left image. Right: residual image (input image – model). Scale is such that peak to peak fluctuations correspond to 1.23% the peak value in the middle image. MBIC ratio = 1.0

★ Figure 4.11

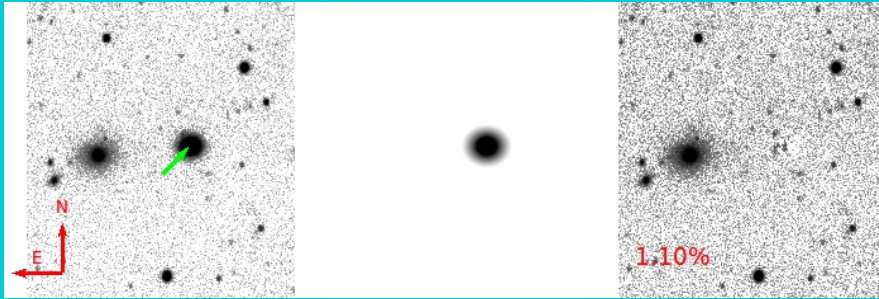


**Figure 4.11:** E with one component. Left: input image. Green arrow indicates the fitted galaxy. Middle: the fitted single Sérsic model. It has the same scale as left image. Right: residual image (input image – model). Scale is such that peak to peak fluctuations correspond to 1.10% the peak value in the middle image. MBIC ratio = 1.03

★ Figure 4.12

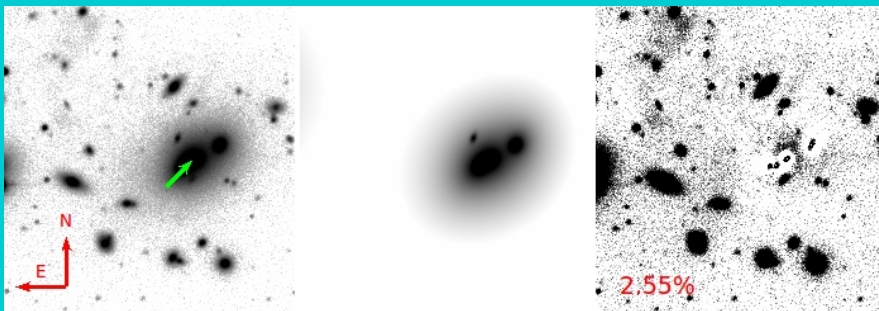


**Figure 4.12:** E with one component. Left: input image. Green arrow indicates the fitted galaxy. Middle: the fitted single Sérsic model. It has the same scale as left image. Right: residual image (input image – model). Scale is such that peak to peak fluctuations correspond to 2.55% the peak value in the middle image. MBIC ratio = 1.4

★ Figure 4.13

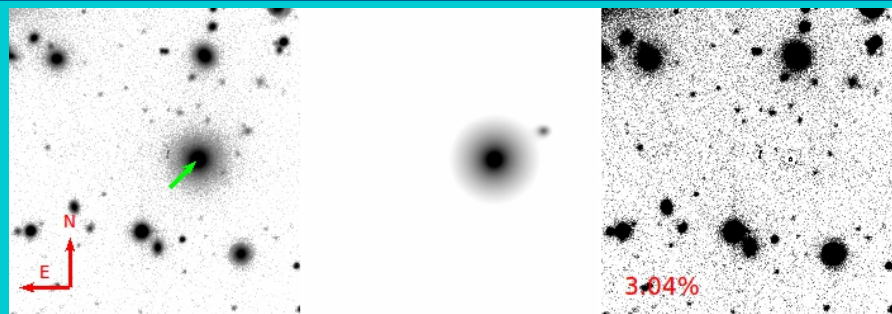


**Figure 4.13:** E with one component. Left: input image. Green arrow indicates the fitted galaxy. Middle: the fitted single Sérsic model. It has the same scale as left image. Right: residual image (input image – model). Scale is such that peak to peak fluctuations correspond to 3.04% the peak value in the middle image. MBIC ratio = 1.03

★ Figure 4.14

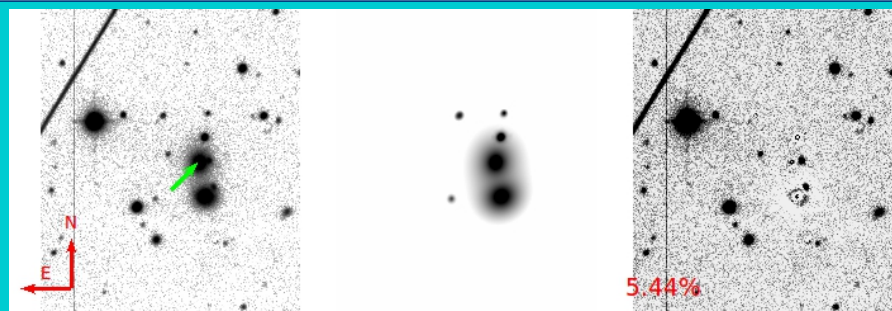


**Figure 4.14:** E with one component. Left: input image. Green arrow indicates the fitted galaxy. Middle: the fitted single Sérsic model. It has the same scale as left image. Right: residual image (input image – model). Scale is such that peak to peak fluctuations correspond to 5.44% the peak value in the middle image. MBIC ratio = 1.04

★ Figure 4.15



**Figure 4.15:** E with one component. Left: input image. Green arrow indicates the fitted galaxy. Middle: the fitted single Sérsic model. It has the same scale as left image. Right: residual image (input image – model). Scale is such that peak to peak fluctuations correspond to 0.73% the peak value in the middle image. MBIC ratio = 1.08

★ Figure 4.16

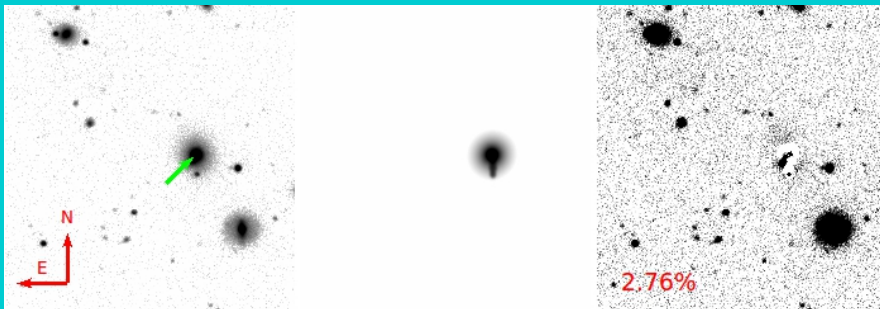


**Figure 4.16:** E with one component. Left: input image. Green arrow indicates the fitted galaxy. Middle: the fitted single Sérsic model. It has the same scale as left image. Right: residual image (input image – model). Scale is such that peak to peak fluctuations correspond to 2.76% the peak value in the middle image. MBIC ratio = 1.18

★ Figure 4.17

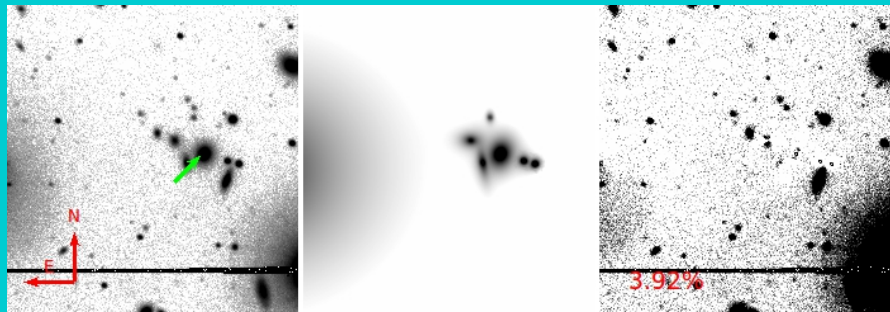
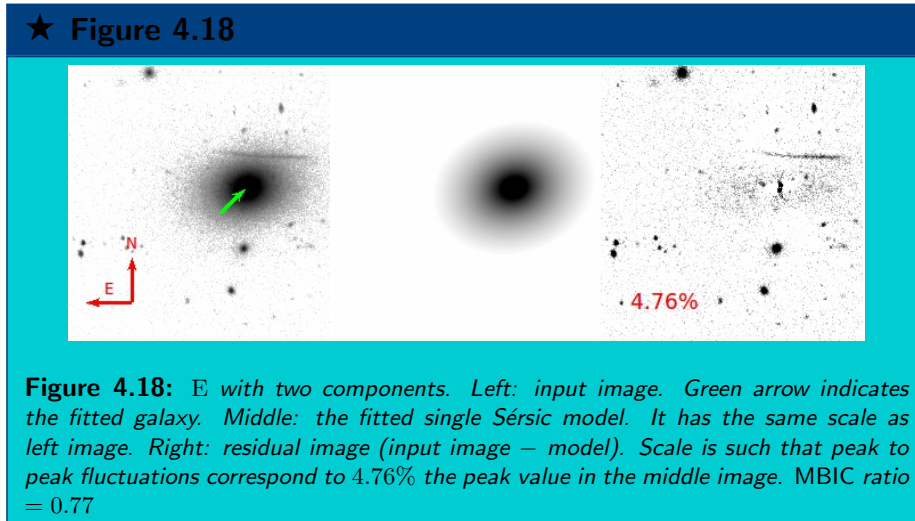


**Figure 4.17:** E with one component. Left: input image. Green arrow indicates the fitted galaxy. Middle: the fitted single Sérsic model. It has the same scale as left image. Right: residual image (input image – model). Scale is such that peak to peak fluctuations correspond to 3.92% the peak value in the middle image. MBIC ratio = 3.09

### 4.3.2 Es with two components (Embedded disks)

Here, we shown E galaxies fitted with two components. The remaining light in the residual image suggests a disk component. Those Figures show Galaxy (left), Single Sérsic model(middle) and residual (right).



★ Figure 4.19

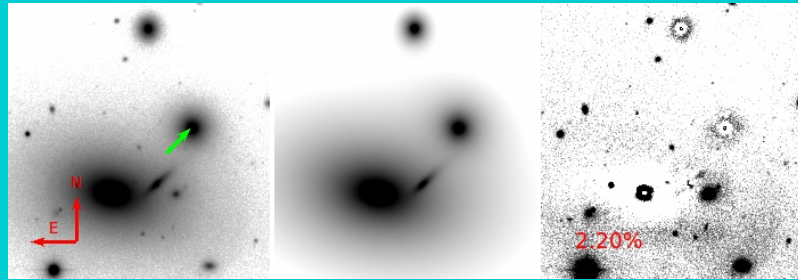


**Figure 4.19:** E with two components. Left: input image. Green arrow indicates the fitted galaxy. Middle: the fitted single Sérsic model. It has the same scale as left image. Right: residual image (input image – model). Scale is such that peak to peak fluctuations correspond to 2.20% the peak value in the middle image. MBIC ratio = 0.77

★ Figure 4.20

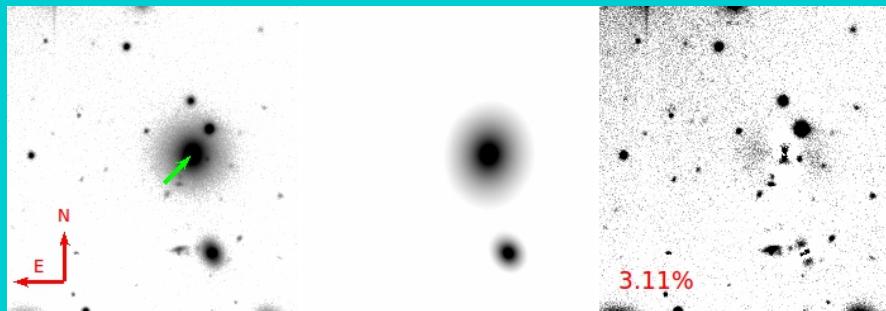


**Figure 4.20:** E with two components. Left: input image. Green arrow indicates the fitted galaxy. Middle: the fitted single Sérsic model. It has the same scale as left image. Right: residual image (input image – model). Scale is such that peak to peak fluctuations correspond to 3.11% the peak value in the middle image. MBIC ratio = 0.75

★ Figure 4.21

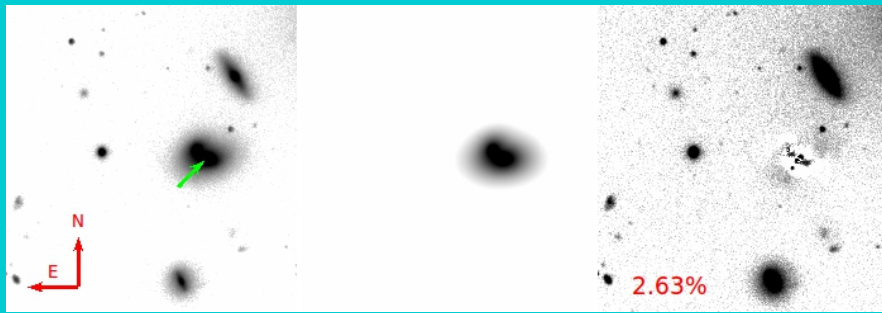


**Figure 4.21:** E with two components. Left: input image. Green arrow indicates the fitted galaxy. Middle: the fitted single Sérsic model. It has the same scale as left image. Right: residual image (input image – model). Scale is such that peak to peak fluctuations correspond to 2.63% the peak value in the middle image. MBIC ratio = 0.66

★ Figure 4.22

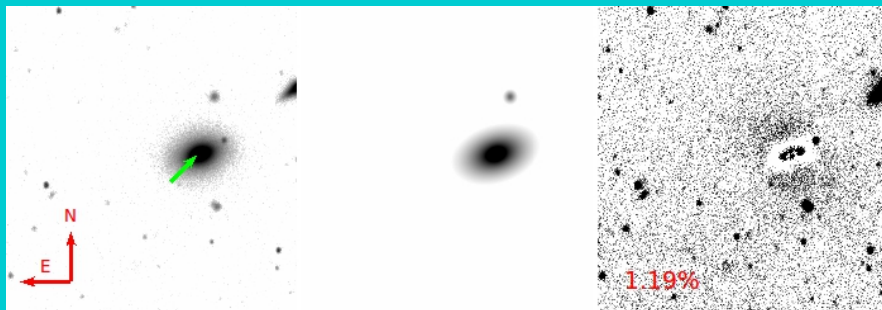


**Figure 4.22:** E with two components. Left: input image. Green arrow indicates the fitted galaxy. Middle: the fitted single Sérsic model. It has the same scale as left image. Right: residual image (input image – model). Scale is such that peak to peak fluctuations correspond to 1.19% the peak value in the middle image. MBIC ratio = 0.78

★ Figure 4.23

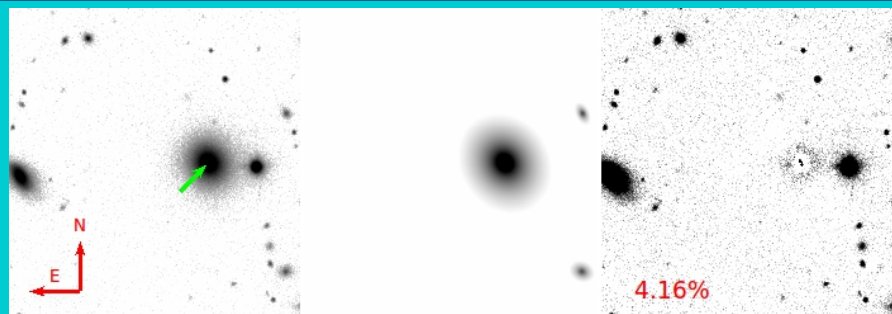


**Figure 4.23:** E with two components. Left: input image. Green arrow indicates the fitted galaxy. Middle: the fitted single Sérsic model. It has the same scale as left image. Right: residual image (input image – model). Scale is such that peak to peak fluctuations correspond to 4.16% the peak value in the middle image. MBIC ratio = 0.86

★ Figure 4.24

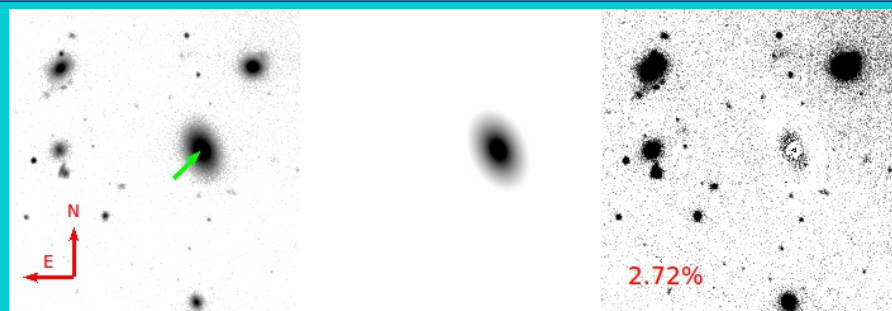


**Figure 4.24:** E with two components. Left: input image. Green arrow indicates the fitted galaxy. Middle: the fitted single Sérsic model. It has the same scale as left image. Right: residual image (input image – model). Scale is such that peak to peak fluctuations correspond to 2.72% the peak value in the middle image. MBIC ratio = 0.73

★ Figure 4.25

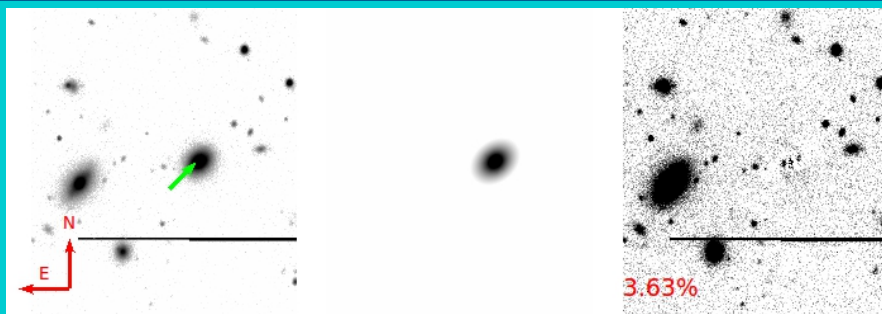


**Figure 4.25:** E with two components. Left: input image. Green arrow indicates the fitted galaxy. Middle: the fitted single Sérsic model. It has the same scale as left image. Right: residual image (input image – model). Scale is such that peak to peak fluctuations correspond to 3.63% the peak value in the middle image. MBIC ratio = 0.9

★ Figure 4.26

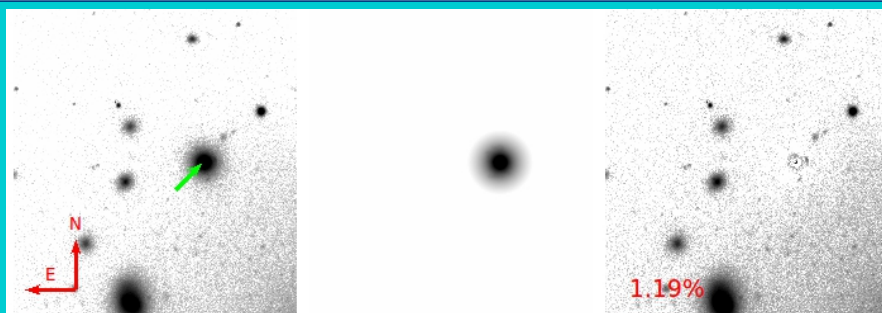


**Figure 4.26:** E with two components. Left: input image. Green arrow indicates the fitted galaxy. Middle: the fitted single Sérsic model. It has the same scale as left image. Right: residual image (input image – model). Scale is such that peak to peak fluctuations correspond to 1.19% the peak value in the middle image. MBIC ratio = 0.91

★ Figure 4.27

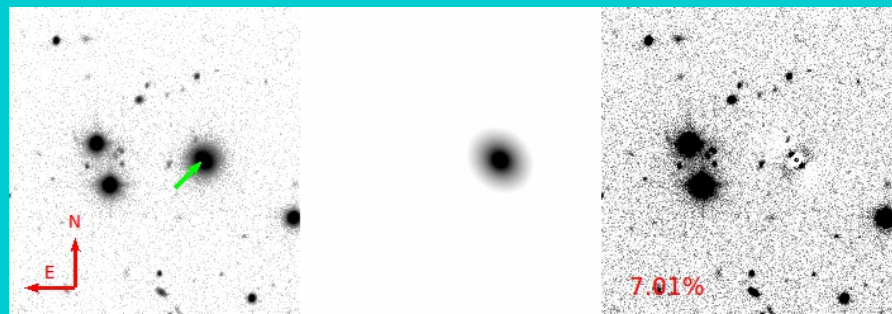


**Figure 4.27:** E with two components. Left: input image. Green arrow indicates the fitted galaxy. Middle: the fitted single Sérsic model. It has the same scale as left image. Right: residual image (input image – model). Scale is such that peak to peak fluctuations correspond to 7.01% the peak value in the middle image. MBIC ratio = 0.82

★ Figure 4.28

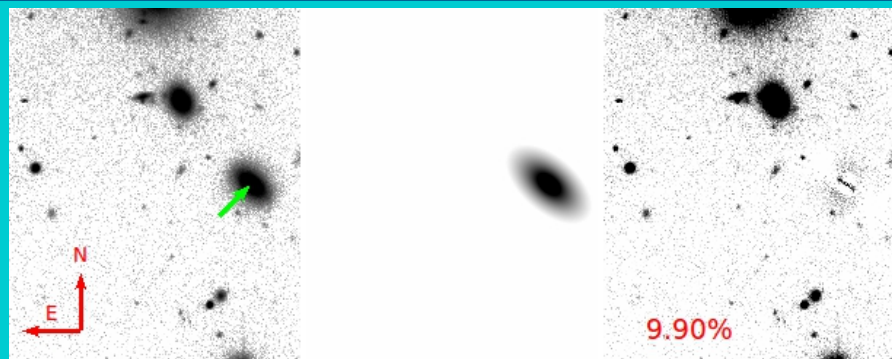


**Figure 4.28:** E with two components. Left: input image. Green arrow indicates the fitted galaxy. Middle: the fitted single Sérsic model. It has the same scale as left image. Right: residual image (input image – model). Scale is such that peak to peak fluctuations correspond to 9.9% the peak value in the middle image. MBIC ratio = 0.8

★ Figure 4.29

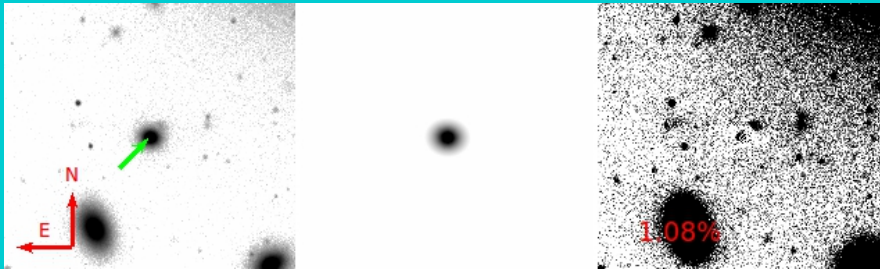


**Figure 4.29:** E with two components. Left: input image. Green arrow indicates the fitted galaxy. Middle: the fitted single Sérsic model. It has the same scale as left image. Right: residual image (input image – model). Scale is such that peak to peak fluctuations correspond to 1.08% the peak value in the middle image. MBIC ratio = 0.68

★ Figure 4.30

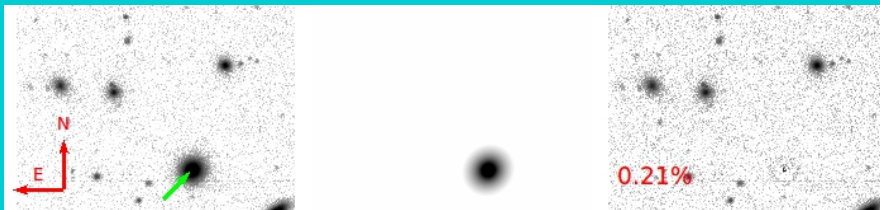


**Figure 4.30:** E with two components. Left: input image. Green arrow indicates the fitted galaxy. Middle: the fitted single Sérsic model. It has the same scale as left image. Right: residual image (input image – model). Scale is such that peak to peak fluctuations correspond to 0.21% the peak value in the middle image. MBIC ratio = 0.94

★ Figure 4.31

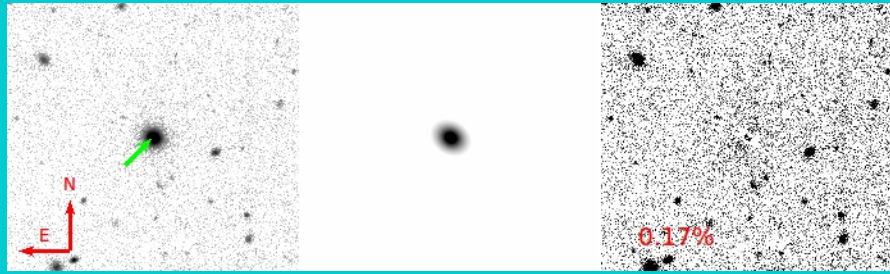


**Figure 4.31:** E with two components. Left: input image. Green arrow indicates the fitted galaxy. Middle: the fitted single Sérsic model. It has the same scale as left image. Right: residual image (input image – model). Scale is such that peak to peak fluctuations correspond to 0.17% the peak value in the middle image. MBIC ratio = 0.72

★ Figure 4.32

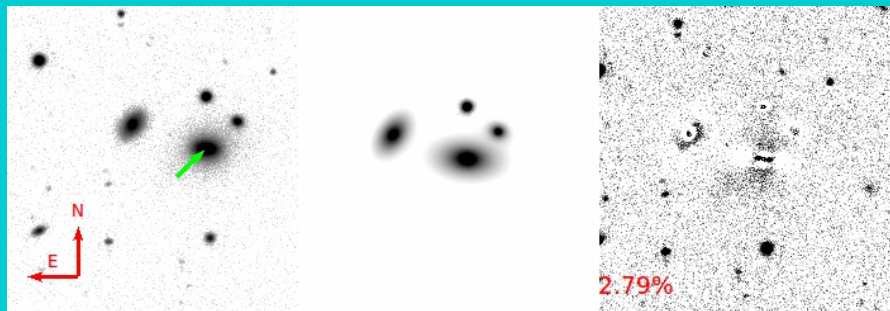
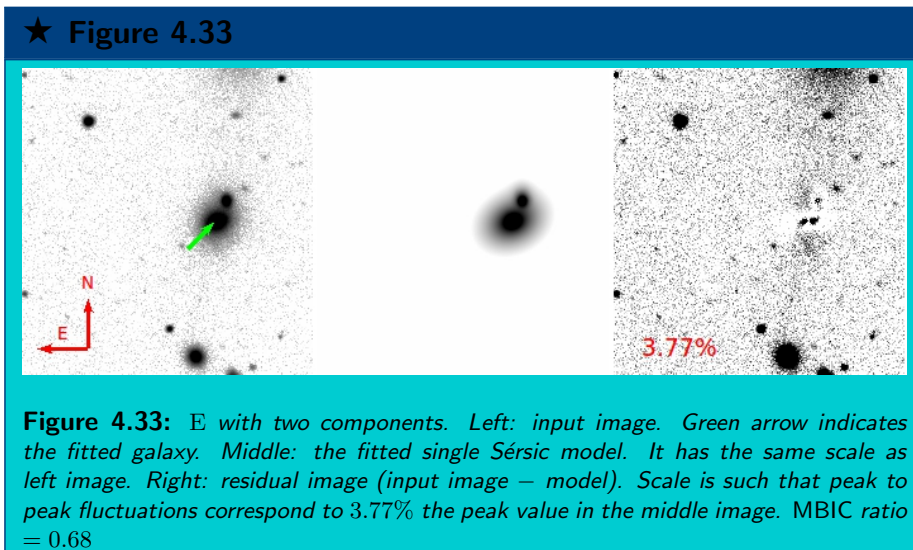


**Figure 4.32:** E with two components. Left: input image. Green arrow indicates the fitted galaxy. Middle: the fitted single Sérsic model. It has the same scale as left image. Right: residual image (input image – model). Scale is such that peak to peak fluctuations correspond to 2.79% the peak value in the middle image. MBIC ratio = 0.67



★ Figure 4.34

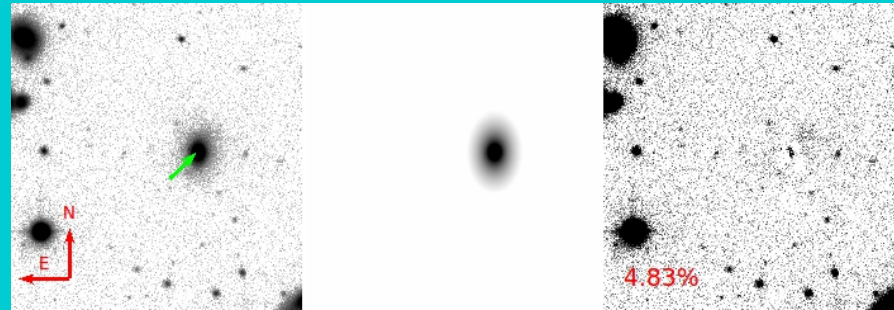


**Figure 4.34:** E with two components. Left: input image. Green arrow indicates the fitted galaxy. Middle: the fitted single Sérsic model. It has the same scale as left image. Right: residual image (input image – model). Scale is such that peak to peak fluctuations correspond to 4.83% the peak value in the middle image. MBIC ratio = 0.95

★ Figure 4.35

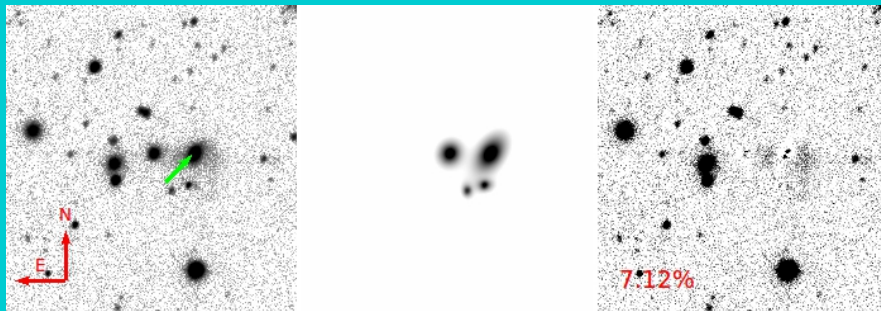


**Figure 4.35:** E with two components. Left: input image. Green arrow indicates the fitted galaxy. Middle: the fitted single Sérsic model. It has the same scale as left image. Right: residual image (input image – model). Scale is such that peak to peak fluctuations correspond to 7.12% the peak value in the middle image. MBIC ratio = 0.95

★ Figure 4.36

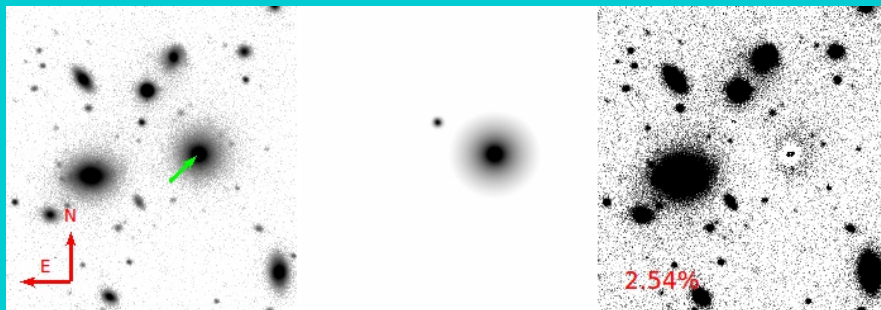


**Figure 4.36:** E with two components. Left: input image. Green arrow indicates the fitted galaxy. Middle: the fitted single Sérsic model. It has the same scale as left image. Right: residual image (input image – model). Scale is such that peak to peak fluctuations correspond to 2.54% the peak value in the middle image. MBIC ratio = 0.83

★ Figure 4.37

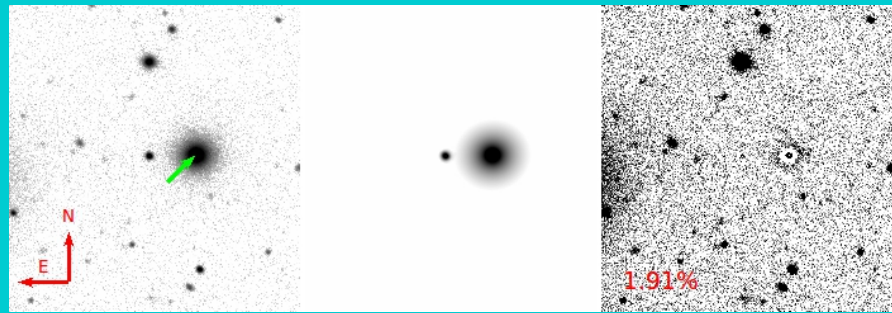


**Figure 4.37:** E with two components. Left: input image. Green arrow indicates the fitted galaxy. Middle: the fitted single Sérsic model. It has the same scale as left image. Right: residual image (input image – model). Scale is such that peak to peak fluctuations correspond to 1.91% the peak value in the middle image. MBIC ratio = 0.95

★ Figure 4.38

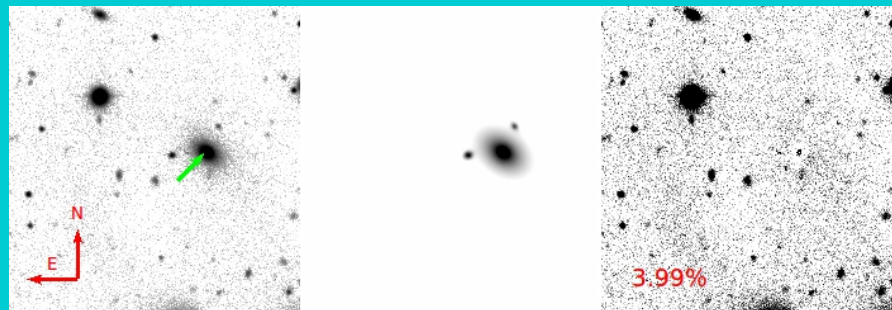


**Figure 4.38:** E with two components. Left: input image. Green arrow indicates the fitted galaxy. Middle: the fitted single Sérsic model. It has the same scale as left image. Right: residual image (input image – model). Scale is such that peak to peak fluctuations correspond to 3.99% the peak value in the middle image. MBIC ratio = 0.95

★ Figure 4.39

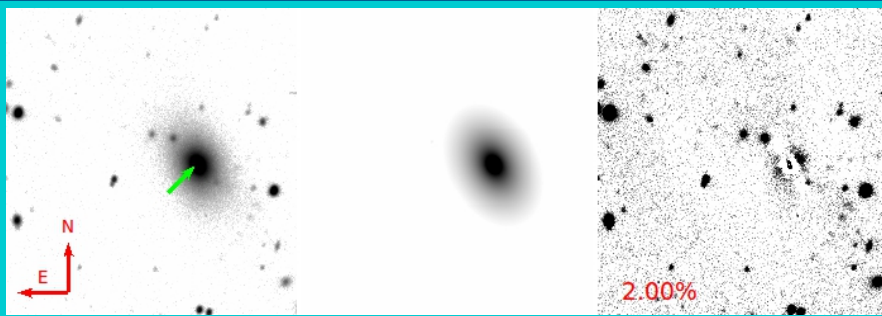


**Figure 4.39:** E with two components. Left: input image. Green arrow indicates the fitted galaxy. Middle: the fitted single Sérsic model. It has the same scale as left image. Right: residual image (input image – model). Scale is such that peak to peak fluctuations correspond to 2.0% the peak value in the middle image. MBIC ratio = 0.91

★ Figure 4.40

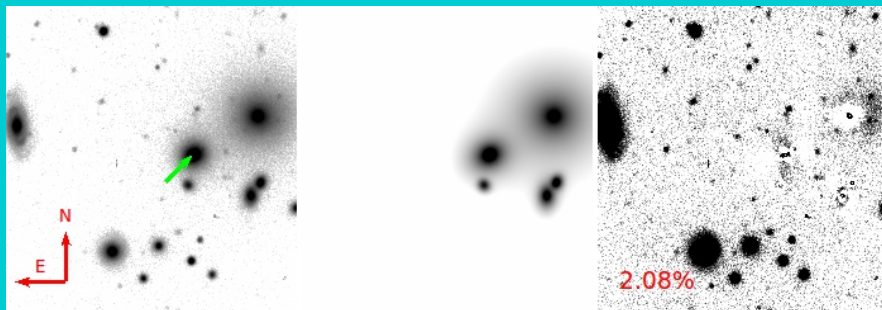


**Figure 4.40:** E with two components. Left: input image. Green arrow indicates the fitted galaxy. Middle: the fitted single Sérsic model. It has the same scale as left image. Right: residual image (input image – model). Scale is such that peak to peak fluctuations correspond to 2.08% the peak value in the middle image. MBIC ratio = 0.78

★ Figure 4.41

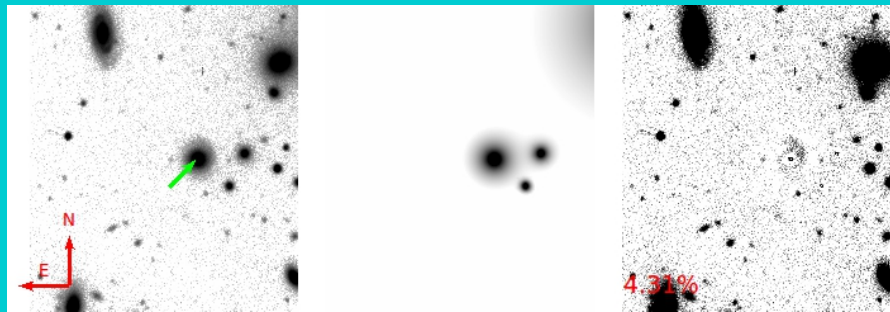


**Figure 4.41:** E with two components. Left: input image. Green arrow indicates the fitted galaxy. Middle: the fitted single Sérsic model. It has the same scale as left image. Right: residual image (input image – model). Scale is such that peak to peak fluctuations correspond to 4.31% the peak value in the middle image. MBIC ratio = 0.87

★ Figure 4.42

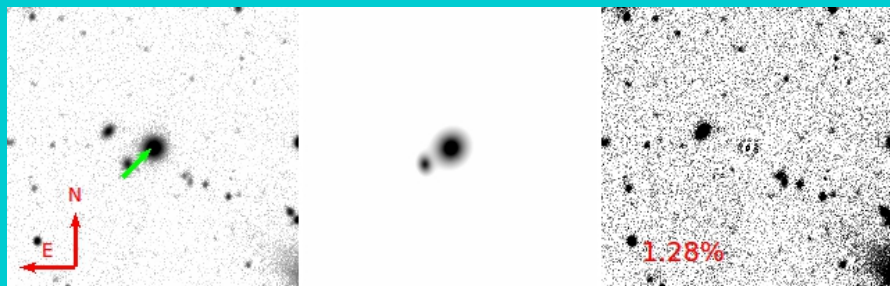


**Figure 4.42:** E with two components. Left: input image. Green arrow indicates the fitted galaxy. Middle: the fitted single Sérsic model. It has the same scale as left image. Right: residual image (input image – model). Scale is such that peak to peak fluctuations correspond to 1.28% the peak value in the middle image. MBIC ratio = 0.74

★ Figure 4.43

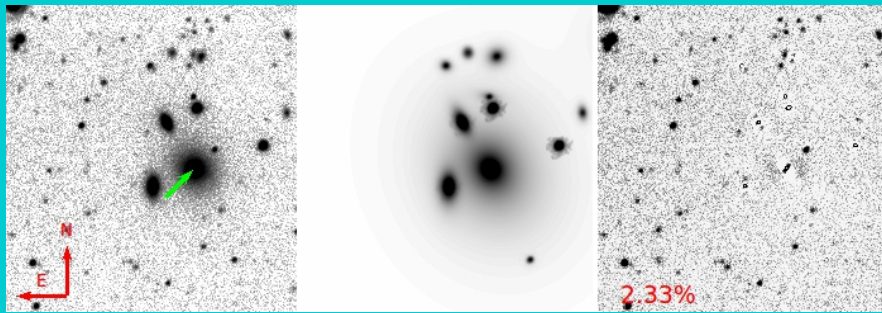


**Figure 4.43:** E with two components. Left: input image. Green arrow indicates the fitted galaxy. Middle: the fitted single Sérsic model. It has the same scale as left image. Right: residual image (input image – model). Scale is such that peak to peak fluctuations correspond to 2.33% the peak value in the middle image. MBIC ratio = 0.95

★ Figure 4.44

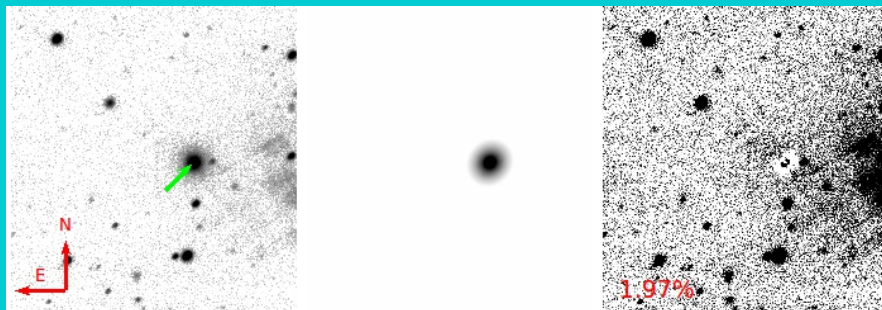


**Figure 4.44:** E with two components. Left: input image. Green arrow indicates the fitted galaxy. Middle: the fitted single Sérsic model. It has the same scale as left image. Right: residual image (input image – model). Scale is such that peak to peak fluctuations correspond to 1.97% the peak value in the middle image. MBIC ratio = 0.7

★ Figure 4.45

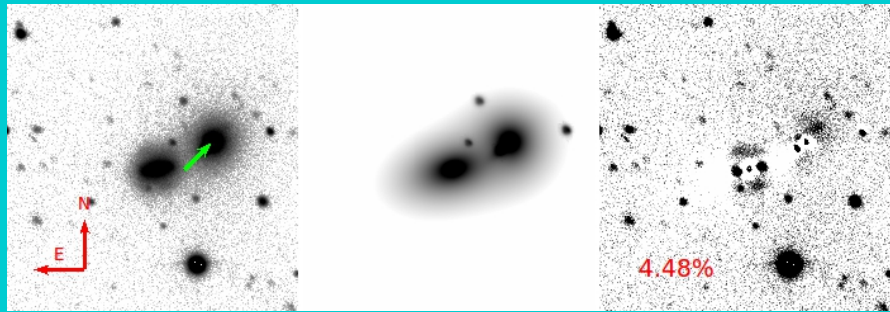
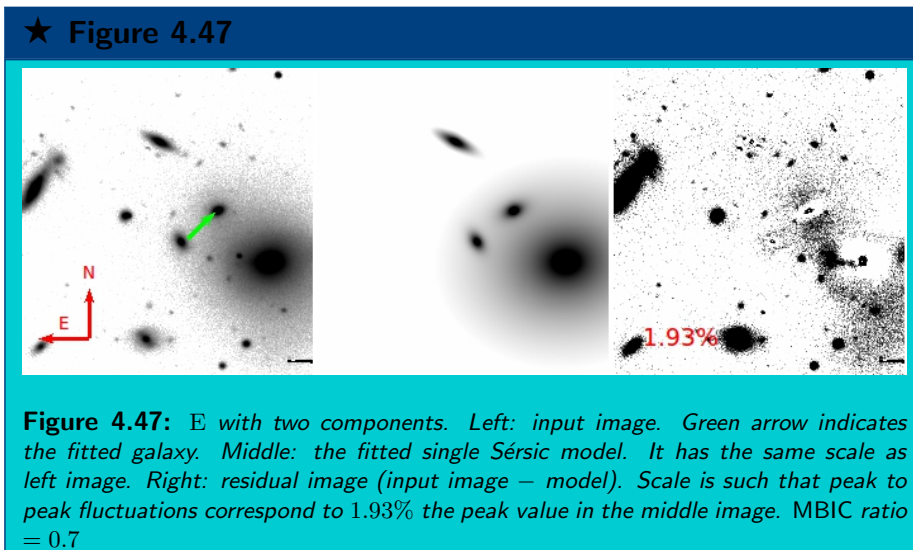


**Figure 4.45:** E with two components. Left: input image. Green arrow indicates the fitted galaxy. Middle: the fitted single Sérsic model. It has the same scale as left image. Right: residual image (input image – model). Scale is such that peak to peak fluctuations correspond to 4.48% the peak value in the middle image. MBIC ratio = 0.9. The shape of the residual shows signs of interaction of merger.

★ Figure 4.46



**Figure 4.46:** E with two components. Left: input image. Green arrow indicates the fitted galaxy. Middle: the fitted single Sérsic model. It has the same scale as left image. Right: residual image (input image – model). Scale is such that peak to peak fluctuations correspond to 7.51% the peak value in the middle image. MBIC ratio = 0.9



## 4.4 Final Catalog

Table 4.4 shows a sample of the final catalog including parameters for BD models, and Table 4.5 contains parameters for SS models. Both Tables cover the same galaxies. As explained in §3.4.1 and §3.4.2, errors were computed from the combination of the ones computed by GALFIT and the ones computed from the fittings of synthetic galaxies (§3.4.1 and 3.4.2).

Columns of Table 4.4 represent: (1) galaxy cluster number in the Abell catalog; (2) Right ascension (epoch 2000); (3) Declination (epoch 2000); (4) ID number for the galaxy; (5) total magnitude; (6) total magnitude error; (7) B/T; (8) B/T error; (9) assigned morphology; (10) effective radius ( $R_e$ ); (11)  $R_e$  error; (12) Sérsic index; (13) Sérsic index error; (14) scale length ( $R_s$ ); (15)  $R_s$  error.

On the other hand, columns of Table 4.5 represent: (1) galaxy cluster; (2) right ascension; (3) declination; (4) ID number; (5) total magnitude; (6) total magnitude error; (7) effective radius ( $R_e$ ); (8)  $R_e$  error; (9) Sérsic index; (10) Sérsic index error; (11) axis ratio; (12) axis ratio error; (13)  $\chi^2_\nu$ ; (14) BPN; (15) Signal to noise ratio.

The complete Table in electronic format can be downloaded from <http://tinyurl.com/7o2rm2q>.

Cluster	RA	Dec	ID	Mag	Mag.err	B/T	B/T.err	Morph	Re (arc.sec)	Re.err	N	N.err	Rs (arc.sec)
A1213	11:15:45.53	29:17:47.7	159	18.45	0.37	0.50	0.28	S0	1.26	0.32	0.48	1.11	1.53
A1213	11:15:59.09	29:15:22.3	211	18.43	1.18	0.53	0.57	S	2.58	0.98	0.96	1.07	2.30
A1213	11:16:53.27	29:20:19.4	115	18.34	0.23	0.62	0.22	S0	1.09	0.31	1.64	1.11	3.03
A1213	11:15:46.93	29:20:10.4	116	18.43	0.11	0.40	0.05	S	1.48	0.10	0.55	0.29	2.64
A1213	11:16:01.08	29:23:43.4	65	18.40	0.21	0.53	0.23	S	1.58	0.70	0.05	1.04	2.75
A1213	11:17:23.05	29:12:32.1	260	18.57	0.16	0.72	0.26	E	0.82	0.26	1.45	1.10	2.96
A1213	11:15:58.00	29:23:28.7	72	18.62	0.71	0.70	0.41	S0	1.10	0.70	1.08	1.47	2.16
A1213	11:16:56.11	29:19:59.2	123	17.82	0.14	0.52	0.06	S0	2.82	0.19	1.41	0.15	34.71
A1213	11:17:22.07	29:09:57.6	295	18.59	0.50	0.47	0.29	S	2.20	0.65	3.26	2.19	2.05
A1213	11:15:53.22	29:10:20.8	287	18.53	0.22	0.58	0.25	S0	0.90	0.31	0.81	1.16	1.97
A1213	11:16:37.40	29:19:56.6	127	18.72	0.37	0.42	0.23	S0	1.37	0.36	0.91	1.11	1.39
A1213	11:16:01.98	29:24:10.7	60	18.42	0.06	0.50	0.05	S	1.66	0.09	0.86	0.21	4.26
A1213	11:16:23.17	29:23:32.3	70	18.75	0.43	0.40	0.20	S	1.08	0.54	1.80	1.22	1.66
A1213	11:15:44.76	29:17:19.5	168	18.82	0.25	0.63	0.25	S0	1.08	0.32	0.34	1.19	1.52
A1213	11:15:46.59	29:15:57.1	192	18.60	0.53	0.47	0.29	S	1.15	0.49	0.58	1.52	2.89
A1213	11:16:11.06	29:12:22.8	263	18.75	1.50	0.63	0.71	S0	1.37	0.81	0.86	0.66	1.56
A1213	11:16:46.30	29:17:16.9	171	18.78	0.50	0.65	0.33	S0	0.80	0.34	1.32	1.28	1.44
A1213	11:16:24.92	29:16:38.3	597	19.00	0.34	0.61	0.27	E	0.73	0.34	0.70	1.51	1.11
A0154	01:11:03.54	17:39:07.4	328	13.08	0.01	0.70	0.00	D	13.00	0.29	4.92	0.05	40.58
A0154	01:11:02.99	17:39:46.7	330	13.11	0.01	0.47	0.00	D	8.54	0.12	3.11	0.03	29.80
A0154	01:11:08.82	17:51:00.3	25	14.71	0.07	0.92	0.25	E/S0	6.92	0.32	6.06	0.51	11.61
A0154	01:10:55.27	17:36:47.3	415	15.04	0.11	0.59	0.26	S0/S	5.29	0.35	4.87	0.87	4.88
A0154	01:11:25.63	17:40:34.6	304	15.11	0.01	0.37	0.01	S0	0.88	0.02	4.42	0.15	4.89
A0154	01:10:48.93	17:39:03.1	361	15.07	0.02	0.33	0.01	S0	5.44	0.47	6.77	0.49	3.17
A0154	01:10:39.95	17:45:36.7	186	15.04	0.10	0.37	0.26	S	8.91	0.71	3.28	0.76	5.03
A0154	01:11:31.32	17:36:35.9	430	15.27	0.10	0.82	0.26	S0	2.90	0.25	3.64	0.72	6.05
A0154	01:11:12.15	17:42:14.8	258	15.29	0.07	0.80	0.04	S	1.60	0.29	7.40	0.89	6.73
A0154	01:10:46.75	17:39:55.0	339	15.40	0.01	0.80	0.01	S0	2.93	0.05	4.46	0.09	3.73
A0154	01:10:58.45	17:37:42.7	393	15.72	0.02	0.60	0.01	S0	1.20	0.03	2.36	0.06	3.81
A0154	01:10:40.64	17:42:19.0	248	15.63	0.08	0.66	0.23	S0	1.97	0.20	2.94	0.56	6.77
A0154	01:11:14.01	17:32:24.5	527	14.55	0.08	0.21	0.24	S	0.86	0.20	0.51	0.63	6.92
A0154	01:10:36.87	17:35:36.7	457	15.94	0.02	0.89	0.01	S0	2.09	0.04	3.85	0.09	13.91
A0154	01:11:07.28	17:34:49.3	477	15.95	0.02	0.51	0.01	S0	1.35	0.03	2.12	0.06	3.31
A0154	01:10:28.01	17:30:14.8	586	16.19	0.07	0.12	0.23	S0/S	1.88	0.16	0.74	0.43	2.45
A0154	01:11:29.83	17:46:10.7	156	16.21	0.03	0.39	0.01	S0	0.68	0.08	9.02	1.45	2.32
A0154	01:11:30.57	17:34:16.0	488	16.24	0.01	0.27	0.01	S	0.78	0.01	0.46	0.09	2.81
A0154	01:10:17.23	17:48:41.4	84	16.32	0.03	0.45	0.01	S0	1.12	0.02	0.95	0.05	2.70
A0154	01:11:00.79	17:37:44.4	396	16.21	0.15	0.53	0.07	S0	1.04	0.24	2.23	0.46	1.79
A0154	01:10:49.54	17:50:35.0	40	16.43	0.08	0.49	0.23	S	2.37	0.20	1.20	0.60	4.22
A0154	01:10:54.98	17:39:12.9	364	16.53	0.02	0.57	0.01	S	1.66	0.01	0.34	0.01	3.05
A0154	01:11:46.26	17:48:43.6	87	16.60	0.06	0.11	0.03	S	1.86	0.54	0.06	0.23	2.14

**Table 4.4:** BD fits. Column (1): Cluster name; (2) Right ascension; (3) Declination; (4) ID; (5) Total Magnitude; (6) Mag error; (7) B/T; (8) B/T error; (9) Assigned Morphology (see §4.2.1); (10) Re; (11) Re error; (12) Sérsic index; (13) Sérsic index error; (14) Rs; (15) Rs error.

Cluster	RA	Dec	ID	Mag	Mag err	Re (arc sec)	Re err	N	N err	q	q err	$\chi^2_\nu$	BPN	SNR
A1213	11:15:45.53	29:17:47.7	159	18.45	0.06	1.66	0.09	1.25	0.57	0.52	0.02	1.12	1.24	3.51
A1213	11:15:59.09	29:15:22.3	211	18.39	0.11	3.16	0.21	1.21	0.98	0.65	0.03	1.13	1.81	2.23
A1213	11:16:53.27	29:20:19.4	115	18.64	0.08	1.30	0.14	1.84	0.81	0.58	0.03	1.12	1.76	2.71
A1213	11:15:46.93	29:20:10.4	116	18.43	0.04	2.65	0.16	1.90	0.22	0.50	0.03	1.14	3.89	1.60
A1213	11:16:01.08	29:23:43.4	65	18.56	0.07	1.86	0.12	1.42	0.70	0.44	0.03	1.12	3.14	2.92
A1213	11:17:23.05	29:12:32.1	260	18.54	0.05	1.19	0.09	3.38	0.78	0.51	0.04	1.17	0.91	4.71
A1213	11:15:58.00	29:23:28.7	72	18.64	0.07	1.46	0.12	1.73	0.74	0.70	0.04	1.12	1.99	3.05
A1213	11:16:56.11	29:19:59.2	123	18.08	0.07	4.65	0.51	2.65	0.27	0.89	0.04	1.12	2.40	1.66
A1213	11:17:22.07	29:09:57.6	295	18.58	0.11	2.82	0.22	1.84	0.99	0.33	0.02	1.13	1.92	2.12
A1213	11:15:53.22	29:10:20.8	287	18.51	0.06	1.46	0.10	2.45	0.66	0.67	0.04	1.10	2.02	3.65
A1213	11:16:37.40	29:19:56.6	127	18.70	0.09	1.73	0.15	1.48	0.80	0.74	0.04	1.15	1.36	2.53
A1213	11:16:01.98	29:24:10.7	60	18.42	0.04	3.41	0.24	2.06	0.22	0.45	0.03	1.13	2.85	1.77
A1213	11:16:23.17	29:23:32.3	70	18.70	0.04	1.90	0.12	1.99	0.33	0.74	0.04	1.13	3.50	1.35
A1213	11:15:44.76	29:17:19.5	168	18.84	0.05	1.29	0.09	1.24	0.60	0.30	0.05	1.12	1.79	3.64
A1213	11:15:46.59	29:15:57.1	192	18.54	0.10	2.54	0.22	2.28	0.84	0.55	0.03	1.13	2.33	2.43
A1213	11:16:11.06	29:12:22.8	263	18.68	0.03	1.82	0.07	1.36	0.20	0.78	0.04	1.14	4.84	1.41
A1213	11:16:46.30	29:17:16.9	171	18.71	0.06	1.20	0.10	2.47	0.72	0.61	0.04	1.09	2.13	3.86
A1213	11:16:24.92	29:16:38.3	597	18.97	0.06	0.97	0.11	1.82	0.82	0.62	0.07	1.32	0.62	3.45
A0154	01:11:03.54	17:39:07.4	328	13.09	0.01	22.94	0.39	5.96	0.04	0.75	0.00	1.53	3.19	1.52
A0154	01:11:02.99	17:39:46.7	330	13.09	0.01	23.30	0.25	4.62	0.02	0.87	0.00	1.81	4.24	0.52
A0154	01:11:08.82	17:51:00.3	25	14.63	0.01	9.04	0.16	6.50	0.06	0.77	0.00	1.10	2.39	8.94
A0154	01:10:55.27	17:36:47.3	415	14.98	0.02	7.37	0.07	3.20	0.37	0.43	0.00	1.32	3.30	5.97
A0154	01:11:25.63	17:40:34.6	304	14.92	0.00	6.67	0.06	4.82	0.04	0.23	0.00	1.28	3.36	21.38
A0154	01:10:48.93	17:39:03.1	361	15.17	0.00	4.87	0.01	1.54	0.01	0.28	0.00	1.21	1.69	23.72
A0154	01:10:46.75	17:45:36.7	186	15.04	0.02	7.66	0.07	1.60	0.38	0.98	0.00	1.24	2.65	6.58
A0154	01:11:31.32	17:36:35.9	430	15.27	0.02	3.73	0.06	3.86	0.34	0.74	0.00	1.15	1.48	6.74
A0154	01:11:12.15	17:42:14.8	258	15.22	0.00	6.75	0.03	1.78	0.01	0.51	0.00	1.34	3.06	13.74
A0154	01:10:58.45	17:37:42.7	393	15.64	0.00	3.88	0.03	3.88	0.04	0.47	0.00	1.20	1.30	17.27
A0154	01:10:40.64	17:42:19.0	248	15.56	0.01	3.99	0.02	3.65	0.04	0.36	0.00	1.22	1.53	24.22
A0154	01:11:14.01	17:32:24.5	527	14.31	0.00	12.28	0.01	3.79	0.01	0.79	0.00	1.34	6.07	7.37
A0154	01:10:36.87	17:35:36.7	457	15.98	0.01	2.41	0.03	4.38	0.08	0.59	0.00	1.15	1.46	15.96
A0154	01:11:07.28	17:34:49.3	477	15.96	0.00	2.96	0.02	2.32	0.03	0.41	0.00	1.25	2.76	15.23
A0154	01:10:28.01	17:30:14.8	586	16.17	0.00	3.54	0.03	1.34	0.01	0.89	0.00	1.14	1.56	9.48
A0154	01:11:29.83	17:46:10.7	156	16.17	0.01	2.91	0.03	2.99	0.05	0.38	0.00	1.19	2.32	17.87
A0154	01:11:30.57	17:34:16.0	488	16.13	0.01	3.44	0.05	3.37	0.06	0.74	0.01	1.20	2.60	12.63
A0154	01:10:17.23	17:48:41.4	84	16.30	0.01	2.41	0.02	2.43	0.04	0.70	0.01	1.10	1.39	12.91
A0154	01:11:00.79	17:37:44.4	396	16.35	0.00	1.57	0.01	2.90	0.06	0.46	0.00	1.22	1.53	23.56
A0154	01:10:49.54	17:50:35.0	40	16.46	0.00	3.85	0.03	1.67	0.02	0.31	0.00	1.22	1.96	7.69
A0154	01:10:54.98	17:39:12.9	364	16.61	0.01	2.54	0.02	1.29	0.02	0.76	0.01	1.50	6.23	12.17
A0154	01:11:46.26	17:48:43.6	87	16.61	0.00	3.17	0.02	1.08	0.01	0.60	0.00	1.13	1.25	11.39

**Table 4.5:** SS fits. Column (1): the Cluster name; (2) Right Ascension; (3) Declination; (4) ID; (5) Total Magnitude; (6) Total Magnitude error; (7) Re; (8) Re error; (9) Sérsic index; (10) Sérsic Index error; (11) Axis ratio; (12) Axis ratio error; (13)  $\chi^2_\nu$ ; (14) BPN; (15) Signal to noise ratio.

## 4.5 Summary

In this Chapter, it is presented the results of DGCG for clusters of galaxies at low- $z$  from the database LOCOS. It is described the DGCG performance and have compared its results with PPP. It was introduced a new approach to quantify galaxy morphology. It can be deemed that our results are comparable to those derived from neural-networks (Lahav et al. 1995, 1996) or multi-parameter studies (Fasano et al. 2012). Our results have been superficially analyzed; however, it can be concluded that our approach is suitable for galaxy classification, and cluster of galaxies using schemes based on the distribution of their galaxy populations (e.g., Oemler 1974). The Bayesian information criterion (Schwarz 1978) has been used to generate a criterion to decide on the minimum number of components that should be considered for E galaxies, and it is presented images to support it. It is presented the final catalog for 1453 galaxies including the SS (Single Sérsic) and BD (Sérsic + exponential) components. The complete catalog can be downloaded from <http://tinyurl.com/7o2rm2q>. In the next chapter, it is presented a complete analysis of the results.



# *Analysis: Scaling Relations, Structural Properties of Cluster Galaxies and the Formation of S0 Galaxies*

In this Chapter, it has been analyzed the most common galaxy scaling relations among their structural parameters. Those scaling relations are in agreement with the literature. The Kormendy relation (Kormendy 1977) has been used to separate classic bulges from pseudobulges. Using this classification, we show new diagnostic diagrams to identify bulges and pseudobulges. Correlations shown in modern works are analyzed and compared with this work. After it has been analyzed the surface brightness profiles and structural parameters of cluster galaxies, we have been arrived at a new view on the formation of S0 galaxies. It is suggested that S0 galaxies are formed by dynamical processes that modify the whole structure of S galaxies, rather than pure ram pressure stripping. We argue that ram pressure can not influence the formation of S0s during cluster assembling, but only during the advanced stages of cluster evolution when clusters have reached virialization, and the intracluster medium (ICM) has reached hydrostatic equilibrium.

## **5.1 Galaxy Scaling Laws**

In this section, it is explored previous relations that were established using smaller samples, classified by eyeball inspection, and 1D surface brightness modelling. Recovering those relations is a good test to verify the reliability of the code and model fittings. Once it is established the validity of our approach, we can search for indicators of galaxy evolution and the effects of the environment. It is presented, below, the well-known density-morphology relation (DMR, Dressler 1980b), the Kormendy relation (KR, Kormendy 1977), the luminosity-size relation (LSR, e.g., Gavazzi et al. 1996; Schade et al. 1997; Nair et al. 2010), the color-magnitude relation CMR (e.g., López-Cruz et al. 2004), the Faber-Jackson relation (FJR, e.g. Faber & Jackson 1976) and the Fundamental plane (e.g., Djorgovski & Davis 1987). Finally, some recent correlations are compared and discussed with our results.

### 5.1.1 Density-Morphology Relation

Dressler (1980b) was the first one to realize that the environment affects galaxy morphology (Dressler 2011). Although, everyone was aware of the differences on the distribution of nebulae in clusters as early as 1906 (Wolf 1906), it was only through Dressler's approach that the density-morphology relation (DMR) was unearthed. We present as a first result our estimation of the DMR using the galaxy types presented in the previous chapter. To quantify the surface galactic density we used the following definition 5.1 (Dressler 1980b; Tran et al. 2003):

$$\Sigma = \frac{11}{\pi r_{10}^2}, \quad (5.1)$$

where  $r_{10}$  is the distance to the 10th farthest galaxy measured in  $Mpc$ . The morphology fraction is computed bin by bin from the histogram of the surface galactic density distribution generated by equation 5.1. Then, in every bin, the morphology fraction is normalized by the total of galaxies.

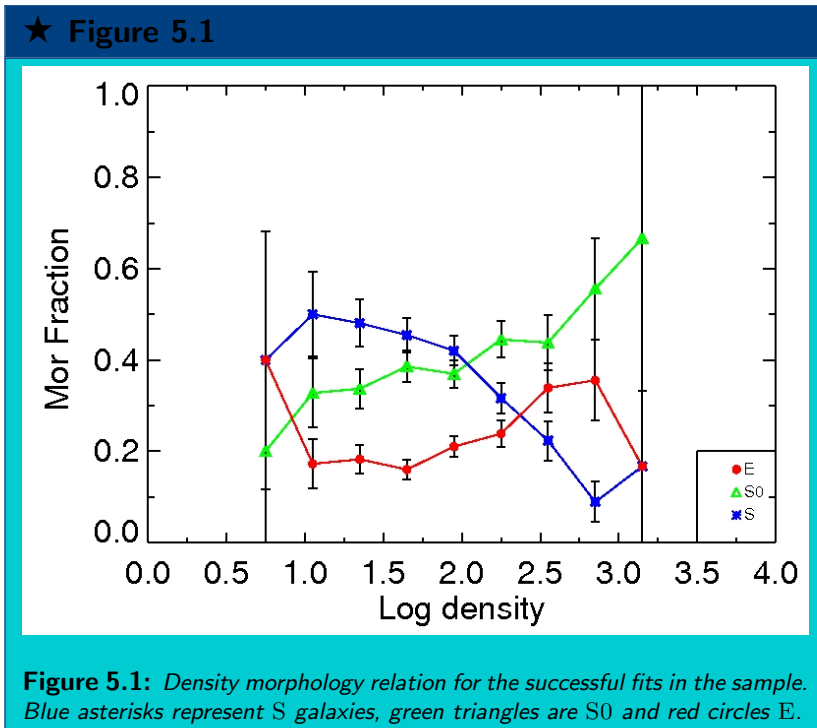
Recovering the DMR provides additional support to our classification approach. Therefore, we are confident that it closely reproduces the results from studies where eye-ball classification was employed. Early attempts fail to recover the DMR with parametric classification.

In Figure 5.1, it is presented the DMR for all the galaxies classified in this study. As can be seen, the DMR is recovered. There are some subtle differences with Dressler (1980b, see also Figure 1.5) however. The surface galactic density is higher than Dressler (1980b). We can attribute this to the fact that we have sampled deeper than Dressler (1980a) on the luminosity distribution of cluster galaxies. We have, therefore, recovered the original trend suggested by Dressler: S galaxies are preferably found in regions of low density. On the other hand, quite the opposite trend is followed by S0 galaxies because they are preferably found in high density regions; however, while the behaviour of E galaxies do not seem to change with redshift, the fraction of S0 galaxies at high- $z$  is lower than in the local clusters (Dressler et al. 1997).

The DMR presented in this work was generated using morphological types estimated after parameterized the surface brightness distribution of galaxies. Other works have also found similar DMR using other approaches than visual classification.

Tran et al. (2003) constructed a similar diagram to the DMR. They made a density-B/T relation. They separated galaxies into two types of galaxies: those with  $B/T \geq 0.4$ , and the other ones with  $B/T < 0.4$ . They noticed that galaxies with  $B/T \geq 0.4$  increase with galactic density, and galaxies with  $B/T < 0.4$  decrease with galactic density. However, we have seen in §4.2.1 that B/T alone fails to segregate S0 from E.

Goto et al. (2003) recovered the DMR for the SDSS. They used parameters of concentration combined with an elongation correction, and a similar parameter to bumpiness (see §1.2.2). They classify galaxies in early-type, intermediate-type, early disk, and late disk. Early-type, intermediate-type, and late-disk galaxies follow the DMR. The fraction of the first two increase with galaxy density while the fraction of late-disk decreases. On



the other hand, their early-disk galaxies do not follow the DMR.

Thomas & Katgert (2006a) used spectral classification of galaxies to construct the DMR for 2295 galaxies of ENACS (Thomas & Katgert 2006b). Their DMR is not well defined as the shown in Figure 5.1.

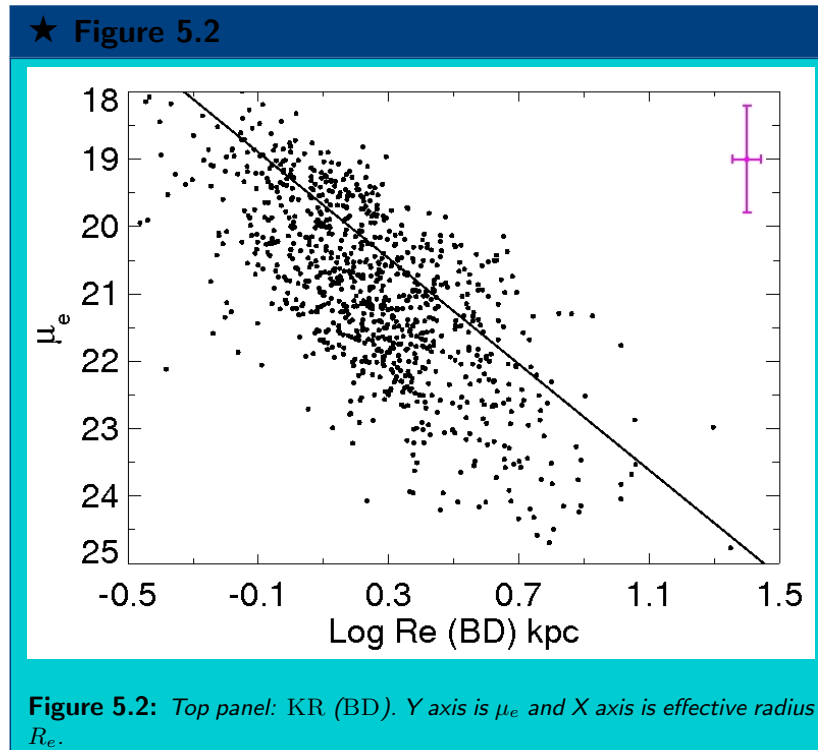
Tasca et al. (2009) used concentration, asymmetry, and gini parameters (check §1.2.2) to separate early-type, spirals and irregulars. Using this classification, they construct the DMR to study its evolution up to redshift 1 and its dependence on galaxy luminosity and stellar mass.

Ma & Ebeling (2011) use a similar method to the used here to classify galaxies and recover the DMR for one cluster (MACSJ0717.5+3745  $z = 0.545$ ). Finally, Calvi et al. (2012) use MORPHOT (Fasano et al. 2012) to classify galaxies and obtain morphology-mass relations.

To our knowledge, this might be the first occasion that the DMR has been well recovered with a large sample using other approach than the direct galaxy classifications performed by an expert.

### 5.1.2 The Kormendy Relation

The relation between  $\mu_e$  and  $R_e$  for E was discovered by Kormendy (1977). Since then, it is known as the Kormendy relation (KR). This relation indicates that E galaxies with large  $R_e$  have large  $\mu_e$  (i.e. they are fainter) while E galaxies with low  $R_e$  have low  $\mu_e$  (i.e. they are brighter). Some bulges of S0 and S also follow the KR. The KR generated with our data for E and bulges of S0 and S is presented in Figure 5.2.



The fitted solid line of Figure 5.2 is

$$\mu_e = (3.93 \pm 0.011) \log R_e + 19.29 \pm 0.003, \quad (5.2)$$

The fit for just E galaxies gives

$$\mu_e = (3.21 \pm 0.022) \log R_e + 19.14 \pm 0.006, \quad (5.3)$$

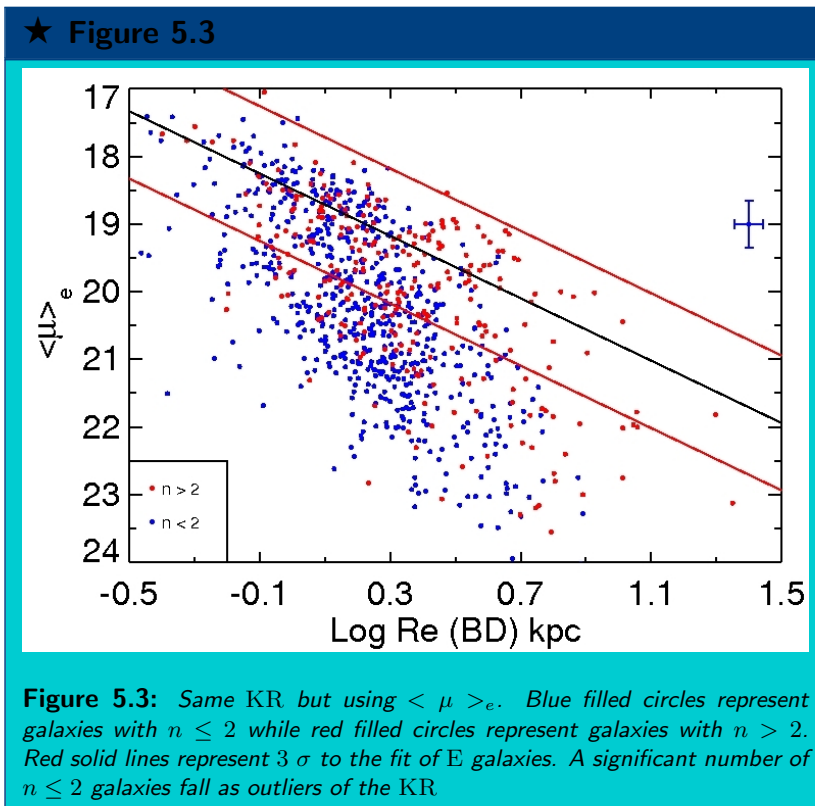
The original KR Kormendy (1977) is

$$\mu_e = (3.02) \log R_e + 19.74, \quad (5.4)$$

which is closely agree with our results.

### Identification of Pseudobulges using the Kormendy Relation

Sérsic index has been used to separated pseudobulges from bulges because pseudobulges usually have Sérsic index less than 2 (Kormendy & Kennicutt 2004; Fisher et al. 2010). On the other hand, Gadotti (2009) used KR to separate bulges from pseudobulges. Gadotti argue that pseudobulges do not follow the same relations of bulges as is the case of KR. Pseudobulges are formed from secular processes caused by the galactic disk (See §1.3.4. Hence, those pseudobulges are expected to have a rotational component and a low Sérsic index (Kormendy & Kennicutt 2004). Because bulges and pseudobulges are formed differently and have different dynamics, pseudobulges are expected to fall as outliers of the normal relations of bulges.



In Figure 5.3, it is plotted the KR using the mean surface brightness at the effective radius  $\langle \mu \rangle_e$  instead of  $\mu_e$ . Galaxy bulges with  $n > 2$  are indicated with red filled circles while galaxy bulges with  $n \leq 2$  are indicated with blue filled circles. We have found the same result as Gadotti (2009): a significant amount of  $n \leq 2$  galaxies fall outside

of KR. Gadotti call true bulges those that fall on the KR; while the ones outside the KR are considered pseudobulges. We have found that 65% of bulges with  $n < 2$  are pseudobulges according to Gadotti's definition, i.e. pseudobulges are those which lie  $3\sigma$  outside of the KR. From our simulations (§3.4), a large uncertainty arise in the recovery of  $n$ . Therefore, given the quality of the data employed in this thesis, and for the surface brightness modelling adopted and developed in this study: Gadotti's definition is adopted to differentiate bulges from pseudobulges.

### 5.1.3 Luminosity-Size Relation

Another well-known relation is the luminosity vs. size relation (LSR). Brighter galaxies have large sizes while fainter galaxies have small sizes. The size can be measured in  $R_e$ ,  $R_{90}$ <sup>1</sup>, or Petrosian radius (Petrosian 1976). LSR is shown in Figure 5.4. The top panels show the relations for SS models, and the bottom panels show the relations for BD models. The left panels of Figure 5.4 show the LSR using  $R_e$  while the right panels show the LSR using  $R_{90}$ . The  $R_{90}$  radius shown in Fig. 5.4 were computed from the Sérsic model (see appendix B).

A linear fit for the LSR as a function of  $R_e$  gives

$$\log(L) = (1.18 \pm 0.001) \log Re + 9.6 \pm 0.0003, \quad (5.5)$$

while for  $R_{90}$ , it reads:

$$\log(L) = (1.16 \pm 0.000067) \log R_{90} + 8.9 \pm 0.000076, \quad (5.6)$$

similarly, Nair et al. (2010) found a parametrization for the LSR in the  $r$  band (for E and E/S0):

$$\log(L) = (1.32 \pm 0.03) \log R_{p90} + 9.1 \pm 0.03, \quad (5.7)$$

where  $R_{p90}$  is the Petrosian radius containing the 90% of total light. The last equation was found for E galaxies. Nair et al. (2011) found that LSR has less dispersion, if it is derived from Petrosian radius due to insensitivity to the shape of the galaxy profile.

---

<sup>1</sup>This radius contains the 90% of total light

★ Figure 5.4

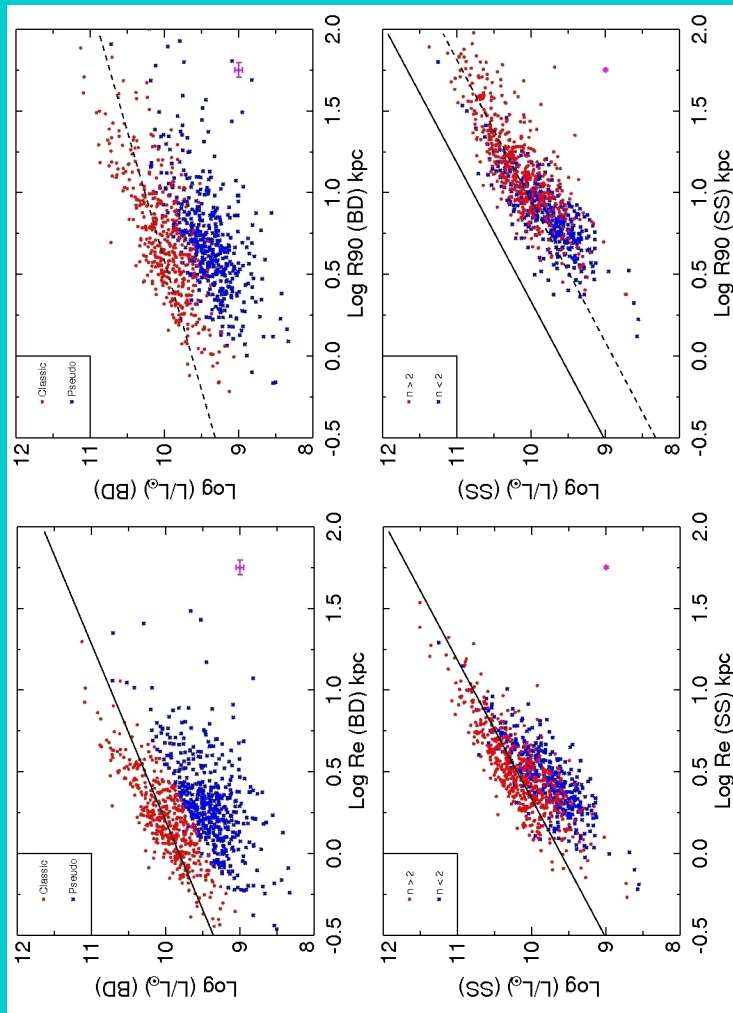
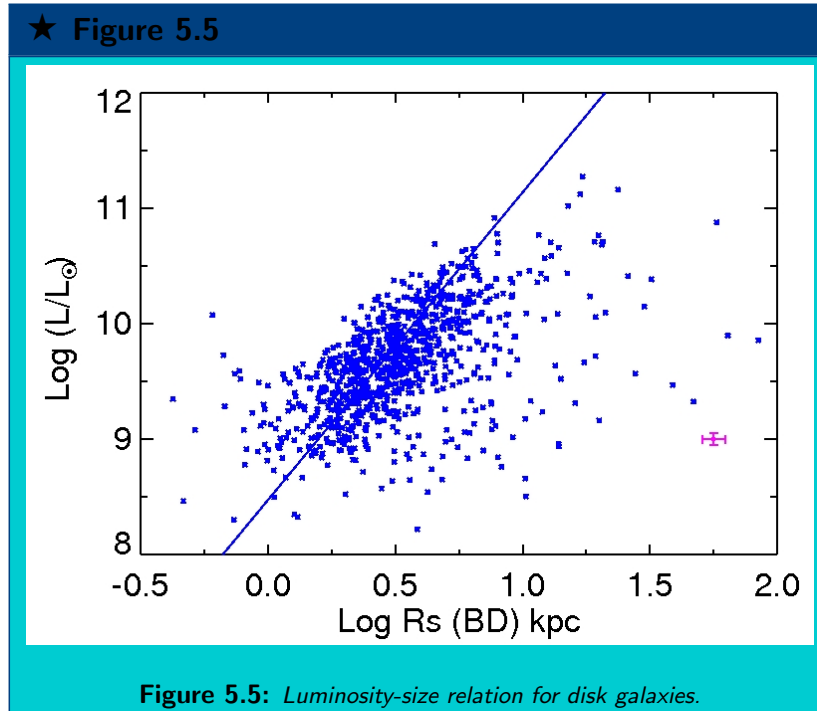


**Figure 5.4:** Luminosity-Size relations. Top left panel: luminosity-size relation for bulges BD using  $R_e$ . Top right panel: Luminosity-size relation for bulges BD using  $R_{90}$ . Bottom left panel: luminosity-size relation for SS models using  $R_e$ . Bottom right panel: luminosity-size relation for SS models using  $R_{90}$ . Blue dots are galaxies with Sérsic index  $< 2$  and red dots are galaxies with Sérsic index  $> 2$  for bottom panels. Solid lines represent the fit for  $R_e$ , and dashed lines represent fit for  $R_{90}$

Nair et al. (2010) found that the LSR computed with the  $R_{p90}$  has less dispersion than the one computed with  $R_{p50}$  (or  $R_e$ ) which is the Petrosian radius containing the 50% of total light. To test this, it is plotted in the bottom left and right panels the LSR for  $R_e$  and  $R_{90}$  respectively. The dispersion of LSR using  $R_{90}$  is 17% smaller than the one using  $R_e$ . The bottom left panel shows that galaxies with  $n < 2$  do not follow the LSR of galaxies with  $n > 2$ . On the contrary, the bottom right panel shows that those galaxies with  $n < 2$  follow the LSR for  $R_{90}$ . Moreover, the LSR of Schade et al. (1997) is limited to galaxies that were well described by a de Vaucouleurs profile ( $n = 4$ ). Their results on the LSR are in agreement with the results found in Fig. 5.4. We conclude, in agreement with Nair et al. (2010, 2011), that  $R_{90}$  gives a better measurement for the global LSR relation.

Using the KR from the previous section, we were able to separate pseudobulges and classic bulges in the top panels of Figure 5.4. As can be seen, pseudobulges do not follow the same LSR for classic bulges. As has been explained in §5.1.2, pseudobulges do not follow the same relations of classic bulges. Moreover, the same effect discussed above for  $R_e$  and  $R_{90}$  is observed for bulges: the LSR has less dispersion with  $R_{90}$  than  $R_e$ . Nevertheless, even using  $R_{90}$ , pseudobulges still do not follow the LSR of classic bulges.

There is a similar LSR for disks. This is shown in Figure 5.5. A linear fit gives  $\log(L) = (2.65 \pm 0.004) \log R_s + 8.47 \pm 0.002$ . This result is in agreement with the ones found by Courteau et al. (2007); Saintonge & Spekkens (2011) for the  $I$  band and the one with Schade et al. (1996) in the  $R$  band.



### 5.1.4 Color-Magnitude Relation

The plot of the color of cluster galaxies versus their magnitude gives a nearly horizontal line defined as the red sequence. This red sequence is normally populated by early-type galaxies. At the same time, late-type galaxies populate a “blue cloud” in the CMR.

The scatter of the CMR around the red sequence is very small. This means that the early-type galaxies in clusters have nearly the same colors only weakly depending on the magnitude.

López-Cruz et al. (2004) had computed the CMR for cluster galaxies. Here, we have extended their work, separating morphology in the CMR and using absolute magnitude instead of apparent magnitude. This allow us to put all the cluster galaxies in one diagram. Our CMR is shown in Figure 5.6. The equation of the solid line is  $B - R = -(0.05 \pm 0.0006) * R + 0.47 \pm 0.012$ . The tilt of the CMR of Figure 5.6 ( $-0.046$ ) is in perfect agreement with the one found for the Coma cluster (López-Cruz 1997; López-Cruz et al. 2004).

Early-type galaxies, in Figure 5.6, fall into an almost perfect line. On the other hand, galaxies with ongoing star formation conform the blue cloud. Right panel of Figure 5.6 shows the dispersion of CMR for each morphological type around the red sequence. The peaks of every morphological type in the right panel of Fig. 5.6 are in agreement with the ones found by Fasano et al. (2012). They also have a small shift of the peak of the distributions for E ( $\mu = 1.64$ ) and S0 ( $\mu = 1.63$ ). These Figures also show that S galaxies have a greater dispersion on the CMR than both E and S0 galaxies. This shows that S galaxies are forming stars.

Actually, the dispersion of the CMR for S galaxies shows a bimodal distribution. Even that, the large dispersion of the CMR of S galaxies, in comparison with the ones of E and S0, is due to ongoing star formation, there are some S galaxies on the red sequence. To exclude the possibility of redness in Figure 5.6 due to inclined S galaxies, we have plotted also in panel D of Figure 5.6 all the S with disk axis ratio greater than 0.3. As can be seen, there is still a large proportion of red S on the red sequence in comparison to the blue S. In their CMRs, Valentinuzzi et al. (2011) also found red S on the red sequence and found that the population of those S depends on local density.

We suggest that those red S could be identified with the class of anemic S suggested by van den Bergh (1976) and with the ones found by the Galaxy Zoo project (Masters et al. 2010); van den Bergh considered that anemic S had characteristics intermediate between S0 and S. Those galaxies are van den Bergh (1976)'s S gas poor. Elmegreen et al. (2002) have suggested that those anemic S turn into S0.

★ Figure 5.6

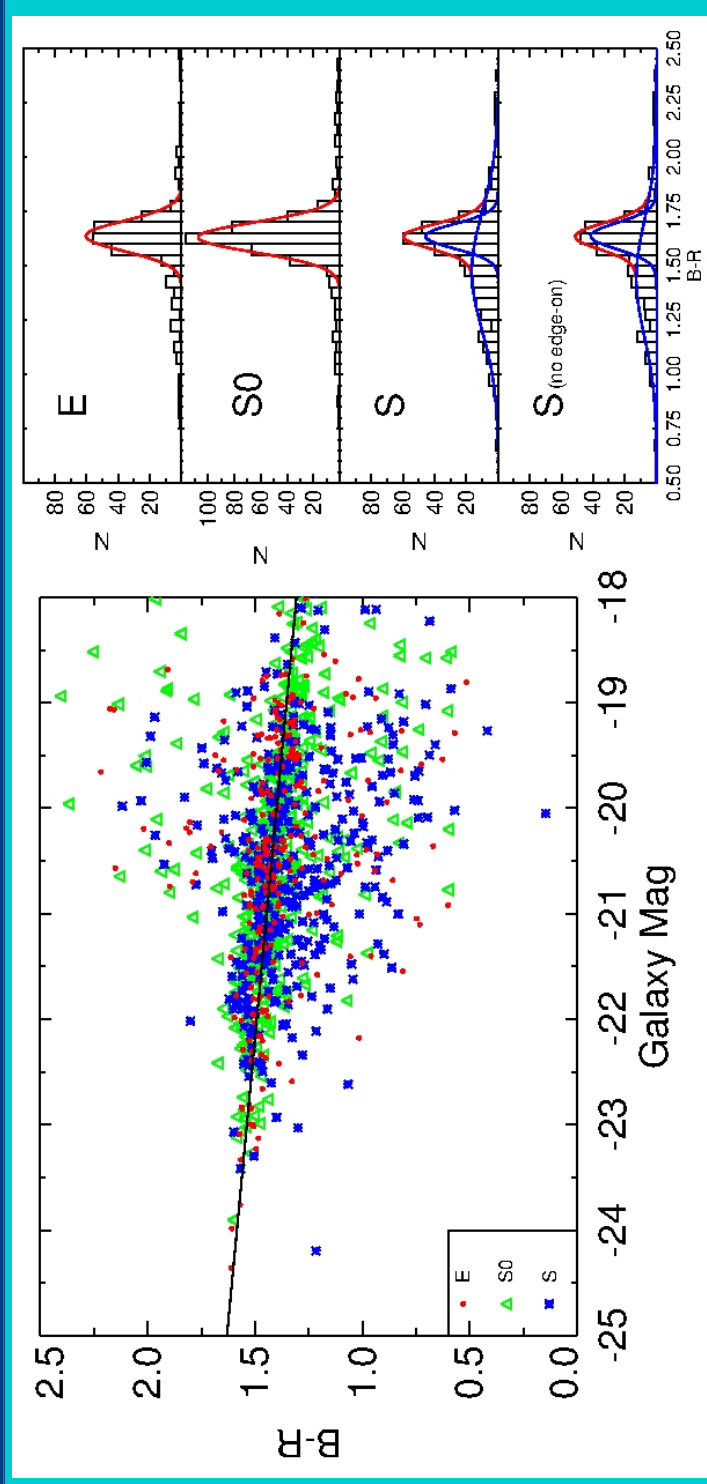


**Figure 5.6:** Left panel: CMR.  $B-R$  vs.  $R$ . Red circles are E, blue asterisks are S and green triangles are S0. Right Panel:  $B-R$  histograms for each morphological type. From top right to bottom panel: E galaxies ( $\mu = 1.64$ ,  $\sigma = 0.069$ ). S0 galaxies ( $\mu = 1.63$ ,  $\sigma = 0.069$ ). Red S ( $\mu = 1.63$ ,  $\sigma = 0.06$ ), and blue S ( $\mu = 1.47$ ,  $\sigma = 0.27$ ). Red S ( $\mu = 1.44$ ,  $\sigma = 0.06$ ) and blue S ( $\mu = 1.44$ ,  $\sigma = 0.26$ ) excluding the edge-on galaxies

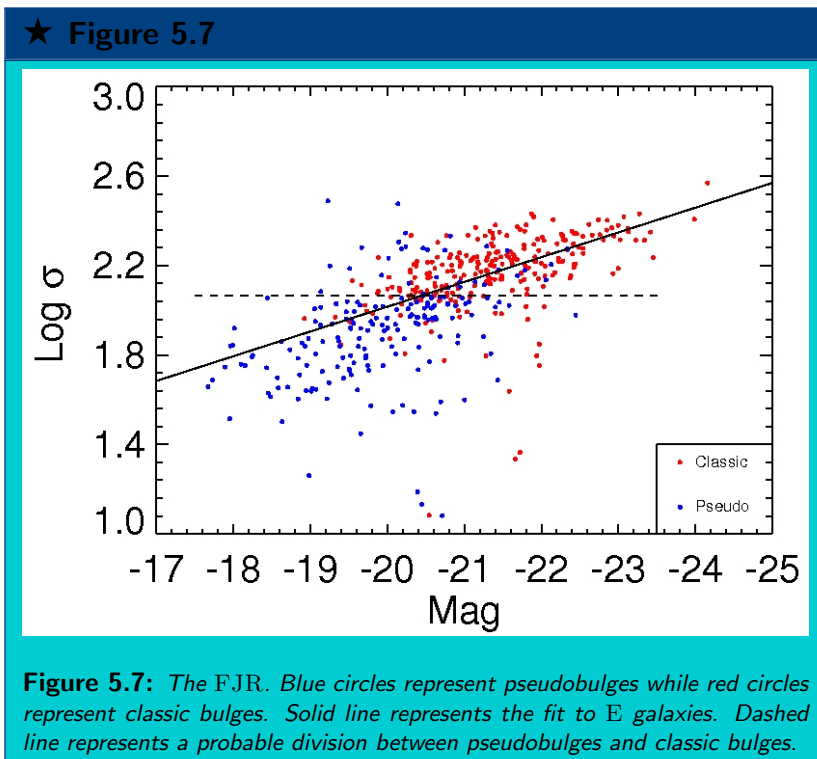
### 5.1.5 The Faber-Jackson Relation

Faber & Jackson (1976) discovered that the velocity dispersion of E scales with luminosity (see equation 5.8). This relation is known as FJR.

$$L \sim \sigma^4, \tag{5.8}$$

The FJR is plotted in Figure 5.7 for the whole sample. The fit solid line for E galaxies in Fig 5.7 is

$$\log \sigma = (-0.11 \pm 0.003) \text{ Mag} - 0.23 \pm 0.06, \tag{5.9}$$



We also have separated bulges (red filled circles) and pseudobulges (blue filled circles) in Fig. 5.7. The dashed line cuts the FJR at  $\log \sigma = -2.06$ ; it indicates an arbitrary division between bulges and pseudobulges. Pseudobulges fall below the dashed line while classic bulges fall above of it.

Pseudobulges populate the low part of the FJR because, as explained before, they are rotationally supported. Hence, their velocity dispersion is low. There are other studies where pseudobulges fall below the FJR (Kormendy & Kennicutt 2004; Jiang et al. 2011).

On the other hand, classic bulges fall in the high velocity dispersion region of FJR. This is because classic galaxies have higher random velocities than ordered velocities.

Position on the FJR of Fig. 5.7 suggests the physical origin of the bulges. In the upper side of this relation, bulges are formed by mergers. On the other hand, bulges in the low part of the FJR are formed by secular processes. Besides the KR, here we have provided an additional diagnostic diagram that can be used to separate pseudobulges from classic bulges.

### 5.1.6 Fundamental Plane and its Dispersion

The FJR, and Tully-Fisher relations (Tully & Fisher 1977) are projections of a relation known as *Fundamental plane* (Djorgovski & Davis 1987). This fundamental plane has less dispersion than the FJR. It was discovered for E galaxies and indicates that luminosity, velocity dispersion ( $\sigma$ ), and size of E galaxies and bulges are correlated. This multidimensional parameter space is defined by the space parameters  $R_e$ ,  $\langle \mu_e \rangle$ ,  $\sigma$ .

Our fundamental plane for E and bulges is depicted in Figure 5.8. We have taken the  $R_e$  and  $\langle \mu_{>e} \rangle$  from BD fits and  $\sigma$  from Ibarra-Medel (2010) (§2.5). The expression for the fundamental plane in of Fig. 5.8 (solid line) is

$$\log R_e = (1.30 \pm 0.015) \log \sigma + (0.328 \pm .004) \langle \mu_e \rangle + (9 \pm 0.1), \quad (5.10)$$

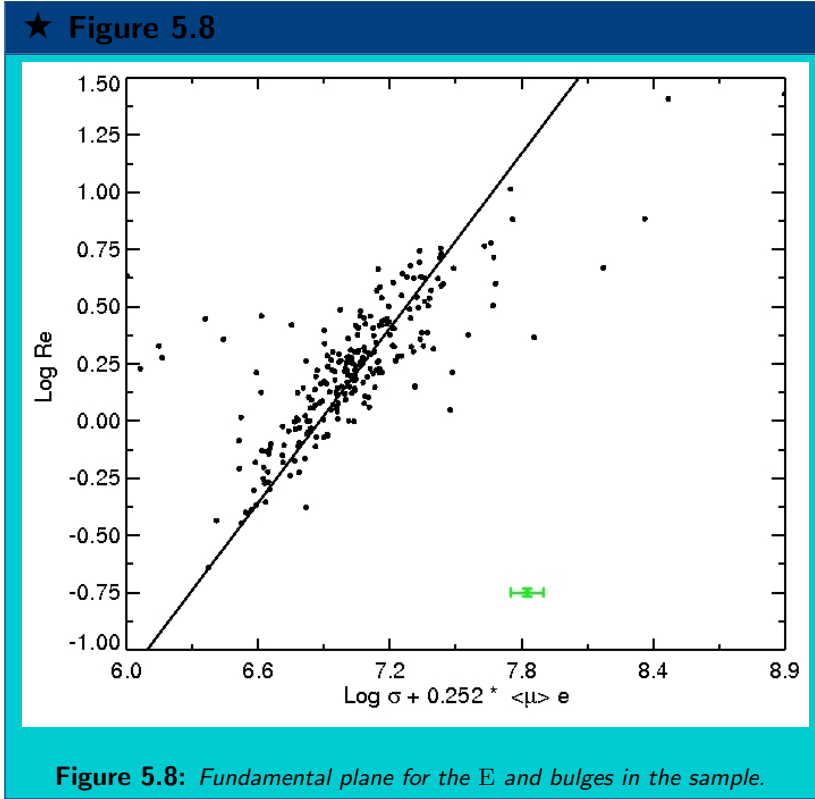
These 3 parameters are related due to the virial theorem. This theorem states that, for an isolated dynamical system in a stationary state of equilibrium, the potential energy is two times the kinetic energy. Following the procedure of Djorgovski et al. (1988), the virial theorem implies that galaxies must satisfy a relation similar to equation 5.11.

$$R \sim k_S k_E \sigma^2 I^{-1} (M/L)^{-1}, \quad (5.11)$$

where  $k_S$  represents the density, luminosity, and kinematic structure of the galaxy. The parameter  $k_E$  is the ratio of absolute potential energy to kinetic energy for a galaxy:  $k_E = 2$  means that the system is virialized.

Assuming that  $k_S k_E (M/L)^{-1}$  is constant, the exponents of  $\sigma$  and  $I$  are 2 and  $-1$  respectively as shown in equation 5.11; however, observations show deviations from those numbers. With our data, we have found  $1.3 \pm 0.015$  and  $-0.82 \pm 0.015$  for  $\sigma$  and  $I$  respectively. These results are in agreement with the range of values found by other authors (e.g., Recillas-Cruz et al. 1991; Lucey et al. 1991; Pahre et al. 1998; Hyde & Bernardi 2009; La Barbera et al. 2010; Springob et al. 2012). Those deviations imply that  $k_S k_E (M/L)^{-1}$  is not constant. In fact, there is some dependence of  $k_S k_E (M/L)^{-1}$  on galactic mass or other fundamental plane variables, and probably they are responsible of the dispersion on the fundamental plane.

To study the differences between bulges and pseudobulges, we re-plot the fundamental plane in the Figure 5.9. Classic bulges are the red filled circles and pseudobulges the blue filled circles.



The expression for the Fundamental plane of classic bulges is

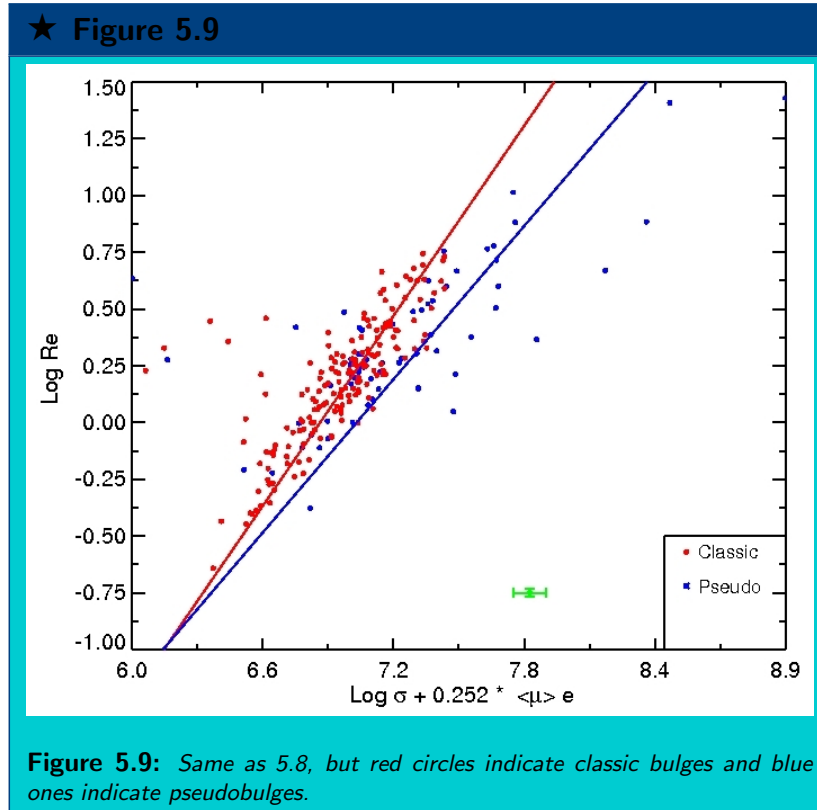
$$\log R_e = (1.43 \pm 0.023) \log \sigma + (0.36 \pm 0.006) \langle \mu \rangle_e + 9.8 \pm 0.2, \quad (5.12)$$

and for the pseudobulges is

$$\log R_e = (1.16 \pm 0.04) \log \sigma + (0.29 \pm 0.01) \langle \mu \rangle_e + 8.1 \pm 0.08, \quad (5.13)$$

The fit of the fundamental plane for classic bulges has a lower dispersion ( $\chi^2_\nu = 7.24$ ) than the one for pseudobulges ( $\chi^2_\nu = 9.65$ ). The reduction of the dispersion for classic bulges is reduced 72%. The explanation of this reduction is hidden in the coefficient  $k_S k_E (M/L)^{-1}$  of equation 5.11. First of all, as we explain in §5.1.2, pseudobulges do not follow the relation of classic bulges, and they are more rotationally supported structures than classic bulges. This introduces different variations in the coefficient  $k_S k_E$  for classic bulges and pseudobulges.

Other works have found that the dispersion of the fundamental plane is due to mean stellar age and metallicity (Gargiulo et al. 2009; Springob et al. 2012). Somehow, this



is in agreement with this work because classic bulges are redder (see below §5.2.2). Nevertheless, they argue that different stellar populations introduce variations in  $M/L$ , and, as a consequence, those variations produce the dispersion. We agree with this, but probably another possibility is that pseudobulges are structurally different from classic bulges, or pseudobulges are evolving to classic bulges. The recent studies of Kormendy et al. (2011) show that black holes in pseudobulges do not follow the known correlation between black hole mass and bulge luminosity. This finding supports the physical nature of bulges and pseudobulges.

★ Figure 5.10

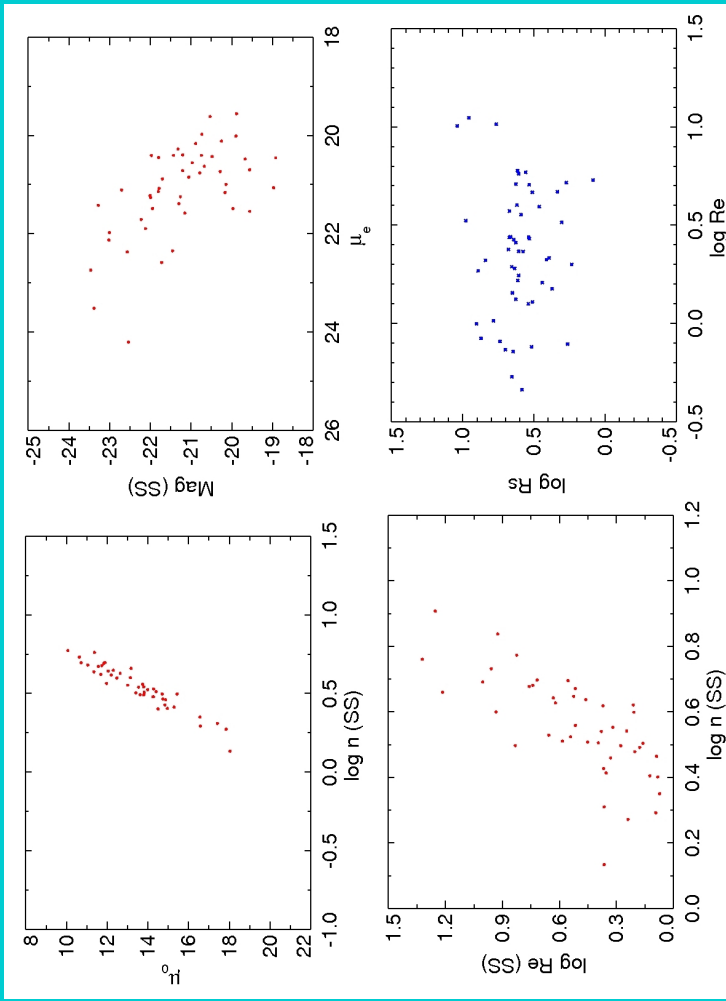


**Figure 5.10:** Top left: Central surface brightness vs. Sérsic index (SS) for E galaxies. Top right:  $\text{Mag}$  vs.  $\mu_e$  for E galaxies. Bottom left:  $R_e$  vs.  $n$  relation (SS) for E galaxies.  $R_s$  vs.  $R_e$  for S galaxies. The galaxies presented here are the ones of Dressler (1980a) catalog.

### 5.1.7 Correlations Suggested in Modern Works

Here, it is revisited and analyzed some recently introduced scaling relations obtained with 1-D techniques. The KR and the LSR were already explored in sections 5.1.2, 5.1.3 respectively. The luminosity vs. Sérsic index is shown in section 5.2.3. In Figure 5.10, we explored the rest of the relations found in Gutiérrez et al. (2004); Graham (2011). In general, we broadly agree with the relations revised in those papers. To avoid confusion by misclassified galaxies, we have restricted our comparison to use galaxies classified by Dressler (1980a).

The top left panel of Figure 5.10 shows the relation  $\mu_0$  vs.  $n$  (SS) which it is also found in the Figure 7 of Graham (2011). This relation is a mere property of the Sérsic function. Figure 3.1 shows that when Sérsic index increases,  $\mu_0$  also increases (the surface brightness at  $R = 0$ ). Therefore, this is just a mathematical property of the Sérsic function, and it is not a physical property of the galaxies.

The top right panel of Fig. 5.10 shows the relation Mag vs.  $\mu_e$  for E galaxies. This plot is also shown in Figure 8 of Graham (2011) and Figure 5 of Gutiérrez et al. (2004). The same trend for E galaxies is also shown in Figure 2 of Kormendy et al. (2009). This relation shows that brighter galaxies have fainter  $\mu_e$ . This relation can be obtained from KR and LSR.

The bottom left panel shows the  $R_e$  vs.  $n$  relation (SS) for E galaxies. We believe that this correlation is probably artificial. If one combines the KR, Magnitude vs.  $n$  relation, and equation B.14 (see appendix B), one can obtain the following relation between  $R_e$  and  $n$ :  $A \log R_e = B \log n + 10 \log(1+z) + C$ . Where  $A$ ,  $B$  and  $C$  are constants and  $z$  is the redshift. Hence, if the galaxy sample is at the same redshift, this correlation becomes visible as long as Kormendy and Mag. vs  $n$  relations are satisfied. Hence, this correlation is not new, and it can be obtained from old correlations. Another explanation for this relation can be due to parameter coupling (see Fig 3 of Weinberg (2012)).

In Figure 8 of Gutiérrez et al. (2004), there is a correlation between  $R_e$  (bulge) vs  $R_s$  (disk) for S galaxies. For comparison, we have plotted in the bottom right panel of Figure 5.10 the same relation  $R_e$  vs.  $R_s$  for S galaxies. As can be seen, in our plot there is no correlation between  $R_e$  and  $R_s$ . We believe that Gutiérrez et al. (2004) have an artificial correlation of parameters due to the lack of degrees of freedom induced by their 1-D techniques. Therefore, their conclusion that the scale length of Coma spiral galaxies are 30% smaller than those of spiral galaxies found in the field is questionable.

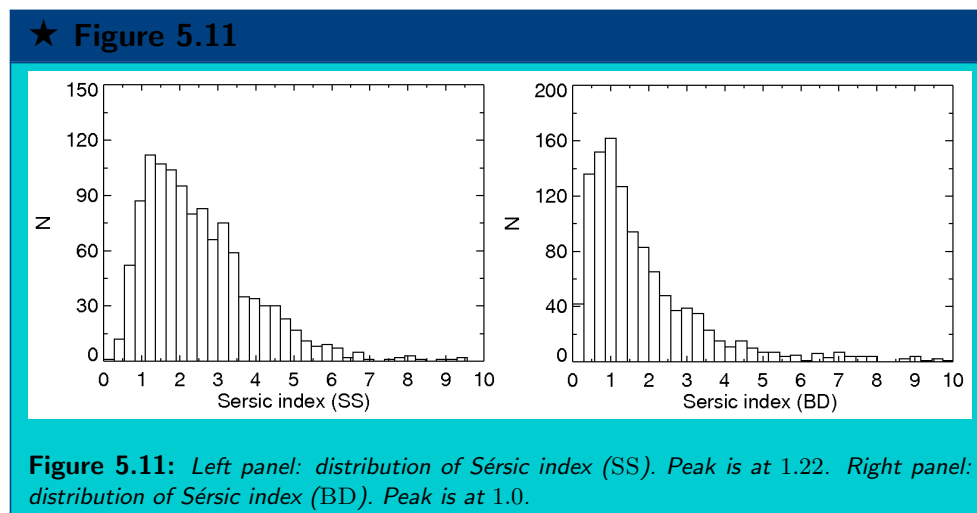
## 5.2 Structural Properties of Cluster Galaxies: Clues to the formation of S0 Galaxies

In this Section, it is studied the structural differences among morphology types. It is presented the histogram of the distribution of the Sérsic index. This shows which formation dominates the bulges of galaxies in clusters at low redshift. Moreover, the  $B - R$  color is compared with the structural properties of galaxies; it is shown that bulges and pseudobulges had different properties in those diagrams. The luminosity vs. Sérsic index

relation is also shown. This shows that the Sérsic index escalates with luminosity. Also, this probes that the Sérsic function is real, and it is not an arbitrary model for galaxies. Finally, using our classification method and analysing the properties among morphological types, we have found differences between S0 and S. This supports the idea that S0 galaxies are not simply swept S galaxies.

### 5.2.1 Distribution of Sérsic Index

The histogram of the distributions of Sérsic index for the galaxies in our sample is depicted in 5.11. In the left panel of this Fig., it is the distribution of the Sérsic index for the SS models, while, in the right panel, it is the distribution for the BD models. The peak of the distribution for SS models is at 1.22 whereas the peak for BD models is at 1.0.



Blanton et al. (2003); Blanton & Moustakas (2009) have a similar histogram to Figure 5.11 with 77153 galaxies with  $z < 0.05$  from SDSS database. Their peak of the histogram is at 1.3. They did not perform directly model fitting to their galaxies as we did. Instead, they compute the Petrosian radius for two different apertures ( $r_{50}/r_{90}$ ), and compare it with artificial galaxies to recover the Sérsic index<sup>2</sup>. Hence, our analysis is more detailed than Blanton et al. (2003); Blanton & Moustakas (2009). On the other hand, Fisher & Drory (2011) made a study of the local Universe (galaxies within 11 Mpc) and found that the majority of galaxies have pseudobulges. As a consequence, one expects that their Sérsic indexes are below to 2 (Kormendy & Kennicutt 2004). Therefore, the result of Figure 5.11 is in qualitative agreement with Blanton et al. (2003); Blanton & Moustakas (2009); Fisher & Drory (2011).

The results given by Figure 5.11 implies that secular processes dominates the formation of bulges at low redshift. Bulges formed by mergers are few in comparison to them. Secular

<sup>2</sup>Equation B.26 of Appendix B we give an empirical relation between  $r_{50}/r_{90}$  and Sérsic index

processes tend to form bulges with  $n < 2$  (Kormendy & Kennicutt 2004), while merger and tidal stripping form bulges with  $n > 2$  (Aguilar & White 1986; Nipoti et al. 2006). This is a consequence that, in a cosmological context, the merger rate is larger at high redshift than a low redshift.

### 5.2.2 $B - R$ Color and Structural Properties

Here, it is studied the properties of galaxies in diagrams like  $B - R$  vs. Sérsic index and CMR. Figure 5.12 shows 3 panels with the plot of  $B - R$  vs. Sérsic index. The top right panel shows  $B - R$  vs.  $n$  for BD models separated by bulge type. The bottom left panel shows  $B - R$  vs.  $n$  for SS models separated by morphological type. Finally, the bottom right panel shows the  $B - R$  vs.  $n$  for BD models separated by morphological type.

Bottom panels of Figure 5.12 reveals some interesting trends with Sérsic index. Galaxies with  $n < 2$  have red and blue colors. On the other hand, high Sérsic galaxies ( $n > 2$ ) are only red. This also implies that bulges with  $n > 2$  are always red independently of the disk size.

This trend was also found by Blanton & Moustakas (2009), but they used the Sloan colors  $g - r$ . As explained in the previous section 5.2.1, their Sérsic indexes were computed with Petrosian apertures and synthetic galaxies. Here, again we confirm their result, but we followed a detailed analysis.

In the top right panel of Figure 5.12, pseudobulges (blue filled circles) and classic bulges (red filled circles) show different properties. Pseudobulges are preferentially blue, and, as a consequence, the majority of pseudobulges have preferentially  $n < 2$ . This result has also been found by Kormendy & Kennicutt (2004); Gadotti (2009). On the contrary, classic bulges are always red within the whole range of Sérsic index. Note that this differences between bulges and pseudobulges are only appreciated if they are morphological separated using the KR (see §5.1.2). This two different populations of bulges with  $n < 2$  can not be seen if the Sérsic index is used to separate bulges and pseudobulges.

Given these results, it can be concluded that galaxies with  $n > 2$  are made of old stars, and galaxies with  $n < 2$  are made of both old and young stars. As explained above, this bimodality for galaxies with  $n < 2$  is due to two different types of bulges: classic bulges, which are the ones made of old stars, and pseudobulges, which are the ones made of young stars. Even with some overlap towards red colors, the secular processes that make pseudobulges rarely forms galaxies with  $n > 2$ . On the contrary, if mergers produce classic bulges, then they exhaust the gas during the process and could often form galaxies with  $n > 2$ .

★ Figure 5.12

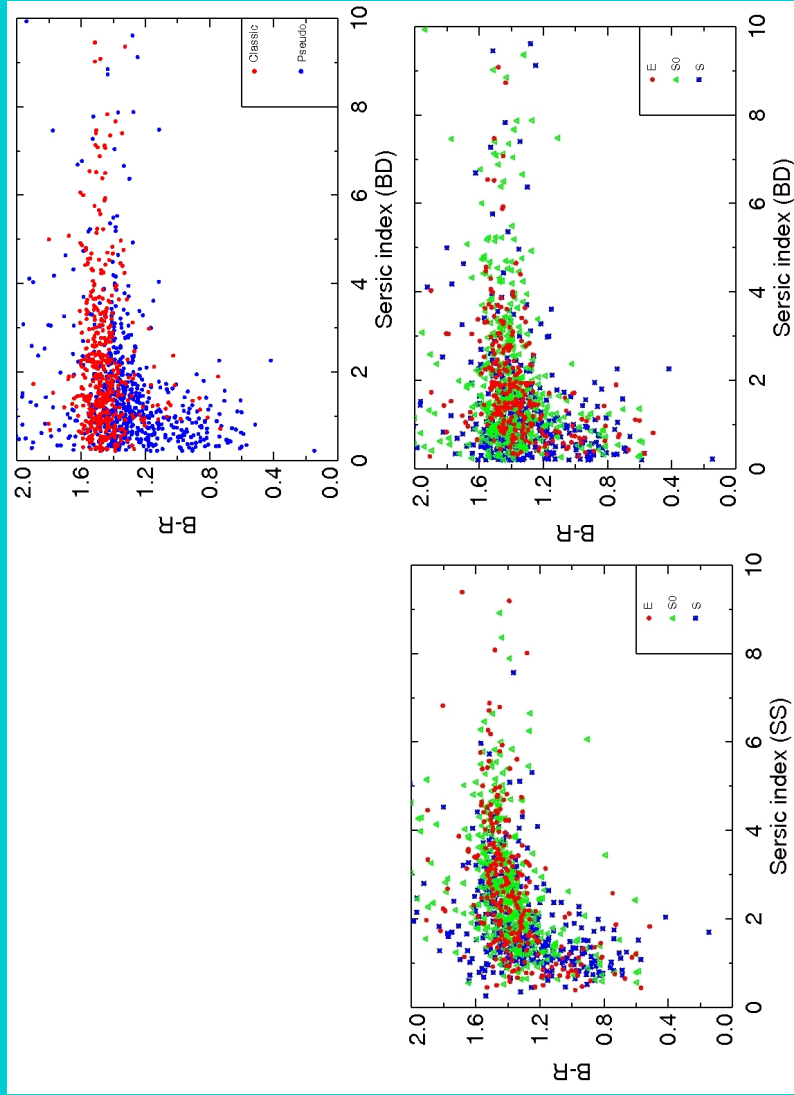
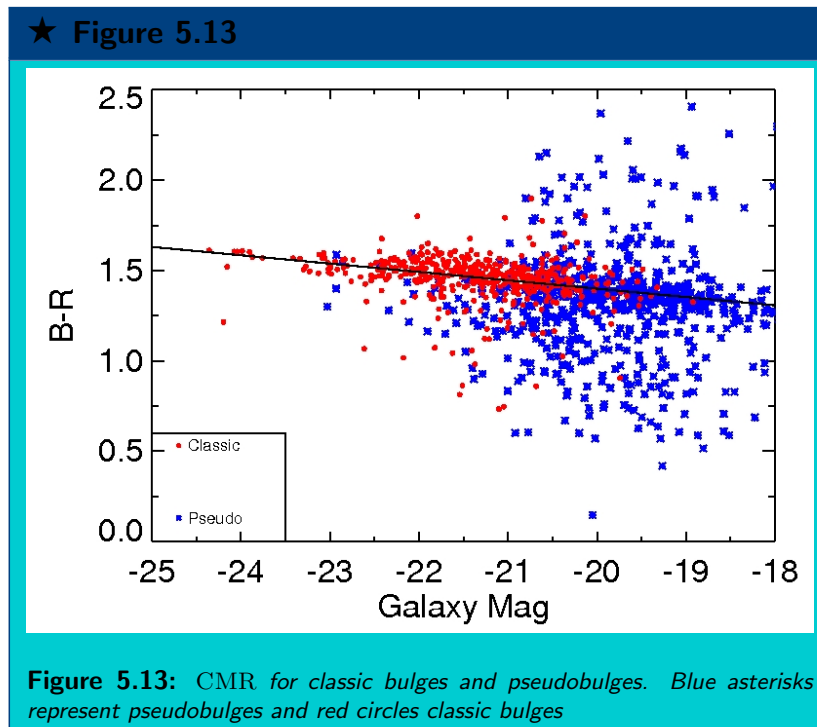


**Figure 5.12:** Top right panel: color ( $B - R$ ) vs. Sérsic index for BD models. Blue points represent pseudobulges and red ones classic bulges. Bottom left panel: color ( $B - R$ ) vs. Sérsic index for SS. Red circles are E, blue asterisks are S and green triangles are S0. Bottom right panel: color ( $B - R$ ) vs. Sérsic index for BD fits

Differences between classic bulges and pseudobulges on the CMR are shown in Figure 5.13. Classic bulges are preferentially found in the brightest side of the red sequence of Figure 5.13. On the other hand, one can distinguish two populations of pseudobulges in this Figure: (1) pseudobulges that lie in the blue cloud, and (2) pseudobulges that lie on the faint end of the red sequence. 69% of pseudobulges lie on the CMR while the rest lies in the “blue cloud”. Red sequence pseudobulges are not found in the sample studied by Gadotti (2009). Figure 5.13 shows that position on the red sequence gives clues about the formation of the bulge.

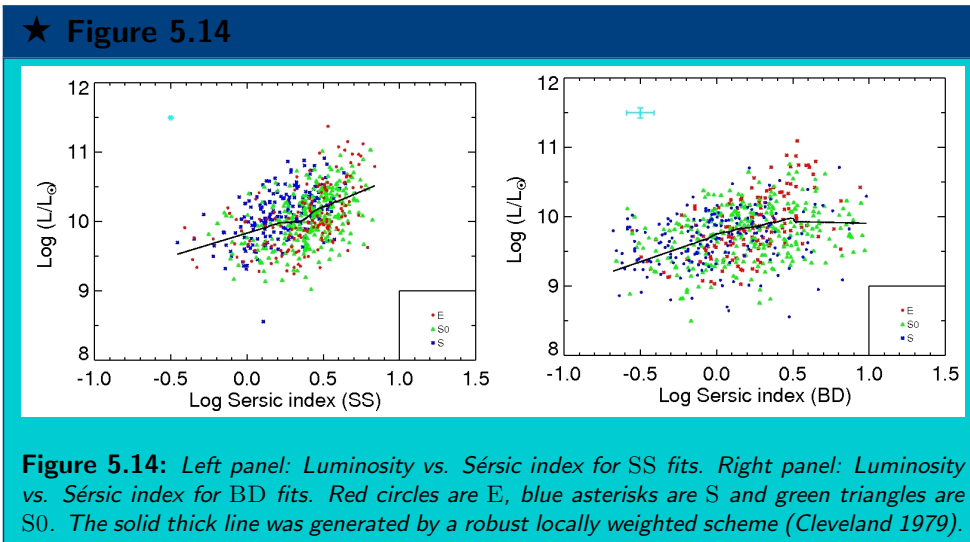
Those red sequence pseudobulges are probably an effect of the cluster environment. Secular processes dominate bulge formation in clusters at this epoch (see Fig. 5.11), and it is expected that those galaxies were forming stars (Kormendy & Kennicutt 2004). Nevertheless, because ram pressure is present only within clusters, disk gas is swept, and, as a consequence, the star formation is halted. Red sequence pseudobulges might represent a transitional phase in S0 galaxy formation.



### 5.2.3 Luminosity vs Sérsic Index

Left panel of Figure 5.14 shows the plot of luminosity vs.  $n$  for SS models, and right panel of Figure 5.14 the one for BD models.

This plot shows that brighter galaxies have higher  $n$  and vice versa. This same trend is



found, with a larger dispersion due to errors, for fits with the BD models (right panel of Fig. 5.14). The solid thick lines in Figure 5.14 were generated by a robust locally weighted scheme (Cleveland 1979).

This trend proves that  $n$  is a real physical parameter, and Sérsic function is not an arbitrary function for galaxies. This relation is in agreement with Blanton et al. (2003), Sandage (2005), and Kormendy et al. (2009). Nevertheless, the solid thick lines show that the growth of the index with brightness levels off, tending towards 4 ( $n \rightarrow 4$ ). This is also seen in Blanton et al. (2003); López-Cruz et al. (2011).

It can be seen that S galaxies follow a different trend in the left panel of Figure 5.14, which suggests they have different structures from E and S0 galaxies. This difference is discussed in §5.2.4.

### 5.2.4 Are S0 Galaxies originated by Ram Pressure?

It is believed that ram pressure is one the main responsible to transform S to S0 galaxies (§1.5.1). As ram pressure only affects the gas component of the galaxies, it is expected that the stellar distribution remains the same. Therefore, if the ram pressure is the main responsible for the formation of S0 galaxies, then there must not be significant differences in the stellar component between S and S0 galaxies.

Here, it is compared the structural properties of E, S0, and S galaxies. In Figure 5.15, it is shown the histogram of the distribution of  $n$  for S, S0 and E galaxies. In the left panel, it is shown the distribution of the Sérsic index for the whole sample, and in the right panel is shown the distribution of  $n$  for the galaxies which were classified by (Dressler 1980a).

★ Figure 5.15

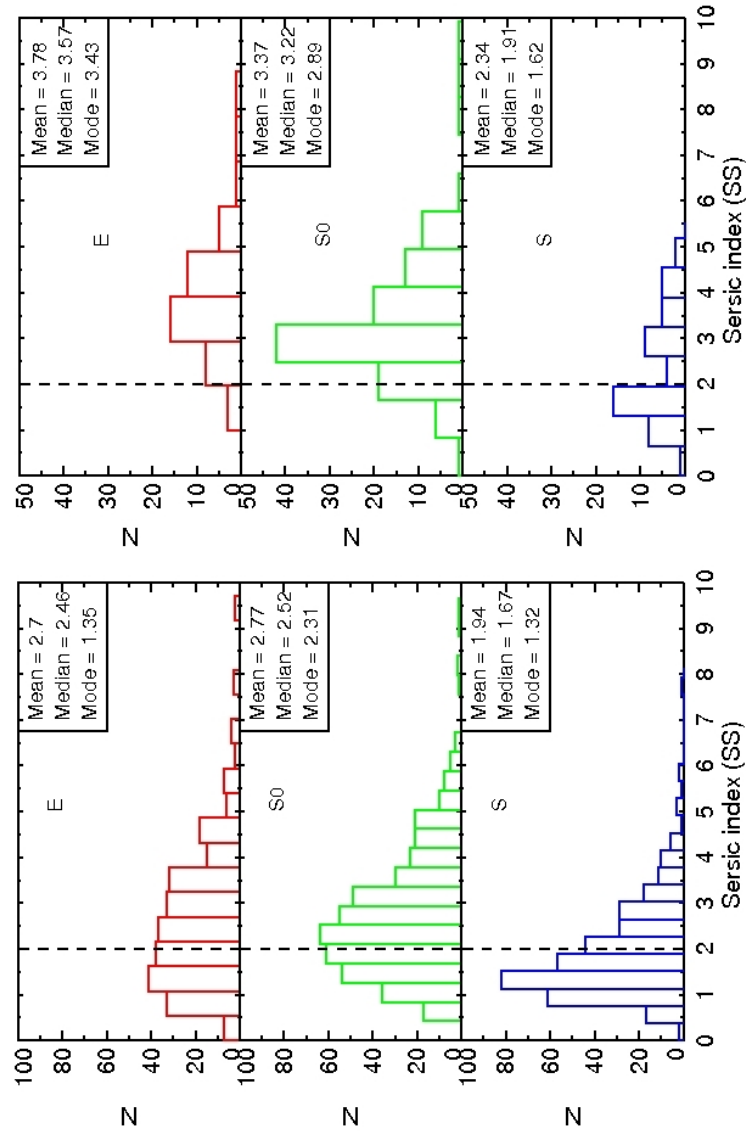
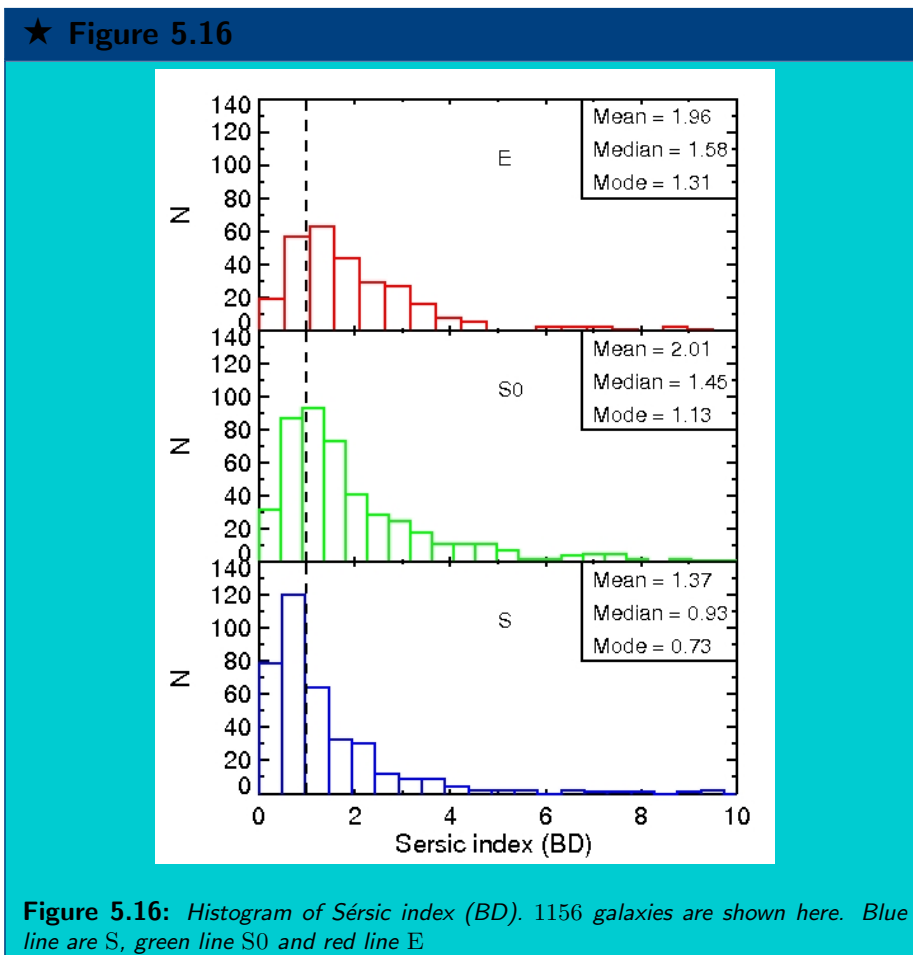


**Figure 5.15:** Left panel: Histogram of  $n$  for SS. Right panel: Same as left panel but for Dressler's galaxies. Red line E, green line S0 and blue line are S

In the Figure 5.15, S galaxies follow a different distribution than those from E and S0. The mean, mode, and median of Sérsic indexes for S0 in the Figure 5.15 are different from S galaxies. In addition, a Kolmogorov-Smirnov test rejects that S and S0 distributions to be the same at the 99% confidence level. Except for some E, in the right panel can be seen that the same distribution is found for Dressler's classification. Hence, this is not an artificial result of our classification.



As can be seen in the left panel of Figure 5.15, E galaxies have some galaxies with low Sérsic index while this is not seen in the distribution of E galaxies classified by Dressler. Those galaxies of the left panel of Figure 5.15 with low Sérsic index are dE found principally in the Coma cluster (A1656). They are not seen by Dressler because his sample is not as deep in magnitude as ours.

The results of the Sérsic distributions for each morphological type are in agreement with the ones found by Fasano et al. (2012), but they use a different scheme for classification. They use 21 parameters directly computed from the galaxy image. Here, as explained in §4.2, it is used 4 parameters.

Sérsic index depends on the stellar distribution of the galaxy. Nevertheless, as we have mentioned, SS models fail to reproduce the structures of S and S0 while, at the same time, it gives a smooth fit for E galaxies. Even though, the SS models represent an “average” of the stellar distribution of the bulge and disk. Hence, one expect that S and S0 have the same structure if S0 are swept S galaxies. As this is not seen in Figure 3.1, it can be concluded that ram pressure is not the main candidate for S0 formation.

The Sérsic distribution for BD models is shown in Figure 5.16. As can be seen, there are still differences in the Sérsic distributions for each morphological type. The mean, mode and median are different for S and S0 galaxies. Again, a Kolmogorov-Smirnov test rejects S0 and S distributions being the same at the 99% confidence level. It can be concluded that S0's bulges are different from S's bulges. Once again, it is unlikely that ram pressure could make those differences on the stellar distribution of bulges.

We set aside to the Sérsic index, and in the left and right panels of Figure 5.17 is shown the distribution of the effective radius for the SS and BD respectively. Those Figures also show that the distributions of effective radius vary for each morphological type. In the right panel, it is appreciated how the bulge's  $R_e$  at the peak of the S distribution is greater than the bulge's  $R_e$  at the peak of the S0. This result is a consequence of the results presented in Figures 5.15 and 5.16 because the  $R_e$  is correlated with  $n$ . A high  $n$  indicates that the surface brightness is concentrated, and; consequently, the effective radius becomes small. Hence, this shows that S0's bulges concentrates are lighter than S bulges.

★ Figure 5.17

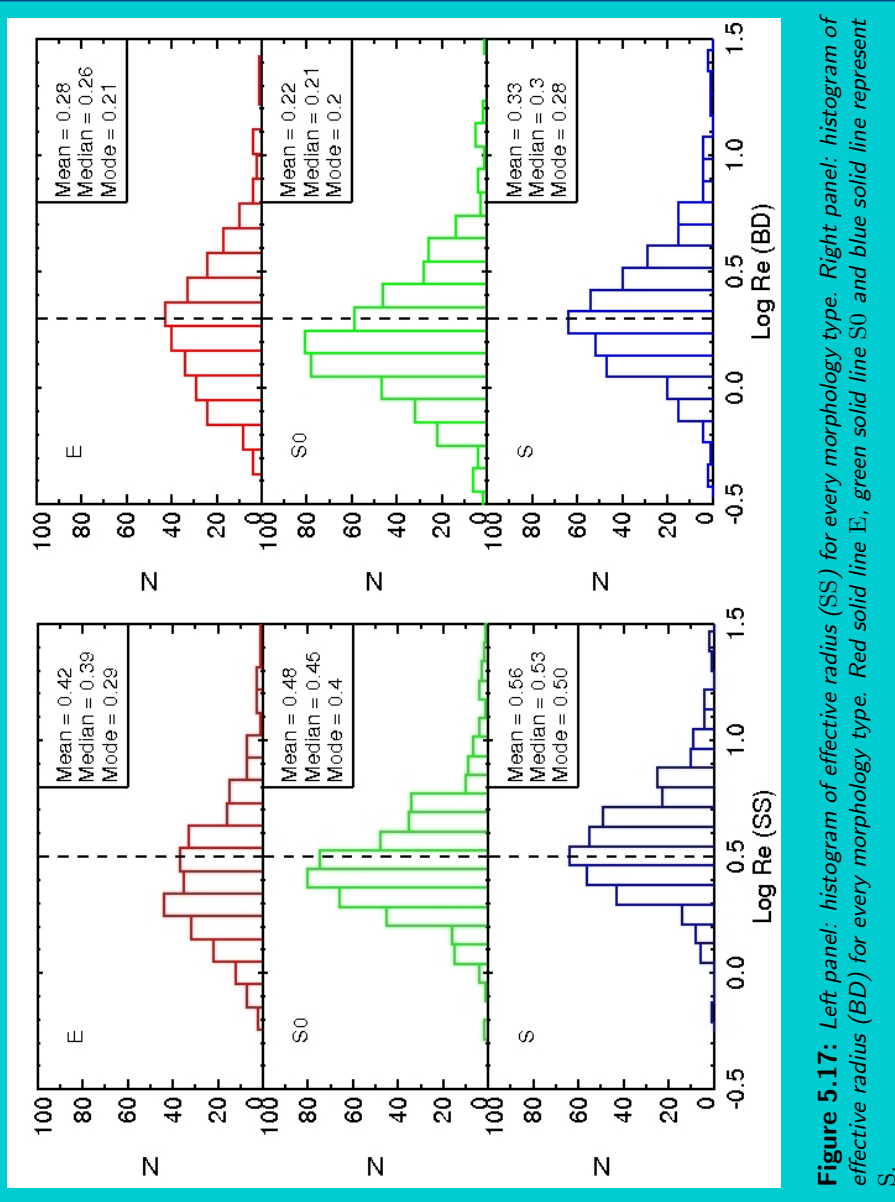


Figure 5.17: Left panel: histogram of effective radius (SS) for every morphology type. Right panel: histogram of effective radius (BD) for every morphology type. Red solid line E, green solid line S0 and blue solid line represent S.

Finally, it is also explored in Figure 5.18 the distribution of the central surface brightness  $\mu_0$ . The left panel of it shows a bimodality with peaks centered at  $19.09 \text{ mag / arcsec}^2$  and  $15.21 \text{ mag / arcsec}^2$ . The right panel of Fig. 5.18 shows the distribution of the central surface brightness  $\mu_0$  separated by morphology. As can be seen, the peak at 19.09 is dominated by late-type galaxies, and the one at 15.21 is dominated by early-type galaxies.

Tully & Verheijen (1997); McDonald et al. (2009) have found a similar bimodality in the near infrared for galactic disks in the Ursa Major and Virgo clusters, respectively. They have also found that one peak is dominated by early-type galaxies while the other one is dominated by late-type galaxies. This shows again that S0 and S galaxies are structurally different.

In Fig. 5.19 is plotted the histograms of  $\mu_0$  of bulges (BD models) for every morphological type. Even with a large dispersion, there are differences among every morphological type. The histograms show an increase in surface brightness for the bulges in the sequence  $S \rightarrow S0 \rightarrow E$ .

As explained above, since ram pressure only affects the gas, it is unable to explain the differences in central surface brightness of bulges of Figures 5.18 and 5.19. The fact that S0 galaxies have a larger  $\mu_0$  than S galaxies indicates that other physical process induced by the environment should accelerate the evolution of bulges. For instance, bulges of S0 could have been accumulated stellar mass either by mergers or tidal interactions.

We believe that this result supports Dressler (1980b) argument about the origins of S0 formed by gravitational interactions instead of ram pressure. Dressler (1980b) arrived at his conclusion by estimation of “sizes” of bulges for S, S0, and E galaxies. We believe that what he was estimating was central surface brightness. Dressler concludes that S0 could not be formed by ram pressure or evaporation because bulges of S0 were “larger” than bulges of S; however, we conclude that S0 bulges are denser than those of S galaxies, see Fig. 5.19.

### Surface Brightness Profiles

In the last Section, we have been shown evidence from our fittings that the distribution of the model parameters is different among morphological types. Here, we put it all together to show differences on the surface brightness profiles among each morphological type. This shows differences of structural properties between S and S0 more noticeable.

★ Figure 5.18

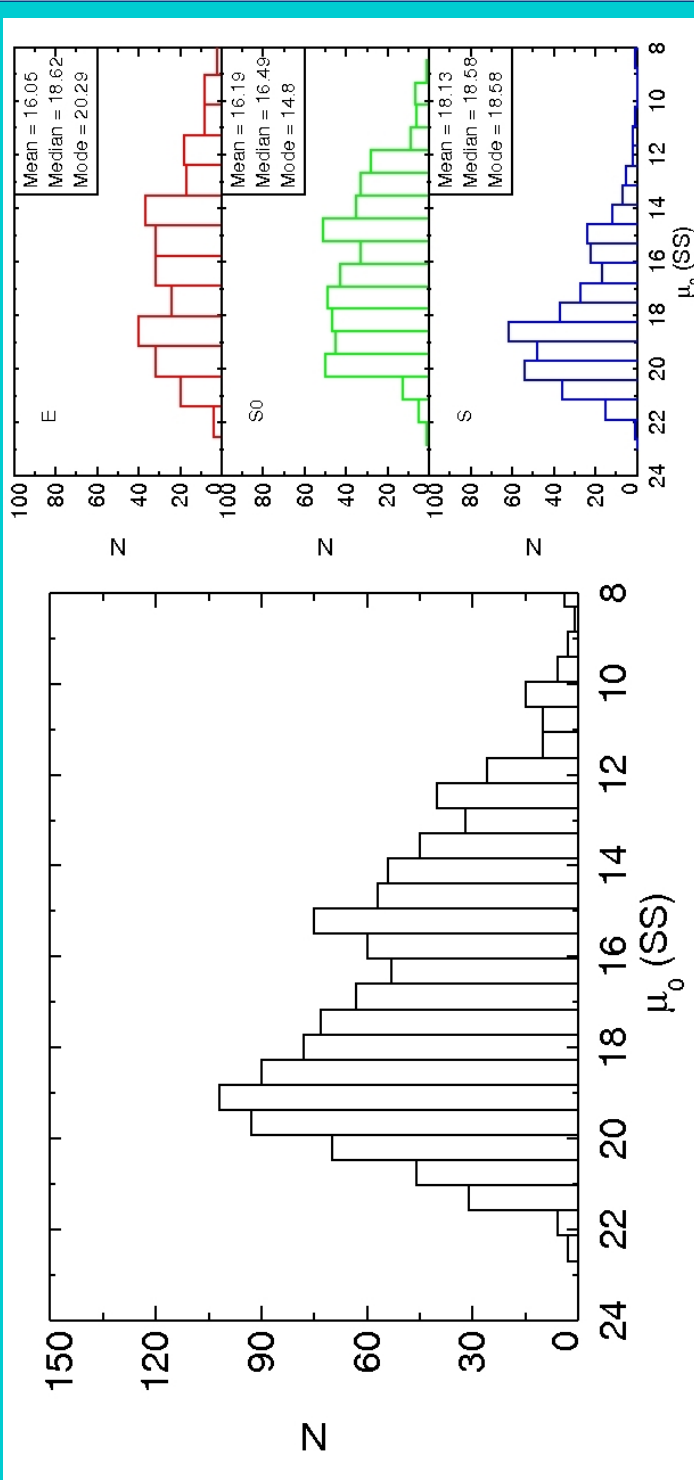


**Figure 5.18:** Left panel: histogram of the central surface brightness  $\mu_0$  (SS). Right panel: histogram of central surface brightness (SS) for every morphology type. Top right panel: histogram of  $\mu_0$  for E galaxies. Middle right panel: histogram of  $\mu_0$  for S0 galaxies. Bottom right panel: histogram of  $\mu_0$  for S galaxies

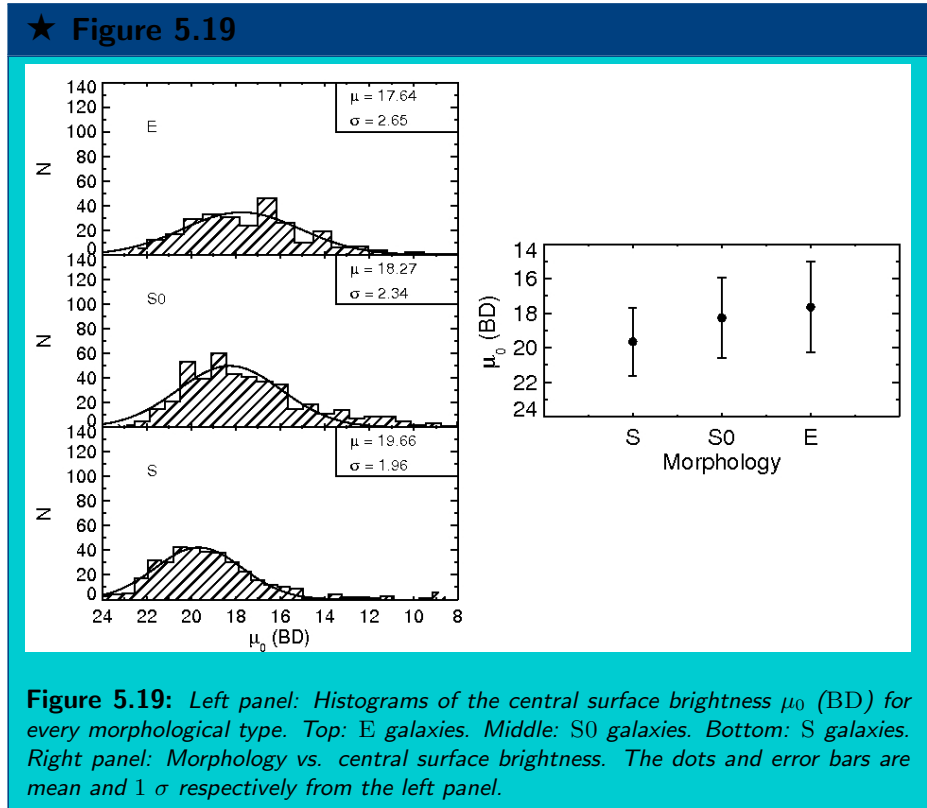
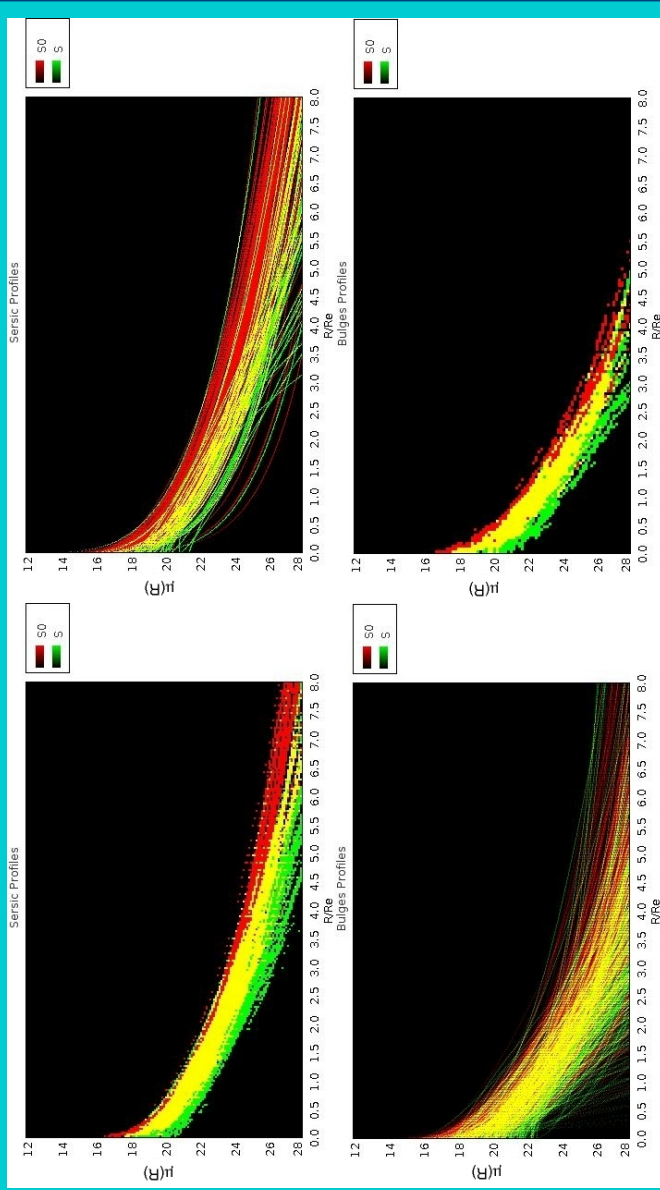


Figure 5.20 shows the surface brightness profiles of S0 and S. The top left panel shows the Sérsic profiles ( $\mu(R)$  vs.  $R/R_e$ ) of the SS models. The top right panel shows the Sérsic profiles of the SS models for the Dressler classified galaxies. The bottom left panel shows the Sérsic profiles of the bulges ( $\mu(R)$  vs.  $R/R_e$  BD models). Finally, the bottom right panel shows the same Sérsic profiles of the bottom left panel, but it highlights the regions where the profile density is high. In all the panels, the  $R_e$  is the effective radius of the galaxy (SS models). Red lines represent profiles of S0 galaxies while green lines represent profiles of S galaxies. Finally, yellow lines represent the regions where the profiles of S0 and S overlap (i.e. red + green = yellow).

★ Figure 5.20

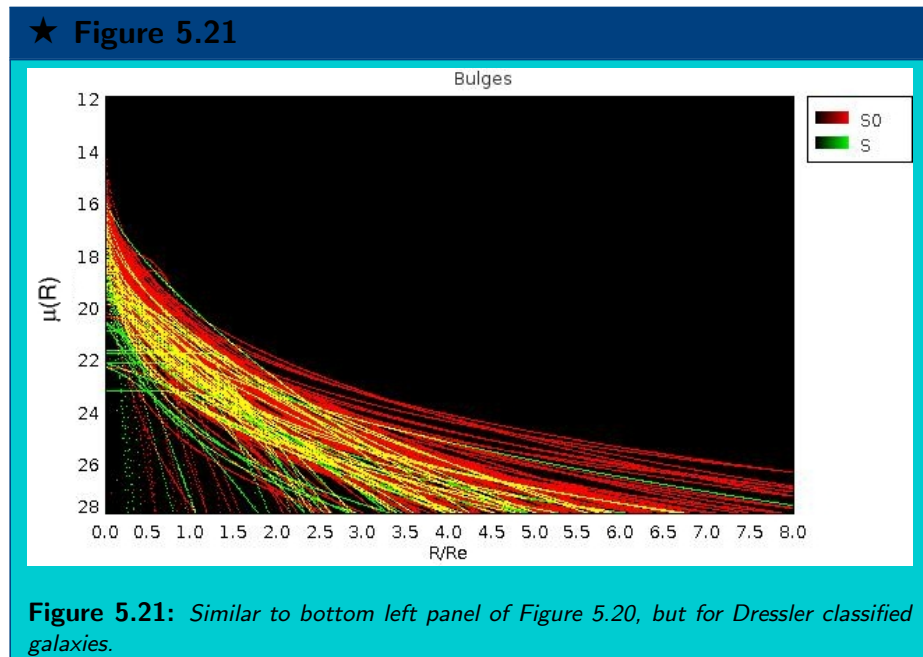


**Figure 5.20:** Top Left panel: Sérsic profiles ( $\mu(R)$  vs.  $R/R_e$ ) for S0 (red lines) and S galaxies (green lines). Here, it is shown those regions where profile density is high. Top right panel: Sérsic profiles ( $\mu(R)$  vs.  $R/R_e$ ) for Dressler's S0 (red lines) and Dressler's S galaxies (green lines). Bottom left panel: Bulges Sérsic profiles ( $\mu(R)$  vs.  $R/R_e$ ) for S0 (red lines) and S galaxies (green lines).  $R_e$  here is the effective radius of the whole galaxy. Bottom right panel: plot similar to bottom left panel, but here it is shown those regions where profile density is high. Yellow lines in all the panels mean overlapped profiles (red + green = yellow).

As can be seen in the top left panel of Figure 5.20, S0 Sérsic profiles are quite different from S galaxies. While some of them are structurally similar (yellow profiles), we clearly notice the green region (S) and red region (S0). Therefore, in average, S0 galaxies are structurally different from S galaxies. This difference with S galaxies is also pronounced for the Dressler classified galaxies (top right panel of Figure 5.20 and Figure 5.21). Those differences are also seen for the bulge profiles of the bottom panels of Figure 5.20. They show that, relative to the galactic luminosity, S0 bulges are larger than S bulges.

As has been pointed out, this may favor bulge enhancement over disk fading as the main process responsible of the galaxy transformation from S to S0. This could explain the differences between S0 and S profiles. This result complements the one found in Figure 5.15: S0 are structurally different from S galaxies.

We might then suggest that if S galaxies transform into S0 the whole structure of the galaxy is modified. A simple minded gas removal by appealing to ram pressure stripping would fail to produce the profile properties depicted in Figure 5.20 and 5.21. This result is in agreement with Dressler (1980b); Christlein & Zabludoff (2004).



## SPH Simulations of Ram Pressure

In this thesis, we briefly explored the effect of ram pressure stripping using smoothed particle hydrodynamics (SPH) simulations (Gingold & Monaghan 1977), hoping to improve the results of Gunn & Gott (1972).

Gas is stripped when the pressure of the ICM is greater than the restoring gravitational force of the disk (Gunn & Gott 1972). Balancing these forces leads to an analytic expression for a radius inside which gas can not be stripped. The shear flows between the remaining disk gas and the wind can develop Kelvin-Helmholtz (KH) instabilities. The growth of KH instabilities may remove additional gas from the galaxy. Some works show that SPH has problems solving these instabilities (e.g. Agertz et al. 2007). Nevertheless, the SPH simulations are only accurate when the total simulation time step is less than the KH growth time.

We examined the impact of ram pressure using computer simulations. The simulations we generated for this study used smoothed particle hydrodynamics (SPH) as implemented in GASOLINE (Wadsley et al. 2004). SPH is a technique to approximate numerical solutions for the equations of fluid dynamics through the use of particles (Gingold & Monaghan 1977; Monaghan 2005; Springel 2010). All the simulations were run on computers that are part of SHARCNET<sup>3</sup> which is located in Canada.

We created a computational wind tunnel to test galaxy stripping as disk galaxies fall into clusters. We have differences in radius in comparison to the analytical formula of Gunn & Gott (1972). This discrepancy is the pressure difference between the gas disk and the wind. The wind pressure modifies the surface density of the gas, which changes the gravitational force restore of the disk. Also, the formula of Gunn & Gott (1972) does not take into account the gravity of the bulge and the dark halo. In the simulations including radiative cooling, the disk gas becomes clumpy. When the gas is compressed, the gas density moves to the peak of the cooling function. Thus, the disk gas cools in a short time and turns the disk clumpy. Kapferer et al. (2009); Roediger (2009) also found this clumpiness in their simulations with SPH.

We have tested how disk gas can be stripped from the galaxy in order to turn a S into S0; however, given the results in this section, we believe that ram pressure has a minor effect in comparison with tidal forces or galaxy interactions.

See Appendix E for more details about those simulations.

---

<sup>3</sup>Shared Hierarchical Academic Research Computing Network webpage: <https://www.sharcnet.ca>

## 5.3 Discussion

### 5.3.1 Structural Properties of Galaxies in Clusters at Low Redshift

Using DGCG code, we have recovered the classical physical relations known for galaxies: the KR, LSR, FJR, and the FP (§5.1). The new parameterization agrees with previous works (Kormendy 1977; Djorgovski & Davis 1987; Nair et al. 2010). Small disagreements are probably due to older techniques (and probably older data) than the ones used in this work. For example, the use of one-dimensional fittings for surface brightness analysis (Jedrzejewski 1987). We argue that our technique is the best for two reasons: 1) it is used a two-dimensional surface brightness models which takes over one-dimensional model fitting (Peng et al. 2002). 2) It has been shown in §3.4.1 that simultaneous fitting gives is a better approach than the masking method for regions of high density of galaxies.

The CMR of Figure 5.6 shows that both S0 and E galaxies fall into the red sequence line, and, consequently, they have an old stellar population. On the other hand, we found 2 types of S galaxies: 1) the ones that populate the “blue cloud”, and 2) the ones that fall also into the red sequence. These last are red because they have stopped their star formation. Red S has also been found by the *Galaxy Zoo* project (Masters et al. 2010), and previously by van den Bergh (1976), and more recently by Valentinuzzi et al. (2011). We believe that our red S are a consequence of the cluster environment because there is a larger population of red S than blue S. This last can be seen in the panel C of Figure 5.6. Ram pressure is probably the responsible for sweeping gas from S disks and, consequently, halting star formation.

It has been confirmed the luminosity vs. Sérsic index trend in Figure 5.14. As explained in §5.2.3, it gives evidence that the Sérsic function 3.1 is a real physical component (Caon et al. 1993; Binggeli & Jerjen 1998; Sandage 2005; Blanton & Moustakas 2009). This trend shows that brighter galaxies have higher Sérsic indexes.

Regardless of the disk size, galaxies and bulges with Sérsic indexes  $\gtrsim 2$  are hosted by red galaxies (see bottom left and bottom right panels of Figure 5.12). This trend is also found in Figure 1 of Blanton & Moustakas (2009). The lack of blue galaxies with  $\gtrsim 2$  in Figure 5.12 indicates that the process to transform a blue galaxy with  $\lesssim 2$  to a red galaxy with  $\gtrsim 2$  is either quick or it halts its star formation first and increase its Sérsic index later. If the latter is the case, S galaxies move in the Y-axis of Figure 5.12 first. Then, they move in X-axis growing their Sérsic index. In other words, before S became galaxies with  $gtrsim2$ , they halt their star formation first, then they changed structurally. Nevertheless, if there is a rapid transformation, then mergers might be increasing the Sérsic index.

The histogram of the distribution of the Sérsic index of Figure 5.11 shows a peak at 1.22 for SS models and another peak at 1.0 for BD models. If physical processes such as mergers are the dominant, then one would expect the peak of the distribution at 4 (Aguilar & White 1986; Nipoti et al. 2006). Because this is not the case and pseudobulges tend to have Sérsic indexes less than 2 (Kormendy & Kennicutt 2004), secular processes are the dominant in clusters at low redshift. This is due to the high galaxy velocities in clusters at low redshift ( $\gtrsim 1000$ ) (Sarazin 1988) that makes mergers unlikely to take place. Although, not exclusively to clusters, this result has also been found by Blanton et al.

(2003); Blanton & Moustakas (2009); Fisher & Drory (2011). This is a consequence that, in a cosmological context, the rate of mergers decreased over time due to the expansion of the Universe (White & Rees 1978). In the future, it will be interesting to reproduce histograms like Fig. 5.11 for high redshift galaxies to see if mergers take over secular processes.

### Pseudobulges

Pseudobulges are different from classic bulges because they were not formed by mergers, but they were formed by secular processes (Kormendy & Kennicutt 2004). As a result, pseudobulges become flatter, have rotational support, and they do not follow the relations given for classical bulges.

As explained in §5.1.2, using the same classification method as Gadotti (2009), We have used the KR to separate pseudobulges from classic bulges.

Since pseudobulges might be rotational supported, it is expected that they have low velocity dispersion, and, therefore, pseudobulges fall below the FJR. On the other hand, due to their high dispersion, classic bulges populate the upper side of FJR. Then, as can be seen, Figure 5.7 shows a division between bulges formed either by mergers or secular process.

Figure 5.9 shows a difference in the FP for classic bulges and pseudobulges. In agreement with Carollo (1999); Kormendy & Kennicutt (2004), the FP of pseudobulges falls below the FP of normal bulges with a different slope. We also found that pseudobulges have a larger dispersion along the fundamental plane of classic bulges. We believe this is due to differences in structure between classic bulges and pseudobulges, and this is reflected in the parameter  $k_S$  of equation 5.11. Furthermore, pseudobulges had a rotational component which provides less velocity dispersion.

Even there is an overlapping, in the top right panel of Figure 5.12 shows two types of bulges with  $n < 2$ : 1) classic bulges which are always red for the whole range of Sérsic index values, and 2) Pseudobulges which populate the blue part of the diagram. As pseudobulges are formed through secular processes with the disk, it is expected that they become blue. On the other hand, classic bulges are red because they were formed by mergers. This division between classic bulges and pseudobulges in Figure 5.12 can only be distinguished if bulges were classified using either KR or other method that does not involve the Sérsic index.

Finally, Figure 5.13 separates classic bulges and pseudobulges on the CMR. In that Figure, we have found two types of pseudobulges: blue cloud pseudobulges and red sequence pseudobulges. These last ones have not been found in the CMR of Gadotti (2009). Thus, we believe that those red sequence pseudobulges belong exclusively to galaxy clusters. They might derive from the combined effects of cluster environment (i.e. ram pressure).

### 5.3.2 Important Physical Processes acting on Cluster Galaxies

In Section 1.5, we have explained the physical processes within clusters which have a direct impact on galaxy properties. All of these are acting simultaneously. The question is which physical processes are responsible for the formation of S0 galaxies. Physical processes such as harassment, tidal effects and galaxy mergers affect the stellar distribution of galaxies. On the other hand, hydrodynamical processes such as ram pressure, starvation, thermal evaporation affect the gas distribution. If the gravitational process controls the DMR, then there must be a difference in stellar structure for different morphological types.

It has been shown through the distribution of Sérsic index (Figs. 5.15 and 5.16), the distribution of  $\mu_0$  (Figs. 5.18 and 5.19), and the Sérsic profiles (Fig. 5.20) that S and S0 galaxies are structurally different. Moreover, bulges of S0 galaxies have higher central surface brightness than S galaxies. Therefore, this supports the idea that S0 galaxies are not swept S galaxies. Rather, bulges and disks of S have to suffer structural transformations. This can be possible only through gravitational processes. Hydrodynamical processes alone can not reproduce this structural transformation.

Gravitational processes such as harassment, galaxy merger, and tidal effects are probably turning S galaxies into S0 (Dubinski 1999). Although, galaxy merging is less likely to succeed because galaxy velocities inside clusters are too high. Nevertheless, this might occur if a group of galaxies falls into clusters (Wilman et al. 2009). This is because there are gravitational interactions among galaxies before they fall into the cluster.

Nevertheless, probably there are some S0 galaxies that formed from S through hydrodynamical processes. This is seen in Fig. 5.20 where there is an overlapping between the surface brightness profiles of S and S0 (yellow profiles in Figure 5.20). Probably, we are facing with two (or more) classes of S0s (see Figure 8 of Sandage (2005)). Another alternative is that those S0 galaxies are a temporary stage before they change structurally. van den Bergh (2009) also found that ram pressure is insufficient to explain the transformation of S to S0. He found no difference between the luminosity distributions of S0 in clusters, groups and the field. This result disagrees with the argument that ram pressure is the channel that lead to the formation of S0 galaxies. This is because massive galaxies should be hardest to strip gas from their deepest potential wells. On the contrary, given the evidence that ram pressure stripping is widespread in the Virgo cluster, Kormendy & Bender (2012) argue that it is not necessary to remove all the gas to stop star formation. Nevertheless, as explained above, our results found that gravitational interactions might be the mechanism responsible for the formation of S0 galaxies. The results found in this thesis about the origin of S0 is in agreement with other works using other approaches to address the DMR (Dressler 1980b; Christlein & Zabludoff 2004; Burstein et al. 2005; Boselli & Gavazzi 2006; van den Bergh 2009; Just et al. 2010).

Even we have promoted tidal effects, mergers, harassment, etc. as the main mechanisms for S to S0 transformation, hydrodynamical processes may still play an important role. For instance, Figure 5.6 shows evidence for red S. In addition, the low Sérsic index region ( $n < 2$ ) of Figure 5.12 is populated by red and blue galaxies. This means star formation is halted before the bulge could change in structure. This suggests ram pressure swept gas out of the galaxy before tidal processes could change the galaxy structure.

### 5.3.3 How are S0 galaxies formed?

In the last Section, we argue that gravitational processes are the ones that control DMR. Here, it is explained the big picture of the S to S0 transformation.

According to the DMR Dressler (1980b); Dressler et al. (1997, See also §1.3), the proportion of E galaxies in clusters remains constant over time. For that reason, E galaxies seems to be the relics of galaxy clusters. These galaxies probably formed before cluster virialization through galaxy mergers. After the cluster virialization, the galaxy velocities within a cluster became high ( $\sim 1000$  km/s), and galaxy mergers were less frequent.

In contrast, S0 galaxies are preferably found in regions of high density while S galaxies are preferably found in less dense regions. Moreover, the proportion of S and S0 galaxies in clusters changes with redshift. Namely, S proportion in clusters is greater at high redshift than at low redshift. On the contrary, S0 proportion in clusters is greater at low redshift than at high redshift. For that reason, it is believed that S galaxies transform into S0 galaxies in clusters.

Dressler (1980b); Dressler et al. (1997) provided evidence that S turn into S0 inside galaxy clusters, but how were they formed? It seems that, before this morphological transformation, S galaxies halt their star formation. This is seen in Figure 5.6 by the presence of red S. As discussed in the last Section, ram pressure played this role here. It acts on S galaxies before they transform into S0 galaxies. Nevertheless, this is happening at the present epoch while at earlier epochs the situation could have been different.

After the star formation is halted, tidal effects, and/or galactic interactions might be responsible for the transformation of S to S0. Those physical processes increased the S Sérsic indexes. For that reason, we believe that high Sérsic index ( $n > 2$ ) galaxies are red. An alternative could be that S0 are formed by unequal mass mergers (Bekki 1998), and the S galaxies “quickly” transform into S0 without exhausting the gas first and grow their bulge later. Nevertheless, because the velocity of cluster galaxies is high, galaxy mergers are rare events. Nevertheless, galaxy mergers might occur if those galaxies are processed within groups before they become part of the cluster (Merritt 1984; Wilman et al. 2009).

**Other proposals for the formation of S0 galaxies:** van den Bergh (2009) points out that gas ejection by active nuclei may produce absence of significant amounts of gas in some field lenticular galaxies. Another proposal is given by Burstein et al. (2005): they suggest E + A galaxies seen at moderate redshift are S0 which went through a temporary stage of star formation. Those proposals may provide alternative interpretations for the formation of S0 galaxies in the field. Furthermore, these scenarios could be explored with the Large Millimeter telescope (GTM/LMT) by tracing CO in cluster galaxies at different redshifts.



# 6 Conclusions and Suggestions for Future Work

---

S0 galaxy formation within clusters involves many physical processes. Identifying the dominant physical process is a difficult task, and probably it varies through time and galaxy environment. An essential step, it is to study the structural properties of clusters galaxies at low redshift as it has been done in this work. In this Chapter, it is summarized the major results of this Thesis. At the end, it is provided the future work where we have identified areas of interesting further research.

## 6.1 Conclusions

In this work, the structural properties of 1453 galaxies of 21 clusters at low redshift  $z < 0.08$  were analyzed. Their structural properties can help us to understand the origin of the density morphology relation (DMR). Next, it is listed the main conclusions of this work.

- (1) We have developed the **Driver for GALFIT** (Peng et al. 2002, 2010) on **Cluster Galaxies** (DGCG §3.3). It is a script based on PERL that allows GALFIT (Peng et al. 2002) to fit surface brightness models to cluster galaxies.
- (2) DGCG (version 1.0) fits Sérsic (SS) or Sérsic + exponential (BD) models to galaxies in regions of high galactic density such as galaxy clusters. DGCG creates initial parameters from SExtractor (Bertin & Arnouts 1996) for GALFIT.
- (3) DGCG algorithm was tested on images with artificial galaxies. One test consisted to run DGCG on a field of de Vaucouleurs components (Sérsic index = 4), and the other one to run it on a field of BD models. BD model parameters are harder to recover than SS (§3.4.2). The SS test results are quantitatively similar to the results found by Häussler et al. (2007) (§3.4.1).
- (4) It has been shown through the fitting of synthetic galaxies that simultaneous fitting is a better technique than masking neighbor galaxies (§3.4.1). Masking method gives poor accuracy to the parameters when the fitted galaxy is in a region of high galactic density. Hence, simultaneous fitting must be used in clusters of galaxies.

In addition, 2-D fitting techniques perform better than 1-D techniques in crowded fields. This is due to the fact that 1-D techniques can not perform simultaneous fitting for galaxies that are blended in the line of sight.

- (5) GALFIT (Peng et al. 2002) magnitudes have been compared with those of PPP (López-Cruz et al. 2004) (§4.1.4). In general, it is found that PPP and GALFIT magnitudes are in reasonable agreement ( $\text{GALFIT mag} - \text{PPP mag} \mu = 0$ ,  $\sigma = 0.0721$ ). Nevertheless, some galaxies have their magnitudes underestimated by PPP. This is because the high galactic density affects the magnitude computation for circular apertures (in this case PPP). On the other hand, DGCG does not have this problem because it uses simultaneous fitting for neighbor galaxies.
- (6) We have introduced a new classification method where the bulge to the total luminosity ratio was combined with bumpiness (BPN), Sérsic index, and axis ratio (§4.2). It has been recovered 77% from the total of E, 64% from the total S0 galaxies and 63% from the total of S when they are compared with Dressler. Given the intrinsic dispersion among classifiers (Lahav et al. 1995; van den Bergh 2012), we believe this is an acceptable rate. The classification of our sample produces 330 E galaxies, 566 S0 galaxies and 557 S galaxies.
- (7) It has been introduced a modified version of the Bayesian Information Criterion (MBIC) §4.3. From a number of fitted models, MBIC selects the best model for a given data without over-fitting. Using MBIC for E galaxies with SNR greater than 10, it was found that 13% of E are better fitted with an SS model, and 87% with a BD model.
- (8) It has been recovered the well-known relations for galaxies such as DMR (Fig. 5.1 §5.1.1), Kormendy relation (KR §5.1.2) and luminosity-size relation (LSR §5.1.3). KR and LSR for this sample are  $\mu_e = (3.93 \pm 0.011) \log R_e + 19.29 \pm 0.003$  (Fig. 5.2) and  $\log(L) = (1.18 \pm 0.001) \log R_e + 9.6 \pm 0.0003$  (Fig. 5.4) respectively. In addition, it has been recovered the LSR relation for disks (Fig. 5.5). It is similar to the ones found by Schade et al. (1996); Courteau et al. (2007); Saintonge & Spekkens (2011).
- (9) Applying the method of Gadotti (2009), KR was used to separate pseudobulges from classic bulges (Fig. 5.3, §5.1.2). Pseudobulges were classified as outliers of the KR. It has been found 65% of galaxies with  $n < 2$  are pseudobulges, and 77% of pseudobulges have  $n < 2$ .
- (10) LSR determined by  $R_{90}$  gives a relation with less dispersion than the one computed with  $R_e$  (Fig. 5.4, §5.1.3). The dispersion is reduced 17%. This is because  $R_e$  is more sensitive to the profile shape than  $R_{90}$ . Moreover, if  $R_e$  is used, galaxies with  $n < 2$  do not follow the LSR relation for SS. Conversely, those galaxies follow the LSR relation using  $R_{90}$ . Hence,  $R_{90}$  gives a better physical measurement for the global LSR relation. This result is in agreement with Nair et al. (2010, 2011).

The LSR relation of bulges shows that pseudobulges follow a parallel LSR relation to classic bulges such that pseudobulges are less luminous than bulges for a given size.

- (11) The tilt in the color magnitude relation (CMR) (Fig. 5.6, §5.1.4) is the same for the CMR of the Coma cluster (López-Cruz 1997; López-Cruz et al. 2004). This is due to the proximity of the cluster.
- (12) S galaxies have a larger dispersion than E and S0 galaxies in the CMR (Fig. 5.6). The peak of E galaxies in the  $B - R$  color has a smaller shift towards red relative to the peak of S0. This small difference between E and S0 peaks is also found in Fasano et al. (2012).
- (13) Some S are found along the red sequence (right panels of Fig. 5.6). We believe that those red S are an intermediate step in the transformation of S to S0.
- (14) We have discovered an alternative way to tell bulges from pseudobulges. They are well separated on the Faber-Jackson relation (FJR, §5.1.5). Pseudobulges fall in the low dispersion region while classic bulges are found in the high dispersion region (see Fig. 5.7). Hence, FJR can be used as a diagnostic diagram to separate bulges formed either by mergers or secular processes.
- (15) It was reproduced the Fundamental Plane for E galaxies and bulges (§5.1.6). Classical bulges and pseudobulges have been separated in it. The Fundamental plane of pseudobulges falls towards low densities of the one of classical bulges. This is in agreement with Carollo (1999); Kormendy & Kennicutt (2004). In addition, pseudobulges have a larger dispersion in the Fundamental plane than classical bulges.
- (16) It has been recovered the relations shown in Gutiérrez et al. (2004); Graham (2011) which they were obtained with 1-D techniques. However, there is a disagreement with the Figure 8 of Gutiérrez et al. (2004), where they found a correlation between  $R_e$  and  $R_s$  (Fig. 5.10). The correlation may be a product of parameter coupling due to the low degrees of freedom in comparison with 2-D techniques.
- (17) The histograms of the distribution of Sérsic index for SS and BD (Fig. 5.11 §5.2.1) show similarity with Blanton et al. (2003); Blanton & Moustakas (2009). They have a peak around 1.3 for galaxies from SDSS with  $z < 0.05$  while our peaks are at 1.22 and 1.0 for SS and BD models respectively. Blanton et al. (2003) did not fit the galaxies with the Sérsic function. Instead, they correlate the  $r_{50}/r_{90}$  ratio with simulated galaxies to estimate the Sérsic index. Hence, our detailed analysis confirmed the works of Blanton et al. (2003); Blanton & Moustakas (2009); Fisher et al. (2010).
- (18) Galaxies with  $n < 2$  are bimodal with respect to color ( $B - R$ ). This bimodal distribution depends on bulge morphology. Namely, pseudobulges populate the blue side while classic bulges populate the red side.  
On the other hand, galaxies with  $n > 2$  are preferentially red (Fig. 5.12, §5.2.2). This suggests the physical process that increases the Sérsic index also halts the star formation.
- (19) It has been discovered two populations of pseudobulges in the CMR: “blue cloud” and red sequence (Fig. 5.13). These last ones are probably a consequence of ram pressure stripping.

- (20) It was recovered the luminosity vs. Sérsic index relation (§5.2.3). It shows that high Sérsic index galaxies are brighter than low Sérsic galaxies. This trend with luminosity shows that Sérsic index is a real physical parameter, and it is a reasonable function to fit surface brightness models. This trend is also shown in other works (Blanton et al. 2003; Sandage 2005; Kormendy et al. 2009; López-Cruz et al. 2011).
- (21) The histogram of the distribution of Sérsic index for S is different from the ones of E and S0 galaxies (Fig. 5.15). This suggests that S galaxies are structurally different from E and S0 galaxies. Hydrodynamical processes are unable to reproduce these differences.
- (22) The distribution of the effective radius for the BD and SS differs for every morphology. The bulge effective radii of S0 galaxies are systematically smaller than the ones of S galaxies (Fig. 5.17).
- (23) It has been found a bimodal distribution of the central surface brightness  $\mu_0$  (Fig. 5.18). The peak centered at 19.09 is populated by late-type galaxies while the other peak centered at 15.21 is populated by early-type galaxies. Probably mergers or tidal interactions produce a brighter  $\mu_0$  for the early-type galaxies.
- (24) It has been found that the mean of the central surface brightness ( $\mu_0$ ) of E's bulges is brighter than the  $\mu_0$  of S0, and the mean of  $\mu_0$  for S0 is brighter than the one of S (Fig. 5.19). We believe this is because gravitational interactions are increasing the  $\mu_0$  of E and S0 galaxies.
- (25) The distribution of Sérsic index (Figures 5.15 and 5.16), central surface brightness (Figures 5.18 and 5.19), and surface brightness profiles (Fig. 5.20) show differences in structure among S, S0 and E galaxies (§5.2.4). It seems S's bulges must be modified in order to become a S0 galaxy.
- (26) It has been briefly explored the effects of ram pressure with SPH simulations. A wind tunnel was used to simulate the effect of the fall of S in clusters. The results of these simulations are in agreement with Gunn & Gott (1972) formula. The remaining disk gas turned clumpy. This gas clumpiness has been observed in other SPH simulations (Kapferer et al. 2009; Roediger 2009).

Physical differences between S and E/S0 rule out ram pressure as the main physical process responsible to convert S to S0 galaxies. If S galaxies are the progenitors of S0s, they have suffer structure and transformations in their bulges and disk components. Physical processes such as cluster/galaxy tidal, merger are candidates for the origin of S0s inside clusters environment. The results found in this Thesis complemented other works with different approaches to identify the origin of S0s (Dressler 1980b; Christlein & Zabludoff 2004; Burstein et al. 2005; Boselli & Gavazzi 2006; van den Bergh 2009; Just et al. 2010).

## 6.2 Future Work

In this Thesis, it has been solved a small piece of the puzzle about the origin of S0 galaxies. More questions are needed to be addressed.

For instance, are cluster tidal interactions more effective than galaxy mergers? Is the pre-processing of galaxies in groups relevant? How many S0 galaxies came from unequal mass mergers? How many S0 galaxies came from red S galaxies? Are there differences between these two groups of S0 galaxies?

In what follows, it is summarized areas of future research for both the modelling and origin of S0:

- (1) N-body simulations of cluster formation with very high resolution will help to study how bulges grow from low to high Sérsic index. This will help to study the differences between cluster tidal and galaxy merger.
- (2) A similar study for high redshift clusters will help to notice the differences in evolution of the structural parameters. For instance, the distribution of the Sérsic index at high redshift will determine which process is the dominant one at that redshift. As galaxy mergers and tidal interactions are dominant at high redshift, the peak of the distribution of the Sérsic index is expected to be close to  $\sim 4$  (Aguilar & White 1986; Nipoti et al. 2006).
- (3) Now that it has been determined if an extra-component (§4.3) could better fit the galaxies, a new version of the code will do this automatically. The new version of DGCG is expected to fit any additional parameter as long as the data requires it. This can be combined to improve DGCG with a semi-montecarlo method and the use of GPUs to speed the process. Extra parameters can be useful if the science question requires it. For instance, high redshift galaxies are irregular; therefore, it will be useful to know how they differ from perfect ellipsoids.
- (4) Finally, even though we have found that ram pressure is not the main process for the formation of S0 galaxies, a more detailed morphological classification is needed to separate Sa, Sb, and Sd. In order to compare structural properties of S0 and Sa and to determine their physical properties.



*No acabarán mis flores,  
no cesarán mis cantos,  
yo cantor los elevo.  
Se difunden, se esparcen  
y aunque parezca que amarillean  
vivirán en el interior de la casa  
del Ave de plumas preciosas.*

- Cantares mexicanos, manuscrito 1628 bis, folio 16 v.,  
Biblioteca Nacional de México.



# The Levenberg Marquardt algorithm

GALFIT is the heart of DGCG, and the Levenberg-Marquardt algorithm (L-M) (Marquardt 1963) is the heart of GALFIT. It uses the L-M program of Press et al. (1992). Therefore the L-M algorithm deserves a brief explanation. For fully details of the algorithm, the reader is referred to Press et al. (1992).

Given a set of a data with its measurements errors, we want to find the *best fit-parameters*  $a_0 \dots a_{M-1}$  for the model  $y(x) = y(x | a_0 \dots a_{M-1})$  which better represent the data.

A method widely used is the maximum likelihood estimator. Which basically is:

$$\text{minimize over } a_0 \dots a_{M-1} : \sum_{i=0}^{N-1} [y_i - y(x_i | a_0 \dots a_{M-1})]^2, \quad (\text{A.1})$$

then, it is to find the particular set of parameters which give the most probable for the data set to be occurred. In other words, it is to find the parameters which make equation A.2 greater.

$$P(\text{data} | \text{model}) = \prod_{i=0}^{N-1} \left( \frac{1}{\sigma_i \sqrt{2\pi}} \right) \exp \left\{ -\frac{1}{2} \left( \frac{y_i - y(x_i)}{\sigma_i} \right)^2 \right\}, \quad (\text{A.2})$$

equation A.2 can be reduced to

$$\chi^2 \equiv \sum_{i=0}^{N-1} \left( \frac{y_i - y(x_i | a_0 \dots a_{M-1})}{\sigma_i} \right)^2 \quad (\text{A.3a})$$

$$\chi^2(\mathbf{a}) = \sum_{i=0}^{N-1} \left( \frac{y_i - y(x_i | \mathbf{a})}{\sigma_i} \right)^2, \quad (\text{A.3b})$$

the task is to find the set of parameter that makes A.3 smaller. To do this, we must proceed in an iterative manner. The L-M find the increments  $\delta \mathbf{a}$  alternating between

$$\delta a_l = \frac{1}{\lambda \alpha_{ll}} \beta_l \quad \text{or} \quad \lambda \alpha_{ll} \delta a_l = \beta_l, \quad (\text{A.4})$$

and

$$\sum_{i=0}^{M-1} \alpha_{ki} \delta a_i = \beta_k, \quad (\text{A.5})$$

where

$$\beta_k \equiv -\frac{1}{2} \frac{\partial \chi^2}{\partial a_k} \quad (\text{A.6a})$$

$$\alpha_{ki} \equiv \frac{1}{2} \frac{\partial^2 \chi^2}{\partial a_k \partial a_i}, \quad (\text{A.6b})$$

and  $\lambda$  is a non-dimensional fudge factor. The L-M uses equation A.5 when is far from the minimum, or equation A.6 when it is close. The algorithm does it through equations:

$$\alpha'_{jj} \equiv \alpha_{jj}(1 + \lambda) \alpha'_{jk} \equiv \alpha_{jk} \quad (j \neq k), \quad (\text{A.7a})$$

and then replacing equations A.5 and A.4 with:

$$\sum_{i=0}^{M-1} \alpha'_{ki} \delta a_i = \beta_k, \quad (\text{A.8})$$

when  $\lambda$  is large the equation A.8 is similar to A.4. On the other hand, if  $\lambda$  approaches to zero, equation A.8 is similar to A.5.

Given an initial parameters  $\mathbf{a}$ , the L-M recipe is as follows:

- Compute  $\chi^2(\mathbf{a})$ .
- Pick a modest value for  $\lambda$ , for instance  $\lambda = 0.001$
- ( $\star$ ) Solve the linear equations A.8 for  $\delta \mathbf{a}$  and evaluate  $\chi^2(\mathbf{a} + \delta \mathbf{a})$ .
- If  $\chi^2(\mathbf{a} + \delta \mathbf{a}) \geq \chi^2(\mathbf{a})$ , increase  $\lambda$  by a factor of 10, and returns to step  $\star$ .
- If  $\chi^2(\mathbf{a} + \delta \mathbf{a}) < \chi^2(\mathbf{a})$ , decrease  $\lambda$  by a factor of 10, update the trial solution  $\mathbf{a} \leftarrow \mathbf{a} + \delta \mathbf{a}$  and go back to  $\star$ .

A condition for stopping is necessary. This can be done when  $\chi^2(\mathbf{a})$  decreases to a negligible amount.

Side effect: The initial parameters  $\mathbf{a}$  should be close to the global minimum; otherwise the algorithm probably would get stuck in a local minimum. Actually, this depends on the fitting problem. If there are more than 1 minimum, the choice of the initial parameters becomes critical.

# *B* The Sérsic Profile: A Mathematical Reference

In this appendix we have collected useful formulas associated to the Sérsic Function. The purpose of this appendix is not to provide the full derivations, but to give a mathematical reference and fix the notation used through out this thesis. Details about the derivations of every equation can be found in Graham & Driver (2005).

The Sérsic profile is expressed as follows:

$$I(R) = I_e \exp \left\{ -k \left[ \left( \frac{R}{R_e} \right)^{1/n} - 1 \right] \right\}, \quad (\text{B.1})$$

where  $I(R)$  is the surface brightness at radius  $R$ ,  $I_e$  is the surface brightness at the effective radius,  $n$  is the Sérsic index,  $R_e$  is the effective radius (defined as the radius where the galaxy concentrates half of the light),  $k$  is a parameter coupled to  $n$  in order to give to  $I_e$  the surface brightness at the effective radius.

The luminosity within radius  $R$  is given by:

$$L(< R) = \int_0^R 2\pi I(R') R' dR' \quad (\text{B.2a})$$

$$L(< R) = I_e R_e^2 2\pi n \frac{e^k}{k^{2n}} \gamma(2n, x), \quad (\text{B.2b})$$

where  $x = k(R/R_e)^{1/n}$ , and  $\gamma$  is the incomplete gamma function.

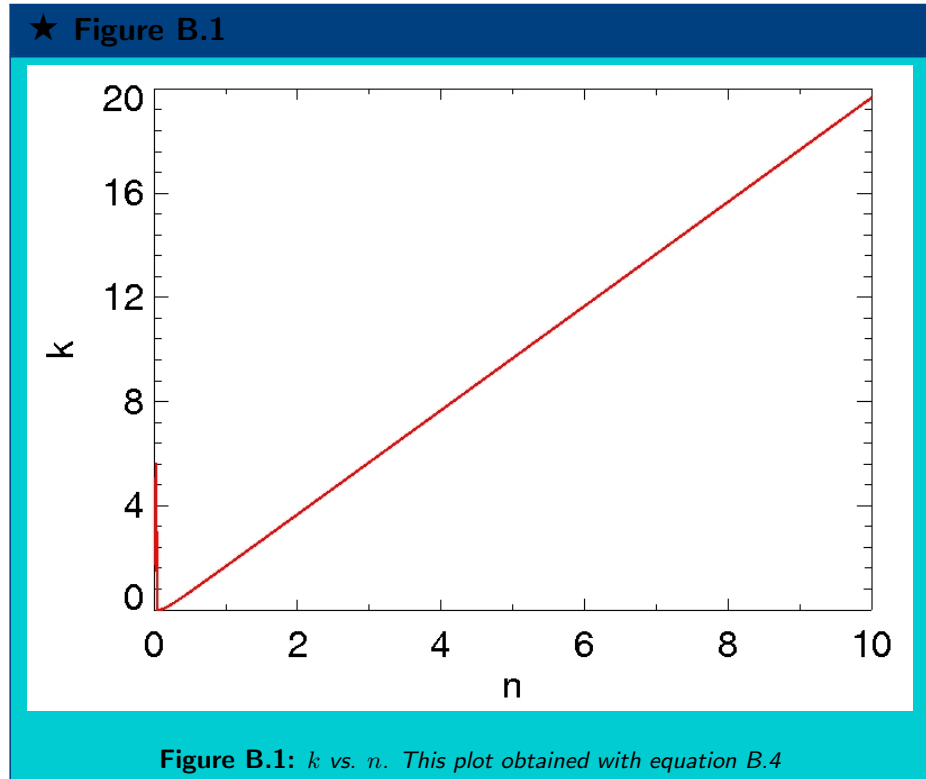
If one wants to compute the total luminosity, the  $\gamma(2n, x)$  term in equation B.2b must be replaced with  $\Gamma(2n)$ :

$$L_{tot} = I_e R_e^2 2\pi n \frac{e^k}{k^{2n}} \Gamma(2n), \quad (\text{B.3})$$

In order to find the relation between  $k$  and  $n$ , the following equation must be solved numerically:

$$\Gamma(2n) = 2\gamma(2n, k), \quad (\text{B.4})$$

where  $\Gamma$  is the gamma function. Figure B.1 shows the plot of  $k$  vs.  $n$ . Not all the range of  $n$  behaves as a straight line. In fact, in Figure B.2 the range  $0.0 < n < 0.1$  is plotted. It shows that a straight line is a poor approximation.



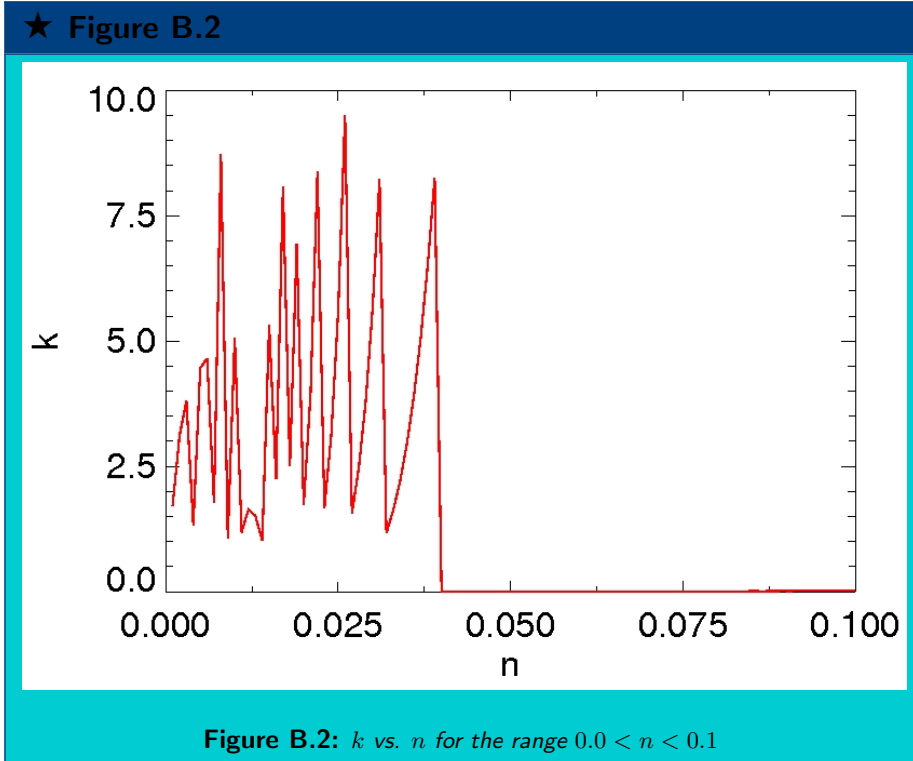
Nevertheless, there are some good approximations for  $n$ :

$$k = 1.9992n - 0.3271 \quad 0.5 < n < 10, \quad (\text{B.5})$$

$$k \approx 2n - 0.331 \quad n \gtrsim 2, \quad (\text{B.6})$$

$$k \approx 2n - \frac{1}{3} + \frac{4}{405n} + \frac{46}{25515n^2} + \frac{131}{1148175n^3} - \frac{2194697}{30690717750n^4}, \quad (\text{B.7})$$

GALFIT uses equation B.6 to compute the value of  $k$  given  $n$ . For  $n < 2$ , it calculates  $k$  interpolating from a Table.



The magnitude within  $R$  is given by:

$$m(< R) = \mu_e - 5 \log R_e - 2.5 \log \left[ 2\pi n \frac{e^k}{k^{2n}} \gamma(2n, x) \right], \quad (\text{B.8})$$

this is the Sérsic function using magnitudes:

$$\mu(R) = \mu_e + \frac{2.5k}{\ln(10)} [(R/R_e)^{1/n} - 1], \quad (\text{B.9})$$

the relation between  $\mu_0$  and  $\mu_e$  is given by:

$$\mu(R = 0) \equiv \mu_0 = \mu_e - 2.5k / \ln(10) \quad (\text{B.10a})$$

$$\mu_0 = \mu_e - 1.822, \quad n = 1 \quad (\text{B.10b})$$

$$\mu_0 = \mu_e - 8.327, \quad n = 4, \quad (\text{B.10c})$$

the relation between the mean surface brightness at effective radius ( $\langle \mu \rangle_e$ ) and surface brightness at effective radius  $\mu_e$  is:

$$\langle \mu \rangle_e = \mu_e - 2.5 \log[f(n)] \quad (\text{B.11a})$$

$$\langle \mu \rangle_e = \mu_e - 0.699, \quad n = 1 \quad (\text{B.11b})$$

$$\langle \mu \rangle_e = \mu_e - 1.393, \quad n = 4, \quad (\text{B.11c})$$

where:

$$f(n) = \frac{ne^k}{k^{2n}} \Gamma(2n), \quad (\text{B.12})$$

the magnitude within effective radius:

$$m(< R_e) = \langle \mu \rangle_e - 2.5 \log(\pi R_e^2), \quad (\text{B.13})$$

now, the relation between total magnitude, mean surface brightness at  $R_e$  and effective radius:

$$m_{tot} = \langle \mu \rangle_e - 2.5 \log(2\pi R_e^2), \quad (\text{B.14})$$

equation B.15 shows another form of the Sérsic function.

$$I(R) = I_0 \exp[-(R/R_s)^{1/n}], \quad (\text{B.15})$$

where  $R_s$  is the scale radius and  $I_0$  is the surface brightness at the galaxy's center.

B.16 shows the relations between parameters of B.15 and B.1.

$$I_0 = I_e e^k \quad (\text{B.16a})$$

$$R_e = k^n R_s \quad (\text{B.16b})$$

$$R_e = 1.678 R_s, \quad n = 1, \quad (\text{B.16c})$$

$$R_e = 3466 R_s, \quad n = 4. \quad (\text{B.16d})$$

The Sérsic function of B.15 is shown in magnitudes:

$$\mu(R) = \mu_0 + \frac{2.5}{\ln(10)} \left( \frac{R}{R_s} \right)^{1/n}, \quad (\text{B.17})$$

the same relation as above, but for exponential:

$$\mu(R) = \mu_0 + 1.086(R/R_s), \quad n = 1, \quad (\text{B.18})$$

the mean surface brightness at radius  $R$  can be calculated from:

$$\langle \mu \rangle_R = \mu_0 - 2.5 \log \left[ \frac{2R_s^2 n}{R^2} \gamma(2n, R) \right], \quad (\text{B.19})$$

total luminosity is given by:

$$L_{tot} = \pi I_0 R_s^2 \Gamma(2n + 1), \quad (\text{B.20})$$

the bulge to disk luminosity ratio is given by:

$$\frac{B}{D} = \frac{n \Gamma(2n) e^k}{k^{2n}} \left( \frac{R_e^2}{R_s^2} \right) \left( \frac{I_e}{I_0} \right), \quad (\text{B.21})$$

the relation between bulge to total luminosity ratio and bulge to disk luminosity ratio is calculated with:

$$\frac{B}{T} = \frac{1}{1 + \frac{1}{B/D}}, \quad (\text{B.22})$$

the Petrosian index at radius  $R$  can be computed with the Sérsic index:

$$2.5 \log[\eta(R)] = \mu(R) - \langle \mu \rangle_R, \quad (\text{B.23})$$

also the Kron radius is computed by:

$$R_1(x, n) = \frac{R_e \gamma(3n, x)}{k^n \gamma(2n, x)}, \quad (\text{B.24})$$

where again  $x = k(R/R_e)^{1/n}$

To compute  $R_{90}$ , which is the radius containing the 90% of total light, one can combine equations B.3 and B.2b to obtain the following equation:

$$\gamma(2n, x) = 0.9, \quad (\text{B.25})$$

which must be solved numerically. Although, equation B.26 shows a good approximation to the relation between  $R_{90}/R_e$  and  $n$ :

$$\frac{R_{90}}{R_e} \approx 1.53 + 0.73n + 0.07n^2, \quad (\text{B.26})$$

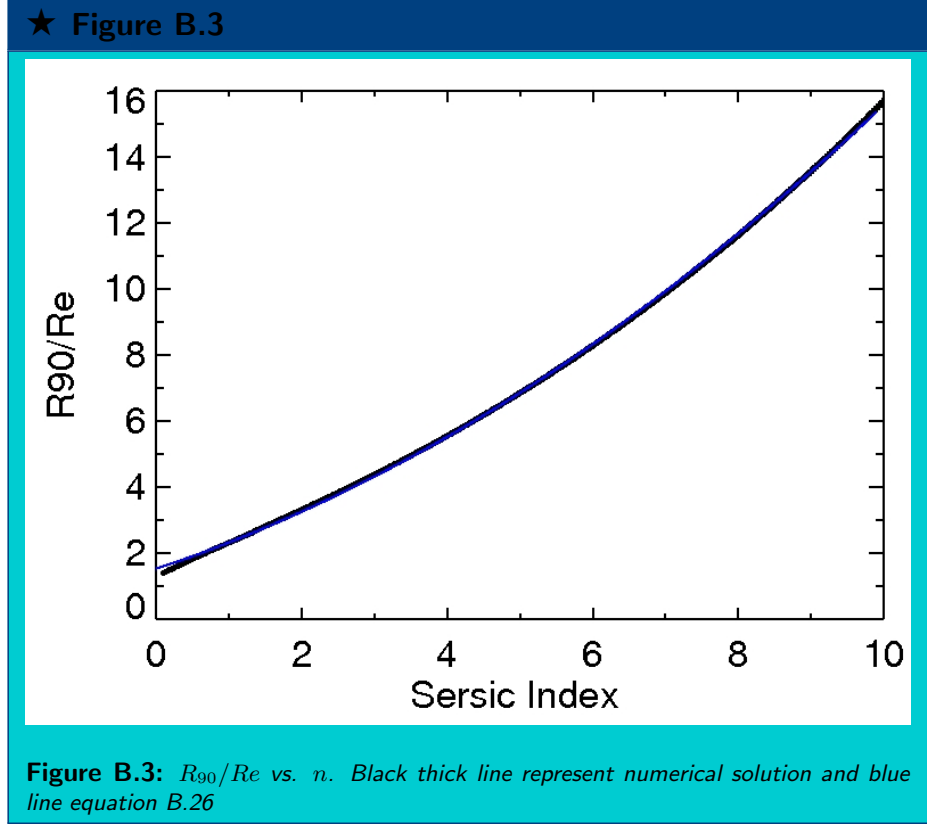


Figure B.3 shows the numerical solution of B.25 (black thick line) and also the equation B.26 (blue line).

If  $R_{90}$  and  $R_e$  are computed with the Petrosian formula, then the Sérsic index can be recovered with equation B.26.

The propagation of errors for every parameter is estimated using equations B.27, B.28, B.29 and B.30

$$\sigma_{R_e} = 1.678\sigma_{R_s}, \quad (\text{B.27})$$

$$\sigma_{B/T}^2 = \sigma_{F_b}^2 \left( \frac{F_d}{(F_b + F_d)^2} \right)^2 + \sigma_{F_d}^2 \left( \frac{F_b}{(F_b + F_d)^2} \right)^2, \quad (\text{B.28})$$

$$\sigma_{\langle \mu \rangle_e}^2 = \sigma_{mag}^2 + \sigma_{R_e}^2 \left[ \frac{5 \log e}{R_e} \right]^2, \quad (\text{B.29})$$

$$\sigma_{\mu_e}^2 = \sigma_{\langle \mu \rangle_e}^2 + \sigma_n^2 \left[ 2.5 \log e \left( \psi_0(2n) + \frac{1}{n} - 2 \ln k \right) \right]^2, \quad (\text{B.30})$$

where  $F_b$  and  $F_d$  are the flux of the bulge and disk respectively, and  $\psi_0$  is the polygamma function.



# Maximum distance allowed for Galaxies to remain in the Sample

In this appendix, we show a completeness analysis of the Sérsic's parameters by diameter selection. Specifically, we compute the maximum distance allowed for Sérsic galaxies to remain in the sample. We show here that the Sérsic index distribution is not biased because of the observations restrictions of LOCOS sample. The following analysis is based on the work of Disney & Phillipps (1983).

The maximum distance  $d$  for a galaxy to include it in the sample is given by the following equation:

$$d = \frac{(0.4 \ln 10)^n}{\sqrt{\pi\Gamma(2n+1)}} \frac{(\mu_{lim} - \mu_o)^n}{\theta_{lim}} 10^{0.2(\mu_o - M + 5)}, \quad (C.1)$$

where  $\mu_{lim}$  and  $\theta_{lim}$  is the surface brightness and radius limits given by the observations respectively.  $M$  is the absolute magnitude,  $\mu_o$  is the central surface brightness and  $n$  is the Sérsic index.

Maximum distance occurs at:

$$\mu_{o,max} = \mu_{lim} - \frac{n}{0.2 \ln 10}, \quad (C.2)$$

which substituting C.2 in C.1 gives the following equation:

$$d = \frac{(0.4 \ln 10)^n}{\sqrt{\pi\Gamma(2n+1)}} \frac{n^n}{(0.2 \ln 10)^n \theta_{lim}} 10^{0.2(\mu_{lim} - \frac{n}{0.2 \ln 10} - M + 5)}, \quad (C.3)$$

for the clusters in this study, we have a  $\theta_{lim} = 0.85$  with a cut off in apparent magnitude of 18. This gives a absolute magnitude of  $M_R = -17$  for the Coma cluster (the nearest cluster in this study) and  $M_R = -19.85$  for A1650 (the farthest cluster in this study). Equation C.3 is plotted in left and right panel of Figure C.1 for Coma and A1650 clusters respectively for a galaxy at the magnitud cut off limit. The green lines in the Figures show the distances to the cluster.

For the range adopted in Sérsic index, the sample is complete for our clusters. In other words, the observations allow to recover cluster galaxies of any value of the Sérsic index.

★ Figure C.1

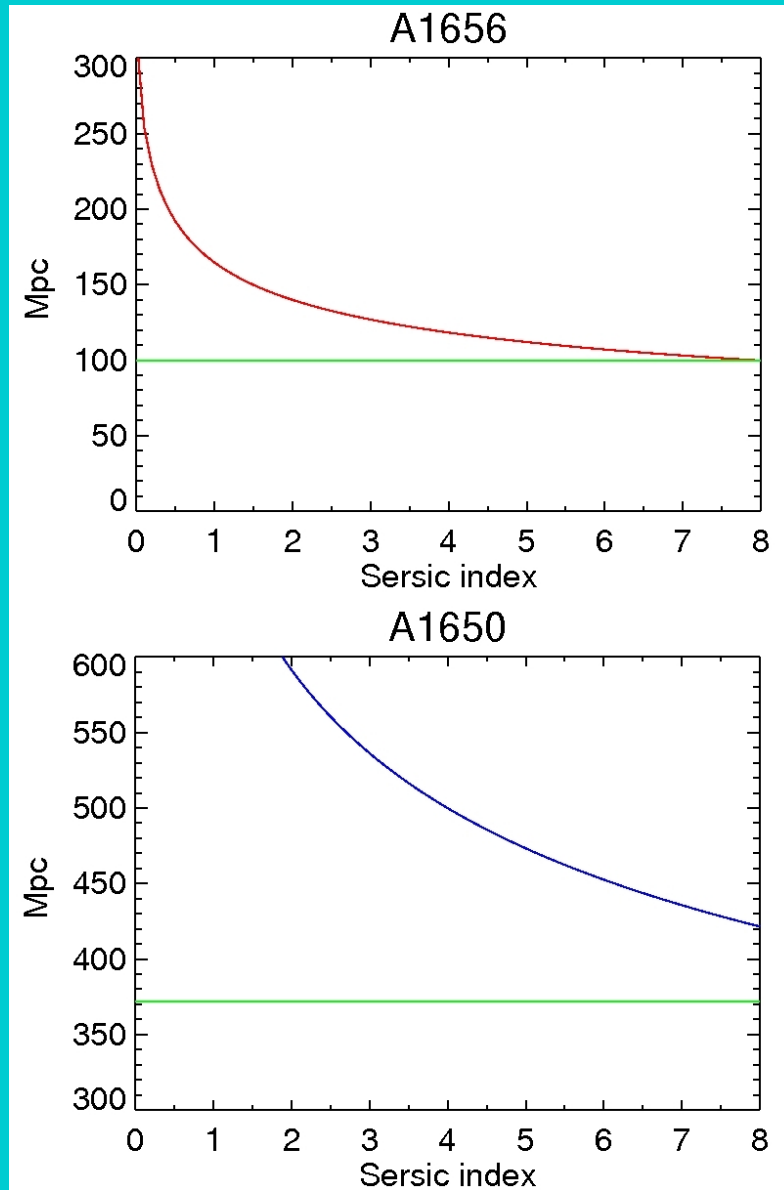


**Figure C.1:** Top panel: Maximum distance vs. Sérsic index given by equation C.3 for the Coma cluster. Parameters for the Coma cluster are:  $\mu_{im} = 21.39$  and  $M = -17$ . Green line indicates the distance to the cluster. Bottom panel: Same as top panel but for cluster A1650. Parameters for this cluster are:  $\mu_{im} = 21.67$  and  $M = -19.85$ . Green line indicates the distance to the cluster.

# *D* How to Use DGCG

In this appendix we provide a brief tutorial on how to use DGCG.

DGCG in a nutshell: It takes the SExtractor output, and formats it for GALFIT. In other words, DGCG is a wrapped script which allows to GALFIT (Peng et al. 2002) to work in an automatic way. DGCG is written in PERL.

GALFIT fits surface brightness models to galaxies. It needs a FITS image and a parameter text file. In order to work properly, masks and PSFs must be provided to GALFIT. DGCG take all what GALFIT needs and run it for all the galaxies in a single image. User interaction is not needed.

Check Peng et al. (2002) and Peng et al. (2010) or the official webpage to know more details about GALFIT.

DGCG makes easier the work on crowded galaxy fields. For example, galaxy clusters.

Input:

- A FITS image of the field that contains the galaxies of interest.
- ASCII configuration file for DGCG.

Below we enumerate the programs that are needed to run DGCG.

- (1) GALFIT. Download and install GALFIT from official webpage at: <http://users.obs.carnegiescience.edu/peng/work/galfit/galfit.html>
- (2) WCSTOOLS. Download and install WCSTOOLS from webpage at: <http://tdc-www.harvard.edu/software/wcstools/>
- (3) Create the following environment variables (or add those to your .bashrc file in your home directory):

```
WCSTOOLS=/Path/To/WCSTOOLS
GALFIT=/Path/To/GALFIT/
```

```
export GALFIT
export WCSTOOLS
```

- (4) SExtractor. Download and install SExtractor. There are several pages where you can download SExtractor just Google at it.
- (5) DGCG package:

```
dgcg.pl
makeseg.pl
splitimage.pl
output.pl
check.pl
ascii2table.py
bdsigmas.txt
```

NOTE: the python script needs the pyfits module in order to work; please install it.

- (6) Some extra-programs you probably need:

```
ds9kron.pl
joinsexcat.pl
makemask.pl
makesatbox.pl
```

The procedure to make DGCG run is shown below. Not all the steps are necessary but recommended.

**PSFs** . Create a list of PSFs for GALFIT. These can be created from the stars of the image. Check how to create PSFs at:

<http://users.obs.carnegiescience.edu/peng/work/galfit/TFAQ.html#psfmake>

PSF files must be named as PSF-X-Y.fits, where "X" and "Y" are the (X,Y) position of the PSF in the image.

As an alternative you can use the program makepsf.pl to create PSF files from SExtractor catalog

**Cosmic rays** (OPTIONAL). It's much better if the cosmic rays are removed from the image.

One way is to use cosmicrays tool in IRAF:

```
cl > noao
```

```
cl > imred
```

```
cl > crutil
```

```
cl > cosmicrays image.fits threshold=5*stdev(sky) fluxratio=5
```

According to “Cleaning Images of Bad Pixels and Cosmic Rays Using IRAF” tutorial, a threshold of 5 times standard deviation of sky value is recommended. fluxratio is the ratio between the neighbor pixels with the main pixel. In interactive mode, a fluxratio vs flux is plotted; pressing “t” the value of fluxratio can be change. cosmic rays in the plot can be deleted with “d”. Bad points are changed to good points with “u”. With “q” it exits and removes the image of cosmic rays.

sky value can be checked with imstat:

```
cl > imstat image[107:175,254:315]
```

obviously in a empty region of the image. Also, you can use imexamine and press “m” in an empty sky region.

**SExtractor** It is recommended to get familiar with SExtractor. See “Source Extractor for Dummies” manual.

Check in the configuration file that the file indicated by the PARAMETERS\_NAME variable must have the following columns in this order:

1	NUMBER	Running object number	
2	ALPHA_J2000	Right ascension of barycenter (J2000)	[deg]
3	DELTA_J2000	Declination of barycenter (J2000)	[deg]
4	X_IMAGE	Object position along x	[pixel]
5	Y_IMAGE	Object position along y	[pixel]
6	MAG_APER	Fixed aperture magnitude vector	[mag]
7	KRON_RADIUS	Kron apertures in units of A or B	
8	FLUX_RADIUS	Fraction-of-light radii	[pixel]
9	ISOAREA_IMAGE	Isophotal area	[pixel**2]
10	A_IMAGE	Profile RMS along major axis	[pixel]
11	ELLIPTICITY	1 - B_IMAGE/A_IMAGE	
12	THETA_IMAGE	Position angle (CCW/x)	[deg]
13	BACKGROUND	Background at centroid position	[count]
14	CLASS_STAR	S/G classifier output	
15	FLAGS	Extraction flags	

Check that the output catalog output must be ASCII or ASCII.HEAD:

```
CATALOG_TYPE ASCII
```

to run SExtractor:

```
sex -c file.sex image.fits
```

NOTE: if you can not find a satisfactory SExtractor configuration for your image, then use 2 catalogs (or more) for your image, and then merge them.

**Merge two SExtractor catalogs** . Join 2 or more SExtractor catalogs (OPTIONAL):

```
./joinsexcat.pl MainCat SecondCat FinalCat
```

This script add all the objects of *MainCat* with those of *SecondCat* which do not overlap with *MainCat*.

**Check the bad regions** . Check all the bad regions, and selected them with in a box region with DS9 (OPTIONAL):

```
usage: ./makesatbox.pl SExtractorCatalog Scale Image OutputFile
```

Scale is the value which the box size are multiplied by  
Box size are determined using the Kron Radius

Output File can be visualized in DS9 as a region

DGCG can do this automatically, if user want to

**Visualize the final catalog** Visualize the catalog in the image (OPTIONAL):

```
usage: ./ds9kron.pl SexCatFile FileOut BadRegion Scale Offset
```

BadRegion are the one determined by makesatbox.pl.  
Scale is the value which the Kron ellipse is scaled + offset value

**Merge catalog with PPP** If you had used Picture Processing Program (PPP, Yee 1991) combine this catalog with the one given by SExtractor:

```
./joinppp.pl FILE_PPP FILE_SEX FILEOUT
```

joinppp.pl remove the magnitude and star classification column of SExtractor with the ones in PPP catalog

**Visualize Mask** If you want to visualize the mask image before to run DGCG (OPTIONAL):

usage: ./makemask.pl Image MaskOut SexCat Scale Offset BadBox

DGCG creates a mask before fitting or it can be provided with a mask created with this program.

**Configuration DGCG file** Fill the configuration file for DGCG:

```

Img           = A85.fits # The input image to be fitted
SexCat        = hot.cat  # The input sextractor catalog
SigImg        = none     # The sigma image to use
PsfDir        = psfs     # PSF location (directory)
MagZpt        = 21.630   # Photometric zeropoint
PlateScale    = 0.68     # Plate scale
FitFunc       = BD       # Fit a sersic or BD?
GalClas       = 0.0,0.6 # Range: 0.0 (galaxy) to 1.0 (star)
ConvBox       = 60       # Size of convolution box (pixels)
FitBox        = 6        # Fitting box size.
MagDiff       = 5        # mask if object is x mag fainter
KronScale     = 1.5      # Scale Factor for obj ellipses
SkyScale      = 1.5      # Scale Factor for sky ellipses
Offset        = 20       # Additional offset to scale factor
SkyAnnuli     = 20       # Width of sky annuli
NSer          = 1.5      # Initial parameter for Sersic index
MaxFit        = 10       # Max number of objects for fitting.
MagRange      = 0.0, 19  # magnitude range (MagMin,MagMax)
FlagSex       = 4        # Maximum value of SExtractor flag
ConsFile      = constr   # Parameter constraint file
Region        = 0        # (0) Whole image or (1) region
Boundary      = 0,0,0,0 # Boundary of the region if Region=1
Split         = 5        # Split image into how many parts?
AutoSatRegion = 1        # Automatic comp. of sat. regions
SatRegionScale = 2       # Scale Factor if AutoSatRegion = 1
Ds9SatReg     = bad.reg  # User input ds9 saturation region
FileOut       = a85fits  # Preposition name for output
SexSort       = sort.cat # Output filename of sorted sex cat.
Erase         = 0        # Erase unnecessary files? 1 = yes
Nice          = 0        # Use the "nice" command for GALFIT
Overwrite     = 0        # Overwrite segmentation files?

```

**Constraint File** This is a file which indicates to GALFIT which parameters are restricted.

The following is the example EXAMPLE.CONSTRAINTS which came with the source code of GALFIT

# Component/ # operation	parameter (see below)	constraint range	Comment
3_2_1_9	x	offset	# Hard constraint: Constrains the # x parameter for components 3, 2, # 1, and 9 to have RELATIVE positions # defined by the initial parameter file.
1_5_3_2	re	ratio	# Hard constraint: similar to above # except constrain the Re parameters # by their ratio, as defined by the # initial parameter file.
3	n	0.7 to 5	# Soft constraint: Constrains the # sersic index n to within values # from 0.7 to 5.
2	x	-1 0.5	# Soft constraint: Constrains # x-position of component # 2 to within +0.5 and -1 of the # >>INPUT<< value.
3-7	mag	-0.5 3	# Soft constraint: The magnitude # of component 7 is constrained to # be WITHIN a range -0.5 mag brighter # than component 3, 3 magnitudes # fainter.
3/5	re	1 3	# Soft constraint: Couples components # 3 and 5 Re or Rs ratio to be greater # than 1, but less than 3.

**Run** Run DGCG:

only the dgcg.pl and configuration file is needed

```
./dgcg.pl file.param
```

If you want an output file, and the program run on the background:

```
./dgcg.pl file.conf >& out &
```

the first & indicates that any error will be written in the output.

**Create Outputs** In addition the outputs files of DGCG can be created from fit.log if GALFIT run all the galaxies. Useful if DGCG fails to create the final outputs.

```
usage: makeout.pl ParamFile > ./makeout.pl dgcg.param
```

Sample image and sample input file accompanies the DGCG code.



# *B* *Hydrodynamical Simulations of Ram Pressure Stripping*

During the course of this work, I explored RAM pressure stripping using smoothed particle hydrodynamics (SPH) simulations (Gingold & Monaghan 1977). I collaborated with Dr. James Wadsley from the department of physics and astronomy of McMaster University in Canada. We used GASOLINE code (Wadsley et al. 2004). Here, I report the results from my research visit to McMaster University (Beca Mixta, CONACYT)

## **E.1 Introduction**

I am reporting on a project in which I attempted to simulate the formation S0 (or lenticular) galaxies in collaboration with Dr. James Wadsley. We started working on the project in September 2007 upon my arrival at McMaster University, and it continues through after my departure on September 2008. Below I describe the activities undertaken during this research visit.

In the Hubble's classification scheme (Hubble 1926), S0 galaxies are the connection between E and S. S0 galaxies contain a stellar bulges and a stellar disks, but are usually devoid of gas. A common interpretation is that S0 were S from which the gas was stripped. Since S0 galaxies are typically found in dense environments, it is likely that S0 galaxies evolve from S galaxies through their interaction with the intracluster medium (ICM).

Gas is stripped when the pressure of the ICM is greater than the gravitational restoring force of the disk (Gunn & Gott 1972). Balancing these forces leads to an analytic expression for a radius inside which gas cannot be stripped. The shear flows between the remaining disk gas and the wind can develop Kelvin-Helmholtz (KH) instabilities. The growth of KH instabilities may remove additional gas from the galaxy. Some recent works show that SPH has difficulties resolving these instabilities (e.g. Agertz et al. 2007). Nevertheless, the SPH simulations are only accurate when the total simulation time step is less than the KH growth time.

We examined the impact of RAM pressure using computer simulations. The simulations we run for this study use smoothed particle hydrodynamics (SPH) as implemented in GASOLINE (Wadsley et al. 2004). All of the simulations were run on computers that are part of SHARCNET (Shared Hierarchical Academic Research Computing Network),

which combines the computing resources of 11 universities and colleges across Ontario, Canada using a high speed network. The workhorse for this project was called “requin” a capability cluster with 1536 processors located at McMaster University.

Ideally, we would simulate an entire cluster of galaxies to study how the gas of spiral galaxies is removed. Currently, it is computationally unfeasible to resolve the details of gas removal from an individual galaxy in an object as large as galaxy clusters. Therefore, we devised a wind tunnel test, that is a restricted simulation where the particles are injected at one end, and the galaxy remains static.

## E.2 Description of the Code

GASOLINE is a tree code for doing parallel hydrodynamics simulations with the SPH method. It was developed by James Wadsley. GASOLINE evolved from the PKDGRAV parallel N-body tree code developed by Stadel (2001). The difference between the two codes is that gas dynamics is included in GASOLINE.

The code uses a similar technique to the K-D binary tree<sup>1</sup> (Bentley 1975) to calculate gravity, parallelize work and search. GASOLINE computes gravity using the tree walking procedure of the Barnes & Hut (1986).

Gas dynamics in GASOLINE is computed with SPH (Gingold & Monaghan 1977). The SPH technique can be compared with the interpolation method where the particles are interpolation points. The particles represent fluid quantities and follow naturally the dynamics of gas. By its particle nature, SPH is easy to combine with N-body codes.

SPH approximates the continuum with a kernel function. The computation of the physical quantities at every particle is done with a sum over their neighbor particles using the kernel function. This kernel approximates a local integral.

For the cooling the range of cases include isothermal, adiabatic and implicit energy integration. Hydrogen and Helium cooling process is included. Feedback from star formation, and uniform UV background are incorporated as well.

Finally, GASOLINE use the Kick-Drift-Kick time-step technique (Quinn et al. 1997) to update the position, velocity, energy of a particle over time. The reader is referred to Stadel (2001); Wadsley et al. (2004) for more details of the code, and to Monaghan (2005); Springel (2010) for a review of the SPH technique.

## E.3 Simulations

In order to simulate the motion of the galaxy as it falls into the cluster, the gas particles are given an initial velocity. We then place a spiral galaxy, similar to the Milky Way, in the wind tunnel.

There were several design criteria for the wind tunnel. First, the mass of particles in the wind need to be comparable to the mass of particles in the gas disk. Second, the wind

---

<sup>1</sup>PKDGRAV got its name from the K-D tree.

tunnel must be long enough so that gas stripped from the galaxy does not wrap back on itself.

For our simulations, the wind tunnel consists of 1445368 gas particles distributed through a computational volume  $200 \times 200 \times 400$  kpc . The gas in the wind has properties for typical for the ICM, a density of  $1 \times 10^{-28} \text{ g/cm}^3$  and a temperature of  $3.5 \times 10^7$  K. The velocity of the ICM has a constant value of 1000 km/s. The positions of the ICM particles were randomly distributed. The dark matter halo was modeled with a NFW profile (Navarro et al. 1996), The stellar disk with a exponential surface density and the bulge with a Hernquist profile (Hernquist 1993).

The galaxy contains 33333, 100000, 100000, 100000 in the bulge, disk star, disk gas and dark matter halo respectively. The particle mass are 2959.14, 29573,  $2.29 \times 10^6 M_{\odot}$  for the gas in the disk, star and halo respectively. The ICM is given a total mass  $2784 M_{\odot}$  for the ICM. The temperature of the gas in the disk is  $10^4$  K.

Our initial computational wind tunnel has periodic boundary conditions. This means that any particle going out of one side of volume enters on the opposite side.

The wind tunnel has to be wider than the disk size. Otherwise, the galaxy “see” itself at the edge of the volume box. This will bring unwanted numerical results.

In order to minimize the number of particles in the wind, we used massive gas particles for the regions where there is no interaction between the gas disk and the ICM, beyond 35 kpc from the center of the tube. Otherwise, if we keep the same mass resolution in all the tube, we need to use around 8 million particles, which is computationally expensive. Using the massive particles we only required  $\sim 1$  million particles. Figure E.1 shows the initial setup of this configuration. Notice there are fewer particles outside the disk. The wind remains at constant density because the particles are more massive.

Before any galaxy was placed in the tunnel, the gas box was evolved in isolation for 2 Gyr in order to establish pressure equilibrium. At this point, the galaxy was placed in the tunnel. The tunnel required a couple of modifications. The temperature of wind gas particles which were close to the galaxy were reduced. Otherwise at the beginning of the simulation, these particles will have artificially high pressure due to their proximity to the high density disk particles. SPH smooth density and as a result the pressure wind gas particles is overestimated. The velocity of the wind was increased to 1000 km/s to simulate the galaxy falling into the ICM .

★ Figure E.1

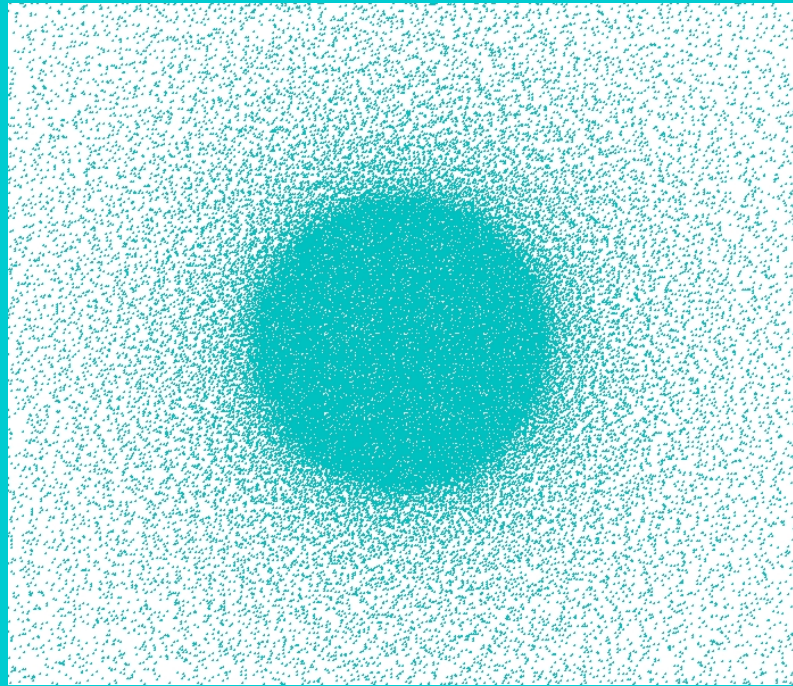


**Figure E.1:** Setup for the wind tunnel. Beyond radius 35 kpc, the mass of the particles starts to grow. This configuration keeps the same density in the entire box.

## E.4 Results

Table E.1 summarize the details of the simulations. We run 2 types of simulations. For the galaxy, the scale radius is 2.48 kpc. The computed Gunn & Gott (1972) radius is 2.83 kpc. The initial mass disk is  $2.95913 \times 10^8$  sun mass. The disk gas particles have a temperature of  $3.5 \times 10^7$  K.

Run	Physics	Final Mass disk (1 Gyr)	Final radius
WTAD	Adiabatic	$1.15436 \times 10^{07}$ sun mass	3.78 kpc
WTCC	Radiative Cooling	$4.61713 \times 10^{07}$ sun mass	1.4 kpc

**Table E.1:** Physics and results of the simulations.

For the simulation including radiative cooling, we got a radius smaller than the computed by Gunn & Gott (1972). This is due to the pressure difference between the wind and the disk gas, which changes the surface density of the galaxy. This changes the gravitational

potential of the gas disk, and as a result it changes the value of Gunn & Gott (1972) formula. On the other hand, for the adiabatic simulations we got a radius bigger than the Gunn & Gott (1972) radius, this is due to the expansion of the gas after it is compressed by the pressure difference.

In all of our simulations gas was removed from the galaxy to the values given in Table E.1. Figure E.2 shows the output for the simulation with radiative cooling after 1 Gyr. In addition, we have discovered that the disk gas is converted into clumps with the simulation including radiative cooling. This is a consequence of the difference in pressure between the ICM and the disk gas as can be seen in Figure E.3. The remaining disk gas turns clumpy. The pressure difference compresses the gas disk, and gas density is moved to the peak of the cooling function. The gas cools in a relative short period of time, thus the gas turns clumpy. Other works with SPH including radiative cooling also found that part of the gas form dense knots (Kapferer et al. 2009; Roediger 2009).

★ Figure E.2

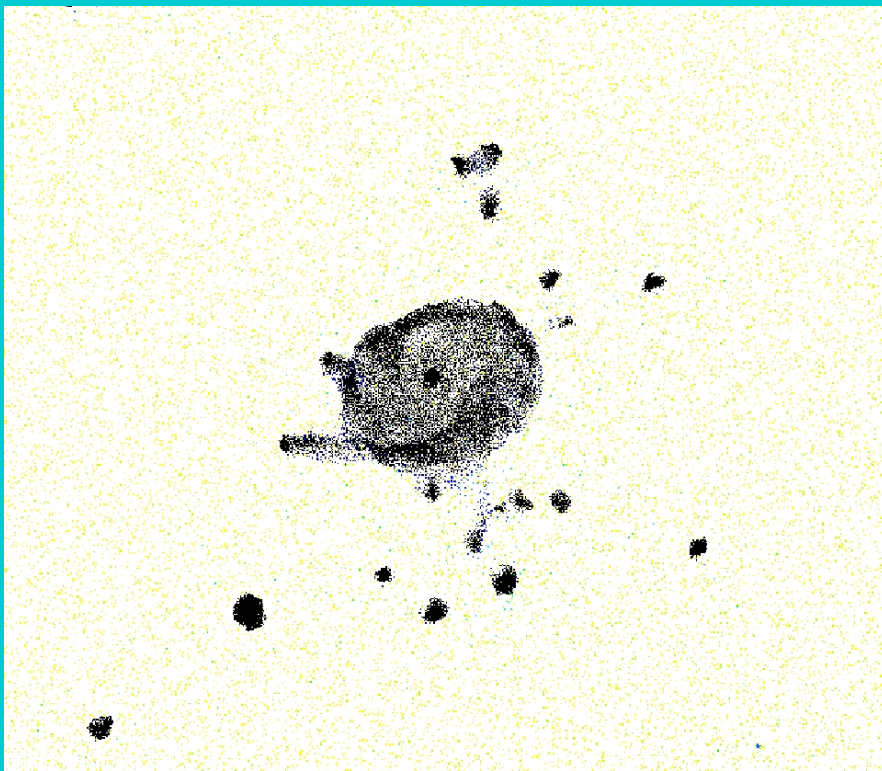
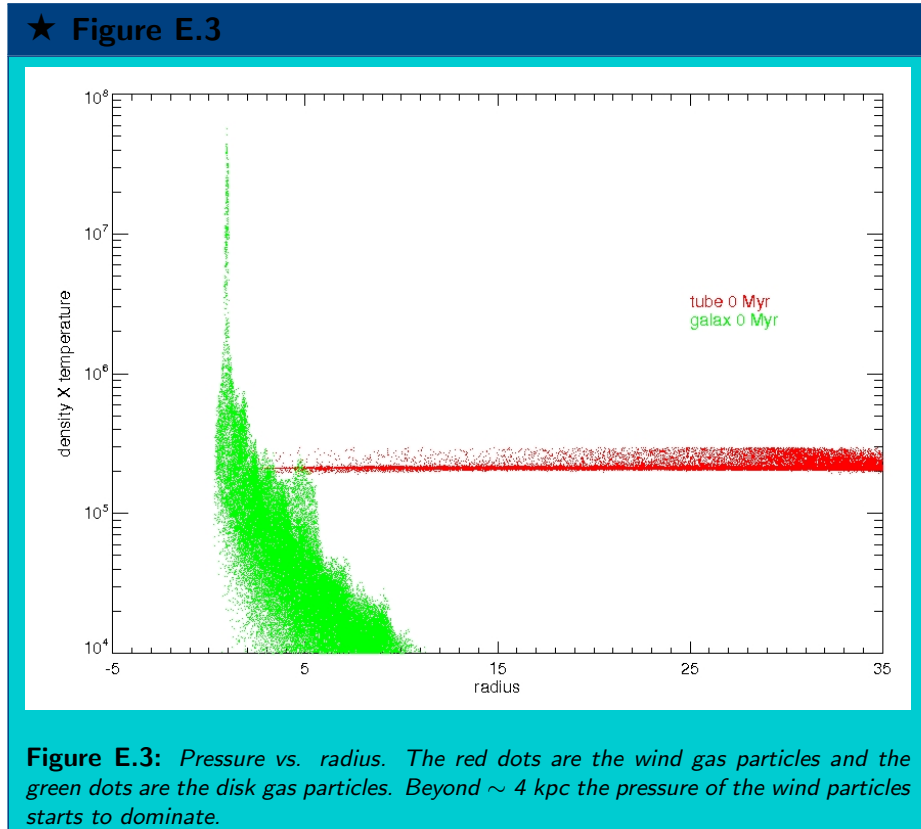


**Figure E.2:** Simulation output of wtcc after 1 Gyr. The image shows the resulting clumpiness of the disk gas.

The gas is stripped and clumped in a short period of time during the simulation ( $\sim 100$



Myr). The galaxy only travels 100 kpc during this time. Observations show that galaxies travel 5 Mpc before they are entirely stripped of gas.

## E.5 Future work

As galaxies fall into galaxy clusters the ICM wind changes. The galaxy accelerates and travels into high density regions of the ICM.

One refinement we made recently was to allow the velocity of the wind to vary to mimic the acceleration of a galaxy as it falls into a cluster. One side of the wind tunnel is no longer periodic, but introduces slabs of particles with properties appropriate for the ICM. At the other edge, the particles are deleted.

During the simulation, the distribution and physical properties of the new slab of gas particles are given according to the position of the galaxy in the cluster. In order to get such properties, we solve the equation for a NFW profile for a cluster mass of  $10^{14}$  sun mass. Thereafter, we plot the radius vs time and we fit a polynomial for it. We use this

to assign velocities to the gas particles. We used a power-law to get a distribution of the density in every time step of the simulation.

At the moment, The velocity of the new slab of gas particles change, resulting in an undesirable change in the gas velocity. introducing particles in a glass distribution rather than a grid will halt the creation of spurious velocities.

We want to add star formation to the simulations in order to know the new stellar distribution. Also, we continue to search for a better treatment of the Kelvin- Helmholtz instability in SPH.

## **E.6 Conclusions**

We generated a computational wind tunnel to test galaxy stripping as disk galaxies fall into clusters. We have differences in radius in comparison to the analytical formula of Gunn & Gott (1972). The reason for this discrepancy is the pressure difference between the gas disk and the wind. The wind pressure modifies the surface density of the gas, which changes the gravitational force restore of the disk. Also the formula of Gunn & Gott (1972) does not take into account the gravity of the bulge and the dark halo. For the simulations including radiative cooling the disk gas becomes clumpy. When the gas is compressed, the gas density moves to the peak of the cooling function. Thus, the disk gas cools in a short period of time, and turns the disk clumpy. Our results are in broad agreement with more detailed simulations for example Kapferer et al. (2009); Roediger (2009).



# *F* DGCG *Main Code*

DGCG has 8500 lines of code. The main part of the code is shown in the following pages:

```
#!/usr/bin/perl
use Math::Trig;
use File::Copy;

require "check.pl";
require "splitimage.pl";
require "makeseg.pl";
require "output.pl";

#           DGCG           #
#           #           #
#   Driver for GALFIT on Cluster Galaxies   #
#           #           #
#   DGCG is a wrapper script for GALFIT     #
#           #           #
#           #           #
# written by Christopher Anorve (Version 1.0) #
#           #           #

$Version="5/Jul/2011";

$paramflag=1;

$StartRun = time();

$ParamFile = @ARGV[0] or ($paramflag =0);
```

```
if($paramflag == 1)
{
    print "DGCG Version: $Version \n";
}
else
{
    print "DGCG Version: $Version \n";
    die "usage: $0 FILE \n";
}

CheckEnviVar();                # check for environment variables

Default();                      # initialize default values

ReadFile($ParamFile);          # Read parameters file

($NCol,$NRow)= GetAxis($Img);
($ExpTime)   = GetExpTime($Img);
($Gain)= GetGain($Img);
($Rdnoise)= GetRdnoise($Img);

## sorting catalog

$Total = CatArSort($SexCat,$SexArSort,$KronScale,$SkyScale,
$Offset,$SkyAnnuli,$NCol,$NRow);

$Total = CatSort($SexCat,$SexSort,$KronScale,$SkyScale,
$Offset,$SkyAnnuli,$NCol,$NRow);

#### segmentation mask

if( !(-e $SegFile) )
{
    MakeImage($SegFile,$NCol,$NRow,16);

    if ($AutoSatRegion == 1)
    {
MakeSatBox($SexCat,$SatRegionScale,$NCol,$NRow,$Ds9SatReg);
    }

    MakeMask($SegFile,$SexArSort,$KronScale,$Ds9SatReg);
}
```

```
SatMask($SegFile,$Ds9SatReg,$Total+1,$NCol,$NRow);

}
elseif( $Overwrite == 1 )
{
    MakeImage($SegFile,$NCol,$NRow,16);

    if ($AutoSatRegion == 1)
    {
MakeSatBox($SexCat,$SatRegionScale,$NCol,$NRow,$Ds9SatReg);
    }
    MakeMask($SegFile,$SexArSort,$KronScale,$Ds9SatReg);
    SatMask($SegFile,$Ds9SatReg,$Total+1,$NCol,$NRow);
}
else
{
    print "Using old mask image $SegFile \n";
}

UpdateSatFlags($SexSort,$Ds9SatReg);

##### Sky segmentation annuli Mask #####

if( !( -e $SkyFile ) )
{
    MakeImage($SkyFile,$NCol,$NRow,16);
    if ($AutoSatRegion == 1)
    {
MakeSatBox($SexCat,$SatRegionScale,$NCol,$NRow,$Ds9SatReg);
    }
    MakeSkyMask($SkyFile,$SexArSort,$SkyScale,$Offset,$Ds9SatReg);
    SatMask($SkyFile,$Ds9SatReg,$Total+1,$NCol,$NRow);
}
elseif( $Overwrite == 1 )
{
    MakeImage($SkyFile,$NCol,$NRow,16);

    if ($AutoSatRegion == 1)
    {
MakeSatBox($SexCat,$SatRegionScale,$NCol,$NRow,$Ds9SatReg);
    }
    MakeSkyMask($SkyFile,$SexArSort,$SkyScale,$Offset,$Ds9SatReg);
    SatMask($SkyFile,$Ds9SatReg,$Total+1,$NCol,$NRow);
}
}
```

```
else
{
    print "Using old mask sky annuli image $SkyFile \n";
}

#####   Obj Pix File #####

if( !(-e $PixFile) )
{
    MakeImage($PixFile,$NCol,$NRow,16);

    if ($AutoSatRegion == 1)
    {
        MakeSatBox($SexCat,$SatRegionScale,$NCol,$NRow,$Ds9SatReg);
    }

    MakeMask($PixFile,$SexArSort,1,$Ds9SatReg); # 1 Kron radius
    SatMask($PixFile,$Ds9SatReg,$Total+1,$NCol,$NRow);

}
elseif( $Overwrite == 1 )
{
    MakeImage($PixFile,$NCol,$NRow,16);

    if ($AutoSatRegion == 1)
    {
        MakeSatBox($SexCat,$SatRegionScale,$NCol,$NRow,$Ds9SatReg);
    }
    MakeMask($PixFile,$SexArSort,1,$Ds9SatReg); # 1 Kron radius
    SatMask($PixFile,$Ds9SatReg,$Total+1,$NCol,$NRow);
}
else
{
    print "Using old mask image $SegFile \n";
}

### creating directories...

if ( !(-e $InputDir) )
{
    mkdir $InputDir;
}

if ( !(-e $OutputDir) )
{
```

```
    mkdir $OutputDir;
}

if ( !(-e $SkyDir) )
{
    mkdir $SkyDir;
}

if ( !(-e $PixDir) )
{
    mkdir $PixDir;
}

if ( !(-e $MaskPixDir) )
{
    mkdir $MaskPixDir;
}

$XChunk = int ($NCol / $Split);
$YChunk = int ($NRow / $Split);

## mask pixels
print "Getting pixels from every object to remove masks \n";
GetPixels($SegFile,$SexSort,$KronScale,$PixPrefix,$XChunk,$YChunk,$Buffer);

$errpix = system("mv $PixPrefix* $MaskPixDir/. ");
CheckError($errpix);

## object pixels
print "Getting pixels from every object to compute final parameters \n";
GetPixels($PixFile,$SexSort,1,$PixPrefix,$XChunk,$YChunk,$Buffer);

$errpix = system("mv $PixPrefix* $PixDir/. ");
CheckError($errpix);

print "Creating Ds9 Box region of all objects \n";
BoxDs9($SexSort,$BoxOut,$BoxSkyOut);

## splitting image files
print "Splitting images \n";
SplitImage($Img,$SegFile,$SkyFile,$SigImg,$Split,$Buffer,$TempDir);

$errpsf = system("ls $PsfDir/PSF*.fits > psf.temp");
#CheckError($errpsf);
```

```

print "==== DGCG In a NutShell ===== \n";
print " DGCG: Driver for GALFIT on Cluster Galaxies \n";
print " Created by Christopher Anorve \n";
print "==== \n";

open (LOGFILE, " > $LogFile");

PrintVar(LOGFILE); # print DGCG options in Log file

#$OffsetFile="$TempDir/$OffsetPos";
$OffsetFile="$OffsetPos";

open (OBS, "> $ListObjs");
open (OUT2, "> $OffsetFile");

open (OUT3, "> $Crashes");
open (OUT4, "> $Fitted");

open (SkyCrashed, "> $SkyCrashes");
open (SkyFitted , "> $SkyFitted");

##### Read in sextractor sorted data #####

$i=0;

open (IN1, $SexSort) || die "Can't open $SexSort !";

while($line=<IN1>)
{
    ($N,$Alpha,$Delta,$X,$Y,$Mg,$Kr,$Fluxr,
    $Isoa,$Ai,$E,$Theta,$Bkgd,$Idx,$Flg,
    $Xlo,$Xhi,$Ylo,$Yhi,$Xslo,$Xshi,
    $Yslo,$Yshi)=split ' ', $line;

    $Num[$i]      = $N;
    $RA[$i]       = $Alpha;
    $Dec[$i]      = $Delta;
    $XPos[$i]     = $X;
    $YPos[$i]     = $Y;
    $Mag[$i]      = $Mg;

```

```
$Kron[$i]      = $Kr;
$FluxRad[$i]   = $Fluxr;
$IsoArea[$i]   = $Isoa;
$AIm[$i]       = $Ai;
$AR[$i]        = 1 - $E;
$Angle[$i]     = $Theta - 90;
$Background[$i] = $Bkgd;
$Sky[$i]       = $Bkgd;
$Class[$i]     = $Idx;
$Flag[$i]      = $Flg;
$XMin[$i]      = $Xlo;
$XMax[$i]      = $Xhi;
$YMin[$i]      = $Ylo;
$YMax[$i]      = $Yhi;
$XSMin[$i]     = $Xslo;
$XSMax[$i]     = $Xshi;
$YSMin[$i]     = $Yslo;
$YSMax[$i]     = $Yshi;

## other stuff:

$Sersic[$i]    = $NSer;

$RSky[$i]      = $SkyScale * $Ai * $Kr + $Offset + $SkyAnnuli;
$RKron[$i]     = $KronScale * $Ai * $Kr;

if ($RSky[$i] == 0)
{
$RSky[$i] = 1;
}

if ($RKron[$i] == 0)
{
$RKron[$i] = 1;
}

$SkyFlag[$i]=1;

$Neighbors[$i] = "$N";

#### subpanel stuff:

$IX[$i] = int ($X / $XChunk) + 1;
$IY[$i] = int ($Y / $YChunk) + 1;
```

```
# Make sure the object coordinate in the subpanel is correct

    if ($IX[$i] == 1)
    {
$XBuffer[$i] = 0;
    }
    else
    {
$XBuffer[$i] = $Buffer;
    }

    if ($IY[$i] == 1)
    {
$YBuffer[$i] = 0;
    }
    else
    {
$YBuffer[$i] = $Buffer;
    }

    $OFFX[$i] = ($IX[$i]-1) * $XChunk - $XBuffer[$i];
    $OFFY[$i] = ($IY[$i]-1) * $YChunk - $YBuffer[$i];

    $i++;
}
close (IN1);

print "Finding Neighbors for every object \n";

FindNeighbors();

if ($Execute != 0)
{

# Sky fitting
# DGCG computes the sky first and leaves it fixed for galaxy fitting.

print "DGCG is going to compute sky \n";

RunSky($TotPix,$MaxTimes);

$errmv = system ("mv fit.log $SkyDir/fit.log.sky");
CheckError($errmv);

$errmv = system ("mv galfit.* $SkyDir/.");
```

```
    CheckError($errmv);

    print "Done sky fitting \n";

    if ($Execute != 2)
    {

## here comes the serious stuff:

DGCG();

$errmv = system("mv obj-* $InputDir/");
CheckError($errmv);

$errmv = system("mv sigma-* $InputDir/");
CheckError($errmv);

$errmv = system("mv out-* $OutputDir/");
CheckError($errmv);

$errmv=system ("mv galfit.* $OutputDir/");
CheckError($errmv);

$errmv=system ("mv mask-* $InputDir/");
    CheckError($errmv);

$errmv =system ("mv *-out.fits $OutputDir/");
CheckError($errmv);

mkdir "$InputDir/$PsfDir";
$errmv = system ("cp $PsfDir/* $InputDir/$PsfDir/");
CheckError($errmv);
$errmv = system ("cp $ConsFile $InputDir/");
CheckError($errmv);

print "Done GALFITting \n";

    }

}

close (LOGFILE);
close (OUT2);
```

```
close (OUT3);
close (OUT4);
close (OBJS);
close (SkyCrashed);
close (SkyFitted);

## Computing running time

my $EndRun= time();

$RunTime = $EndRun - $StartRun;

$RunTimeMin = $RunTime/60;

$RunTimeMin = sprintf "%.3f",$RunTimeMin;

$RunTimeHour = $RunTimeMin/60;

$RunTimeHour = sprintf "%.3f",$RunTimeHour;

$RunTimeDays = $RunTimeHour/24;

$RunTimeDays = sprintf "%.3f",$RunTimeDays;

if ($RunTimeDays >= 1 )
{
    print "Job took $RunTimeDays days \n";
}
elseif ($RunTimeHour >= 1)
{
    print "Job took $RunTimeHour hours \n";
}
elseif ($RunTimeMin >= 1)
{
    print "Job took $RunTimeMin minutes \n";
}
else
{
    print "Job took $RunTime seconds \n";
}
```

```
}

if ($Execute != 3 && $Execute!= 2 && $Execute != 0)
{

    print "Creating outputs files \n";

    $outflag=ReadFitlog("fit.log","fitlog.dgcg");

    if ($outflag == 1)
    {
$filebt = $FileOut.".bt";

$finalflag=MakeOutput("fitlog.dgcg",$filebt,$PlateScale,$MagZpt,
$ConsFile,$Ds9OutName,$Ds9OutNum,$PixPrefix,$PixDir,$OutputDir,
    $InputDir,$Contrast,$Bias,$ExpTime,$ErrPer);

if ($finalflag ==1)
{
    $posflag= PosCor($OffsetFile,$filebt); # correct positions

    if ($posflag == 1)
    {
$sexout=$FileOut.".dgcg";
$joinflag = JoinSexOut($filebt,$ListObjs,$sexout);

if ($joinflag ==1)
{

    print "Ascii output file was succesfully created\n";

    $tablefits=$FileOut.".dgcg.fits";

    print "Creating table fits file \n";

    if ( (-e "ascii2table.py") )
    {
        # Run python script
$errno = system ("./ascii2table.py $sexout $tablefits ");
CheckError($errno);

if($errno == 0)
{
    print "Output files were succesfully created \n";
}
}
}
}
}
}
}
```

```
    }
    else
    {
print "Can't find ascii2table.py file\n";
    }

}
else
{
    print "Can't create Ascii final output file \n";
}

}
else
{
print "Can't create dgcg output file \n" ;
}

}
else
{
    print "Can't create bt output file \n" ;
}

}
else
{
print "Can't create output files \n" ;
}

}

#### erasing files

if ($Erase == 1)
{

    print "Erasing unnecessary files \n";

    $errno = system("rm -r $TempDir");
    CheckError($errno);

    unlink "psf.temp";

    $errno = system("rm $SkyDir/Sky-*");
    CheckError($errno);
```

```
$errno = system("rm $SkyDir/galfit.*");
CheckError($errno);

}

if ($Execute != 0 && $Execute != 2)
{

    $GalTot = $Failures + $Success;

    print "DGCG had $Success success of a total of $GalTot \n";

}

print "Done everything! \n";
```



# List of Figures

1.1	Figure 1 of Bromm & Yoshida (2011) Assembly of the first galaxies . . . . .	3
1.2	The three main types of galaxies considered in this thesis. Left: elliptical galaxy, middle: S0 galaxy, right: Spiral galaxy. Images were taken from the Sloan Digital Sky Survey (SDSS, <a href="http://www.sdss.org">www.sdss.org</a> ) . . . . .	4
1.3	Hubble tuning fork classification scheme. Figure taken from SDSS ( <a href="http://cas.sdss.org">cas.sdss.org</a> ). See text for details. . . . .	5
1.4	De Vaucouleurs classification scheme. This Figure was taken from NED Level 5 ( <a href="http://ned.ipac.caltech.edu/level5">ned.ipac.caltech.edu/level5</a> ). See text for details. . . . .	6
1.5	Left: DMR of Dressler (1980b) for clusters at low redshift $z \sim 0.04$ . Right: DMR of Dressler et al. (1997) for clusters at $z \sim 0.5$ . Figures taken from Dressler et al. (1997) . . . . .	13
1.6	Perseus Cluster. Credit & Copyright R. Jay Gabany . . . . .	15
3.1	The Sérsic function. Sérsic functions with $n = 0.5, 1, 2, 4, 10$ are plotted using different colors as shown in the upper-right part of the Figure. All the curves are normalized to $\mu_e = 20$ . . . . .	36
3.2	Example of SExtractor identification of every object in a plot image of density vs. area. SExtractor constructs a "tree" of the objects. A branch is considered a different object. Image taken from SExtractor's manual . . . . .	42
3.3	Example of SExtractor hot (top) and cold (middle) runs. The combined catalog is shown in the bottom panel. . . . .	43
3.4	Example of the configuration file for DGCG. . . . .	44
3.5	Flow chart for layer 1 . . . . .	45
3.6	Example of an DGCG mask. Top: normal image. Bottom: mask for that region. Fluxes of every object correspond to NUMBER column in the catalog. . . . .	48
3.7	Flow chart for layer 2 . . . . .	49
3.8	Flow chart for layer 3 . . . . .	50
3.9	Flow chart for layer 4 . . . . .	52

- 3.10 *Left panel: Results of DGCG for GEMS simulated galaxies (Sérsic component). From top to bottom: Mag (input)- Mag(fit), Re(fit)/Re(input), n(fit). Horizontal axis is the mean surface brightness at effective radius. The red solid line is the mean and the blue dashed one is 1 sigma. Vertical line represents the surface brightness of the sky. Right panel: same as left panel, but X-axis is the signal to noise ratio (SNR)* . . . . . 57
- 3.11 *Same as 3.10, but here the masking method is used for the neighbor objects instead of deblending. From top to bottom: Mag (input)- Mag(fit), Re(fit)/Re(input), n(fit). Horizontal axis is the mean surface brightness at effective radius. The red solid line is the mean and the blue dashed one is 1 sigma. Vertical line represents the surface brightness of the sky.* . . . . . 59
- 3.12 *Results for the fitting of two components galaxies (Sérsic + Exponential) vs. their signal to noise ratio. From top to bottom: Mag (input)- Mag(fit), Re(fit)/Re(input), n(input) -n(fit). B/T(input) - B/T(fit). The red solid line is the mean and the blue dashed one is 1 sigma. Horizontal axis is the signal to noise ratio. The vertical solid line represents the value of the sky.* . . . . . 60
- 4.1 *Example of a simultaneous fit with DGCG for a galaxy in A1213. Left: input image. Green arrow indicates the fitted galaxy. Middle: the fitted surface brightness model. It has the same scale as left image. Right: residual image (input image – model). Scale is such that peak to peak fluctuations correspond to 2.38% the peak value in middle image. Seven neighbor galaxies were fitted simultaneously.* . . . . . 66
- 4.2 *Histogram of the SNR for the succesful fitted galaxies in the LOCOS database. The fainter magnitude cut in our sample is  $R < 18$  mag.* . . . . . 67
- 4.3 *Top left panel: GALFIT's magnitude vs. PPP's magnitude. Top bottom panel: GALFIT's magnitude - PPP's magnitude vs. PPP's magnitude. Top right panel: histogram of PPP's magnitude - GALFIT's magnitude. Mean: 0 standard deviation: 0.0721* . . . . . 68
- 4.4 *Figure 1 of Tran et al. (2003). Small circles represent E-S0 ( $-5 \leq T \leq -1$ ), triangles S0-a ( $0 \leq T \leq 1$ ), squares S and irregulars ( $2 \leq T \leq 15$ ), and large circles post-starburst galaxies* . . . . . 69
- 4.5 *Top panel: BPN vs Sérsic index (S). Bottom panel: BPN vs weighted mean axis ratio. Axis ratio is weighted by the B/T ratio. Blue asterisks are S, green triangles are S0, and red circles are E* . . . . . 70
- 4.6 *E galaxy in A1913. Left: input image. Green arrow indicates the fitted galaxy. Middle: the single Sérsic model. It has the same scale as left image. Right: residual image (input image – model). Scale is such that peak to peak fluctuations correspond to 2.54% the peak value in the middle image. According to MBIC the galaxy have a disk component as can be shown in the residual image.* 74

- 4.7 E galaxy in A2256. Left: input image. Green arrow indicates the fitted galaxy. Middle: the single Sérsic model. It has the same scale as left image. Right: residual image (input image – model). Scale is such that peak to peak fluctuations correspond to 3.04% the peak value in the middle image. According to MBIC the galaxy do not have a disk component as can be shown in the residual image. . . . . 75
- 4.8 E with one component. Left: input image. Green arrow indicates the fitted galaxy. Middle: the fitted single Sérsic model. It has the same scale as left image. Right: residual image (input image – model). Scale is such that peak to peak fluctuations correspond to 0.38% the peak value in the middle image. MBIC ratio = 1.03 . . . . . 75
- 4.9 E with one component. Left: input image. Green arrow indicates the fitted galaxy. Middle: the fitted single Sérsic model. It has the same scale as left image. Right: residual image (input image – model). Scale is such that peak to peak fluctuations correspond to 3.76% the peak value in the middle image. MBIC ratio = 1.02 . . . . . 76
- 4.10 E with one component. Left: input image. Green arrow indicates the fitted galaxy. Middle: the fitted single Sérsic model. It has the same scale as left image. Right: residual image (input image – model). Scale is such that peak to peak fluctuations correspond to 1.23% the peak value in the middle image. MBIC ratio = 1.0 . . . . . 76
- 4.11 E with one component. Left: input image. Green arrow indicates the fitted galaxy. Middle: the fitted single Sérsic model. It has the same scale as left image. Right: residual image (input image – model). Scale is such that peak to peak fluctuations correspond to 1.10% the peak value in the middle image. MBIC ratio = 1.03 . . . . . 77
- 4.12 E with one component. Left: input image. Green arrow indicates the fitted galaxy. Middle: the fitted single Sérsic model. It has the same scale as left image. Right: residual image (input image – model). Scale is such that peak to peak fluctuations correspond to 2.55% the peak value in the middle image. MBIC ratio = 1.4 . . . . . 77
- 4.13 E with one component. Left: input image. Green arrow indicates the fitted galaxy. Middle: the fitted single Sérsic model. It has the same scale as left image. Right: residual image (input image – model). Scale is such that peak to peak fluctuations correspond to 3.04% the peak value in the middle image. MBIC ratio = 1.03 . . . . . 78
- 4.14 E with one component. Left: input image. Green arrow indicates the fitted galaxy. Middle: the fitted single Sérsic model. It has the same scale as left image. Right: residual image (input image – model). Scale is such that peak to peak fluctuations correspond to 5.44% the peak value in the middle image. MBIC ratio = 1.04 . . . . . 78

- 4.15 E with one component. Left: input image. Green arrow indicates the fitted galaxy. Middle: the fitted single Sérsic model. It has the same scale as left image. Right: residual image (input image – model). Scale is such that peak to peak fluctuations correspond to 0.73% the peak value in the middle image. MBIC ratio = 1.08 . . . . . 79
- 4.16 E with one component. Left: input image. Green arrow indicates the fitted galaxy. Middle: the fitted single Sérsic model. It has the same scale as left image. Right: residual image (input image – model). Scale is such that peak to peak fluctuations correspond to 2.76% the peak value in the middle image. MBIC ratio = 1.18 . . . . . 79
- 4.17 E with one component. Left: input image. Green arrow indicates the fitted galaxy. Middle: the fitted single Sérsic model. It has the same scale as left image. Right: residual image (input image – model). Scale is such that peak to peak fluctuations correspond to 3.92% the peak value in the middle image. MBIC ratio = 3.09 . . . . . 80
- 4.18 E with two components. Left: input image. Green arrow indicates the fitted galaxy. Middle: the fitted single Sérsic model. It has the same scale as left image. Right: residual image (input image – model). Scale is such that peak to peak fluctuations correspond to 4.76% the peak value in the middle image. MBIC ratio = 0.77 . . . . . 81
- 4.19 E with two components. Left: input image. Green arrow indicates the fitted galaxy. Middle: the fitted single Sérsic model. It has the same scale as left image. Right: residual image (input image – model). Scale is such that peak to peak fluctuations correspond to 2.20% the peak value in the middle image. MBIC ratio = 0.77 . . . . . 82
- 4.20 E with two components. Left: input image. Green arrow indicates the fitted galaxy. Middle: the fitted single Sérsic model. It has the same scale as left image. Right: residual image (input image – model). Scale is such that peak to peak fluctuations correspond to 3.11% the peak value in the middle image. MBIC ratio = 0.75 . . . . . 82
- 4.21 E with two components. Left: input image. Green arrow indicates the fitted galaxy. Middle: the fitted single Sérsic model. It has the same scale as left image. Right: residual image (input image – model). Scale is such that peak to peak fluctuations correspond to 2.63% the peak value in the middle image. MBIC ratio = 0.66 . . . . . 83
- 4.22 E with two components. Left: input image. Green arrow indicates the fitted galaxy. Middle: the fitted single Sérsic model. It has the same scale as left image. Right: residual image (input image – model). Scale is such that peak to peak fluctuations correspond to 1.19% the peak value in the middle image. MBIC ratio = 0.78 . . . . . 83

4.23 E with two components. Left: input image. Green arrow indicates the fitted galaxy. Middle: the fitted single Sérsic model. It has the same scale as left image. Right: residual image (input image – model). Scale is such that peak to peak fluctuations correspond to 4.16% the peak value in the middle image. MBIC ratio = 0.86 . . . . . 84

4.24 E with two components. Left: input image. Green arrow indicates the fitted galaxy. Middle: the fitted single Sérsic model. It has the same scale as left image. Right: residual image (input image – model). Scale is such that peak to peak fluctuations correspond to 2.72% the peak value in the middle image. MBIC ratio = 0.73 . . . . . 84

4.25 E with two components. Left: input image. Green arrow indicates the fitted galaxy. Middle: the fitted single Sérsic model. It has the same scale as left image. Right: residual image (input image – model). Scale is such that peak to peak fluctuations correspond to 3.63% the peak value in the middle image. MBIC ratio = 0.9 . . . . . 85

4.26 E with two components. Left: input image. Green arrow indicates the fitted galaxy. Middle: the fitted single Sérsic model. It has the same scale as left image. Right: residual image (input image – model). Scale is such that peak to peak fluctuations correspond to 1.19% the peak value in the middle image. MBIC ratio = 0.91 . . . . . 85

4.27 E with two components. Left: input image. Green arrow indicates the fitted galaxy. Middle: the fitted single Sérsic model. It has the same scale as left image. Right: residual image (input image – model). Scale is such that peak to peak fluctuations correspond to 7.01% the peak value in the middle image. MBIC ratio = 0.82 . . . . . 86

4.28 E with two components. Left: input image. Green arrow indicates the fitted galaxy. Middle: the fitted single Sérsic model. It has the same scale as left image. Right: residual image (input image – model). Scale is such that peak to peak fluctuations correspond to 9.9% the peak value in the middle image. MBIC ratio = 0.8 . . . . . 86

4.29 E with two components. Left: input image. Green arrow indicates the fitted galaxy. Middle: the fitted single Sérsic model. It has the same scale as left image. Right: residual image (input image – model). Scale is such that peak to peak fluctuations correspond to 1.08% the peak value in the middle image. MBIC ratio = 0.68 . . . . . 87

4.30 E with two components. Left: input image. Green arrow indicates the fitted galaxy. Middle: the fitted single Sérsic model. It has the same scale as left image. Right: residual image (input image – model). Scale is such that peak to peak fluctuations correspond to 0.21% the peak value in the middle image. MBIC ratio = 0.94 . . . . . 87

- 4.31 E with two components. Left: input image. Green arrow indicates the fitted galaxy. Middle: the fitted single Sérsic model. It has the same scale as left image. Right: residual image (input image – model). Scale is such that peak to peak fluctuations correspond to 0.17% the peak value in the middle image. MBIC ratio = 0.72 . . . . . 88
- 4.32 E with two components. Left: input image. Green arrow indicates the fitted galaxy. Middle: the fitted single Sérsic model. It has the same scale as left image. Right: residual image (input image – model). Scale is such that peak to peak fluctuations correspond to 2.79% the peak value in the middle image. MBIC ratio = 0.67 . . . . . 88
- 4.33 E with two components. Left: input image. Green arrow indicates the fitted galaxy. Middle: the fitted single Sérsic model. It has the same scale as left image. Right: residual image (input image – model). Scale is such that peak to peak fluctuations correspond to 3.77% the peak value in the middle image. MBIC ratio = 0.68 . . . . . 89
- 4.34 E with two components. Left: input image. Green arrow indicates the fitted galaxy. Middle: the fitted single Sérsic model. It has the same scale as left image. Right: residual image (input image – model). Scale is such that peak to peak fluctuations correspond to 4.83% the peak value in the middle image. MBIC ratio = 0.95 . . . . . 90
- 4.35 E with two components. Left: input image. Green arrow indicates the fitted galaxy. Middle: the fitted single Sérsic model. It has the same scale as left image. Right: residual image (input image – model). Scale is such that peak to peak fluctuations correspond to 7.12% the peak value in the middle image. MBIC ratio = 0.95 . . . . . 91
- 4.36 E with two components. Left: input image. Green arrow indicates the fitted galaxy. Middle: the fitted single Sérsic model. It has the same scale as left image. Right: residual image (input image – model). Scale is such that peak to peak fluctuations correspond to 2.54% the peak value in the middle image. MBIC ratio = 0.83 . . . . . 91
- 4.37 E with two components. Left: input image. Green arrow indicates the fitted galaxy. Middle: the fitted single Sérsic model. It has the same scale as left image. Right: residual image (input image – model). Scale is such that peak to peak fluctuations correspond to 1.91% the peak value in the middle image. MBIC ratio = 0.95 . . . . . 92
- 4.38 E with two components. Left: input image. Green arrow indicates the fitted galaxy. Middle: the fitted single Sérsic model. It has the same scale as left image. Right: residual image (input image – model). Scale is such that peak to peak fluctuations correspond to 3.99% the peak value in the middle image. MBIC ratio = 0.95 . . . . . 92

- 4.39 E with two components. Left: input image. Green arrow indicates the fitted galaxy. Middle: the fitted single Sérsic model. It has the same scale as left image. Right: residual image (input image – model). Scale is such that peak to peak fluctuations correspond to 2.0% the peak value in the middle image. MBIC ratio = 0.91 . . . . . 93
- 4.40 E with two components. Left: input image. Green arrow indicates the fitted galaxy. Middle: the fitted single Sérsic model. It has the same scale as left image. Right: residual image (input image – model). Scale is such that peak to peak fluctuations correspond to 2.08% the peak value in the middle image. MBIC ratio = 0.78 . . . . . 93
- 4.41 E with two components. Left: input image. Green arrow indicates the fitted galaxy. Middle: the fitted single Sérsic model. It has the same scale as left image. Right: residual image (input image – model). Scale is such that peak to peak fluctuations correspond to 4.31% the peak value in the middle image. MBIC ratio = 0.87 . . . . . 94
- 4.42 E with two components. Left: input image. Green arrow indicates the fitted galaxy. Middle: the fitted single Sérsic model. It has the same scale as left image. Right: residual image (input image – model). Scale is such that peak to peak fluctuations correspond to 1.28% the peak value in the middle image. MBIC ratio = 0.74 . . . . . 94
- 4.43 E with two components. Left: input image. Green arrow indicates the fitted galaxy. Middle: the fitted single Sérsic model. It has the same scale as left image. Right: residual image (input image – model). Scale is such that peak to peak fluctuations correspond to 2.33% the peak value in the middle image. MBIC ratio = 0.95 . . . . . 95
- 4.44 E with two components. Left: input image. Green arrow indicates the fitted galaxy. Middle: the fitted single Sérsic model. It has the same scale as left image. Right: residual image (input image – model). Scale is such that peak to peak fluctuations correspond to 1.97% the peak value in the middle image. MBIC ratio = 0.7 . . . . . 95
- 4.45 E with two components. Left: input image. Green arrow indicates the fitted galaxy. Middle: the fitted single Sérsic model. It has the same scale as left image. Right: residual image (input image – model). Scale is such that peak to peak fluctuations correspond to 4.48% the peak value in the middle image. MBIC ratio = 0.9. The shape of the residual shows signs of interaction of merger. 96
- 4.46 E with two components. Left: input image. Green arrow indicates the fitted galaxy. Middle: the fitted single Sérsic model. It has the same scale as left image. Right: residual image (input image – model). Scale is such that peak to peak fluctuations correspond to 7.51% the peak value in the middle image. MBIC ratio = 0.9 . . . . . 96

4.47	E with two components. Left: input image. Green arrow indicates the fitted galaxy. Middle: the fitted single Sérsic model. It has the same scale as left image. Right: residual image (input image – model). Scale is such that peak to peak fluctuations correspond to 1.93% the peak value in the middle image. MBIC ratio = 0.7 . . . . .	97
5.1	Density morphology relation for the successful fits in the sample. Blue asterisks represent S galaxies, green triangles are S0 and red circles E. . . . .	105
5.2	Top panel: KR (BD). Y axis is $\mu_e$ and X axis is effective radius $R_e$ . . . . .	106
5.3	Same KR but using $\langle \mu \rangle_e$ . Blue filled circles represent galaxies with $n \leq 2$ while red filled circles represent galaxies with $n > 2$ . Red solid lines represent 3 $\sigma$ to the fit of E galaxies. A significant number of $n \leq 2$ galaxies fall as outliers of the KR . . . . .	107
5.4	Luminosity-Size relations. Top left panel: luminosity-size relation for bulges BD using $R_e$ . Top right panel: Luminosity-size relation for bulges BD using $R_{90}$ (See appendix B). Blue dots are pseudobulges which were classified using the KR while red dots are classic bulges for top panels. Bottom Left panel: luminosity-size relation for SS models using $R_e$ . Bottom right panel: luminosity-size relation for SS models using $R_{90}$ . Blue dots are galaxies with Sérsic index $< 2$ and red dots are galaxies with Sérsic index $> 2$ for bottom panels. Solid lines represent the fit for $R_e$ , and dashed lines represent fit for $R_{90}$ . . . . .	109
5.5	Luminosity-size relation for disk galaxies. . . . .	110
5.6	Left panel: CMR. $B - R$ vs. $R$ . Red circles are E, blue asterisks are S and green triangles are S0. Right Panel: $B - R$ histograms for each morphological type. From top right to bottom panel: E galaxies ( $\mu = 1.64$ , $\sigma = 0.069$ ). S0 galaxies ( $\mu = 1.63$ , $\sigma = 0.069$ ). Red S ( $\mu = 1.63$ , $\sigma = 0.06$ ), and blue S ( $\mu = 1.47$ , $\sigma = 0.27$ ). Red S ( $\mu = 1.64$ , $\sigma = 0.06$ ) and blue S ( $\mu = 1.44$ , $\sigma = 0.26$ ) excluding the edge-on galaxies . . . . .	112
5.7	The FJR. Blue circles represent pseudobulges while red circles represent classic bulges. Solid line represents the fit to E galaxies. Dashed line represents a probable division between pseudobulges and classic bulges. . . . .	113
5.8	Fundamental plane for the E and bulges in the sample. . . . .	115
5.9	Same as 5.8, but red circles indicate classic bulges and blue ones indicate pseudobulges. . . . .	116
5.10	Top left: Central surface brightness vs. Sérsic index (SS for E galaxies. Top right: Mag vs. $\mu_e$ for E galaxies. Bottom left: $R_e$ vs. $n$ relation (SS) for E galaxies. $R_s$ vs. $R_e$ for S galaxies. The galaxies presented here are the ones of Dressler (1980a) catalog. . . . .	117
5.11	Left panel: distribution of Sérsic index (SS). Peak is at 1.22. Right panel: distribution of Sérsic index (BD). Peak is at 1.0. . . . .	119

5.12 *Top right panel: color ( $B - R$ ) vs. Sérsic index for BD models. Blue points represent pseudobulges and red ones classic bulges. Bottom left panel: color ( $B - R$ ) vs. Sérsic index for SS. Red circles are E, blue asterisks are S and green triangles are S0. Bottom right panel: color ( $B - R$ ) vs. Sérsic index for BD fits . . . . .* 121

5.13 *CMR for classic bulges and pseudobulges. Blue asterisks represent pseudobulges and red circles classic bulges . . . . .* 122

5.14 *Left panel: Luminosity vs. Sérsic index for SS fits. Right panel: Luminosity vs. Sérsic index for BD fits. Red circles are E, blue asterisks are S and green triangles are S0. The solid thick line was generated by a robust locally weighted scheme (Cleveland 1979). . . . .* 123

5.15 *Left panel: Histogram of  $n$  for SS. Right panel: Same as left panel but for Dressler's galaxies. Red line E, green line S0 and blue line are S . . . . .* 124

5.16 *Histogram of Sérsic index (BD). 1156 galaxies are shown here. Blue line are S, green line S0 and red line E . . . . .* 125

5.17 *Left panel: histogram of effective radius (SS) for every morphology type. Right panel: histogram of effective radius (BD) for every morphology type. Red solid line E, green solid line S0 and blue solid line represent S. . . . .* 127

5.18 *Left panel: histogram of the central surface brightness  $\mu_0$  (SS). Right panel: histogram of central surface brightness (SS) for every morphology type. Top right panel: histogram of  $\mu_0$  for E galaxies. Middle right panel: histogram of  $\mu_0$  for S0 galaxies. Bottom right panel: histogram of  $\mu_0$  for S galaxies . . . .* 129

5.19 *Left panel: Histograms of the central surface brightness  $\mu_0$  (BD) for every morphological type. Top: E galaxies. Middle: S0 galaxies. Bottom: S galaxies. Right panel: Morphology vs. central surface brightness. The dots and error bars are mean and  $1 \sigma$  respectively from the left panel. . . . .* 130

5.20 *Top Left panel: Sérsic profiles ( $\mu(R)$  vs.  $R/R_e$ ) for S0 (red lines) and S galaxies (green lines). Here, it is shown those regions where profile density is high. Top right panel: Sérsic profiles ( $\mu(R)$  vs.  $R/R_e$ ) for Dressler's S0 (red lines) and Dressler's S galaxies (green lines). Bottom left panel: Bulges Sérsic profiles ( $\mu(R)$  vs.  $R/R_e$ ) for S0 (red lines) and S galaxies (green lines).  $R_e$  here is the effective radius of the whole galaxy. Bottom right panel: plot similar to bottom left panel, but here it is shown those regions where profile density is high. Yellow lines in all the panels mean overlapped profiles (red + green = yellow). . . . .* 131

5.21 *Similar to bottom left panel of Figure 5.20, but for Dressler classified galaxies. . . . .* 132

B.1  *$k$  vs.  $n$ . This plot obtained with equation B.4 . . . . .* 150

B.2  *$k$  vs.  $n$  for the range  $0.0 < n < 0.1$  . . . . .* 151

B.3  *$R_{90}/R_e$  vs.  $n$ . Black thick line represent numerical solution and blue line equation B.26 . . . . .* 154

C.1	<i>Top panel: Maximum distance vs. Sérsic index given by equation C.3 for the Coma cluster. Parameters for the Coma cluster are: <math>\mu_{lim} = 21.39</math> and <math>M = -17</math>. Green line indicates the distance to the cluster. Bottom panel: Same as top panel but for cluster A1650. Parameters for this cluster are: <math>\mu_{lim} = 21.67</math> and <math>M = -19.85</math>. Green line indicates the distance to the cluster. . . . .</i>	158
E.1	<i>Setup for the wind tunnel. Beyond radius 35 kpc, the mass of the particles starts to grow. This configuration keeps the same density in the entire box. . . . .</i>	170
E.2	<i>Simulation output of wtcc after 1 Gyr. The image shows the resulting clumpiness of the disk gas. . . . .</i>	171
E.3	<i>Pressure vs. radius. The red dots are the wind gas particles and the green dots are the disk gas particles. Beyond <math>\sim 4</math> kpc the pressure of the wind particles starts to dominate. . . . .</i>	172

# List of Tables

1.1	<i>Correspondence of the T type with Hubble type. Data table has been taken from Nair &amp; Abraham (2010)</i> . . . . .	7
1.2	<i>The Bautz-Morgan classification and its standards. Table taken from López-Cruz (2003)</i> . . . . .	16
1.3	<i>The Rood-Sastry classification and its standards. Table taken from López-Cruz (2003)</i> . . . . .	16
2.1	Log of observations . . . . .	25
2.2	Transformation Coefficients to the Kron-Cousins Standard System . . . . .	31
2.3	<i>Clusters used in this thesis. Column (1) name of cluster; (2) redshift; (3) Right Ascension; (4) Declination; (5) Richness; (6) Rood-Sastry Classification (Rood &amp; Sastry 1971); (7) Bautz-Morgan Classification (Bautz &amp; Morgan 1970); (8) extinction coefficient for R band; (9) extinction coefficient for B band; (10) <math>\kappa</math> correction; (11) Integration Time.</i> . . . . .	33
3.1	<i>hot, cold and warm configurations for SExtractor</i> . . . . .	42
3.2	<i>SExtractor output parameters used for this version of DGCG</i> . . . . .	46
3.3	<i>Initial parameters created for main object. Column 1 represents the model's parameter. The value for this parameter is assigned from SExtractor catalog if the model is either a single Sérsic (column 2) or Sérsic + Exponential (column 3). Whether DGCG fit either a single Sérsic or Sérsic + Exponential model depends of the value of FITFUNCTION</i> . . . . .	51
3.4	<i>DGCG Output flags</i> . . . . .	53
3.5	<i>Main differences among GALAPAGOS, SIGMA, PYMORPH and DGCG scripts.</i>	54
4.1	<i>Run time spent per cluster using SS and BD models. Column (1): Abell number of the cluster; (2) CPU clock frequency; (3) Run time for SS model; (4) Run time for BD; (5) number used as input; (6) Fitted galaxies SS model; (7) Fitted galaxies BD model</i> . . . . .	64

4.2	<i>Number of galaxies fitted with SS and BD models. Column (1): the model; (2) number of input galaxies in the SExtractor catalog; (3) Number of fitted galaxies; (4) number of galaxies with flag 1; (5) number of galaxies with flag 2; (6) number of galaxies with flag 4; (7) number of galaxies with flag &gt; 0; (8) number of galaxies with no flag or flag 0.</i>	65
4.3	<i>Number of assigned morphologies for cluster galaxies. Only the good fits are shown. Column (1): Abell cluster; (2) number of E; (3) number of S0; (4) is number of S.</i>	72
4.4	<i>BD fits. Column (1): Cluster name; (2) Right ascension; (3) Declination; (4) ID; (5) Total Magnitude; (6) Mag error; (7) B/T; (8) B/T error; (9) Assigned Morphology (see §4.2.1); (10) Re; (11) Re error; (12) Sérsic index; (13) Sérsic index error; (14) Rs; (15) Rs error.</i>	99
4.5	<i>SS fits. Column (1): the Cluster name; (2) Right Ascension; (3) Declination; (4) ID; (5) Total Magnitude; (6) Total Magnitude error; (7) Re; (8) Re error; (9) Sérsic index; (10) Sérsic Index error; (11) Axis ratio; (12) Axis ratio error; (13) <math>\chi^2_{\nu}</math>; (14) BPN; (15) Signal to noise ratio.</i>	100
E.1	<i>Physics and results of the simulations.</i>	170

## *Bibliography*

- Añorve, C., López-Cruz, O., Ibarra-Medel, H., & León-Tavares, J. 2009, in American Institute of Physics Conference Series, Vol. 1201, American Institute of Physics Conference Series, ed. S. Heinz & E. Wilcots, 131–134
- Abell, G. O. 1958, *ApJS*, 3, 211
- Abell, G. O., Corwin, Jr., H. G., & Olowin, R. P. 1989, *ApJS*, 70, 1
- Abramson, A. & Kenney, J. D. P. 2009, in *The Evolving ISM in the Milky Way and Nearby Galaxies*
- Agertz, O., Moore, B., Stadel, J., Potter, D., Miniati, F., Read, J., Mayer, L., Gawryszczak, A., Kravtsov, A., Nordlund, Å., Pearce, F., Quilis, V., Rudd, D., Springel, V., Stone, J., Tasker, E., Teyssier, R., Wadsley, J., & Walder, R. 2007, *MNRAS*, 380, 963
- Aguerri, J. A. L., Iglesias-Paramo, J., Vilchez, J. M., & Muñoz-Tuñón, C. 2004, *AJ*, 127, 1344
- Aguilar, L. A. & White, S. D. M. 1985, *ApJ*, 295, 374
- . 1986, *ApJ*, 307, 97
- Akaike, H. 1974, *IEEE Trans. Automatic Control*, 19, 716
- Bahcall, N. A. 1999, in *Formation of Structure in the Universe*, ed. A. Dekel & J. P. Ostriker, 135
- Banerji, M., Lahav, O., Lintott, C. J., Abdalla, F. B., Schawinski, K., Bamford, S. P., Andreescu, D., Murray, P., Raddick, M. J., Slosar, A., Szalay, A., Thomas, D., & Vandenberg, J. 2010, *MNRAS*, 406, 342
- Barden, M., Häußler, B., Peng, C. Y., McIntosh, D. H., & Guo, Y. 2012, *MNRAS*, 422, 449
- Barnes, J. & Hut, P. 1986, *Nature*, 324, 446
- Baum, W. A. 1959, *PASP*, 71, 106
- Bautz, L. P. & Morgan, W. W. 1970, *ApJ*, 162, L149

- Bekki, K. 1998, *ApJ*, 502, L133+
- . 1999, *ApJ*, 510, L15
- Bentley, J. L. 1975, *Commun. ACM*, 18, 509
- Bertin, E. & Arnouts, S. 1996, *A&AS*, 117, 393
- Binggeli, B. & Jerjen, H. 1998, *A&A*, 333, 17
- Birkinshaw, M. & Lancaster, K. 2008, in *Lecture Notes in Physics*, Berlin Springer Verlag, Vol. 740, *A Pan-Chromatic View of Clusters of Galaxies and the Large-Scale Structure*, ed. M. Plionis, O. López-Cruz, & D. Hughes, 255
- Biviano, A. 1998, *Coma Berenices: A New Vision of an Old Cluster*
- Blakeslee, J. P., Holden, B. P., Franx, M., Rosati, P., Bouwens, R. J., Demarco, R., Ford, H. C., Homeier, N. L., Illingworth, G. D., Jee, M. J., Mei, S., Menanteau, F., Meurer, G. R., Postman, M., & Tran, K. 2006, *ApJ*, 644, 30
- Blanton, M. R., Hogg, D. W., Bahcall, N. A., Baldry, I. K., Brinkmann, J., Csabai, I., Eisenstein, D., Fukugita, M., Gunn, J. E., Ivezić, Ž., Lamb, D. Q., Lupton, R. H., Loveday, J., Munn, J. A., Nichol, R. C., Okamura, S., Schlegel, D. J., Shimasaku, K., Strauss, M. A., Vogeley, M. S., & Weinberg, D. H. 2003, *ApJ*, 594, 186
- Blanton, M. R. & Moustakas, J. 2009, *ARA&A*, 47, 159
- Block, D., Puerari, I., Stockton, A., & Ferreira, D. 2000, *Toward a New Millennium in Galaxy Morphology*
- Borgani, S. 2004, in *The Riddle of Cooling Flows in Galaxies and Clusters of galaxies*, ed. T. Reiprich, J. Kempner, & N. Soker, 307
- Boselli, A. & Gavazzi, G. 2006, *PASP*, 118, 517
- Bower, R. G. & Balogh, M. L. 2004, in *Clusters of Galaxies: Probes of Cosmological Structure and Galaxy Evolution*, ed. J. S. Mulchaey, A. Dressler, & A. Oemler, 325
- Bower, R. G., Lucey, J. R., & Ellis, R. S. 1992, *MNRAS*, 254, 601
- Bromm, V. & Yoshida, N. 2011, *Annual Review of Astronomy and Astrophysics*, 49, 373
- Brown, J. P. 1997, PhD thesis, UNIVERSITY OF TORONTO (CANADA)
- Burstein, D., Ho, L. C., Huchra, J. P., & Macri, L. M. 2005, *ApJ*, 621, 246
- Buta, R., Corwin, H. G., & Odewahn, S. C. 2007, *The de Vaucouleurs Atlas of Galaxies*
- Butcher, H. & Oemler, Jr., A. 1978, *ApJ*, 219, 18
- Byrd, G. & Valtonen, M. 1990, *ApJ*, 350, 89
- Byun, Y. I. & Freeman, K. C. 1995, *ApJ*, 448, 563

- Calvi, R., Poggianti, B. M., Fasano, G., & Vulcani, B. 2012, *MNRAS*, 419, L14
- Caon, N., Capaccioli, M., & D'Onofrio, M. 1993, *MNRAS*, 265, 1013
- Capaccioli, M. 1987, in *IAU Symposium, Vol. 127, Structure and Dynamics of Elliptical Galaxies*, ed. P. T. de Zeeuw & S. D. Tremaine, 47–60
- Carollo, C. M. 1999, *ApJ*, 523, 566
- Cattaneo, A., Faber, S. M., Binney, J., Dekel, A., Kormendy, J., Mushotzky, R., Babul, A., Best, P. N., Brügggen, M., Fabian, A. C., Frenk, C. S., Khalatyan, A., Netzer, H., Mahdavi, A., Silk, J., Steinmetz, M., & Wisotzki, L. 2009, *Nature*, 460, 213
- Christlein, D. & Zabludoff, A. I. 2004, *ApJ*, 616, 192
- Cibinel, A., Carollo, C. M., Lilly, S. J., Miniati, F., Silverman, J. D., van Gorkom, J. H., Cameron, E., Finoguenov, A., Norberg, P., Pipino, A., Rudick, C. S., Lu, T., & Peng, Y. 2012, *ArXiv e-prints*
- Cleveland, W. 1979, *Journal of the American Statistical Association*, 74, 829
- Coenda, V., Donzelli, C. J., Muriel, H., Quintana, H., Infante, L., & García Lambas, D. 2005, *AJ*, 129, 1237
- Coleman, G. D., Wu, C., & Weedman, D. W. 1980, *ApJS*, 43, 393
- Conselice, C. J. 2003, *ApJS*, 147, 1
- Couch, W. J., Barger, A. J., Smail, I., Ellis, R. S., & Sharples, R. M. 1998, *ApJ*, 497, 188
- Couch, W. J., Ellis, R. S., Sharples, R. M., & Smail, I. 1994, *ApJ*, 430, 121
- Courteau, S., Dutton, A. A., van den Bosch, F. C., MacArthur, L. A., Dekel, A., McIntosh, D. H., & Dale, D. A. 2007, *ApJ*, 671, 203
- Cowie, L. L. & Songaila, A. 1977, *Nature*, 266, 501
- de Jong, R. S. 1995, *Spiral galaxies. The light and color distribution in the optical and near-infrared*
- de Souza, R. E., Gadotti, D. A., & dos Anjos, S. 2004, *ApJS*, 153, 411
- de Vaucouleurs, G. 1948, *Annales d'Astrophysique*, 11, 247
- Disney, M. & Phillipps, S. 1983, *MNRAS*, 205, 1253
- Djorgovski, S. & Davis, M. 1987, *ApJ*, 313, 59
- Djorgovski, S., de Carvalho, R., & Han, M.-S. 1988, in *Astronomical Society of the Pacific Conference Series, Vol. 4, The Extragalactic Distance Scale*, ed. S. van den Bergh & C. J. Pritchett, 329–341

- Dressler, A. 1980a, *ApJS*, 42, 565
- . 1980b, *ApJ*, 236, 351
- . 1984, *ARA&A*, 22, 185
- Dressler, A. 2011, in *Environment and the Formation of Galaxies: 30 years later*, ed. I. Ferreras & A. Pasquali, *Astrophysics and Space Science Proceedings* (Springer Berlin Heidelberg)
- Dressler, A., Oemler, Jr., A., Couch, W. J., Smail, I., Ellis, R. S., Barger, A., Butcher, H., Poggianti, B. M., & Sharples, R. M. 1997, *ApJ*, 490, 577
- Driver, S. P., Hill, D. T., Kelvin, L. S., Robotham, A. S. G., Liske, J., Norberg, P., Baldry, I. K., Bamford, S. P., Hopkins, A. M., Loveday, J., Peacock, J. A., Andrae, E., Bland-Hawthorn, J., Brough, S., Brown, M. J. I., Cameron, E., Ching, J. H. Y., Colless, M., Conselice, C. J., Croom, S. M., Cross, N. J. G., de Propriis, R., Dye, S., Drinkwater, M. J., Ellis, S., Graham, A. W., Grootes, M. W., Gunawardhana, M., Jones, D. H., van Kampen, E., Maraston, C., Nichol, R. C., Parkinson, H. R., Phillipps, S., Pimblet, K., Popescu, C. C., Prescott, M., Roseboom, I. G., Sadler, E. M., Sansom, A. E., Sharp, R. G., Smith, D. J. B., Taylor, E., Thomas, D., Tuffs, R. J., Wijesinghe, D., Dunne, L., Frenk, C. S., Jarvis, M. J., Madore, B. F., Meyer, M. J., Seibert, M., Staveley-Smith, L., Sutherland, W. J., & Warren, S. J. 2011, *MNRAS*, 413, 971
- Dubinski, J. 1999, in *Astronomical Society of the Pacific Conference Series, Vol. 182, Galaxy Dynamics - A Rutgers Symposium*, ed. D. R. Merritt, M. Valluri, & J. A. Sellwood, 491
- Elmegreen, D. M. & Elmegreen, B. G. 1987, *ApJ*, 314, 3
- Elmegreen, D. M., Elmegreen, B. G., & Dressler, A. 1982, *MNRAS*, 201, 1035
- Elmegreen, D. M., Elmegreen, B. G., Frogel, J. A., Eskridge, P. B., Pogge, R. W., Gallagher, A., & Iams, J. 2002, *AJ*, 124, 777
- Emsellem, E., Cappellari, M., Peletier, R. F., McDermid, R. M., Bacon, R., Bureau, M., Copin, Y., Davies, R. L., Krajnović, D., Kuntschner, H., Miller, B. W., & de Zeeuw, P. T. 2004, *MNRAS*, 352, 721
- Faber, S. M. & Jackson, R. E. 1976, *ApJ*, 204, 668
- Fasano, G., Vanzella, E., Dressler, A., Poggianti, B. M., Moles, M., Bettoni, D., Valentini, T., Moretti, A., D'Onofrio, M., Varela, J., Couch, W. J., Kjærgaard, P., Fritz, J., Omizzolo, A., & Cava, A. 2012, *MNRAS*, 420, 926
- Fisher, D. B. & Drory, N. 2011, *ApJ*, 733, L47
- Fisher, D. B., Drory, N., & Kormendy, J. 2010, in *Bulletin of the American Astronomical Society, Vol. 42, American Astronomical Society Meeting Abstracts 215*, 432.05
- Freeman, K. C. 1970, *ApJ*, 160, 811

- Fukugita, M., Nakamura, O., Okamura, S., Yasuda, N., Barentine, J. C., Brinkmann, J., Gunn, J. E., Harvanek, M., Ichikawa, T., Lupton, R. H., Schneider, D. P., Strauss, M. A., & York, D. G. 2007, *AJ*, 134, 579
- Gadotti, D. A. 2009, *MNRAS*, 393, 1531
- Gargiulo, A., Haines, C. P., Merluzzi, P., Smith, R. J., Barbera, F. L., Busarello, G., Lucey, J. R., Mercurio, A., & Capaccioli, M. 2009, *MNRAS*, 397, 75
- Gavazzi, G., Pierini, D., & Boselli, A. 1996, *A&A*, 312, 397
- Gingold, R. A. & Monaghan, J. J. 1977, *MNRAS*, 181, 375
- Gladders, M. D., Lopez-Cruz, O., Yee, H. K. C., & Kodama, T. 1998, *ApJ*, 501, 571
- Glatting, G., P., K., Reske, S., Hohl, K., & Ring, C. 2007, *Med Phys.*, 34, 4285
- Gnedin, O. Y. 2003, *ApJ*, 589, 752
- Goto, T., Yamauchi, C., Fujita, Y., Okamura, S., Sekiguchi, M., Smail, I., Bernardi, M., & Gomez, P. L. 2003, *MNRAS*, 346, 601
- Graham, A. W. 2011, *ArXiv e-prints*
- Graham, A. W. & Driver, S. P. 2005, *PASA*, 22, 118
- Gunn, J. E. & Gott, III, J. R. 1972, *ApJ*, 176, 1
- Gutiérrez, C. M., Trujillo, I., Aguerri, J. A. L., Graham, A. W., & Caon, N. 2004, *ApJ*, 602, 664
- Häussler, B., McIntosh, D. H., Barden, M., Bell, E. F., Rix, H., Borch, A., Beckwith, S. V. W., Caldwell, J. A. R., Heymans, C., Jahnke, K., Joglee, S., Koposov, S. E., Meisenheimer, K., Sánchez, S. F., Somerville, R. S., Wisotzki, L., & Wolf, C. 2007, *ApJS*, 172, 615
- Heckman, T. M. & Kauffmann, G. 2011, *Science*, 333, 182
- Heger, A. & Woosley, S. E. 2002, *ApJ*, 567, 532
- Hernquist, L. 1993, *ApJ*, 409, 548
- Howell, S. B. 2000, *Handbook of CCD Astronomy*
- Hubble, E. P. 1926, *ApJ*, 64, 321
- Hyde, J. B. & Bernardi, M. 2009, *MNRAS*, 396, 1171
- Ibarra-Medel, H. 2010, Master's thesis, INAOE (Mexico)
- Jarosik, N., Bennett, C. L., Dunkley, J., Gold, B., Greason, M. R., Halpern, M., Hill, R. S., Hinshaw, G., Kogut, A., Komatsu, E., Larson, D., Limon, M., Meyer, S. S., Nolte, M. R., Odegard, N., Page, L., Smith, K. M., Spergel, D. N., Tucker, G. S., Weiland, J. L., Wollack, E., & Wright, E. L. 2011, *ApJS*, 192, 14

- Jedrzejewski, R. I. 1987, *MNRAS*, 226, 747
- Jiang, Y.-F., Greene, J. E., Ho, L. C., Xiao, T., & Barth, A. J. 2011, *ApJ*, 742, 68
- Jones, C. & Forman, W. 1999, *ApJ*, 511, 65
- Just, D. W., Zaritsky, D., Sand, D. J., Desai, V., & Rudnick, G. 2010, *ApJ*, 711, 192
- Kapferer, W., Sluka, C., Schindler, S., Ferrari, C., & Ziegler, B. 2009, *A&A*, 499, 87
- Kelvin, L. S., Driver, S. P., Robotham, A. S. G., Hill, D. T., Alpaslan, M., Baldry, I. K., Bamford, S. P., Bland-Hawthorn, J., Brough, S., Graham, A. W., Häussler, B., Hopkins, A. M., Liske, J., Loveday, J., Norberg, P., Phillipps, S., Popescu, C. C., Prescott, M., Taylor, E. N., & Tuffs, R. J. 2012, *MNRAS*, 421, 1007
- King, I. 1961, *AJ*, 66, 68
- Koopmann, R. A. & Kenney, J. D. P. 2004, *ApJ*, 613, 866
- Kormendy, J. 1977, *ApJ*, 218, 333
- Kormendy, J. & Bender, R. 1996, *ApJ*, 464, L119+
- . 2012, *ApJS*, 198, 2
- Kormendy, J., Bender, R., & Cornell, M. E. 2011, *Nature*, 469, 374
- Kormendy, J. & Djorgovski, S. 1989, *ARA&A*, 27, 235
- Kormendy, J., Fisher, D. B., Cornell, M. E., & Bender, R. 2009, *ApJS*, 182, 216
- Kormendy, J. & Kennicutt, Jr., R. C. 2004, *ARA&A*, 42, 603
- Krajnović, D., Bacon, R., Cappellari, M., Davies, R. L., de Zeeuw, P. T., Emsellem, E., Falcón-Barroso, J., Kuntschner, H., McDermid, R. M., Peletier, R. F., Sarzi, M., van den Bosch, R. C. E., & van de Ven, G. 2008, *MNRAS*, 390, 93
- Kron, R. G. 1980, *ApJS*, 43, 305
- La Barbera, F., de Carvalho, R. R., de La Rosa, I. G., & Lopes, P. A. A. 2010, *MNRAS*, 408, 1335
- Lahav, O., Naim, A., Buta, R. J., Corwin, H. G., de Vaucouleurs, G., Dressler, A., Huchra, J. P., van den Bergh, S., Raychaudhury, S., Sodre, Jr., L., & Storrie-Lombardi, M. C. 1995, *Science*, 267, 859
- Lahav, O., Naim, A., Sodré, Jr., L., & Storrie-Lombardi, M. C. 1996, *MNRAS*, 283, 207
- Landolt, A. U. 1992, *AJ*, 104, 340
- Larson, R. B., Tinsley, B. M., & Caldwell, C. N. 1980, *ApJ*, 237, 692
- Lauer, T. R., Ajhar, E. A., Byun, Y.-I., Dressler, A., Faber, S. M., Grillmair, C., Kormendy, J., Richstone, D., & Tremaine, S. 1995, *AJ*, 110, 2622

- Laurikainen, E., Salo, H., Buta, R., & Vasylyev, S. 2004, *MNRAS*, 355, 1251
- Leir, A. A. & van den Bergh, S. 1977, *ApJS*, 34, 381
- Lintott, C. J., Schawinski, K., Slosar, A., Land, K., Bamford, S., Thomas, D., Raddick, M. J., Nichol, R. C., Szalay, A., Andreescu, D., Murray, P., & Vandenberg, J. 2008, *MNRAS*, 389, 1179
- López-Cruz, O. 1997, PhD thesis, UNIVERSITY OF TORONTO (CANADA)
- Lopez-Cruz, O. 2001, in *Revista Mexicana de Astronomia y Astrofisica Conference Series*, Vol. 11, *Revista Mexicana de Astronomia y Astrofisica Conference Series*, 183
- López-Cruz, O. 2003, in *The Garrison Festschrift*, ed. R. O. Gray, C. J. Corbally, & A. G. D. Philip, 109
- López-Cruz, O., Aguilar, L. A., & Añorve, C. 2011, in *Revista Mexicana de Astronomia y Astrofisica*, vol. 27, Vol. 39, *Revista Mexicana de Astronomia y Astrofisica Conference Series*, 100–108
- López-Cruz, O., Barkhouse, W. A., & Yee, H. K. C. 2004, *ApJ*, 614, 679
- Lucey, J. R., Bower, R. G., & Ellis, R. S. 1991, *MNRAS*, 249, 755
- Ma, C.-J. & Ebeling, H. 2011, *MNRAS*, 410, 2593
- Marquardt, D. W. 1963, *Journal of the Society for Industrial and Applied Mathematics*, 11, 431
- Massey, P., A. T. H. C. J. G. S. B. & Silva, D. 1994a, *0.9m Telescope Manual*
- . 1994b, *Direct Imaging Manual for Kitt Peak*
- Massey, P. & Jacoby, G. H. 1992, in *Astronomical Society of the Pacific Conference Series*, Vol. 23, *Astronomical CCD Observing and Reduction Techniques*, ed. S. B. Howell, 240
- Massey, P., Silkey, M., Garmany, C. D., & Degioia-Eastwood, K. 1989, *AJ*, 97, 107
- Masters, K. L., Mosleh, M., Romer, A. K., Nichol, R. C., Bamford, S. P., Schawinski, K., Lintott, C. J., Andreescu, D., Campbell, H. C., Crowcroft, B., Doyle, I., Edmondson, E. M., Murray, P., Raddick, M. J., Slosar, A., Szalay, A. S., & Vandenberg, J. 2010, *MNRAS*, 405, 783
- McDonald, M., Courteau, S., & Tully, R. B. 2009, *MNRAS*, 394, 2022
- McNamara, B. R. & Nulsen, P. E. J. 2007, *ARA&A*, 45, 117
- Méndez-Abreu, J., Aguerri, J. A. L., Corsini, E. M., & Simonneau, E. 2008, *A&A*, 478, 353
- Merritt, D. 1984, *ApJ*, 276, 26

- . 2006, *Reports on Progress in Physics*, 69, 2513
- Mihos, C. 2004, in *Clusters of Galaxies: Probes of Cosmological Structure and Galaxy Evolution*, ed. J. S. Mulchaey, A. Dressler, & A. Oemler, 277
- Moffat, A. F. J. 1969, *A&A*, 3, 455
- Monaghan, J. J. 2005, *Reports on Progress in Physics*, 68, 1703
- Moore, B., Katz, N., Lake, G., Dressler, A., & Oemler, A. 1996, *Nature*, 379, 613
- Morgan, W. W. 1958, *PASP*, 70, 364
- . 1959, *PASP*, 71, 394
- Mulchaey, J. S., Davis, D. S., Mushotzky, R. F., & Burstein, D. 2003, *ApJS*, 145, 39
- Naab, T. & Burkert, A. 2003, *ApJ*, 597, 893
- Nair, P., van den Bergh, S., & Abraham, R. G. 2011, *ApJ*, 734, L31
- Nair, P. B. 2009, PhD thesis, University of Toronto (Canada)
- Nair, P. B. & Abraham, R. G. 2010, *ApJS*, 186, 427
- Nair, P. B., van den Bergh, S., & Abraham, R. G. 2010, *ApJ*, 715, 606
- Navarro, J. F., Frenk, C. S., & White, S. D. M. 1996, *ApJ*, 462, 563
- Nipoti, C., Londrillo, P., & Ciotti, L. 2006, *MNRAS*, 370, 681
- Noonan, T. W. 1970, *PASP*, 82, 821
- Nulsen, P. E. J. 1982, *MNRAS*, 198, 1007
- Oemler, Jr., A. 1974, *ApJ*, 194, 1
- . 1976, *ApJ*, 209, 693
- Pahre, M. A., de Carvalho, R. R., & Djorgovski, S. G. 1998, *AJ*, 116, 1606
- Peletier, R. F., Davies, R. L., Illingworth, G. D., Davis, L. E., & Cawson, M. 1990, *AJ*, 100, 1091
- Peng, C. Y., Ho, L. C., Impey, C. D., & Rix, H. 2002, *AJ*, 124, 266
- Peng, C. Y., Ho, L. C., Impey, C. D., & Rix, H.-W. 2010, *AJ*, 139, 2097
- Petrosian, V. 1976, *ApJ*, 209, L1
- Pignatelli, E., Fasano, G., & Cassata, P. 2006, *A&A*, 446, 373
- Plionis, M., López-Cruz, O., & Hughes, D., eds. 2008, *Lecture Notes in Physics*, Berlin Springer Verlag, Vol. 740, *A Pan-Chromatic View of Clusters of Galaxies and the Large-Scale Structure*

- Press, W. H., Teukolsky, S. A., Vetterling, W. T., & Flannery, B. P. 1992, *Numerical recipes in C (2nd ed.): the art of scientific computing* (New York, NY, USA: Cambridge University Press)
- Quinn, T., Katz, N., Stadel, J., & Lake, G. 1997, *ArXiv Astrophysics e-prints*
- Recillas-Cruz, E., Serrano, A., Cruz-Gonzalez, I., & Carrasco, L. 1991, *A&A*, 249, 312
- Rix, H. & White, S. D. M. 1992, *MNRAS*, 254, 389
- Roediger, E. 2009, *Astronomische Nachrichten*, 330, 888
- Rood, H. J. & Sastry, G. N. 1971, *PASP*, 83, 313
- Rosati, P., Borgani, S., & Norman, C. 2002, *ARA&A*, 40, 539
- Saintonge, A. & Spekkens, K. 2011, *ApJ*, 726, 77
- Salim, S., Fang, J. J., Rich, R. M., Faber, S. M., & Thilker, D. A. 2012, *ArXiv e-prints*
- Sandage, A. 2005, *ARA&A*, 43, 581
- Sandage, A. & Bedke, J. 1994, *The Carnegie Atlas of Galaxies. Volumes I, II.*
- Sandage, A., Sandage, M., & Kristian, J. 1975, *Chicago, University of Chicago Press, Vol. 9, Galaxies and the Universe*, ed. Sandage, A., Sandage, M., & Kristian, J., 839
- Sandage, A. & Tammann, G. A. 1981, *A revised Shapley-Ames Catalog of bright galaxies*
- Sandage, A. & Visvanathan, N. 1978a, *ApJ*, 225, 742
- . 1978b, *ApJ*, 223, 707
- Sarazin, C. L. 1988, *X-ray emission from clusters of galaxies*, ed. Sarazin, C. L. (ESO Cambridge University Press), 13
- Schade, D., Barrientos, L. F., & Lopez-Cruz, O. 1997, *ApJ*, 477, L17
- Schade, D., Carlberg, R. G., Yee, H. K. C., Lopez-Cruz, O., & Ellingson, E. 1996, *ApJ*, 465, L103
- Schlegel, D. J., Finkbeiner, D. P., & Davis, M. 1998, *ApJ*, 500, 525
- Schneider, P. 2006, *Extragalactic Astronomy and Cosmology*, ed. Schneider, P. (SPRINGER), 88–99
- Schombert, J. M. 1988, *ApJ*, 328, 475
- Schwarz, G. 1978, *Ann. Statist.*, 6, 461
- Sérsic, J. L. 1968, *Atlas de galaxies australes*, ed. Sersic, J. L. (ESO)
- Simard, L., Mendel, J. T., Patton, D. R., Ellison, S. L., & McConnell, A. W. 2011, *ApJS*, 196, 11

- Simard, L., Willmer, C. N. A., Vogt, N. P., Sarajedini, V. L., Phillips, A. C., Weiner, B. J., Koo, D. C., Im, M., Illingworth, G. D., & Faber, S. M. 2002, *ApJS*, 142, 1
- Skibba, R. A., Bamford, S. P., Nichol, R. C., Lintott, C. J., Andreescu, D., Edmondson, E. M., Murray, P., Raddick, M. J., Schawinski, K., Slosar, A., Szalay, A. S., Thomas, D., & Vandenberg, J. 2009, *MNRAS*, 399, 966
- Spergel, D. N., Bean, R., Doré, O., Nolta, M. R., Bennett, C. L., Dunkley, J., Hinshaw, G., Jarosik, N., Komatsu, E., Page, L., Peiris, H. V., Verde, L., Halpern, M., Hill, R. S., Kogut, A., Limon, M., Meyer, S. S., Odegard, N., Tucker, G. S., Weiland, J. L., Wollack, E., & Wright, E. L. 2007, *ApJS*, 170, 377
- Springel, V. 2010, *ARA&A*, 48, 391
- Springel, V., White, S. D. M., Jenkins, A., Frenk, C. S., Yoshida, N., Gao, L., Navarro, J., Thacker, R., Croton, D., Helly, J., Peacock, J. A., Cole, S., Thomas, P., Couchman, H., Evrard, A., Colberg, J., & Pearce, F. 2005, *Nature*, 435, 629
- Springob, C. M., Magoulas, C., Proctor, R., Colless, M., Jones, D. H., Kobayashi, C., Campbell, L., Lucey, J., & Mould, J. 2012, *MNRAS*, 420, 2773
- Stadel, J. G. 2001, PhD thesis, UNIVERSITY OF WASHINGTON
- Struble, M. F. & Rood, H. J. 1987, *ApJ*, 323, 468
- Tal, T., van Dokkum, P. G., Nelan, J., & Bezanson, R. 2009, *AJ*, 138, 1417
- Tasca, L. A. M., Kneib, J.-P., Iovino, A., Le Fèvre, O., Kovač, K., Bolzonella, M., Lilly, S. J., Abraham, R. G., Cassata, P., Cucciati, O., Guzzo, L., Tresse, L., Zamorani, G., Capak, P., Garilli, B., Scodeggio, M., Sheth, K., Zucca, E., Carollo, C. M., Contini, T., Mainieri, V., Renzini, A., Bardelli, S., Bongiorno, A., Caputi, K., Coppa, G., de La Torre, S., de Ravel, L., Franzetti, P., Kampczyk, P., Knobel, C., Koekemoer, A. M., Lamareille, F., Le Borgne, J.-F., Le Brun, V., Maier, C., Mignoli, M., Pello, R., Peng, Y., Perez Montero, E., Ricciardelli, E., Silverman, J. D., Vergani, D., Tanaka, M., Abbas, U., Bottini, D., Cappi, A., Cimatti, A., Ilbert, O., Leauthaud, A., Maccagni, D., Marinoni, C., McCracken, H. J., Memeo, P., Meneux, B., Oesch, P., Porciani, C., Pozzetti, L., Scaramella, R., & Scarlata, C. 2009, *A&A*, 503, 379
- Thomas, T. & Katgert, P. 2006a, *A&A*, 446, 31
- . 2006b, *A&A*, 446, 19
- Tonry, J. & Davis, M. 1979, *AJ*, 84, 1511
- Toomre, A. & Toomre, J. 1972, *ApJ*, 178, 623
- Tran, K., Simard, L., Illingworth, G., & Franx, M. 2003, *ApJ*, 590, 238
- Trimble, V. 1987, *ARA&A*, 25, 425
- Trujillo, I. & Aguerri, J. A. L. 2004, *MNRAS*, 355, 82

- Tully, R. B. & Fisher, J. R. 1977, *A&A*, 54, 661
- Tully, R. B. & Verheijen, M. A. W. 1997, *ApJ*, 484, 145
- Valentinuzzi, T., Poggianti, B. M., Fasano, G., D'Onofrio, M., Moretti, A., Ramella, M., Biviano, A., Fritz, J., Varela, J., Bettoni, D., Vulcani, B., Moles, M., Couch, W. J., Dressler, A., Kjærgaard, P., Omizzolo, A., & Cava, A. 2011, *A&A*, 536, A34
- Van den Bergh, S. 1960, *ApJ*, 131, 215
- van den Bergh, S. 1976, *ApJ*, 206, 883
- . 1998, *Galaxy Morphology and Classification*, ed. van den Bergh, S.
- . 2009, *ApJ*, 694, L120
- . 2012, *ApJ*, 754, 68
- Vikram, V., Wadadekar, Y., Kembhavi, A. K., & Vijayagovindan, G. V. 2010, *MNRAS*, 1327
- Visvanathan, N. & Sandage, A. 1977, *ApJ*, 216, 214
- Wadadekar, Y., Robbason, B., & Kembhavi, A. 1999, *AJ*, 117, 1219
- Wadsley, J. W., Stadel, J., & Quinn, T. 2004, *New Astronomy*, 9, 137
- Weinberg, M. D. 2012, *ArXiv e-prints*
- White, S. D. M. 1976, *MNRAS*, 177, 717
- . 1979, *MNRAS*, 189, 831
- White, S. D. M. & Rees, M. J. 1978, *MNRAS*, 183, 341
- Wilman, D. J., Oemler, Jr., A., Mulchaey, J. S., McGee, S. L., Balogh, M. L., & Bower, R. G. 2009, *ApJ*, 692, 298
- Wolf, M. 1906, *Astronomische Nachrichten*, 170, 211
- Yahil, A. & Vidal, N. V. 1977, *ApJ*, 214, 347
- Yee, H. K. C. 1991, *PASP*, 103, 396
- Yee, H. K. C., Ellingson, E., & Carlberg, R. G. 1996, *ApJS*, 102, 269
- Yee, H. K. C. & López-Cruz, O. 1999, *AJ*, 117, 1985